Persistent scatterer interferometry to monitor mining related ground surface deformation for data-driven modelling

Kemeling, Ilona

Persistent scatterer interferometry to monitor mining related ground surface deformation for data-driven modelling

Ph.D. Thesis, November 2006

Ilona Kemeling,

Department of Geography
Durham University

Supervised by

Prof. David N. Petley

Prof. Antony J. Long

Prof. Robert J. Allison

ABSTRACT

The monitoring, interpretation and prediction of gradual ground surface deformation are critical factors in the understanding of earth systems. In many parts of the world, particularly in coastal areas where resources are often easily transportable and where steep cliffs allow access to underlying strata, the patterns of natural ground surface deformation are complicated by mining or extraction activities. To accurately estimate the amount of sea-level rise and its total affect on, for example, frequency of flooding or salt-water intrusion, the amount of ground surface deformation, either subsidence or uplift, need to be understood in great detail. Ground surface dynamics over an area of contemporary deep mining, is investigated through two research objectives.

A feasibility study of conventional InSAR and Persistent Scatterer InSAR (PSI) in a rural setting was carried out. Rural areas are generally avoided for the application of these techniques for the measurement of gradual ground surface deformation due to the lack of coherence between scenes. The results demonstrate that the new PSI technique significantly outperformed conventional InSAR in the detection of gradual ground surface deformation. However, limitations to the technique were identified in the low density and limited distribution of permanent scatterers. The behaviour of the deformation rate over time appears to be biased to a linear trend.

Furthermore, in order to understand the link between underground mining activities and local ground surface response a data-driven model has been developed and evaluated. Based on different mining scenarios, this model is able to estimate the total subsidence in a four dimensional space. It was found that local ground surface deformation can be forecasted accurately, based on an angle of draw and four variables. Five key indicators, which are the extent of the disturbed area, the total period of deformation, the peak rate, the moment of the peak rate and the total deformation, are relevant to understand the impact of underground excavations on the surface and to place it in a wider Earth system.

ACKNOWLEDGEMENTS

In the first year of this research I had the opportunity to work with Mark Bulmer, Research Assistant Professor at the Joint Center for Earth Systems Technology (JCET) in Maryland in The United States. I am thankful to have been given this opportunity and this collaboration was the basis for the rest of the InSAR analysis. Over the following two years of my research I had the privilege to work with Professor Ramon Hanssen and his team, Gini Ketelaar, Petar Marinkovic and Freek van Leijen at the Department of Earth Observation and Space Systems (DEOS) of the Faculty of Aerospace Engineering in Delft, the Netherlands. This team is part of the leading edge of radar interferometry development.

Thanks to the European Space Agency (ESA) Earth Observatory Category-1 Scientific research project, the COBRA project was able to use 36 radar scenes against reproduction costs. The other essential datasets for this research came from CPL. Many interesting discussions with Ian Scott, Allan Williams and other members of the Engineering team at CPL have played a crucial role in the development and outcomes of this research. The excellent cooperation was partly thanks to the external relations officer of CPL, David Pybus.

I am very thankful to my colleagues Dr. Nick Rosser, Dr. Michael Lim, Dr. Stuart Dunning mainly for their good companionship and much appreciated assistance in different stages of this research. In Professor David Petley, Professor Antony Long and Professor Robert Allison I have found very engaging and intelligent supervisors, who helped me in several crucial moments to finish this work. I am especially thankful to Antony for his useful comments in the final stages of this work. And I am grateful for the patience and amount of freedom I was given by them to find my own way.

My parents, sisters and the rest of the family have been very supportive. Most of all I want to thank Karin Viergever for her support, understanding and patience especially in the final stages of this research. I hope to return the favour to her.

TABLE OF CONTENTS

LIST OF FIGURES

LIST OF TABLES

CHAPTER 1. INTRODUCTION

1.1. Research aims and objectives

This thesis presents the results of an investigation into the processes that control surface deformation associated with deep mining. The work forms part of a larger project undertaken by Durham University on behalf of Cleveland Potash Ltd that sought to improve our understanding of the effects of mining-induced subsidence on coastal cliff behaviour. The research detailed in this thesis addresses the temporal and spatial variability in surface deformation associated with mining activities that have occurred since the 1970s. It involves two related aspects.

First, the potential of using remote sensing techniques for resolving surface deformation in the study area is examined. The technique used is Synthetic Aperture Radar Interferometry (InSAR), a method widely used to determine surface deformation in arid or urban areas, but rarely tested previously in rural, temperate latitude settings such as North Yorkshire.

The second aspect of the research entails the development of a data-driven model for predicting patterns of surface deformation based on patterns of known mineral extraction. An extensive dataset of surface monitoring data, collected using conventional levelling surveys since the opening of the mine, provides one element of a unique database suitable for model development. A second dataset relates to the detailed chronology of sub-surface mineral extraction, which provides essential information on the pattern of mining activity itself. When combined, these observations enable the development and subsequent testing of a predictive model in a robust manner. Each aspect of the research has a set of distinct aims:

- The first main objective is to test the use of Synthetic Aperture Radar Interferometry (InSAR) and Persistent Scatterer InSAR (PSI) in a rural and temperate research area experiencing gradual ground surface deformation; and further:
    - To generate an independent monitoring dataset for local gradual ground surface deformation
    - To estimate future rates of deformation based on the generated dataset

Due to coherence loss, rural and temperate areas are mostly avoided and the understanding of the relationship between coherence and land cover is limited. The PSI technique should be more feasible in such areas, because of the application of point scatterers and the unwrapping method of this technique. The actual datasets that result from the PSI technique in areas with low coherence need to be tested.

- The second main objective is to develop a model that can estimate the temporal and spatial behaviour of ground surface deformation based on patterns of known mineral extraction and a dataset of ground-based surface monitoring data; and further:
    - To determine the variables that control a mining-related ground surface deformation process.
    - To analyse the correlation between the variables of a driving process and the variables of a surface deformation process, based on large datasets.
    - To create and test a modelling tool that enables scenario studies and accurate estimations of future ground surface deformation.

The availability of large monitoring datasets such as those generated with InSAR or from annual levelling surveys offers the opportunity to forecast deformation based on past behaviour of the surface.

1.2. Research context

The emerging awareness of the vulnerability of human civilisation to changes in relative sea-levels has placed the study of ground surface deformation processes high on the scientific agenda. Ground surface level is the relative negative of sea-level and is therefore an important factor to consider in sea-level research (Shennan and Horton, 2002). Fluctuations in sea-level can be due to tidal cycles or factors related to climate change such as thermal expansion of ocean waters and the melting of land ice. Climate change is a natural environmental process that has occurred continuously, associated with glacial and interglacial periods (Goudie and Viles, 1998). However, since the invention of the steam engine in 1740, the impact of human activities to environmental systems, and in particular to climate change, has become so significant that this period has been recently referred to as the 'Anthropocene' (Crutzen, 2002).

The ground surface level in the United Kingdom is generally measured relative to the average sea level in Newlyn between 1915 an 1921 (Bannister et al., 1998). The actual sea-level at that location is now approximately 130 mm higher (Fig. 1.1). The rate of sea-level change would correspond with approximately 1.7 mm a^{-1}. This is based on the assumption that the ground surface change in Newlyn was zero over that period.

Threats associated with sea-level rise in coastal areas, such as increase in flooding, shore erosion and salt water intrusion are equally present in the case of ground surface deformation (Carbognin, 1997). The existing knowledge of local ground surface deformation processes is often limited. For mining activity planning in the proximity of vulnerable coastlines, the extent of the area of disturbance and the amount and rate of subsidence over time are important factors to consider.

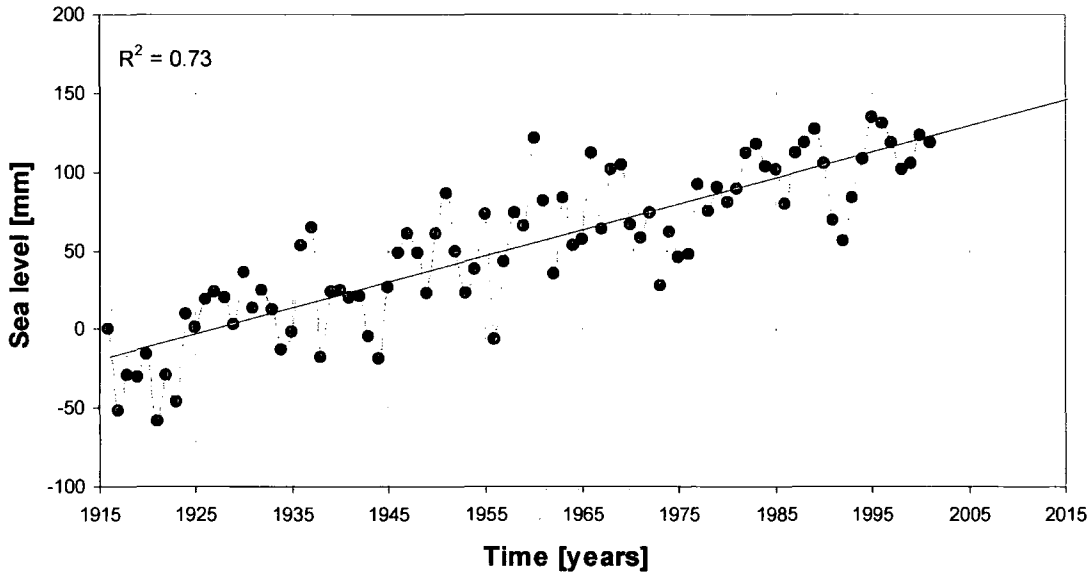

Figure 1.1: Annual sea-level change in Newlyn, Cornwall. Source: Permanent Service for Mean Sea Level (Proudman Oceanographic Laboratory)

Cleveland Potash Limited (CPL) mines at depths of 0.8 to 1.3 kilometres for potash, a rock containing potassium (Fig. 1.2). The mine is situated in the Boulby area, a coastal area in North East England. The amount of material extracted is substantial and volumetric effects migrate to the surface, inducing ground surface deformation (CPL, 1999). The undermined area subsides at maximum rates varying between 40 and 50 mm a^{-1}, reaching a maximum vertical displacement of approximately 70 cm locally (1996-1998 estimation) (CPL, 1999). From the extent of the current mining activities, the total area affected by ground surface deformation is estimated to be 15,000 hectares (150 km^2).

Figure 1.2: Potassium, a mineral used mainly as a component of fertilizer

The Boulby potash mine workings are partly under land and partly under sea in an area with an eroding coastline (Rawson and Wright, 2000). The existing methods of monitoring the ground surface deformation in the Boulby area were able to measure the subsidence based on accurate levelling surveys, resulting in two-dimensional subsidence profiles. A correlation between mining activities and ground surface deformation had not yet been found. It was therefore difficult for CPL to plan future mining activities that would limit the disturbance of the coastline.

Due to the rapid changes occurring in the Anthropocene the dynamic environmental processes taking place in different parts of the Earth system, such as the oceans, the atmosphere and the lithosphere, should be investigated in great detail (Cloetingh et al., 2005). Integration of the monitoring and modelling of such processes at different temporal and spatial scales will increase this understanding and improve our control over Earth's environment. New methods of thinking about these processes, the availability of remote sensing datasets and the increasing processing power of computers provides the opportunity to develop new methods of monitoring and modelling such processes. In addition to the ongoing research of Quaternary and longer-term neotectonics, there is a need for a better understanding of processes in the lithosphere acting at a smaller temporal and spatial scale (Cloetingh et al., 2005).

1.2.1. Modelling of ground surface deformation

Underground mining has taken place in Western Europe since the beginning of the Industrial Revolution in the 18th century and has had a great impact on the English landscape. Thanks to the development of materials and techniques used in mining and an increase in knowledge of the geology, mining is now taking place at considerable depths. The mining subsidence models currently available to estimate the amount of surface deformation caused by underground mining activities were developed based on shallow (<200 m) coal and ironstone mining in the 19th century (Kratzsch, 1983).

Mining companies are legally obliged to monitor the affects of their activities to the surface. In addition the administration of mine plans is increasing in detail and accuracy thanks to advances in surveying technique. The effects of very deep (>1 km) mining on the surface are poorly estimated based on existing models. As a consequence, rather than using models, repeated ground surveys in combination with spatial and temporal interpolation is used to monitor complex gradual surface deformation processes related to deep underground mining. Levelling measurements show that very deep mining causes ground surface deformation that is characterised by a saucer-shaped depression rather than by several troughs located directly above the mine workings. This is different from ground surface deformation related to shallow underground mining activities, where a more direct relationship between mining and surface deformation occurs. The large amounts of surface and excavation data should be applied to increase our understanding of the relationship between the processes underground and at the surface.

It is difficult to predict the area of ground surface deformation and the rate of ground surface deformation caused by extensive deep mining. This is because the rate and extent of closure in the mine workings are different from the ground surface deformation (Abernethy, 2000; Kratzsch, 1983; Whittaker and Reddish, 1989). A data-driven ground surface deformation model would make it possible to estimate ground surface deformation under different mining scenarios. This would enable comparison of the effect of the layout of the mine workings and different mining management strategies on the landscape.

1.2.2. Feasibility of InSAR for monitoring ground surface deformation

In the last decade, a new technique known as Synthetic Aperture Radar Interferometry (InSAR) has become operational. InSAR is a radar remote sensing technique which applies phase difference between two radar scenes with slightly different viewing geometries to accurately measure elevation or elevation change at the surface. The applicability of InSAR has been demonstrated in a number of studies (Carnec and Delacourt, 2000; Gabriel et al., 1989; Massonnet and Feigl, 1998; Raucoules et al., 2003; Rocca et al., 2000; Schmidt and Bürgmann, 2003). However, the applicability of InSAR and more specifically Differential InSAR (DInSAR) is problematic in areas subject to gradual ground surface deformation with a temperate climate and rural land use (Hanssen, 2001). Due to atmospheric disturbances and the rural nature of the land cover, such areas often have a low coherence, or uniformity between neighbouring pixels when InSAR techniques are applied. This

translates into deformation measurements of low accuracy. However, certain structures in a rural setting such as buildings or bare rock can act as permanent scatterers, which translate into groups of pixels that have a high coherence. The Persistent Scatterer InSAR technique (PSI), based on the use of these objects is theoretically better suited to areas with high decorrelation than conventional InSAR (Ferretti et al., 2001; Kampes, 2006). Feasibility studies in of conventional InSAR and PSI will increase our understanding of the limitations of these techniques (Hanssen, 2001; Kampes, 2006).

1.2.3. Available data

The following datasets were available or collected during this research.

- Surface processes: Annual relative elevation change at 258 fixed stations derived from levelling surveys and distributed along roads in the area from 1976 to 2004 (CPL dataset).
- Mining activity: Records of all potash and salt mine panels from 1973 to 2004, including the starting date of mining, the location of the centre and the squared area that was mined (CPL dataset).
- Geology: Data from 26 boreholes in the research area, including the depth of layer boundaries (CPL dataset).
- Radar data: 36 ERS1 and ERS2 single look complex scenes acquired between 9 September 1992 and 17 August 2002 (ESA dataset).

1.3. Conclusion

Development of (radar) remote sensing is often driven by data availability and to a much lesser extent by the actual information demand from data users, such as subsidence engineers. Now that InSAR is reaching operational maturity, the focus should shift towards information demand. In the mining industry a demand for continuous monitoring datasets, which allow for the forecast of future behaviour of the surface, is emerging. One of the limitations of InSAR for continuous monitoring of gradual deformation processes is the loss of coherence in vegetated or wet areas. However, most research takes place in urban areas or dry-land environments. Also, the specific data requirements for data driven subsidence forecast-models is under-examined and should be considered in the development of InSAR techniques.

In this research the feasibility of InSAR is tested in an area affected by mining-related ground surface deformation. Both conventional InSAR and the more advanced Persistent Scatterer InSAR (PSI) are tested in the research area to determine whether a continuous monitoring dataset can be generated that could be used as input to the data-driven subsidence forecast model. The research area has a temperate climate and rural land use and is located on the North Yorkshire coast. Additional aspects of this research are data-driven modelling of an environmental process, advanced GIS techniques and a relational database applied to solve the complex relationship between two dynamic processes.

In chapter two, a review of the existing literature on ground surface deformation is given. The three main disciplines looking at this process from different angles are tectonic geomorphology, subsidence engineering as well as geodesy and remote sensing. Chapter three discusses the research area, its main characteristics and geological history as background to understanding the local ground surface deformation caused by mining activities. The following chapter (four) describes the methodology of the research described in this thesis. In chapter five, the results of both parts of the research are described, followed by a discussion chapter (six). Chapter seven is the final chapter and describes the main conclusions of this research, and gives recommendations for future research.

CHAPTER 2. GROUND SURFACE DEFORMATION, A REVIEW

'Nothing endures but change.'

(Heraclitus (540 BC - 480 BC), from Diogenes Laertius, Lives of Eminent Philosophers)

2.1. Introduction

Ground surface deformation can range from local mine shaft collapse, affecting one house, to gradual plate tectonics that affect the movement of whole continents. These processes can be caused by natural or human activity but are most often caused by a complex combination of several natural and human drivers. The systems of causes and effects of ground surface deformation are complex and the understanding of them is increasingly relevant.

Habitation of more vulnerable areas due to population growth is making people more vulnerable to ground surface deformation processes (Carbognin, 1997). Vulnerable areas include low coastal, steep mountains and areas along the edges of continental plates naturally prone to earthquakes. Underground mining activities that peaked in the 19th century and continue today, are leaving us with a growing heritage of ground surface deformation. Ground surface deformation processes can take place in the form of subsidence, land slides and earthquakes, affecting an increasing number of humans.

The relevance of understanding the dynamic ground surface is further increased in the light of global climate change. Ground surface deformation is an environmental process and is affected by climate. Landslide occurrence is expected to increase as a consequence of more storminess, increased precipitation and the defrosting of permafrost soils in vulnerable mountainous areas (Borgatti and Soldati, 2003). The probable rise of the mean sea-level shall increase the impact of subsidence in coastal areas and increase related problems, such as salt water inflow, coastal erosion and flooding.

To protect ourselves and to understand ground surface deformation, the complexity of the involved processes needs to be understood. Three scientific disciplines study the causes, processes and effects of ground surface deformation. Each has its own perspective and is developing in its own direction: tectonic geomorphology, mining subsidence engineering as well as geodesy and remote sensing. The scale and detail in which these disciplines study surface deformation differs. The question is whether ground surface deformation can be

sufficiently measured and predicted by the existing methods, or whether there is need for a more advanced approach to understanding ground surface deformation.

The discipline of tectonic geomorphology studies the processes, structures and landforms associated with deformation of the Earth's lithosphere (Keller and Pinter, 1996). Although tectonics are mostly associated with processes acting at a global or regional scale, such as continental plate movements, the discipline is developing into more local scale processes including erosion and hazard mapping (Keller and Pinter, 1996). Chronologic dating and modelling of geomorphic processes have increased the comprehension of landscape development and the role of ground surface deformation. The availability of digital elevation data and scenes and the accessibility of high speed computing have been identified as current key drivers of development in tectonic geomorphology (Burbank and Anderson, 2001).

Focussing on a more local scale, is the discipline of mining subsidence engineering. Subsidence is defined as land-surface sinking as a consequence of withdrawal of fluids or extraction of solids by humans through mining or as a consequence of natural processes in the ground such as hydro-compaction of sediments and oxidation and shrinkage of organic deposits (Thomas and Goudie, 2000). The main interests of this discipline are safety and profitability inside the mine and the potential damage to the human environment outside the mine. Developments in subsidence engineering include statistical and numerical modelling of ground surface deformation (Ambrožic and Turk, 2003; Chrzanowski et al., 1997).

The third discipline studying ground surface deformation is geodesy and remote sensing, which stems from a different background of geometric and gravimetric analysis (Hanssen, 2001). This discipline is mainly interested in improving the accuracy and reliability of measurements of ground surface movements. Recent developments in remote sensing methods and greater availability of data have increased the spatial scales over which geodesy measurements can be performed.

An important section in this chapter contains the description of new ground-based and remote sensing techniques for ground surface deformation such as radar interferometry (InSAR). The common concepts and methods of monitoring and modelling of ground surface deformation are discussed. The existing knowledge of natural and anthropogenic

drivers of ground surface deformation is reviewed. Additionally, conclusions will be drawn regarding the main problems in understanding and predicting ground surface deformation.

2.2. Gradual ground surface deformation

The focus of this thesis will be gradual (1-100 mm a^{-1}) ground surface deformation acting at a local scale (500-5,000 km^2). Many subsidence processes caused by deep underground mining, ground water and gas extraction demonstrate this type of gradual local ground surface deformation. To explain the specific characteristics and relevance of local gradual ground surface deformation three examples will be described. These examples were chosen, because of their rate and scale of deformation, the proximity of the sea or the applied methods of monitoring and modelling, comparable to the conditions of the Boulby research area described in chapter three.

In the Permian Zechtein basin, close to Boulby lays the Selby coalfield in Yorkshire (Fig. 2.1). Subsidence is taking place at a higher rate and in a smaller area (Stow and Wright, 1997). The majority of the area is less than 50 metres above sea level and comprises a flat river plain.

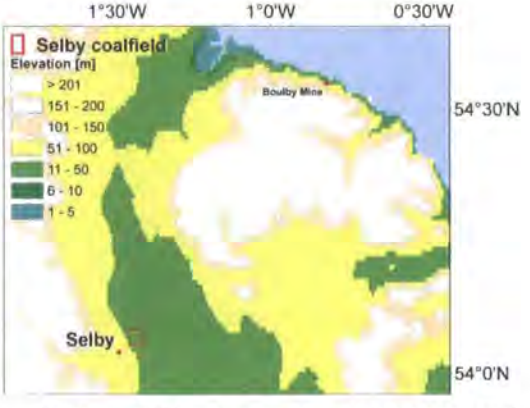

Figure 2.1: Approximate location of Selby coal field, elevation from GTOPO30, city from ESRI world dataset 2002.

The coal was excavated from the Upper Carboniferous (Westphalian) strata of the Upper and Middle Coal Measures Groups located at a depth of 550 m, overlain by Permian Magnesian Limestone and Triassic Sandstones (Al-Rawahy and Goulty, 1995; Burke et al., 2005; Wright and Stow, 1999). The excavations took place in three separate mines, all measuring a width of approximately 250 metres (Fig. 2.2).

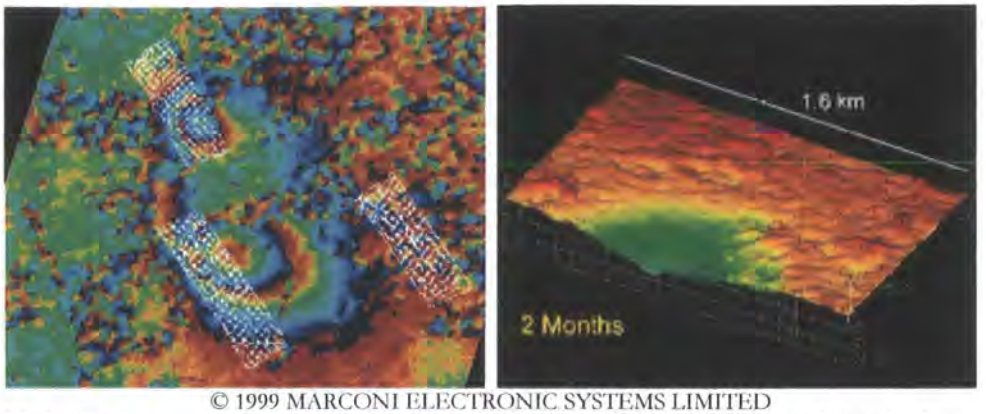

Figure 2.2: An interferogram of two SAR scenes with a temporal baseline of 35 days (left) overlaying the three mines in the Selby coalfield, three-dimensional model based on layer stacking showing the subsidence in a subset after two months (Wright and Stow, 1999).

The extent of the Selby coal mining complex was approximately 285 km^2 when it closed in May 2004 (Wright and Stow, 1999). To monitor the affect of the mining on the surface, levelling surveys were conducted on a six-monthly interval, during operation. In 1999, a study was done to test the feasibility of new InSAR techniques to monitor the subsidence and to improve the reliability of empirical models and subsidence estimations (Wright and Stow, 1999) (Fig. 2.2). One of the conclusions of this research was that it was not possible to use conventional InSAR for a period longer than 35 days, due to loss of coherence. An InSAR technique that was used to extent the monitoring interval was layer stacking. This technique has resulted in a time series of deformation measurements in the winter period, but failed to cover the growing season due to high temporal decorrelation.

A second example of local subsidence is found in the area of Venice, Italy. Subsidence of the lagoon causes increased impact of marine erosion and salt water intrusion and flooding occurs frequently (Carbognin et al., 1995). Induced by the historic value of the city of Venice, several studies have been conducted to monitor and model the subsidence. The extent of the Venice Lagoon and valley is approximately 3,000 km^2 (Fig. 2.3).

Aquitard compaction caused by groundwater withdrawal from the upper 300 metres of the unconsolidated Quaternary sediments, between 1950 and 1970 is found to be a driver of subsidence (Teatini and Gambolati, 1995). To model the subsidence caused by groundwater withdrawal, a finite element model is developed. The thickness of the combined ground layers used in the model is 100 metres. The three dimensional nonlinear numerical model consist of two parts, a three-dimensional flow model and a one-dimensional compaction model. The model was calibrated using levelling data from 1952 to 1973 (Teatini and Gambolati, 1995). In addition, research has suggested that natural land

subsidence of 10 mm a^{-1} acts in the coastal area of Venice. The combination of ground water extraction and construction activities was thought to have increased the subsidence rate to approximately 16 mm a^{-1} in the 1990's (Carbognin et al., 1995).

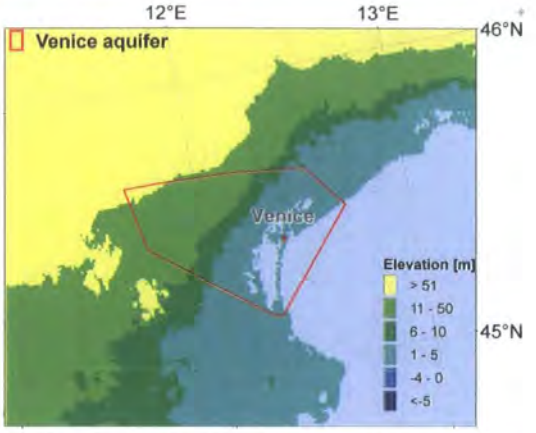

Figure 2.3: Approximate location of Venice aquifer, elevation from GTOPO30, city from ESRI world dataset 2002.

To determine appropriate measures to alleviate flooding in the city of Venice, more research was conducted in recent years, combining levelling survey data with measurements from different InSAR techniques. In contradiction with earlier studies InSAR measurements of Venice city showed a current stability of the surface. In the monitoring period between 1992 and 1996, an annual rate of between -2 and +1 mm a^{-1} was measured (Fig. 2.4).

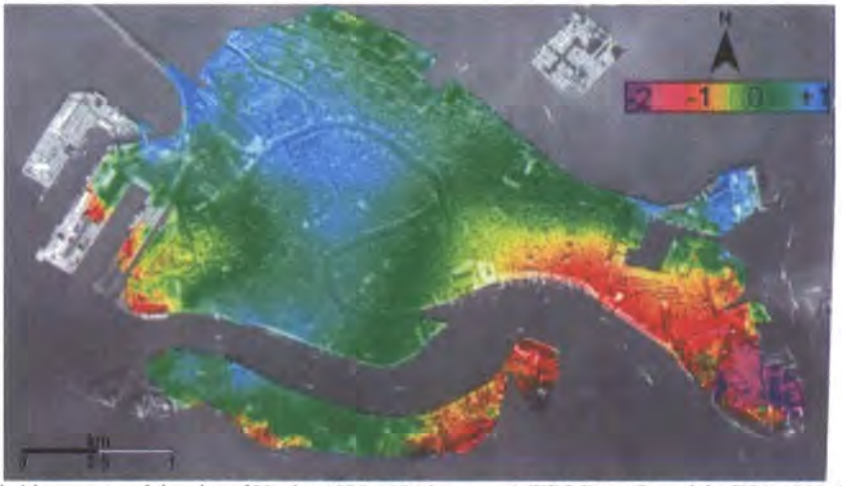

Figure 2.4: Subsidence rate of the city of Venice 1992-1996 in mm a^{-1} (ERS Data Copyright ESA 1998, Processing by GAMMA)

As a result of these findings, subsidence was ruled out as a mayor cause of the increased frequency in flooding of Venice. This is more likely to be related to sea-level rise and climate change related factors (Strozzi et al., 2003; Tosi et al., 2002).

Another example is the subsidence process in Groningen, the Netherlands (Fig. 2.5). Gas extraction since 1964 has caused subsidence over an area of approximately 2,000 km^2. Gas is extracted from a depth of 2900 m. below sea level. Soil compaction caused by surface water fluctuations over short distances is an extra driver for ground surface deformation. To determine the effect of gas extraction the area has been monitored using levelling surveying techniques and GPS at a 5-yearly interval. Based on this monitoring, the gas related subsidence is found to have a low gradient over space in the order of 0.1 mm a^{-1} km^{-1}. The total maximum subsidence is expected to stabilise at 340-450 mm in the year 2050 (fig2.2)(NAM, 2000 in (Hanssen, 2001).

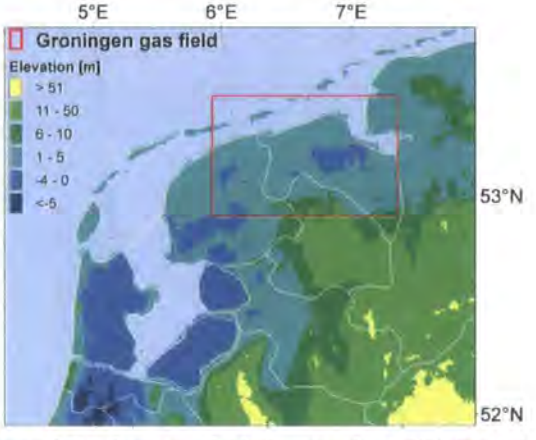

Figure 2.5: Approximate location of Groningen gas field, elevation from GTOPO30, boundaries from ESRI world dataset 2002.

Despite the low rate of subsidence this amount of lowering of the surface can have a considerable impact on the environment in this area. The elevation in this part of the Netherlands is under or close to sea level (Fig. 2.5). The land use in the area is mainly improved grassland and is vulnerable to flooding and salt water intrusion. In some cases damage to drainage structures has taken place (NAM, 2000).

The accuracy of the used monitoring technique is estimated for levelling to be 1,2 mm x distance in km and for GPS to be 2.0 mm + 2.0 mm x distance in km (NAM, 2000). Despite the high accuracy of the measurements, the existing monitoring method fails to measure the spatial and temporal variation in the area, essential to measure the impact on the environment. The model used to estimate the subsidence caused by gas withdrawal is an empirical compaction model based on parameters from laboratory compaction experiments, which are likely to differ from in situ parameters (Fig. 2.6) (NAM, 2000).

To improve the understanding of the temporal and spatial variation of the deformation process and to improve the empirical model a large dataset was required. For this reason, different InSAR techniques have been tested in the area (Bree et al., 2000; Hanssen, 2001; Kampes, 2006; Ketelaar et al., 2005; Kooij et al., 1995). The environmental conditions in Groningen are comparable with the Boulby area, the land use is rural and they both have a coastal location and a temperate climate. The geology is largely comparable between the two locations. Both areas are located in the late Permian Zechstein basin and have a sedimentary geology and sedimentation took place mainly in the Triassic and Cretacious. However, the Boulby area has experienced massive erosion and uplift in the Triassic and Jurassic periods. During the Pleistocene part of the Quaternary, both areas were affected by glaciation.

The application of PSI in the Groningen area has resulted in a valuable monitoring dataset (Ketelaar et al., 2005). The main problem in this area is the limited a-priori understanding of the spatial and temporal variation of the ground surface deformation process caused by gas withdrawal. Therefore it is found difficult to separate this deformation from deformation caused by other deformation processes such as the swelling of clay soil.

The methods to monitor and model subsidence used in the above examples, are similar to methods used for other ground surface deformation processes. In anthropogenic subsidence processes, much of the environmental variables are equally unknown and complex as in landslide or earthquake processes. The advantage in the case of mining is that the drivers of deformation, which is the removal of material, are generally well monitored and much better quantifiable than for example the processes taking place between tectonic plates causing seismic waves and earthquakes.

As seen in the examples, gradual ground surface deformation with rates of a few centimetres per annum can have a significant effect on the local human and natural environment. The effects of such deformation on the topography of the landscape can change the stability of structures on the ground surface, can change the hydrology and ecosystems and can change the equilibrium of slopes and latent landslides.

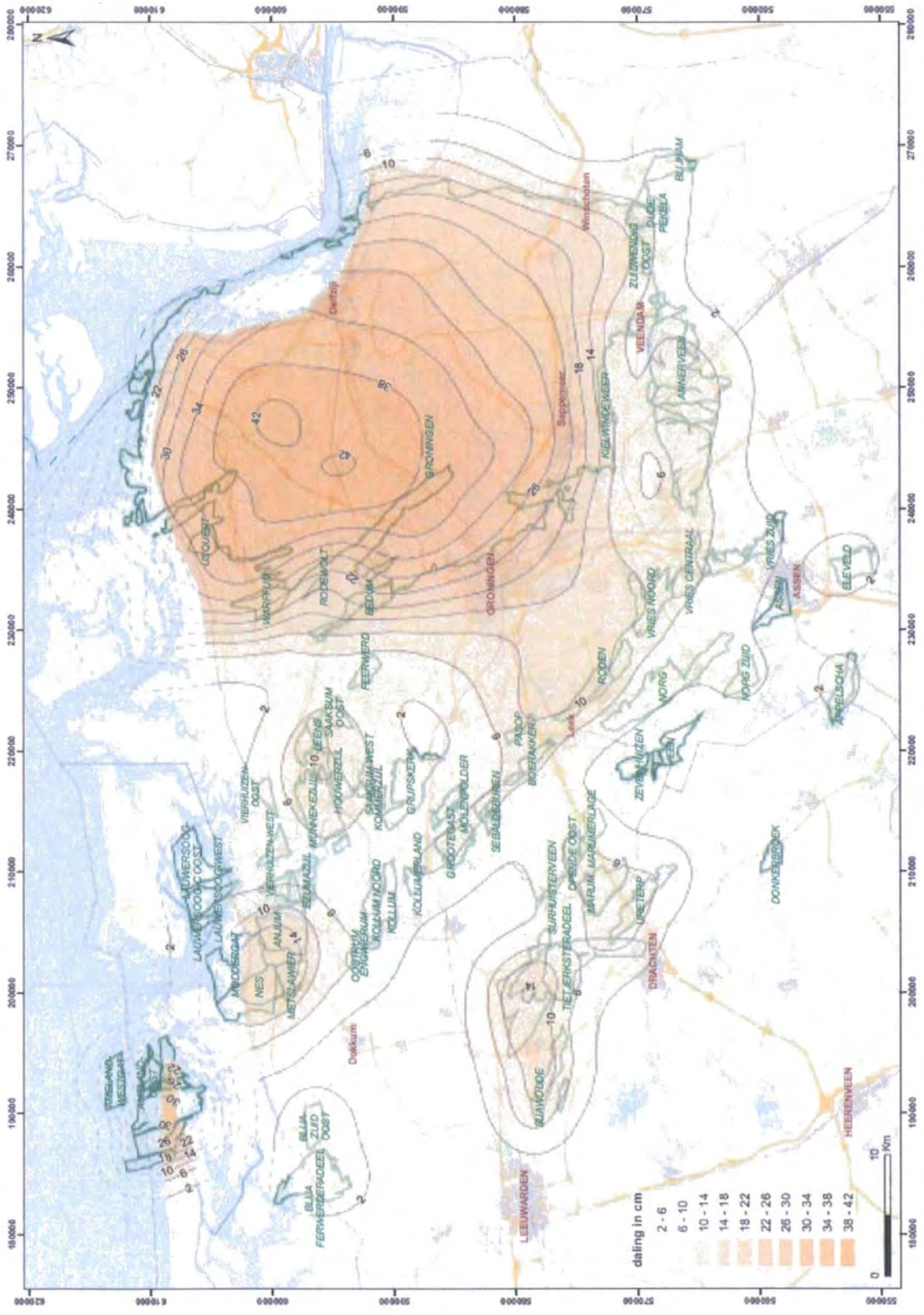

Figure 2.6: Estimation of total subsidence in cm, in Groningen gas field.

A common problem found in the investigation of ground surface deformation processes is the limited feasibility of InSAR. Lack of coherence especially during the growing season in

areas with rural land use has often resulted in the rejection of InSAR as an alternative to labour intensive levelling surveys. Interestingly, the occurrence of ground surface deformation over underground mine workings is an important consideration in land use planning and as a result these areas are rarely used for urban development. There is a need to develop an InSAR technique, such as PSI to increase its feasibility in temperate and rural areas.

PSI has been found feasible in an area with a rural land use and low coherence. However, a lack of understanding of the spatial and temporal variation of the observed deformation process and a high spatial variation in deformation related to clay swelling has caused difficulties in the filtering of valid observations. In addition, a method needs to be developed to understand the spatial and temporal variation of the measured ground surface deformation, in relation to the causing drivers.

2.2.1. Key indicators of ground surface deformation

Due to the complexity of ground surface deformation experienced at a certain area, it is helpful to use key indicators to quantify the effect of an individual process and in the case of human drivers pre-calculate the impact of planning decisions on the environment (Brimicombe, 2003). The following five key indicators are used in this research as a tool to quantify ground surface deformation and to evaluate the performance of different modelling methods. The viability of a modelling method depends on the ability to predict these key indicators.

The five key indicators are:

- The outside shape of the subsidence area: a shape along the outside of the disturbed surface area, where the ground surface is unaffected.
- The total subsidence profile: the magnitude profile of the subsidence area after the moment of recovery.
- The moment of recovery: the date at which the disturbed ground surface area has returned to a stable position [date].
- The maximum rate: the maximum deformation rate of the disturbed ground surface area in distance of vertical change over time [mm a^{-1}].

- The moment of maximum rate: the time at which the disturbed ground surface area has first reached the maximum deformation rate [date].

Factors such as scale, dimensionality and resolution in which the key indicators are expressed will be different for each monitoring and modelling method. In general the higher these factors are, the more information about the deformation process is known. There is a strong correlation between these factors in the applied monitoring method and the possible statistical modelling methods. Three dimensional data driven modelling at high resolution requires three dimensional monitoring at a comparable resolution (Chilès and Delfiner, 1999).

2.3. Drivers of ground surface deformation

Ground surface deformation measured at a specific site at a specific time can be the result of several deformation drivers which act on different temporal and spatial scales. In the examples given in the previous section, it was made clear that gradual ground surface deformation is often caused by a combination of drivers. Based on intensity, duration and extent, a quantitative classification of ground surface deformation drivers can be made (Fig. 2.7).

In the diagram, six types of ground surface deformation processes are compared to gradual mining subsidence. Each process is placed in a box, which is connected to three scales by lines. In relation to gradual mining subsidence, top-soil erosion occurs in a smaller spatial extent, such as a single hill-slope or gully. The intensity or rate of deformation is comparable and is likely to be measured in mm a^{-1}, while the duration of this process is longer and can continue for thousands of years, assuming there is no sudden change in the local land-cover, hydrology or slope angle. Another type that occurs on a smaller extent but with a much higher intensity and shorter duration is the more common type of mining related subsidence, caused by mine-roof collapse.

Processes that influence the measured deformation at a similar or lower intensity, that cover a much larger extent are isostatic adjustment and tectonic uplift. While volcanic and regional earthquake activity usually has a much higher intensity, larger extent and shorter duration (Fig. 2.7). The actual impact of any type of deformation is not merely determined by the power of the drivers, but also by environmental resistance, such as geology, land cover and relief (Burbank and Anderson, 2001). To distinguish between drivers caused by

anthropogenic activity such as mining or by other energy such as volcanic processes, drivers are classified as anthropogenic or natural drivers.

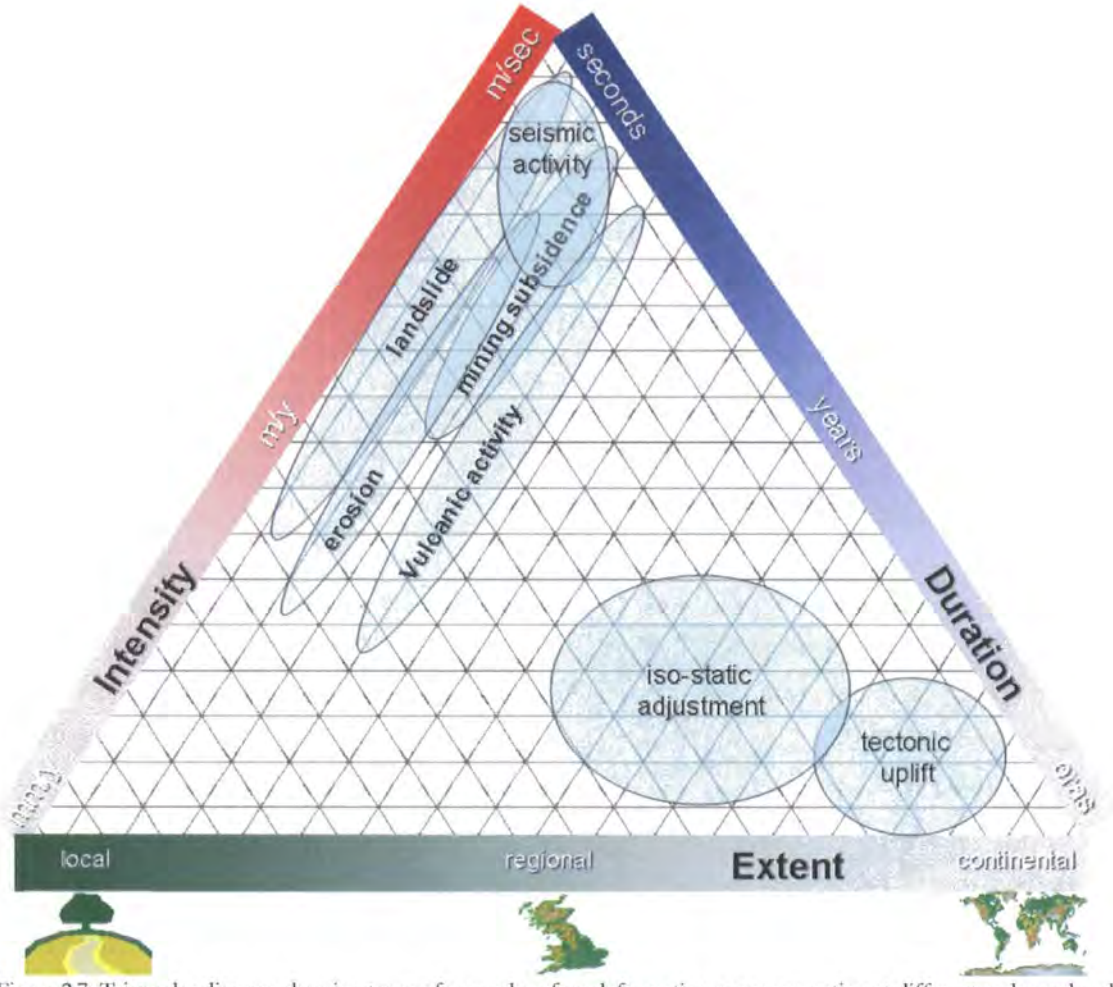

Figure 2.7: Triangular diagram showing types of ground surface deformation processes acting at different scales ordered by intensity, duration and extent.

In a hypothetical situation where an area is experiencing continuous top-soil erosion at rates of up to 20 cm per annum, an occasional landslide and continuous isostatic rebound, the total experienced and measurable vertical deformation would be the sum of the three processes (Fig. 2.8). In the example in Figure 2.8 there appears to be no equilibrium between processes causing uplift and processes causing subsidence. The erosion and landslide are causing much more subsidence than the isostatic adjustment causes uplift. However, looking on a different time-scale both the erosion and landslide can be seen as a reaction of the ground surface to a long period of uplift caused by isostatic adjustment. Even though the three processes in Figure 2.8 are caused by different drivers and may act

on different temporal and spatial scales, they are interrelated and can not be seen as independent or isolated processes.

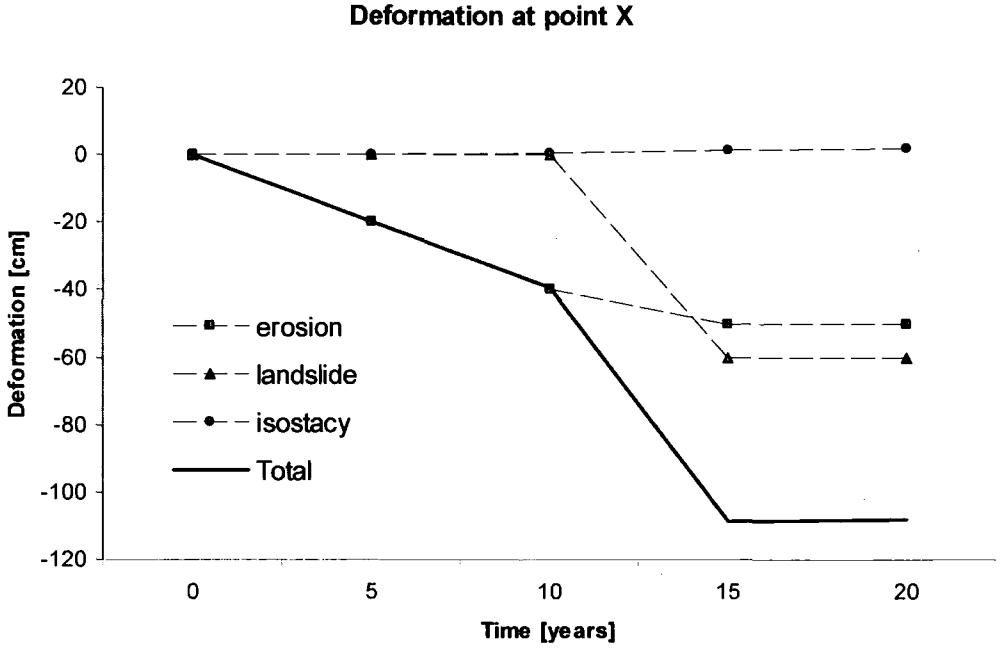

Figure 2.8: Graph of hypothetical deformation related to three different processes during a 20-year period.

Processes acting at different temporal and spatial scale may affect the accuracy of the monitoring and modelling data or may influence the deformation process of interest and should therefore be taken into consideration. The two techniques used to monitor the ground surface deformation in Boulby, levelling and Persistent Scatterer InSAR (PSI), both measure the relative deformation to chosen points of reference.

By choosing the location of the reference points to be in an area unaffected by the studied process, but equally affected to processes acting at a larger spatial scale, this problem can be limited. Processes acting on a smaller spatial scale, cause variation within the research area and will reduce the accuracy of the monitored data regarding the deformation process of interest.

The same is valid for processes acting at a different timescale. If deformation is measured relative to a certain point in time continuous longer term processes would have little influence on the monitoring and modelling of the process of interest and shorter term processes might negatively affect the accuracy.

The formation of continents and oceans is caused by natural ground surface deformation acting on a global scale, with a low intensity but a long duration. Natural co-seismic

deformation can be linked to two types of forces: those acting on the edges of plates (plate boundary forces) and those acting on the base of plates (basal forces). Horizontal movement between plate boundaries is mostly related to earthquakes (Bennett et al., 2003). Sub-duction of continental plates can lead to a range of deformation processes, including gradual mountain building (orogeny) and sudden volcanic eruptions.

In contrast, natural earthquakes can cause local deformation to the ground surface at extreme high intensity and short duration (Fig. 2.7) (Keller and Pinter, 1996). The focuss of this research is on processes with a predominatly vertical component, such as isostasy, settlement and cavity collapse. These three drivers will be discussed in this section.

2.3.1. Isostasy

The rigid outer crust of the Earth or lithosphere floats on the easily deformable asthenosphere, capable of viscous flow. The removal of weight on the lithosphere causes the ground surface to rise gradually in order to recover isostatic equilibrium, due to buoyancy forces. Isostatic dynamics mostly act in a vertical direction and are generally correlated to variations in the density and thickness of the lithosphere (Summerfield, 1991). However, local isostatic rebound can be caused by processes such as moving ice-sheets, extensive erosion or sedimentation and volcanism (Watts, 2001).

Throughout the late Tertiary and Pleistocene periods, the United Kingdom was covered completely or partially by ice masses during a large number of glacials. The reason for isostatic subsidence is the rigidity of the lithosphere. Uneven coverage of the UK during the last glacial and therefore uneven rebound is causing the UK to tilt slightly, causing both uplift and subsidence. The rate of glacio-isostatic maximum land subsidence in The UK is estimated to be -1.2 mm a^{-1} in southwest England. The maximum glacio-isostatic land uplift is estimated to be +1.6 mm a^{-1} in Central Scotland. The Boulby research area is located near the pivot line between these two extremes and is estimated to experience a relating land subsidence rate of -0.17 mm a^{-1}. These rates have been decreasing since the retreat of its last ice coverage, gradually reaching isostasy (Shennan and Horton, 2002).

2.3.2. Cavity collapse

In limestone terrains the sudden collapse of cavities, which develop due to dilution of the limestone, is a common process. Occasionally a similar collapse takes place over lava tubes in lava flows (Summerfield, 1991). Depending on the amount of flexibility in the upper

ground layers and the depth of the seam, mining of solid materials can lead to cavity collapse.

2.3.3. Settlement

Settlement can be caused by lowering of the water table, either naturally or due to ground water withdrawal which will change the bearing capacity of the surface. Extraction of oil, gas or solubles has a similar effect. An example of organic soil subsidence as a consequence of the drainage of organic soil is measured at Holme Fen in England, which has subsided a total of 2.05 metres since drainage began in the 17th century (Stephens et al., 1984). The subsidence is partly due to the change in water pressure and loss of soil texture, and partly due to chemical and physical erosion and can cause problems for agricultural production. Another cause for settlement to occur is the decay of permanently frozen subsoil (permafrost) into thermokarst, a swampy depression.

Deep underground mining of solid materials can also cause settlement of the overlying layers. Excavation of materials from a layer can change the distribution of stresses in the ground. Restoration of the equilibrium after disturbance of the stress fields can either take place suddenly by means of an earthquake-like tremor or more gradually similar to settlement.

In early mining subsidence models it was assumed that the volume of subsidence equalled the total extracted volume. However, this is found to be incorrect due to lateral movement of material and the partial irreversibility of deformation processes in the ground (Kratzsch, 1983). Deformation differs for successive layers from the floor of the seam to the loose surface layer. In the case of deep underground potash mining, the complex deformation process is controlled by physical aspects of the lithology. The displacement at the seam migrates through the overburden rock body to the surface (Fig. 2.9).

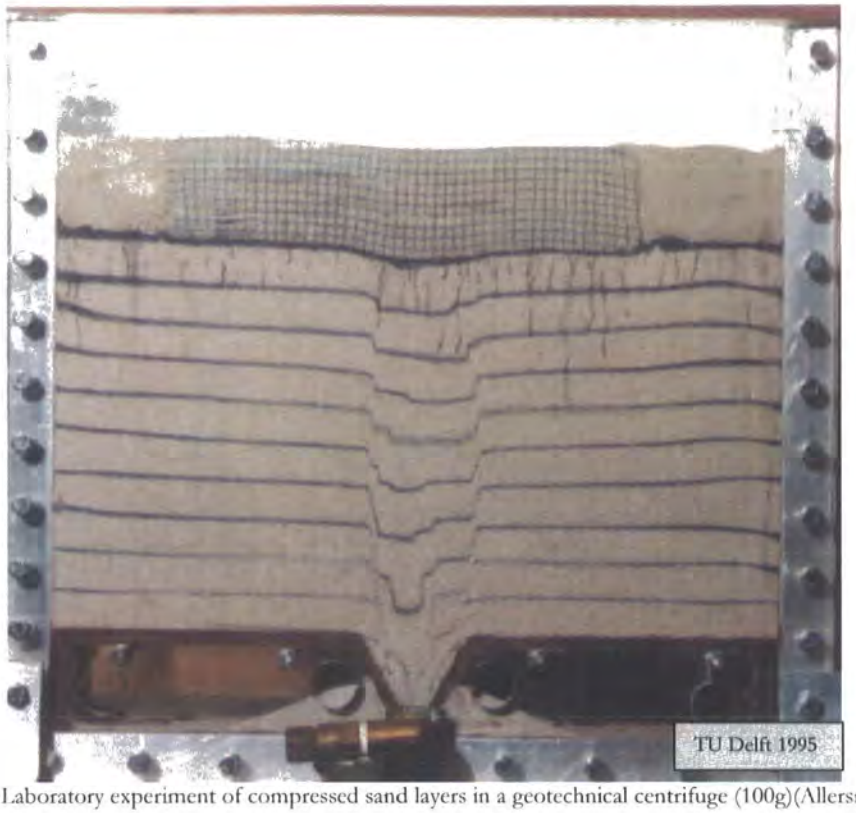

Figure 2.9: Laboratory experiment of compressed sand layers in a geotechnical centrifuge (100g)(Allersma, 1995).

In the experiments done by Allersma (1995), compacted sand and clay layers are placed in a layered sequence divided by a thin layer of colouring, inside a geotechnical centrifuge. By increasing the g-force, the pressure in the test layers is made comparable to the in-situ pressure underground.

Potash deposits in the Boulby area (chapter three) occur at depths between 1,200 and 1,500 m. At these depths, the stress exerted by the undermined rock body exceeds 30 MPa .

Equation 2.1 (source: Kratzsch 1983):

$$p = h \times \rho \times g$$

Where p is pressure [Pa], h is height [m^3], ϱ is density [kg/m^3] and g is the acceleration due to gravity [m/sec^2]. The behaviour of settlement of ground layers under large pressure is complex and depends on the nature of the ground material, but also the presence of faults (Allersma, 1995).

2.4. Monitoring ground surface deformation

The direct cause of potential movement and hazard is potential energy, which can be estimated based on actual movement by means of data collection and measurement of real world processes. Up to the 1990's, monitoring of ground surface deformation has been

limited to the use of ground-based techniques, and more recently the use of the Global Positioning System (GPS). Ground-based geodetic techniques such as triangulation, trilateration and spirit levelling are limited by the facts that they require accessibility of the area of interest and clear lines of sight as they are based on the repeated measurement of distances and angles between devices (Bannister et al., 1998). Expensive terrestrial monitoring surveys are only regularly undertaken in limited areas with high risk of ground surface deformation. The successful measurement of earthquakes is often a coincidence and based on limited observation points.

Remote sensing techniques, where the observations are taken from a position at a certain distance from the process, have begun to be used more intensively since the 1980's and have increased the understanding of geophysical processes considerably (Rawson and Wright, 2000). In specific situations remote sensing techniques are preferred over ground-based geodesy: in ground deformation processes that occur over large areas and show considerable variability in deformation over short distances, for example earthquake ruptures; in ground deformation processes that show considerable complexity over time, for example mining subsidence and in ground deformation that takes place in inaccessible areas, for example steep landslides (Bürgmann et al., 2000).

2.4.1. Ground based techniques in subsidence monitoring

Surveying can be defined as the technique used to measure relative positions of natural and artificial features and the geographical or numerical representation of this information (Bannister et al., 1998). The collection and maintenance of topographic data used as input data for maps, is the most common use of surveying. A specific type of surveying is levelling surveying, where height differences at a series of points relative to the height at a selected initial point are measured.

The definition of elevation or height is the vertical distance between a point and a certain datum. In the United Kingdom the generally agreed datum is the Ordnance Datum Newlyn, sea level measured over a period of six years from 1 May 1915 in Newlyn, Cornwall. Elevation is expressed as Above Ordnance Datum (AOD). Elevation can also be measured to a worldwide reference surface such as the geoid. The geoid is the assumed mean sea level if the Earth was only covered by seas, this would equal the gravitational force of the Earth (Bannister et al., 1998).

2.4.2. Radar remote sensing

Since the turn of the millennium, the interest in radar remote sensing has grown exponentially. A significant increase in the number of available datasets and demand from scientific and other communities has resulted in an increase in the impact of radar remote sensing to the understanding and management of our planet (Woodhouse, 2006). Radar remote sensing is the technique of using waves from the micro-wave part of the electro magnetic spectrum to measure characteristics of objects at a certain distance from the sensor, resulting in imaging data.

The history of radar remote sensing starts in the 19th century and is to a large extent independent of the history of optical remote sensing, which uses visible and near visible waves. Where optical remote sensing seems to have developed from photography, radar remote sensing has more probably developed from other experiments with electro-magnetic waves (Woodhouse, 2006).

The first optical remote sensing scene was made in 1858 by Tournachon, using a camera elevated to approximately 365 m by means of a balloon. Around the same time, the theory of electromagnetic waves was developed by Maxwell and published in 1873 as "Treatise on Electricity and Magnetism". Based on the then existing knowledge on the behaviour of light, magnetism and electricity, he discovered that all three behaved like oscillating waves and were part of the same phenomenon. The electromagnetic wave theory was first tested by experiment in 1886 by Hertz, confirming Maxwell's findings. He also discovered radio waves and their ability to reflect and scatter (Hanssen, 2001).

The knowledge of electricity and magnetism travelling as waves with the ability to create light led to the further discovery of large (micro) wave transmission and radio in the beginning of the 20th century by Marconi and others. During that time ships in the Arctic used a technique called echolocation to detect icebergs, based on the return time of a sound pulse made by a whistle or horn. The ability to use radio waves to detect obstacles was patented by Gernsback in 1904, who built the first radio obstacle detector. The scientific background of this technique was further developed by Marconi and others in the following decades. Between 1919 and 1935, research in radio wave techniques by Watson-Watt, Wilkins and Appleton focussed on the effect of disturbances and layers in the atmosphere on the radio signal (Woodhouse, 2006).

In 1935, the Scottish scientist Watson-Watt patented a device able to measure the location and range of airplanes using radio wave pulses. The interest in radio detection applications grew from 1930 onwards, pushed by the inter-bellum and war politics in Western Europe. Application such as the measurement of movement of objects and imaging radar remote sensing were developed in secret and probably in different laboratories at similar times.

The name Radio Detection and Ranging (radar) is attributed to the US Navy, who developed similar techniques around 1940. During the Second World War radar remote sensing was used extensively by both the Allied, and German forces to detect hostile aircrafts and approaching weather fronts (Boog et al., 2006). From 1944 radars were mounted on aircraft.

After the war the development of radar continued for military applications as well as for meteorology and astronomy. In the 1960's several major discoveries by Bell, Penzias, Wilson and others about our solar system were based on passive radio astronomy and active radar astronomy. In 1961 the distance between Venus and The Earth was measured using radar.

The development of radar for military reconnaissance in aircraft eventually led to the development of imaging radar, where radar measurements were registered on photographic paper. The first imaging remote sensing radars were Side Looking radar (SLR) sensors.

The spatial resolution of SLR was limited, making radar unsuitable for applications that require resolutions of 20 metres or less (Ferretti et al., 2000a). In 1952 the Synthetic Aperture Radar (SAR) technique was developed, based on Doppler beam sharpening, discovered by Wiley. In a SAR instrument, the physical antenna of the SLR was replaced by an artificial antenna using the Doppler shift in echoes. This increased the spatial resolution of radar scenes (Bamler, 2000).

Despite extensive post war interest and investment in military applications, it was only in 1967 that airborne imaging radar was used for civilian mapping purposes. The first mapping expeditions carried out with airborne radar were of cloud covered tropical forests, not mapped previously. Between 1978 and 1981 the first radar instruments were sent to space on the Russian satellite Cosmos 243 and the American satellite Nimbus-5. These first space borne radar remote sensors were used to observe the atmosphere for meteorological applications. Later, more research was done on the possibilities of imaging radar remote

sensing leading to more missions with modified sensors aimed at a growing range of applications (Table 2.1).

Table 2.1: Satellite missions with SAR sensors (Hanssen, 2001), (Woodhouse, 2006). A question mark after a year indicates a planned mission at the time of publication of this thesis.

Mission	Year	Countries	Bands	Main application
Seasat	1978	USA	L	Ocean monitoring and research
SIR-A	1981	USA	L	Land research and topography
SIR-B	1984	USA	L	Land research and topography
Cosmos 1870	1987-1989	USSR	S	Military intelligence
ALMAZ	1991-1992	USSR	S	Military intelligence
Magellan	1989-1992	USA	S	Mapping of Venus
Lacrosse-1,2,3	1988/91/97	USA	S	Military intelligence
ERS-1	1991-2000	Europe	C	Monitoring polar oceans and ice
JERS-1	1992-1998	Japan	L	Earth remote sensing and topography
ERS-2	1995-2002	Europe	C	Environmental monitoring
SIR-C/X-SAR	1994	USA/Italy/Germany	L/C/X	Oceans, ecosystems, hydrology, geology, rain and clouds
Radarsat	1995-	Canada	C	Environmental monitoring
SRTM	2000	USA/Germany	C/X	Digital elevation model
ENVISAT	2001-	Europe	C	Environmental monitoring
ALOS	2006-	Japan	L	Environmental management and disaster monitoring
Radarsat-2	2006?-	Canada	C	High resolution mapping, deformation monitoring.
TerraSAR-X	2006?-	Germany	X	High resolution mapping, deformation monitoring.

From the main applications mentioned in the above table, it appears that the possibilities of radar remote sensing have become more versatile and are driven by technological advancements as well as political agenda.

The three SAR missions of the European Space Agency (ESA) are ERS-1, ERS-2 and most recently Envisat. ESA has been able to establish a continuous C-band radar dataset from 1991, currently covering a period of 15 years with a revisiting time of 35 days. The first satellite ERS-1 was originally designed to look at polar oceans and ice and operated for a period of 9 years. Driven by the quality and quantity of the data, more applications were

discovered. The second satellite ERS-2 was launched in 1995 and operated in tandem mode with ERS-1 for 9 months (Fig.2.10) (Hanssen, 2001).

Figure 2.10: Artist impression of the ERS tandem mission in 1995-1996 (©DLR)

The tandem mission was set up to create tandem scene pairs with one-day temporal baseline. From early experiments with ERS1 scenes the potential of differential InSAR (DInSAR) for deformation monitoring was acknowledged and with that two important factors of disturbance were recognised, topographic distortion and temporal decorrelation. The tandem scene pairs have a low temporal baseline of 24 hours, during which period the temporal decorrelation and ground surface deformation is likely to be low. The interferograms derived from tandem pairs are often used to subtract the topographic distortion from differential interferograms. This will be discussed in more detail in chapter five.

Initially the development of space borne radar remote sensing was driven by the USA and USSR. Besides genuine scientific curiosity, space missions were aimed at military reconnaissance and meteorology, probably driven by the Cold War on one side and large agro-economic interest of the USA and USSR on the other side. While early discoveries were led by Western European scientists, involvement of the USA and USSR after the second world war and later Japan has induced the establishment of the radar remote sensing science. Currently a new revolution in the radar remote sensing science is taking place driven by environmental awareness and a sense of vulnerability to processes such as climate change and earthquakes.

Development of airborne radar remote sensing has continued along side space borne radar remote sensing and currently has many applications, including airborne InSAR and polarimetry (Woodhouse, 2006). Because observations are taken at lower elevation, radar waves are less affected by atmospheric disturbance and the spatial resolution is higher. As a consequence, P-band InSAR, currently not feasible at acceptable resolution from spacecraft is possible from aircraft, allowing ground elevation measurements in vegetated areas. Airborne DInSAR is difficult because it would require repeated flights following fixed flight paths that are monitored accurately. Also the extent of surface area covered by aircraft is smaller.

2.4.3. Main characteristics of radar remote sensing

Reasons for the growing interest in radar remote sensing are the specific characteristics of the electromagnetic waves, which have a larger wavelength than visible light. Radar remote sensing has five main properties that separate this technique from optical remote sensing:

- Radar is an active remote sensing technique and works independent of sunlight;
- Microwaves used in radar penetrate most atmospheric distortion and some canopy, snow and soil, depending on the wavelength;
- Backscatter measurements provide information about the roughness and moisture content of the observed object;
- Polarized radiation used in radar offers the possibility of collecting polarization information of the observed object;
- Phase information collected for each radar measurement allows for high accuracy measurements of distance;

The codes used to distinguish between different wavelength-bands are confusing, due to their military origin. In Table 2.2 the most commonly used radar bands are listed with the corresponding spectral windows given in wavelength and frequency.

Table 2.2: Radar band designations, where X-band is the shortest micro wave and P-band the longest (Lillesand and Kiefer, 2000)

Band	Wavelength λ [cm]	Frequency ν [MHz(10^6 cycles sec^{-1})]
X	2.4 – 3.75	12,500 – 8,000
C	3.75 – 7.5	8,000 – 4,000
S	7.5 – 15	4,000 – 2,000
L	15 – 30	2,000 – 1,000
P	30 - 100	1,000 – 300

Radar remote sensing produces a two-dimensional scene representing the measurements of the surface in a geometrically registered grid. As a consequence, radar scenes are sometimes confused with aerial photographs. However, there are important differences in both geometry and measured value. Radar sensors look sideways to the surface and determine the location of a surface point on the return time of the radar pulse, resulting in phenomena such as scale distortion and relief displacement (Lillesand and Kiefer, 2000).

The difference in measured value originates from the fact that the behaviour of radar waves is more similar to sound than to light waves. Radar sensors measure two values, the radar 'reflection' or coherent backscatter and the radar wave phase. The amount of backscatter is a result of the physical roughness of objects at the Earth's surface rather than the electromagnetic reflectivity used in optical remote sensing. These differences separate radar remote sensing from optical remote sensing (Rocca et al., 2000).

Meteorological applications benefit from the ability of radar to penetrate clouds and to detect information on atmospheric chemistry, water content and temperature. Military and civil applications in air and water transport as well as radar astronomy benefit from the detection and ranging of moving objects, possible with radar. Currently amongst the many applications of radar remote sensing in physical geography are polar ice research, land use mapping, vegetation mapping, biomass estimates and soil moisture mapping (Rosen et al., 2000). One of the most revolutionary recently developed applications of radar remote sensing is ground surface deformation which is made possible monitoring possible by the technique of InSAR.

2.4.4. Synthetic Aperture Radar Interferometry (InSAR)

InSAR is a relatively new radar remote sensing technique, developed mainly in the last two decades using existing space borne radar sensors that were not designed for this technique (Table 2.1). InSAR adds a valuable asset to the science of radar remote sensing: the ability

to measure angles (Hanssen, 2001). Although the first principles of InSAR were introduced in the early 1970s for looking at the moon and Venus, increased availability of terrestrial radar scenes and the high spatial resolution of the SAR sensors since 1992 have made InSAR an important niche in radar science (Massonnet and Feigl, 1998).

Around the change of the millennium a large number of reviews on the theory and applications of InSAR have been published, indicating a wide field of potential applications for this technique (Bürgmann et al., 2000; Hanssen, 2001; Klees and Massonnet, 1999; Massonnet and Feigl, 1998; Rosen et al., 2000; Wegmuller et al., 2004). The applicability of InSAR for the monitoring of ground surface deformation caused by anthropogenic activity has been the topic of several studies from 1992 onwards (Table 2.3).

Tabel 2.3: InSAR tested on different ground surface deformation processes

authors	Wegmuller et al	Wegmuller et al	Wright Stow	Perski	Wegmuller et al	Raymond Rudant
location	Italy	Mexico	England	Poland	Germany	France (mulhouse)
process	groundwater withdrawal	groundwater withdrawal	coal mining	coal mining	coal mining	deep potassium mining
effected area	large (valley)	large (city)	medium (70 km2)	large (1500 km2)	small (16 km2)	large (200 km2)
Land use	Urban/rural	Urban	Rural	Urban	Urban	Rural
used interval	5 years	3 months	35 days	35 days	35 days	35 days
number ERS	2 (tandem) + 10	4	4 (2 tandem) + 12	16 (3 tracks)	4	4
monitoring period	1992-1996 (5)	1996-1997 (2)	1993-1998 (6)	1992-1999 (8)	1995-1997 (3)	1992-1993 (1)
accuracy (mm a $^{-1}$)	1	50	~20	5	100	low
Max subs (mm a $^{-1}$)	4	400	480	480	2000	3600

2.4.5. Main characteristics of InSAR

Interference is universally known as a phenomenon of deformed sound waves, eg. the disturbance of radio signals that originate from two different sources. Interference occurs if two radar waves of the same wavelength superimpose and form a new wave. In the InSAR technique this phenomenon is used to generate an interferometric phase, a measurement that can be used to calculate relative ground surface elevation and deformation.

A complex SAR scene contains two sets of pixel values. In addition to the amount of scattering or backscatter, the radar sensor registers the phase of the reflected radar signal. The measured phase value φ is the phase in radians of the last wavelength, ignoring the number of complete wavelengths the wave has undergone (Fig. 2.11). The InSAR

technique uses the phase difference ($\Delta\varphi$) or interferometric phase between two or more coherent waves measuring the same object (Eq.2.3).

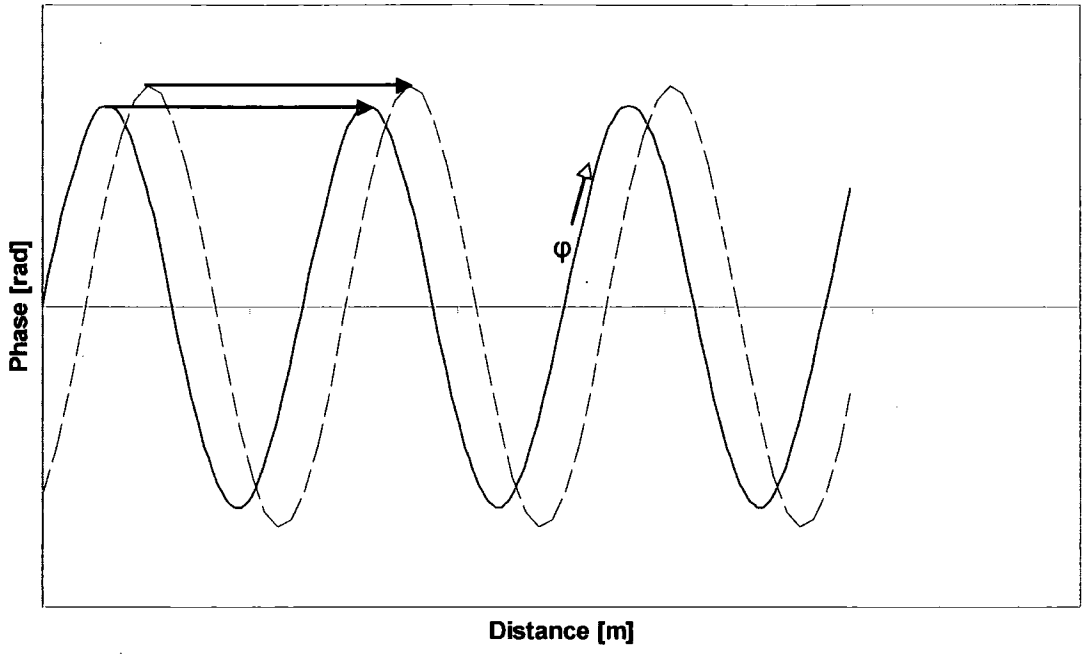

Figure 2.11: Schematic sinusoidal representation of two coherent radar waves. The black arrows point out the length of one wavelength which is identical for the two waves.

A requirement for wave interference is coherence between waves measuring the same object. Coherence is obtained if the wavelengths (λ) of two waves are equal, regardless of whether the amplitude (A) and number of wavelengths ($k\lambda$) are equal.

The first radar sensors were non-coherent, which means that the radar wave sent out had inconsistent wavelengths and could therefore not be used for InSAR (Fig. 2.4). Also passive radiometry is by definition non-coherent, as natural radar waves have random wavelengths and is therefore not suitable for InSAR.

The waves in Figure 2.11 are coherent, because the wavelengths are identical as depicted by the two black arrows. The phase difference equals the vertical distance between the two black arrows and is also constant over time. Phase differences can not exceed 2π or 360°, which corresponds to the length of one wavelength. In the case of ERS-1 C-band InSAR, which uses a wavelength of 56 mm, only a distance between 0 and 56 millimetres can be measured. It is therefore essential to realise that InSAR measures relative distance changes between neighbouring measurements and over time.

Equation 2.3 (Woodhouse, 2006):

$$\Delta\varphi = \left(\frac{d}{\lambda}\right) \times 2\pi$$

Where

- $\Delta\varphi$ is interferometric phase,
- d is distance [m],
- λ is wavelength [m].

By simultaneously measuring the interferometric wave at neighbouring pixels, the relative distance between sensor and ground surface can be derived. From this information a digital elevation model (DEM) can be generated. An interferogram is an image showing the interferometric phase which ranges between 0 and 2π (Fig. 2.12). The fringes or displacement features in an interferogram are areas with equal displacement around a point or line of maximum displacement. A change in colour corresponds with a certain phase difference, and a cumulative distance in elevation or deformation. (Wright and Stow, 1999).

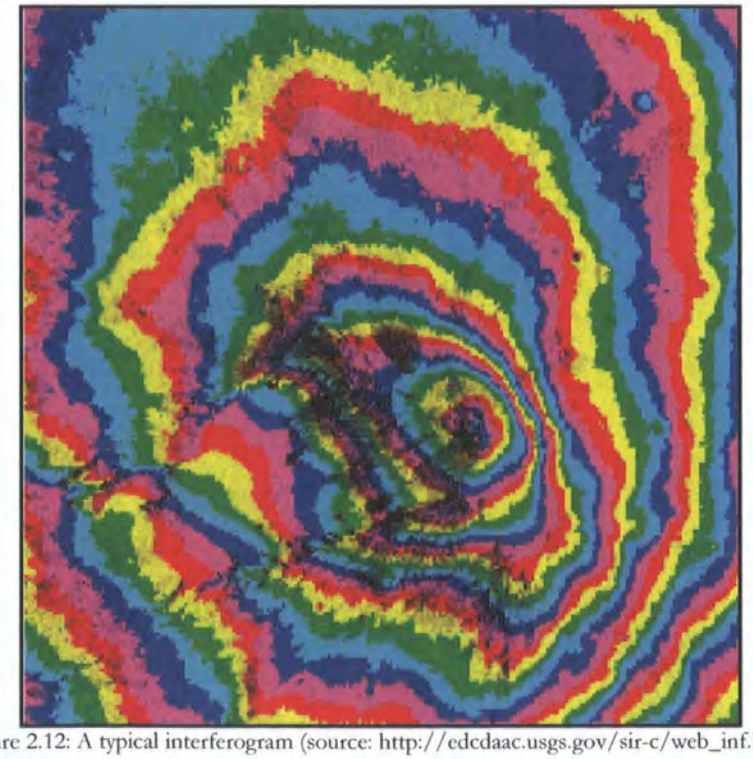

Figure 2.12: A typical interferogram (source: http://edcdaac.usgs.gov/sir-c/web_inf.html)

The radar scenes used to generate an interferogram cover the same area at the surface, but the specific location of the radar sensor and time of registration is unique for each radar scene. The difference between two scenes in spatial location is quantified by means of the

perpendicular and parallel baselines [m]. The difference between two scenes in time of registration is quantified by means of the temporal baseline [days]. The variation in baselines determines the type of information contained in the interferometric phase and is an important consideration in the selection of radar scenes, see chapter five.

In across-track InSAR only one signal is send out by a radar sensor, which is received by two relatively displaced antennas. With this InSAR technique a small spatial baseline is used to determine the exact three-dimensional position of the observed surface. The interferometric phase contains a third dimension by observing the surface from two different look angles.

In along-track InSAR, where the two receptors are placed along the flight track of the airplane or satellite, a small temporal baseline is used. The relative displacement results in a small time difference of the two scenes, (approximately 100 milliseconds in an airplane). Instead of a third dimension, this displacement results in temporal change detection. This type of InSAR is used to observe wave patterns in the sea, or the monitoring of moving targets. Repeat-pass InSAR is a combination of these two InSAR techniques and uses both spatial and temporal baselines. With repeat-pass InSAR two or more scenes are taken with the same sensor at a different time, resulting in a temporal baseline this can be minutes, days or years.

2.4.6. Differential InSAR (DInSAR)

One of the advantages of repeat-pass InSAR is that the deformation of a surface can be monitored over certain time intervals. In DInSAR the interferometric phase is used to determine the ground surface deformation. Unfortunately, the DInSAR interferometric phase (φ_{unw}) value generally contains four sources of information: the topographic phase (φ_{topo}), the displacement phase (φ_{disp}), the path delay phase (φ_{path}) and the noise (decorrelation) phase (φ_{noise}).

Equation 2.4: (Wegmüller et al., 1999):

$$\varphi_{unw} = \varphi_{topo} + \varphi_{disp} + \varphi_{path} + \varphi_{noise}$$

To derive the actual displacement φ_{disp}, from φ_{unw} , the three phases (φ_{topo}, φ_{path}, and φ_{noise}) have to be estimated based inherent or alternative information (Rosen et al., 2000) and subtracted from the interferometric phase. The difference between the used methodology

for InSAR and DInSAR analysis is that for the latter two interferograms are created both using the same master scene (Fig. 2.13).

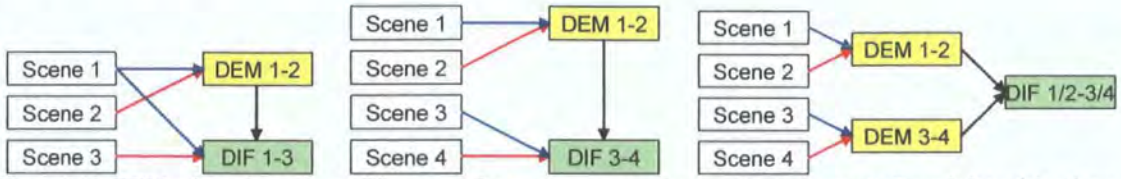

Figure 2.13: DEM subtraction scheme (blue arrow for master scene, red arrow for slave scene). From left to right: three-pass DInSAR, four-pass DInSAR and DEM subtraction.

In three pass DInSAR, one slave scene has an acquisition date one day after the master scene with which it forms a tandem pair, and the second slave scene has an acquisition date some time after the tandem pair. The interferogram created with the master scene and the second slave scene contains information on the height difference between the two acquisition dates and the ground surface deformation that occurred during the period between the two dates. To isolate the ground surface deformation information, the interferogram created with the tandem pair is subtracted from this interferogram.

The unwrapped interferometric phase (φ_{unw}) can be converted to elevation or deformation by a process referred to as unwrapping. To calculate the elevation for each pixel in the scene, a reference point with a known elevation is selected. From the reference point the elevation is calculated moving from neighbouring pixel to neighbouring pixel, using the relative change in interferometric phase. The total vertical change in elevation covered by one interferometric fringe (colour scale) equals the altitude of ambiguity, which can be calculated from the spatial baselines.

The altitude of ambiguity is determined by the perpendicular baseline and the physical characteristics of the spacecraft. To calculate the altitude of ambiguity for ERS interferograms, equation 2.5 can be used.

Equation 2.5: altitude of ambiguity (Capes and Haynes, 1996).

$$\Delta z \approx \frac{9416}{B_{perp}}$$

In the unwrapping process, object – sensor distance information is used to create a DEM.

2.4.7. Interferometric coherence and decorrelation factors

The first unwanted phase φ_{topo}, is generally estimated based on a DEM of the ground surface. Scenes taken at different moments in time from different orbits or even different

platforms will have a spatial baseline. This is due to the fact that the spacecraft will pass the second time slightly displaced. As a consequence the interferometric phase will contain a third dimension showing the relief of the ground surface. A third scene with a relatively much smaller temporal baseline can be used to eliminate the part of the interferometric phase caused by relief. In cases where the use of a third radar scene results in an increased unknown atmospheric distortion, an external DEM is preferred.

Although radar waves penetrate atmospheric distortion such as clouds or pollution, they are not totally unaffected by it. A small shift in phase can be caused, especially if there are water particles in the air. This phase is called the atmospheric phase (φ_{path}) and is thought to consist of two components, a spatially homogenous delay indicating distortion in the higher atmosphere and the clustered distortion caused by finite clouds with high moisture content. The effect of atmospheric distortion on the interferometric phase is studied extensively (Hanssen, 2001).

After the removal of the topographic phase and the atmospheric phase, a third unwanted phase remains simply referred to as φ_{noise}. This noise is difficult or impossible to remove and is caused by system noise and temporal decorrelation. System noise is especially relevant is the amount of scattering is low in which case the valuable information can be dominated by unwanted signal fluctuation. Temporal decorrelation is caused by changes at the observed ground surface due to changes in scattering capacity due to for example vegetation changes.

To distinguish between pixels with valuable information and pixels that are dominated by noise, an index is used. Interferometric coherence (γ) is an index estimated for each pixel in an interferogram as an indication of the signal to noise ratio and the accuracy of the interferometric phase. In the rest of this thesis with coherence the estimated interferometric coherence is meant. Coherence ranges between 0 and 1 where 0 means the measurement in that pixel is just noise and 1 means absence of phase noise.

Ideally the coherence estimation for each pixel is based on a statistically meaningful set of measurements of the same point at the surface. In the case of ERS radar scenes, used in this research only one measurement is collected per pixel during one registration. To solve this problem, a window including some pixels in azimuth and range direction is used to determine the coherence in the centre pixel (Ferretti et al., 2000a). Decorrelation is the

term used for loss of coherence and is defined as the noise detectable over a spatial extent smaller than a regular coherence estimation window.

DInSAR techniques used to monitor ground surface deformation are currently operational in areas with urban land use or those with sparse vegetation and a dry climate. This is because coherence over time of backscattering characteristics at the surface allow for InSAR measurements over certain time intervals. However, often deformation processes occur in areas with less favourable conditions. Previous studies of the technique have recognised that whilst the technique shows great promise, further research is needed to constrain the effects of, for example, surface vegetation (Massonnet and Feigl, 1998).

These effects are particularly significant in temperate agricultural areas in which vegetation growth and farming activities such as ploughing cause significant modification to the surface of the land. Even in optimal conditions investigations of the use of DInSAR have met problems associated with the lack of temporal coherence between the topometric (surface) surveys and the periods of radar observation (Carnec and Delacourt, 2000) that have left many unanswered questions about the effectiveness of the technique. The balance between a large time lapse, needed for ground surface deformation to be significant and a small time lapse important to avoid coherence loss has to be found (Wright and Stow, 1999). Pixels which have a coherence below 0.3 are considered too decorrelated to contain any useful information (Woodhouse, 2006).

Coherence is a dimensionless rate indicating the level of temporal decorrelation caused by change in scattering per pixel. It can be calculated using slightly different algorithms, but is based on the correlation between pixels of the two radar scenes used to create an interferogram and the neighbouring pixels. The coherence value is an estimation and becomes biased if the coherence is low.

In rural areas different types of temporal decorrelation occur. Some land cover types cause high decorrelation over short time intervals. Areas covered with water or vegetation have a temporal decorrelation of minutes rather than days and are therefore unsuitable for InSAR analysis. Some areas are bare and part of the time ideal for InSAR analysis. However, agricultural activities such as ploughing, mowing and burning of moor land also have significant impact on temporal decorrelation of the surface. In temperate climates the occurrence of these activities is variable both in the time span of one year and between years, as they are dependent upon the weather conditions (Wright and Stow, 1999).

The process of ground surface deformation in the Boulby research area can be considered gradual: less than 50 mm a^{-1}, compared to for example Selby coalmines with 11 cm per 35 days. The research area is rural, but has some potential persistent scatterers like houses and roads. The coastal cliffs and rock platform at the foot of the cliffs should provide coherent data for the interferograms.

Selection of the best possible radar dataset is important to minimise the amount of decorrelation. The selection should consider weather conditions and select registration dates with comparable weather conditions. Seasonal registration, as done in the Selby area (Wright and Stow, 1999) has to be considered, to exclude the high decorrelation in the growing season. Distortions in the ground surface or atmosphere causing respectively high φ_{noise} and φ_{path} can be compensated by analysis techniques. Two techniques mentioned in literature are layer stacking and permanent scatterers (Ferretti et al., 2001). Both methods will benefit from the available long time series of radar scenes and reference data.

2.4.8. Persistent scatterer interferometry (PSI)

Atmospheric phase distortion is generally spatially correlated within one interferogram but uncorrelated with phase distortions in other interferograms. The phase distortion caused by ground surface deformation is generally both temporally and spatially correlated. By analysing the phase trend in long time series of interferograms, the atmospheric distortion for each interferogram can be estimated and removed. Long time series of interferograms can often not be generated with three of four pass differential InSAR due to loss of coherence in vegetated areas. The use of a selection of pixels with relatively high coherence and low amplitude dispersion can avoid this problem (Colesanti et al., 2003).

The technique of persistent scatterer interferometry (PSI) to measure ground surface deformation using radar scenes is in development. Although much of the technique is based on InSAR, it is an advancement which has overcome many of the limitations of InSAR. PSI was originally developed by Ferretti et al, following research in 1997 (Usai, 1997; Usai and Hanssen, 1997) in which was recognised that areas with high temporal decorrelation often contain isolated points of high correlation (persistent scatterers) (Ferretti et al., 1999; Ferretti et al., 2000a; Ferretti et al., 2001).

In both conventional InSAR and PSI an interferogram is created by subtracting the phase values of two SAR scenes. The difference between the two methods is the approach used for the unwrapping of the interferogram. In conventional InSAR this is done pixel by pixel

for each interferogram. In PSI the unwrapping is done simultaneously with the estimation of parameters of interest at randomly distributed 'persistent scatterer' points in the area using a large number of interferograms.

2.5. Modelling ground surface deformation

In the understanding of ground surface deformation, different types of models can be applied. In tectonic geomorphology a model can be a schematic representation of a landscape indicating interacting processes. In subsidence engineering a model often entails a numerical two or three dimensional matrix to calculate the impact of forces, geometry and material properties, which can be tested using application software. In geodesy and remote sensing a model is often thought of as a set of mathematical algorithms, sometimes incorporating rasters or matrices. Models provide insight into interrelationships within complex systems, by means of simplifying reality to the essential system aspects (Waveren et al., 1999).

Environmental processes are by definition affected by a multitude of factors and surrounding processes. These processes are therefore rarely linear in time and in space (Abernethy, 2000). Despite the difficulties associated with placing complex environmental processes into boxes, it can be helpful to classify the main characteristics of ground surface deformation processes. An adequate classification can help to conceptualise the underlying processes and determine the most appropriate monitoring and modelling techniques.

As a result of complex spatial and temporal processes that influence ground surface deformation, deterministic models are often rather poor at the prediction of the effect of deformation processes on the ground surface (Chrzanowski et al., 1997). A recent development is that on account of the increasing availability of monitoring data the result of deformation is becoming more accurately known than the drivers of deformation. This development demands a shift in the way ground surface deformation is modelled.

2.5.1. Empirical methods

Mining subsidence science was developed to attempt to mitigate the damage caused by subsidence to objects at the surface. In the early years subsidence models were based on data from shallow coal mining activities that took place at depths of up to approximately 90 metres. The requirement for a set of universal rules to pre-calculate subsidence in

undermined areas with unknown environmental variables has resulted in a large number of empirical models.

These models attempt to estimate some of the key indicators using parameters and equations found valid for certain ground surface deformation processes. The empirical study of mining subsidence started in 1825 in Belgium, because surface damage caused by shallow mining activities in the densely populated city of Liege was commissioned. The studies by Gonot (1858), Callon (1874) and Dumont (1875) focussed on the mechanism of transmission of movement in the ground layers.

The concept of a dome or cone shaped zone of disturbance forming over excavation activities emerged for the first time in research by the Jicinsky (1882) and Rziha (1884). The general idea was that movements were transmitted normal to the mineral seam and not necessarily vertically. This idea was later proven wrong by Fayol (1885) and others after that (Young and Stoek, 1916). Fayol carried out experimental research which led to his formulation of a number of fundamental ideas about mining subsidence, including the key observation that movement of the ground is transmitted vertically from all depths of the working, but deeper workings have less impact on the surface than shallow workings. He also stated that subsidence takes place beyond the excavation zone, but to a measurable distance, moving further with the progression of the excavation activities.

These ideas were further developed by the Dixon (1885) and Dickinson (1898), who formulated the concepts of lateral movement, or "draw", and the existence of a leading and following wave of disturbance. These two concepts are essential to our modern understanding of ground deformation mechanics because they imply the existence of resistance to movement of the ground. Halbaum (1903, 1905) came up with the idea that individual ground strata act as a cantilever under their own weight, which influences the spatial and temporal behaviour of the disturbance at the surface.

The understanding of the influence of factors such as relative strength, inclination and thickness of the individual strata was further developed by O'Donahue (1907). He acknowledged the existence of subsidence over mines deeper than 600 metres. In experiments he measured 300 to 450 millimetres of total deformation over a mine at 730 metres below the surface. Previously, it was generally considered that mining deeper than 600 metres below the surface would not cause subsidence (Whittaker and Reddish, 1989).

Further recognition of the effects of deep underground mining was given by Perz (1948), who examined the temporal behaviour of subsidence. He stated that only after a period of five years, 100% of the total subsidence has taken place. Both Perz's concept of a measurable limit in time and Fayol's concept of a measurable limit in space (Kratzsch, 1983). An example of an empirical subsidence model which is currently widely applied in the United Kingdom is the model described in the Subsidence Engineers' Handbook (SEH) (NCB, 1966).

In the SEH-model, the spatial extent of the disturbed surface area is estimated by means of two profiles, the longitudinal subsidence profile and the transverse subsidence profile. These two transects are drawn respectively parallel and perpendicular to the direction of the advance of the excavations. The maximum subsidence factor (S/m) and the horizontal distance between the centre of the extraction and the limit of the disturbed area are calculated from the width to depth (w/h) ratio of individual excavation panels (Fig. 2.14).

In the example an excavation panel at a depth (h) of 100 metres has a width (W) of 30 metres, a seam thickness (m) of 3 metres and length (L) of 140 metres. The w/h ratio is 0.3 which means that the associated maximum subsidence factor is 0.10 in the case of solid stowing and 0.18 S/m in the case of strip-packing or caving, read from a nomograph. The horizontal distance from the centre of the excavation panel to the limit of the disturbed area associated is 0.63 * h, read from a second nomograph.

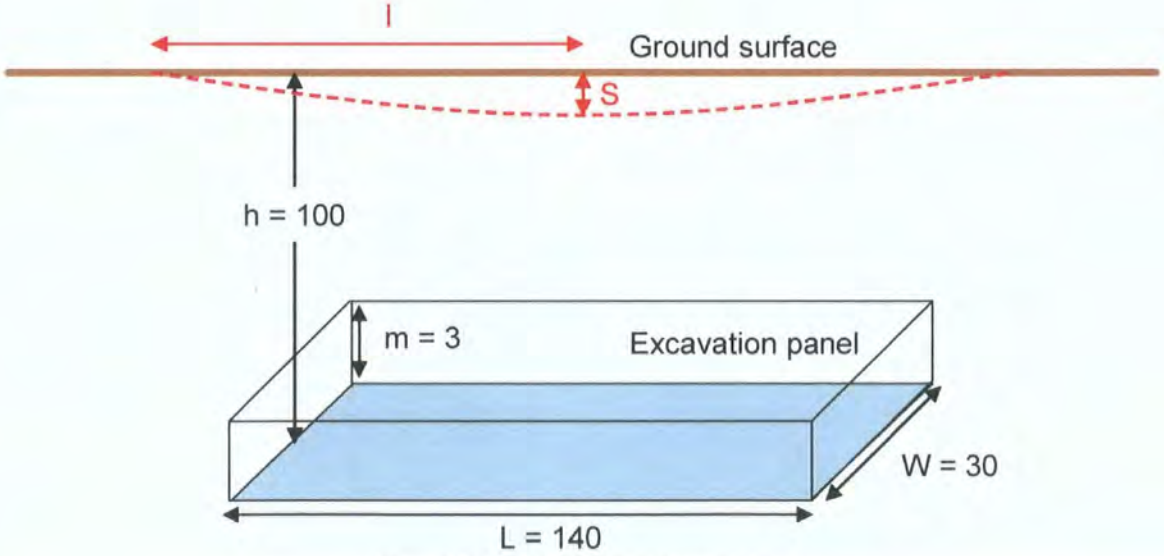

Figure 2.14: SEH-model, input parameters

Consequently, a seam thickness of 3 metres should result into a vertical deformation of 0.30 to 0.54 metres at the ground surface, in a circular area around the centre of the excavation panel with a radius of 63 metres (NCB, 1966). The shape of the bowl can be calculated in terms of from a graph based on the w/h ratio and the depth of the excavation seam.

The relation between subsidence and time is represented by two variables, the total duration of subsidence and the face advance in distance per annum. The first variable can be derived from the third nomograph based on parameters h, the angle of draw and face advance. The angle formed when drawing a straight line between the centre of the excavation panel and the edge of the surface deformation is referred to as the angle of draw. For the example in Figure 2.14, the angle of draw can be calculated as the inverse tangent of the depth (h) and the above determined radius (63 m) and is 32°. Assuming a face advance of 300 metres per annum, the total duration should be approximately 5 months.

The SEH-model is based on specific underground mining conditions. The length of an excavation panel should be 1.4 *h and the excavation panels should be rectangular (NCB, 1966). Also, only two types of mining practise are considered, solid stowing (loosely defined in literature as good hand or slusher packing or pneumatic solid stowing) or strip-packing (immediate caving and no stowing present). The two types are considered as extreme situations, the engineer will have to find an average between the two estimations, based on site specific situations. The universality of such empirical models is limited due to the range in limiting conditions.

Empirical models, which use lookup tables and nomograms based on real data such as the SEH-model, require measurable and clearly defined input parameters. In many deformation processes these parameters are rather difficult to determine due to the inherent complexity of natural systems; the complex stress conditions; the high temperatures; the complex groundwater conditions and the non-linear rheology of the rocks in this environment.

The SEH-model has been used widely in the United Kingdom and is worldwide regarded as the definitive prediction model (Ferrari, 1996). In a research, British Waterways evaluated the predictions to long monitoring datasets and found differences between the amount of subsidence estimated and measured of up to 700% (Ferrari, 1996).

2.5.2. Deterministic and numerical methods

Deterministic modelling is a method in which the physical process causing the deformation is studied. This method could be referred to as a 'bottom up' approach. The physical and mechanical processes are analysed to the smallest possible detail to predict the behaviour of the complete ground based on the behaviour and interactions of all relevant components. Monitoring data are only used to validate the final model equations. The mathematical multidimensional capability of computers has led to the development of numerical models for understanding complex deformation systems.

In Canada numerical modelling was applied to study processes of gradual ground surface deformation related to potash extraction (Chrzanowski et al., 1997). Extensive monitoring data of two separate potash mines covering a period of seven years was used to evaluate numerical models (Fig. 2.15). Initially the modelling of the ground deformation was confined to laboratory research that focussed on rock mechanics. After a couple of years, evidence from monitoring data showed that there was a need to model the ground deformation at a more holistic method to improve the reliability of the pre-calculations of subsidence.

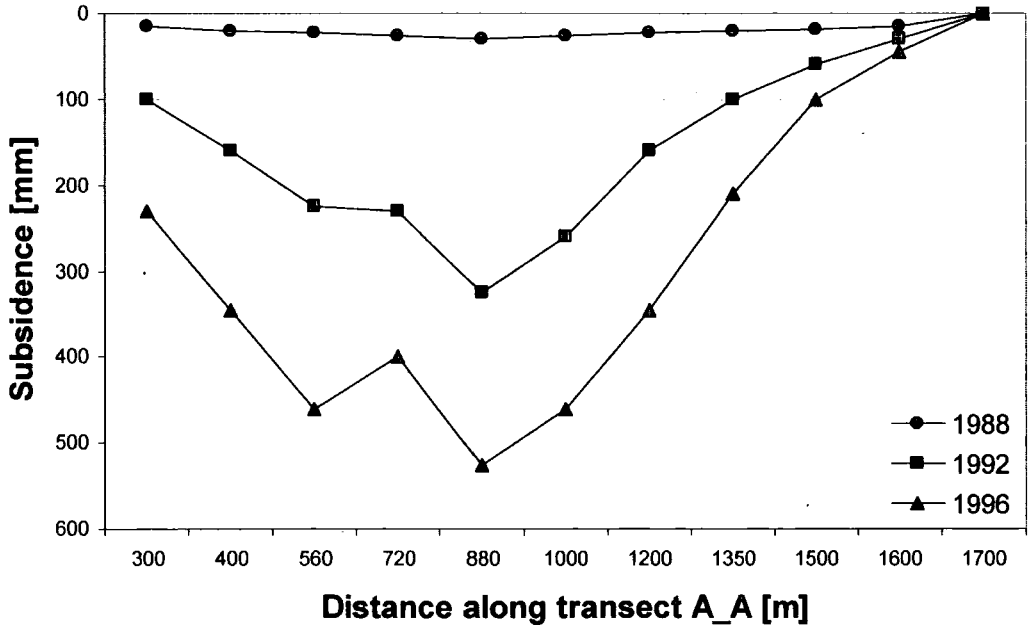

Figure 2.15: Subsidence measured using levelling, Potacan potash mine in Canada (Chrzanowski et al., 1997)

The empirical knowledge of rock mechanics was combined with a sequential finite element method (Fig. 2.16). This method considers the salt-rock as a non-Newtonian fluid. The overlying brittle rocks are seen as non-tension material. The extensive monitoring dataset

was used to calibrate and evaluate the Finite Element Method for Multipurpose Applications (FEMMA) (Chrzanowski et al., 1997).

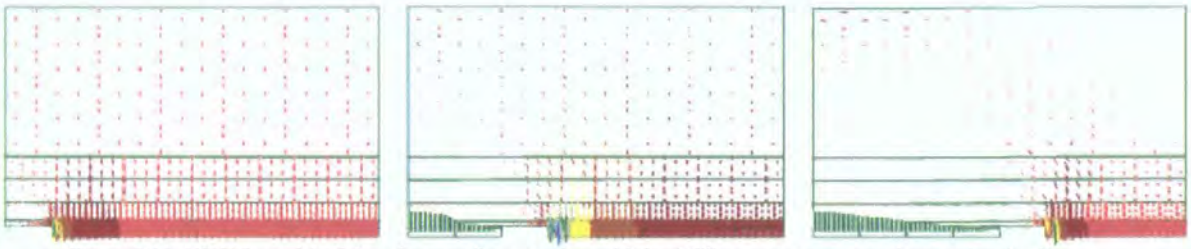

Figure 2.16: UDEC-model of deep long-wall excavation with backfilling; stress states at three points in time.

After evaluation of the modelling results with the monitoring data, the conclusion was that the FEMMA model underestimates the deformation by 2 to 3 times (Fig. 2.17). The authors recommended further refinement of the mesh and inclusion of more mechanical processes, such as brittle salt-rock flow from the immediate roof.

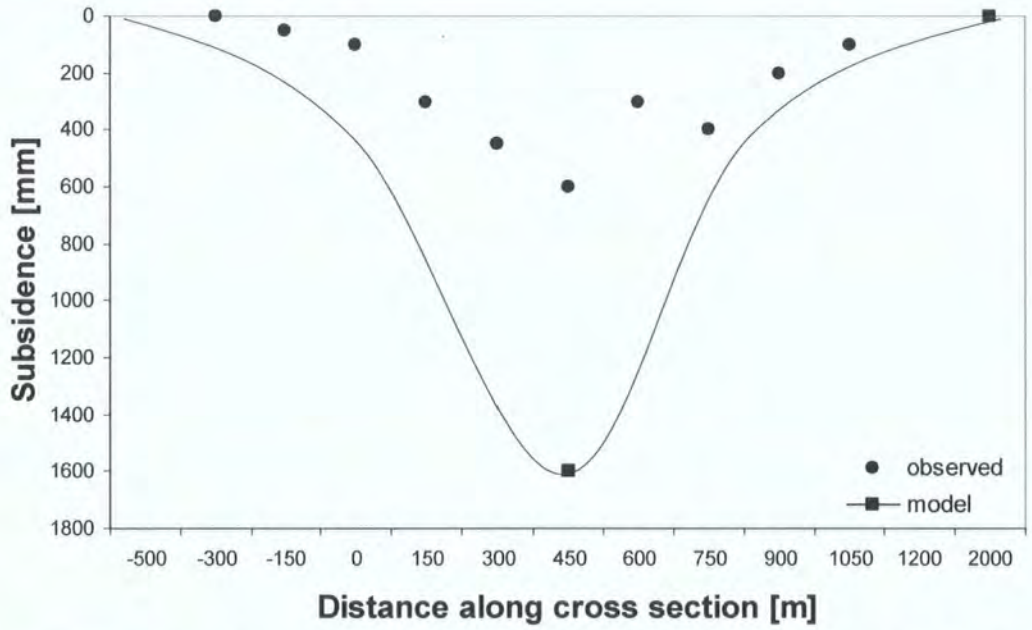

Figure 2.17: Observed and estimated subsidence based on the FEMMA model (Chrzanowski et al., 1997).

Similar problems were found in Australia, where a numerical model was built to pre-calculate the subsidence related to longwall coalmining at a depth of 300 meters, using the Universal Distinct Element Code (UDEC). This 2D code allows modelling of highly jointed rock masses. Overlying ground layers are represented by separate blocks that can slip, slide, separate, rotate and deform individually. The way in which the blocks respond depends on set parameters and on the loads applied to the system.

To fit the modelling result to the monitoring data, the authors had to refine the model several times. The model persistently underestimated the observed subsidence. This was attributed to two limitations of the UDEC, the assumed ordered rather than random behaviour of the immediate roof strata collapse and the limited dimensionality (Coulthard, 1999).

Other codes used for mining related ground surface deformation modelling are: Fast Lagrangian Analysis of Continua (FLAC) and The Finite Element/ Discrete Element System (ELFEN). The first is a two-dimensional continuum code designed for modelling ground and rock behaviour. It is a general analysis and design application used by geotechnical, civil, and mine construction engineers and is applied to complex problems in technical research. The explicit finite difference formulation of the code makes FLAC suitable for the modelling of geomechanical problems which consist of different stages. The formulation can be adjusted to large displacements and tensions in non-linear material behaviour.

ELFEN is a 2D/3D numerical modelling package that combines Finite Element (FE) and Discrete Element (DEFT) analysis technology. The third dimension and the FE technology will facilitate the spatial modelling required in this research. Like FLAC, ELFEN has pre-programmed software extensions for specified uses of the ELFEN model, like potash mining subsidence.

2.5.3. Influence function methods

This method of modelling is based on the idea of infinitesimal elements of the extraction area at depth h having an influence on the surface. Influence function methods are used in empirical and deterministic modelling, depending on whether the parameters are derived from data or assumption.

A point at the seam level representing an 'extraction element' (E) creates an elementary trough at the surface. The resulting ground surface deformation is calculated as the sum of the elementary troughs. The weighting given to the influence of each element depends on the location of that element in the influence circle, which is divided into a number of influence sectors (Sheorey et al., 2000).

Kratzsch (1983) described the seven engineering principles used in influence function methods. Some of these principles are used for the cone subsidence model described in the

following chapters of this thesis. The first is the limit angle principle. The limit angle principle (Kratzsch, 1983) is based on the idea that the zone of disturbance caused by extraction unit (E_1 or E_2) radiates outwards and upwards (Fig. 2.18). The angle of draw (α) is independent of the depth of E and the perimeter of the area of disturbance is determined by the depth of the excavation.

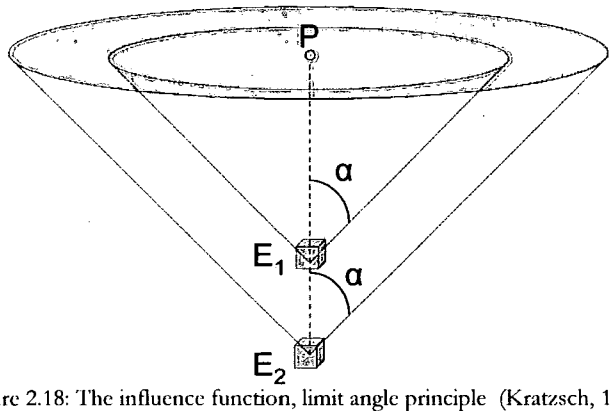

Figure 2.18: The influence function, limit angle principle (Kratzsch, 1983)

The angle of draw principle implies that a deformation bowl has a measurable limit, beyond which no deformation takes place. In practice, measured deformation gradually approaches zero at a certain distance from the centre of the deformation bowl. In the case of deep mining, the decrease of measurable deformation can be gradual. Following on from the limit angle principle is the principle of rotational symmetry, which implies that each extraction element forms an identical cone shaped zone of disturbance, see Figure 2.19.

While the zone of disturbance is a cone formed by the angle of draw and the depth of the excavation element, the elementary trough formed at the ground surface can be assumed to be bell-shaped. The influence function $k_z(r)$, in % of influence as a function of the horizontal distance (r) from a point at the surface can be used to determine the influence of an element on the surface. This is found to be valid if the ground layers are sufficiently homogeneous and do not contain faults or other irregularities. The relief at the surface determines whether the elementary through is circular or ellipsoid.

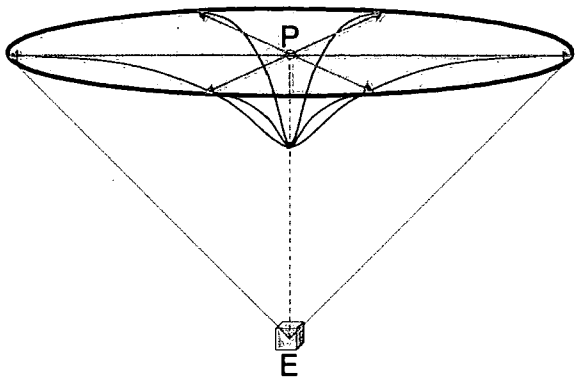

Figure 2.19: Influence function, principle of rotational symmetry

The next principle is that of equivalence, which implies that each extraction element has an equivalent influence on the surface deformation (Fig. 2.20).

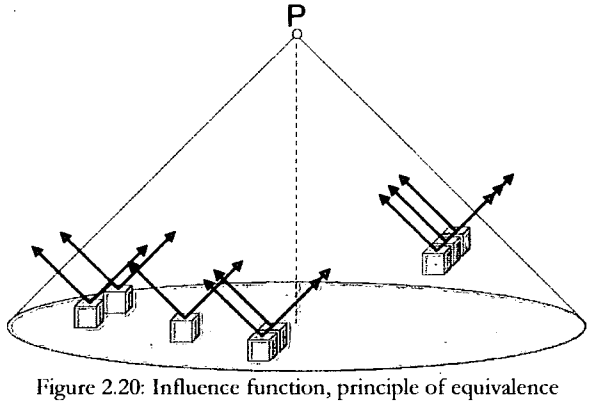

Figure 2.20: Influence function, principle of equivalence

The principle of equivalence is based on the assumption that each excavation unit behaves identically, causing an elementary disturbance profile. The contribution of each excavation unit to the disturbance experienced at point P is determined by its horizontal and vertical distance to P.

The principle of equivalence assumes that there is no interaction between elements and that distribution or clustering of excavation elements does not influence the impact of the excavations on the ground surface. Each excavation unit is independent of neighbouring units and the influences can be added to calculate the total effect, as defined by the next principle of superposition (Fig. 2.21).

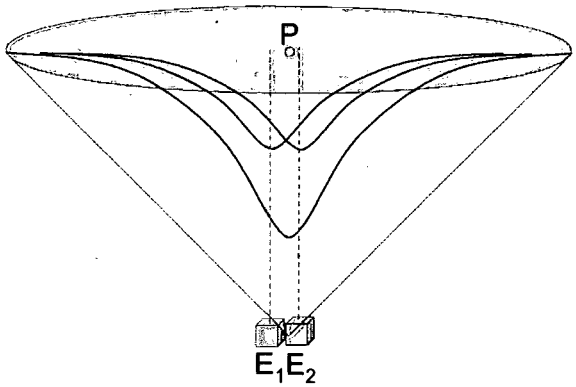

Figure 2.21: Influence function, principle of superposition

The concept of a group of excavation units that have an influence on the deformation of the ground surface can be reversed into the concept of a group of points at the surface affected by one excavation unit. This principle of reciprocity entail that the shape of the surface deformation profile corresponds to the shape of the influence curve of the excavation units (Fig. 2.22).

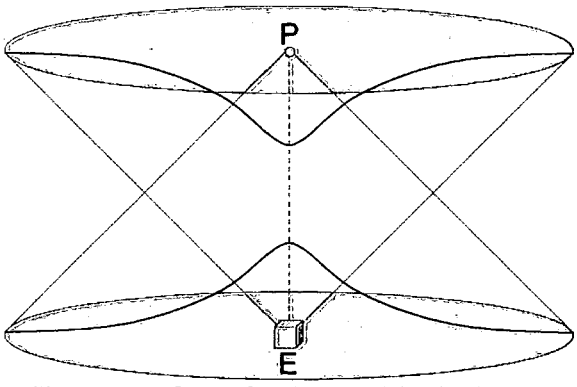

Figure 2.22: Influence function, principle of reciprocity

In other words, the reciprocity concept allows for regression analysis between surface data and excavation data and therefore sets the basis for the cone model, discussed in the following chapters of this thesis.

Two much debated principles are that of the constancy of volume and that of transitivity. As mentioned in the empirical modelling section, some scientists argue that the total cubic volume of the subsidence bowl equals the total cubic volume of closure in the excavation units (Fig. 2.23).

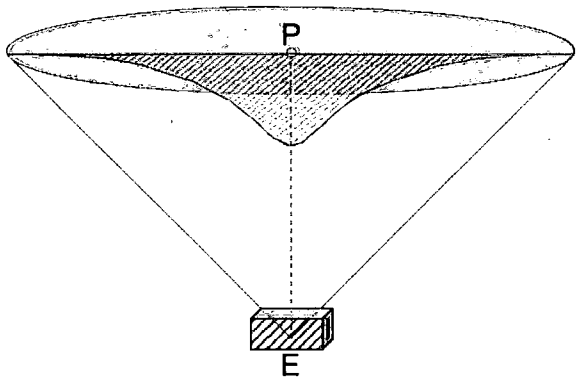

Figure 2.23: Influence function, principle of constancy of volume

The principle transitivity refers to a linear development of deformation over time. Based on this principle, the shape of the influence profiles of the excavation units are assumed to transform identically over time (Fig. 2.24).

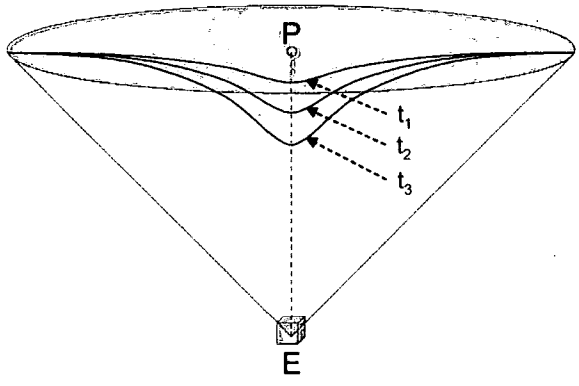

Figure 2.24: Influence function, principle of transitivity

These last two principles may be valid in some cases, but is generally regarded as inconclusive and too simplistic in most cases. Physical processes in the ground layers that take place during mining, such as fluid transport, loosening of strata and compression of loosened layers have considerable impact on the volume and development of the subsidence bowl. Absorption or delay of strain by the ground layers will have impact on the development of subsidence over time, transitivity is therefore not assured.

An example is the modified influence function model developed by Shorey (2000), explicitly built for subsidence related to Indian coal mining. The influence circle has a radius of h * tan θ, where h is the depth of the seam and θ is the angle of draw. The circle is divided into ten rings, each ring is divided into 64 sectors, resulting in 640 influence elements. The weight of each element is a function of the surface area of the ring, the K_z influence function, the subsidence factor (S_{max}/seam height) and the horizontal position of the element in relation to the centre.

The advantage of influence function models over one or two dimensional deterministic or empirical models is the ability to estimate the ground surface deformation at any point on the surface at any point in time. However, their high mathematical complexity make influence function models difficult to understand (Whittaker and Reddish, 1989).

2.5.4. Statistical methods

The term geo-statistics was first used by Matheron (1962) and initially referred to the application of statistical analysis to geology and Earth science related systems. Since then developments in geographical information science have widened the field of geo-statistics which now refers more to the broad field of environmental spatial-statistics. Any natural variables that are distributed in space or in time and space can be quantified based on geo-statistics (Chilès and Delfiner, 1999). For statistics to be functional, large representative datasets of those natural variables are required.

A problem with a data driven model can be that the actual process becomes a 'black box'. For example, (Ambrožic and Turk, 2003) have used the 'Artificial Neural Network' (ANN) approach to predict subsidence based on earlier occurrence of subsidence without knowing the geological and geo-mechanical conditions between the mine workings and the deforming surface. However, because the ANN method predicts subsidence without any interpretation of the physical process it is less effective for understanding the subsidence processes themselves (Hastie et al., 2001).

2.6. Conclusion

A better understanding of temporal and spatial behaviour of ground surface deformation processes may lead to a better understanding of the underlying drivers, their interaction and methods of control. An improved understanding of ground surface deformation necessitated the integration of recent developments (i) in the field of tectonic geomorphology on understanding landscape building processes, (ii) in the field of subsidence engineering on process modelling and (iii) in the field of geodesy on data accuracy.

Data from ground-based monitoring methods such as levelling surveying and Global Positioning System (GPS) can be interpolated to create two-dimensional subsidence lines or three-dimensional subsidence maps. However, the quality of interpolated estimations depends on distribution of data in space and time (Chilès and Delfiner, 1999). Because

ground-based monitoring techniques are labour intensive. Monitoring is restricted to areas that are highly likely to show deformation. Recent developments in remote sensing techniques such as PSI may enable the acquisition of highly accurate subsidence datasets with a more ideal distribution of data points.

Applying deterministic modelling methods, the pre-calculation of subsidence requires the inclusion of all relevant processes and their mechanics. This has lead to several problems. Firstly, the accuracy of pre-calculation will decrease if some of the relevant drivers are partly or completely unknown or non-measurable (Kratzsch, 1983). Secondly, the extent of the ground layers overlying the mining seam may be highly variable, containing many faults and a complicated geometry. In empirical modelling, the accuracy of the prediction depends on the accuracy of the relevant parameters. Empirical models are often too general to work as a reliable pre-calculation tool. Most empirical models are based on coal mining taking place at less than 90 meters depth.

The key indicators that are essential in the understanding of ground surface deformation defined in this thesis are:

1. The outside shape of the subsidence area: a shape along the outside of the disturbed surface area, where the ground surface is unaffected.
2. The total subsidence profile: the magnitude profile of the subsidence area after the moment of recovery.
3. The moment of recovery: the date at which the disturbed ground surface area has returned to a stable position [date].
4. The maximum rate: the maximum deformation rate of the disturbed ground surface area in distance of vertical change over time [mm a^{-1}].
5. The moment of maximum rate: the time at which the disturbed ground surface area has first reached the maximum deformation rate [date].

The examples of earlier studies of ground surface deformation given in this chapter are summarised in Table 2.4. The ability of the applied monitoring or modelling method to estimate the key indicators, numbered K1-K5, is compared. For the first two indicators, outside shape and total profile, the dimensionality is given. If for example the value in the table is 1D, this means that the method is able to express a certain indicator in one dimension.

Table 2.4: Summary of previous studies, the observed deformation process and the ability to express the 5 key indicators

reference	location	model	driver	S_{max} [mm]	depth [km]	extent ca. [km²]	monitoring	model	KI1	KI2	KI3	KI4	KI5
NCB, 1966	hypothetical	Subsidence engineers' handbook	coal mining	600	0.24	1	no	E	2D	2D	yes	no	no
Helm, 1983	US and New-Zealand	Depth-porosity model	fluid withdrawal	1200	0.9 to 4.5	3 to 90	no	D	no	1D	no	1D	no
Helm, 1984	US and New-Zealand	Aquitard-drainage model	fluid withdrawal	1200	0.9 to 4.5	3 to 90	levelling	D/E	no	1D	yes	yes	yes
Raymond,1996	France (mulhouse)	nnt	potash mining	3600		200	InSAR	nnt	3D	3D	no	no	no
Chrzanowski, 1997	Canada	FEMMA	potash mining	600	0.4 to 1.1	20	levelling and GPS	D	2D	2D	yes	no	no
Coulthard, 1999	Australia	UDEC	longwall coal mining	850	0.3	1	levelling	D	2D	2D	no	no	no
Perski, 1999	Poland	nnt	coal mining	3500	0.2	1500	InSAR	nnt	3D	3D	no	no	no
Wright, 1999	England	nnt	coal mining	2500	0.3	70	InSAR	nnt	3D	3D	no	no	no
Sheorey, 2000	India	Modified Influence Function Model	coal mining	2200	<0.4	1	nnt	D/E	3D	3D	yes	yes	yes
Wegmuller, 2004	Italy	nnt	fluid withdrawal	20		1500	InSAR	nnt	3D	3D	no	no	no
Wegmuller, 2005	Mexico	nnt	fluid withdrawal	800		1500	InSAR	nnt	3D	3D	no	no	no
Wegmuller, 2005	Germany	nnt	coal mining	6000	0.3	16	InSAR	nnt	3D	3D	no	no	no

The two most important limitations of currently existing models are:

⇒ Inability to accurately pre-calculate temporal and spatial variation and extent of ground surface deformation due to limited dimensionality

⇒ Lack of universality in applied method, need to establish new variables for each situation

An alternative modelling approach will be discussed in the following chapters of this thesis. This approach is based on the correlation between large, comprehensive datasets of both subsidence and the mining activity. Using these data, the spatial and temporal patterns of monitored surface deformation can be correlated with the method, volume and rate of extraction of mining. This is essentially a data-driven 'top-down' approach, which is now considered by some to be a more appropriate way to analyse such complex systems (Hastie et al., 2001). The principles of the influence function method are used as the theoretical basis of the cone model.

The action-reaction relationship between excavation and deformation can be used to understand the far more complicated chain of physical processes taking place in the ground during the re-stabilisation of a new equilibrium in the zone of disturbance. This type of statistical analysis of the key variables determining the behaviour of the driving process and the surface deformation process, as well as correlating the two groups of variables requires multi-variable regression.

The major requirement for this approach is the availability of monitoring datasets of sufficiently high spatial and temporal resolution to allow meaningful relationships to be established (Kemeling et al., 2004). Recent developments in remote sensing techniques, most notably InSAR, are beginning to allow for acquisition of such extensive subsidence datasets, providing greatly enhanced capabilities for the analysis of the behaviour in space and time of subsidence processes (Chilès and Delfiner, 1999).

InSAR analysis can result in an extensive subsidence dataset, giving a value for each pixel of approximately 20 m^2. To acquire reliable measurements from conventional InSAR, a balance needs to be found between a short enough time interval to conserve coherence and a long enough time interval to allow for a measurable amount of deformation to have taken place. This balance is hard to find in areas with land use of a highly temporally decorrelating nature such as some types of agriculture.

This has lead to the formulation of the key objectives of this research as described in sections 1.1 and 1.2 of this thesis. The first main objective is to test the use of InSAR and PSI in a rural and temperate research area experiencing gradual ground surface deformation. The second main objective is to develop a model that can estimate the temporal and spatial behaviour of ground surface deformation based on patterns of known mineral extraction and a dataset of ground-based surface monitoring data

CHAPTER 3. THE RESEARCH AREA: BOULBY, ENGLAND.

'In the English landscape everything is older than we think'
(Prof. Hoskins quoted in Spratt and Harrison, 1989)

3.1. Introduction

Since the production of mine plans became statutory in 1872 in the United Kingdom, they have been included in land use planning (Bell et al., 2000). The land use over most underground mine workings is rural or vegetated. This research is based in the Boulby area, located on the east coast of northern England (Fig. 3.1).

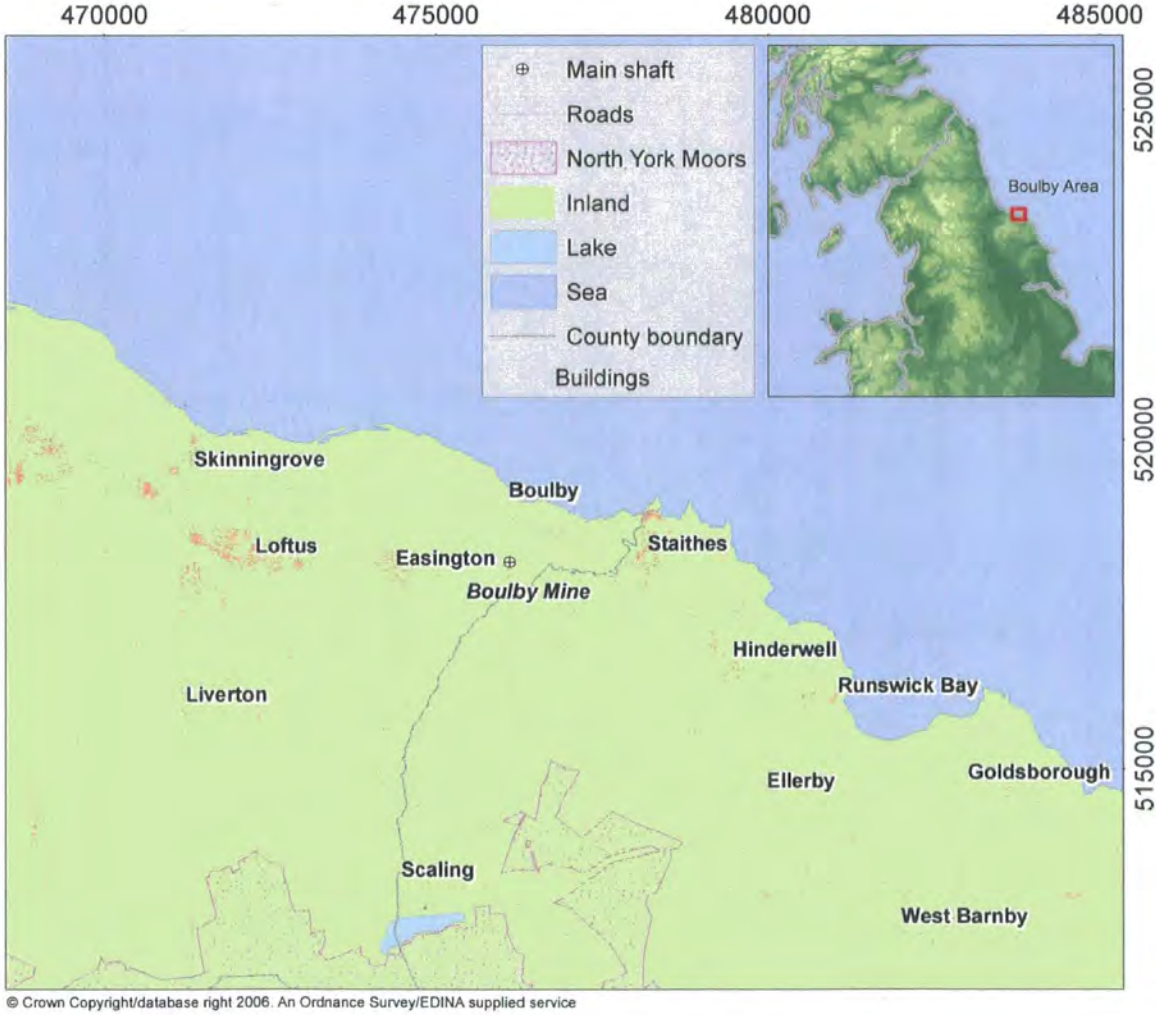

Figure 3.1: Location of the Boulby area (OS, 2003).

The Boulby area has an extent of approximately 216 km^2, measuring 15 kilometres north-south and 14.5 kilometres in east-west direction. The area is centred at approximately 54° 51' North and 1° 15' West, or in OSGB coordinates NZ47610 51819 (Fig.3.1). The area is

divided into two sections by a north south running border. The eastern part of the Boulby area is part of the Unitary Authority of Redcar and Cleveland Borough. The western part forms part of North Yorkshire County. The local geological history entails periods of sustained uplift, subsidence, erosion and sedimentation. At present, the area is subject to contemporary mining-related ground surface deformation. In this chapter the characteristics of the Boulby research area are discussed.

3.2. Climate

The general climate of the United Kingdom is referred to as maritime temperate or Cfb in the Köppen classification. Temperate climates are variable over both long periods (months) and short periods (hours) and weather conditions are hard to predict. The year-round influence of the atmospheric polar front and the surrounding large water bodies result in more water in the atmosphere than other areas at the same latitude. The chart in Figure 3.2 shows the monthly averages of some climatic variables for the East and North East of England Region calculated over the period 1971- 2000 (Hollis and Perry, 2004).

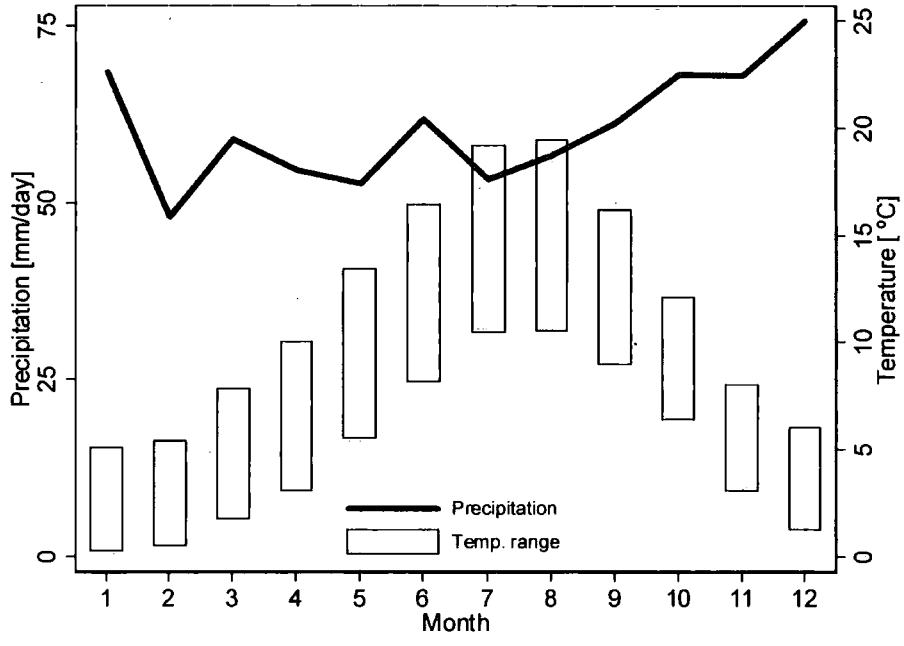

Figure 3.2: Climate chart for east and north-east England, the temperature is given as a bar ranging between the average daily minimum and maximum values.

The amount of humidity in the atmosphere is often high due to the high number of rainy days occurring evenly in all four seasons of the year. The number of rainy days ranges between 8 and 12 per month throughout the year (Fig. 3.3). Humidity in the atmosphere causes a spatially variable distortion in radar scenes.

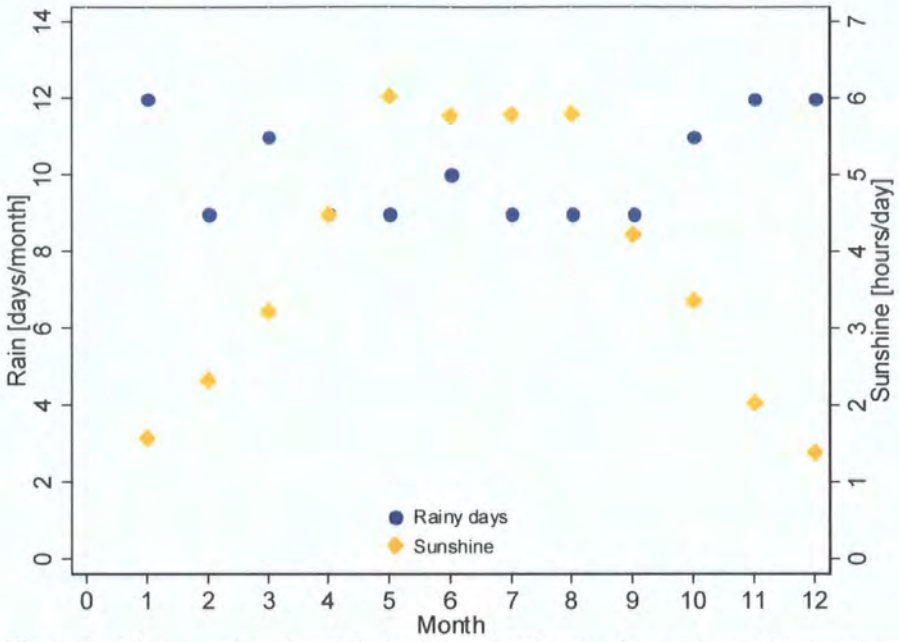

Figure 3.3: Climate chart for east and north-east England, the value for rainy days represents the average number of days with more than 1 mm of rainfall. The value for sun hours represents the mean monthly hours of sunshine.

The chance of an undisturbed atmosphere is highest when direct sunlight hits the ground surface. The average daily sunshine changes considerably from 1.4 hours in December to just over 6 in May.

3.3. Geology

3.3.1. Borehole data

The research area is covered by three sets of surface borehole data providing data on the geological history of the area. The boreholes cover most of the inland research area (Fig. 3.4). The first set is S1-S7, S9-S13 and S20, in total 13 boreholes concentrated in the area currently undermined. Another set of boreholes is W1-W4, lying in the area south west of the area currently undermined, where the potash layer is low. A third set is A1-A20, boreholes located further south west up to a distance of 11 kilometres from the research area.

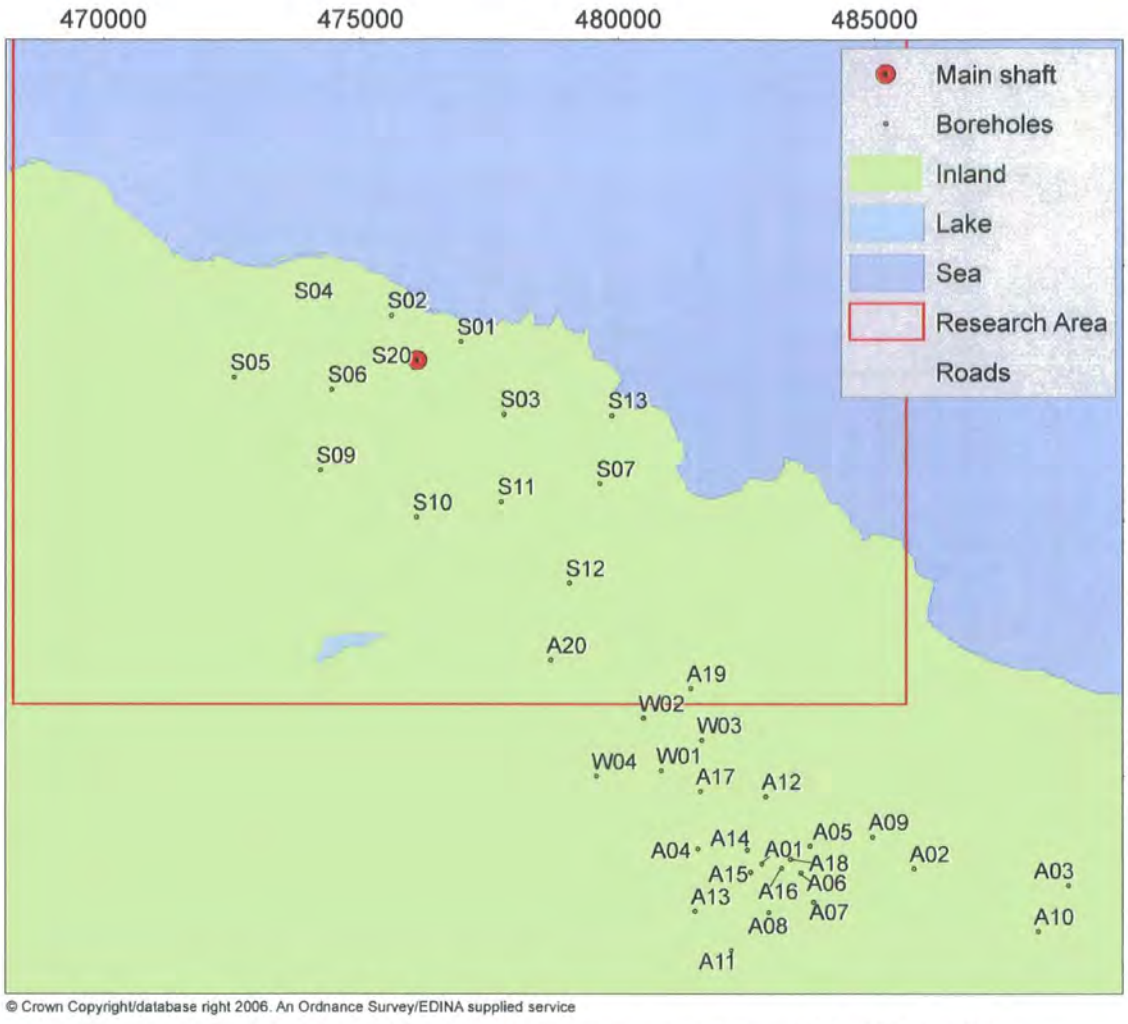

Figure 3.4: Borehole locations (37) in relation to the Boulby area (red square) (OS, 2003; OS, 2006).

These 37 boreholes give information on the depth of the boundaries between the main strata. For all these boundaries the three dimensions were derived[1]. The boundaries between layers that are determined are shown in Figure 3.5.

[1] Because the boreholes do not enter the earth perfectly vertical, the x and y co-ordinates of the boundaries within one borehole vary slightly. Only for the S boreholes were exact x, y and z co-ordinates calculated as a function of the depth. For the W and A boreholes, the x and y co-ordinates of the boundaries are equal to the x and y co-ordinates at the collar of the borehole. The z co-ordinate is directly calculated from the depth.

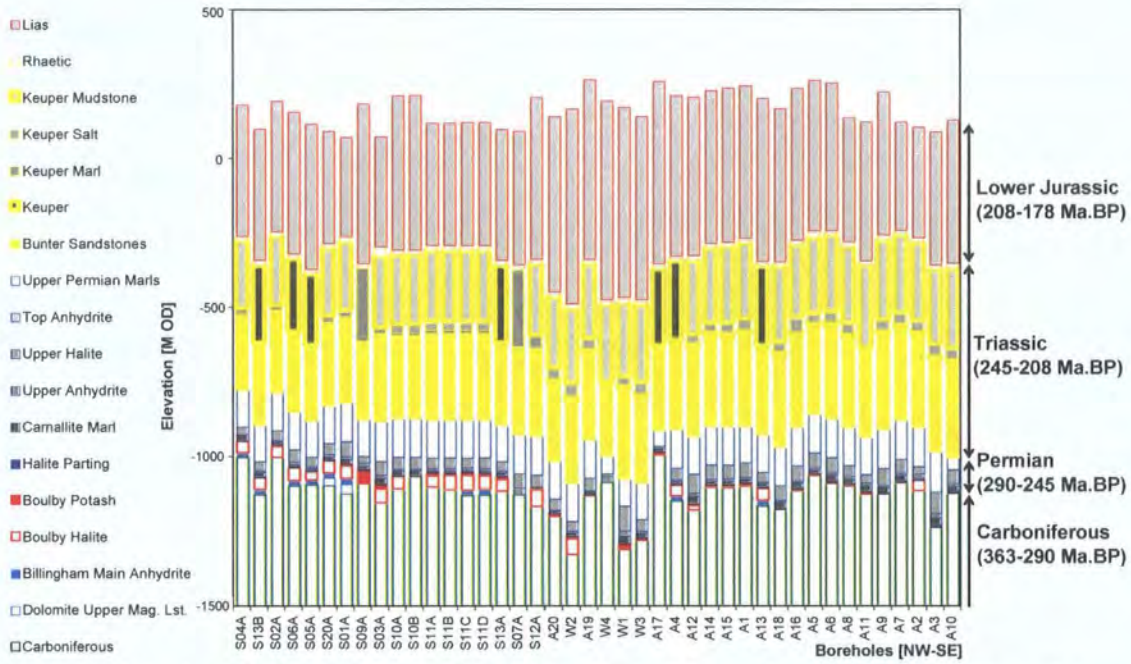

Figure 3.5: Geological layers in 37 boreholes, ordered from NW to SE, a time line is given on the right axis. Ages according to Summerfield (1991).

The boreholes in Figure 3.5 are ordered in north-west to south-east direction, based on the distance from S04 (Fig. 3.4). The boreholes are merely placed in an order and the spacing is evened out, the graph does not represent a profile. Despite this distortion, there seems to be a south east oriented dip visible along this line in the Triassic, Permian and Carboniferous layers. This is confirmed by an earlier study which mentions a 5° regional dip in south-east direction (Milne, 1978). The different layers can be clustered into four main geological periods: The Carboniferous, The Permian, The Triassic and The Jurassic (Fig. 3.4 and 3.5), which will be discussed in more detail in the following section.

Borehole S20 is located in the main shaft of the Boulby Potash mine. The potash and salt mining takes place in the Permian zone, which is located around 1100 metres M OD (Fig. 3.5 and 3.6). The diagram in Figure 3.6 is an illustration used by CPL and the layers are drawn schematically. It shows the special construction measures that were required to reach the potash under the Triassic water bearing sandstone layer.

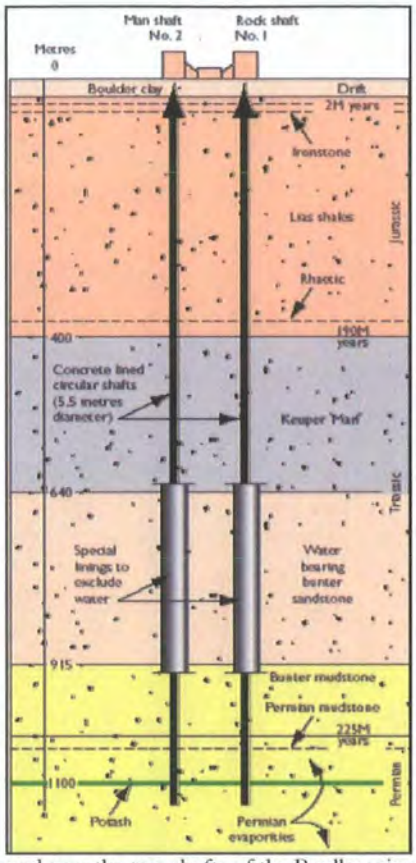

Figure 3.6: Diagram of the geology found near the two shafts of the Boulby mine, roughly based on borehole S20. The 'Man Shaft' or main shaft is the shaft used for the transport of men into the mine, the 'Rock Shaft' is used for transport of material out of the mine and equipment into the mine. (source CPL 2002)

3.3.2. Geological history of the Boulby area

The Boulby area forms part of the Cleveland Basin (Fig. 3.7), which consists of almost horizontally-bedded sedimentary deposits. It was part of the Upper Permian Zechstein sea that covered most of the land that forms the current Europe. The formation of the Cleveland Basin as a depression is mainly caused by Permo-Triassic subsidence (Rayner and Hemingway., 1974). Periods of massive sedimentation, erosion and uplift followed and currently the maximum elevation in the research area is 272 M OD in the south east.

Today, the research area is considered to be naturally tectonically stable, experiencing continuous marine erosion (Rawson and Wright, 2000). However this relative stability is disturbed by anthropogenic influences to the geology in the past three centuries. Mining induced subsidence is one of the anthropogenic processes typical of the 'Anthropocene', a term used to indicate the period of increased human influence on the Earth's systems (Crutzen, 2002).

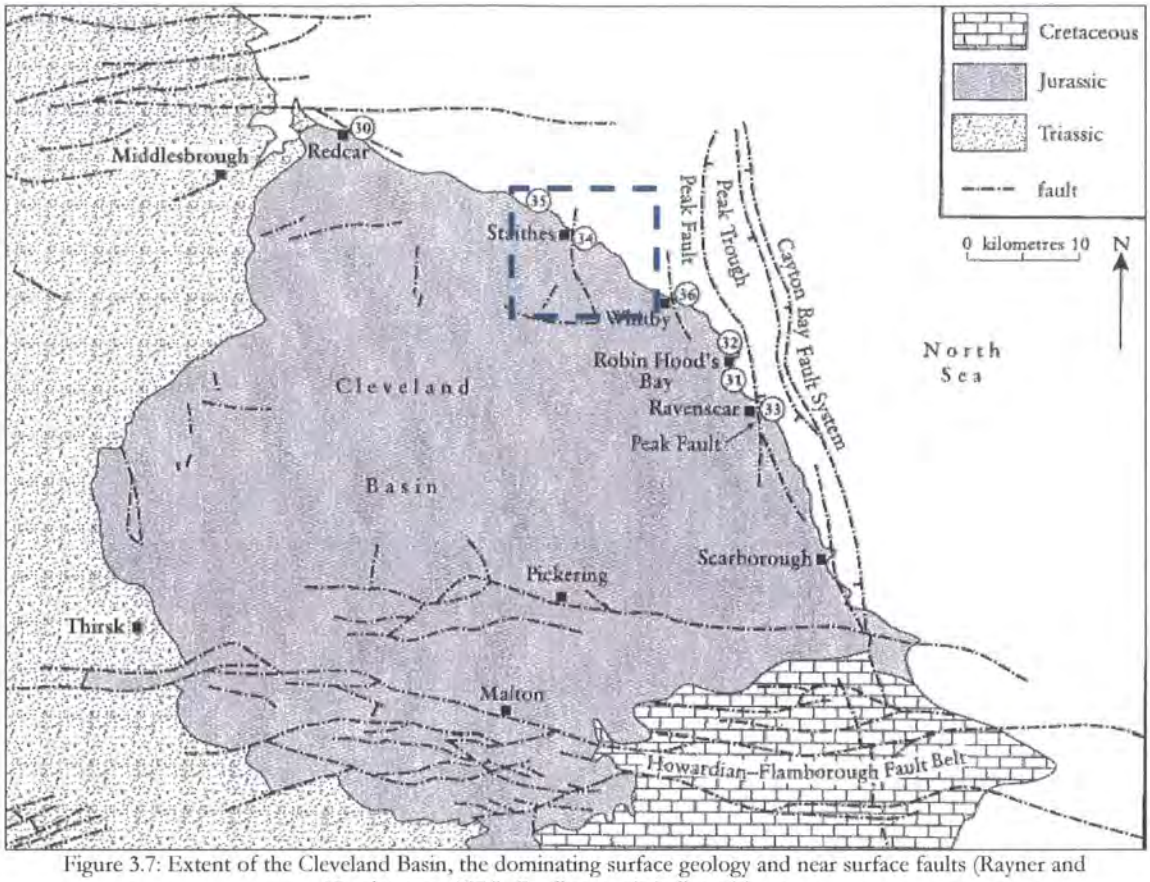

Figure 3.7: Extent of the Cleveland Basin, the dominating surface geology and near surface faults (Rayner and Hemingway., 1974). Boulby area is indicated in green.

3.3.2.1. Carboniferous period (363-290 Ma. BP)

The Cleveland Basin was formed in the Carboniferous period although it is believed to have been a rather shallow basin at the start of the following Permian period (Rayner and Hemingway., 1974). The Lower Carboniferous basement of the Cleveland Basin dates from between 363 and 320 Ma. BP. The east of England was believed to be an upland area in the beginning of this period as a result of the Caledones orogeny that formed the north-south oriented Pennines (Anderson and Owen, 1980). A long period of alternating eustatic transgression and regression followed. Local differences in gravity, possibly related to subsurface granite blocks, lead to a block and basin structure, where basins would subside two or three times faster than blocks in periods of regression. Rates of subsidence are estimated to have reached 0.3 mm a^{-1} and have locally caused displacements of 655 metres (Rawson and Wright, 2000).

Gradual lowering of the sea, which covered almost all of England and Wales, allowed for terrestrial conditions in which land expanded from a landmass in the north of the current British Isles. The conditions were equatorial and the climate tropical (Simms et al., 2004).

The buried remains of the Upper Carboniferous tropical forests have developed into present day coal beds in the midlands and northern England. In the Boulby area these are located too deep to allow for profitable coal mining (Spratt and Harrison, 1989). Throughout the Upper Carboniferous period, from around 320 Ma. BP, most of the relief was denudated during a 34 Ma period of desert weathering (Simms et al., 2004).

3.3.2.2. Permian period (290-245 Ma. BP)

In the transition to the Permian period a period of massive earth deformation started. Collision of several tectonic plates lead to the formation of Pangea and that of the mountain ranges in Northern Europe. In the Permian period most of England was part of Pangea which was still located near the equator but had desert conditions causing the extinction of most land and marine species (Anderson and Owen, 1980). In the Lower Permian period the climate was (sub-) tropical, such that deposits in the Boulby area have been classed as piedmont breccias, thin uniform layers with fragmented rock.

In the Boulby area, nine thin evaporite layers capped by the Top Anhydrite are located at a depth of approximately -1200 meters OD. These evaporites were formed during three cycles in the Lower Permian period (Fig. 3.5). The Upper Permian Marls that overlie the evaporites were deposited during the Upper Permian period (Fig. 3.5). Because of the flat topography, incursion of the Upper Permian Zechstein Sea into the Cleveland Basin may have been a rapid but smooth change (Rayner and Hemingway., 1974). This would explain the conservation of the now valued evaporites. Initially the sea in the basin was between 100 and 200 metres deep, but an extensive process of marine deposition started to fill up the basin.

Over time, the covered evaporites experienced cycles of syn-sedimentary subsidence(Rayner and Hemingway., 1974). Evidence is found for tectonic deformation in the Permian layers (Milne, 1978). Horizontal overfolds and overtrusts, visible in the mine walls are signs of lateral flow of material and plastic deformation. Gravitational deformation seems to have taken place causing the evaporite layers to be uplifted and to interact with the Triassic Bunter Sandstone.

3.3.2.3. Triassic period (245-208 Ma. BP)

The Permian layers are covered by less fossiliferos Triassic sandstone and marl layers. From 250 Ma BP the Triassic period was characterised by large quantities of material being deposited under shallow marine conditions.

Keuper Marl consists of red-brown dolomitic mudstone or silty mudstone with a laminated structure. In this layer mineral beds of gypsum, anhydrite and halite are found. A thin top layer of grey material deposited in the Rhaetian Era (219-213 Ma. BP) indicates the end of this period.

3.3.2.4. Jurrassic period (208-146 Ma. BP)

Massive uplift of the Market Weighton Block, an extensive granite formation to the south of the Cleveland Basin started in the Jurassic period, from 213 Ma BP. This contiguous uplift changed the Cleveland Basin from a shallow sea into a coastal delta. From around 170 Ma BP the Basin was a (sub) tropical delta and traces of dinosaur remains are found (Osborne and Bowden, 2002).

Lias was formed during the first of three Jurrasic periods, referred to as the lower Jurassic (208-178 Ma. BP). On the current coastline Lias is exposed, for example forming the almost flat wavecut platforms. A part of the Middle Lias, the Cleveland Ironstone formation, was deposited during the Upper Pliensbachian – Domerian period. Tilting of the Cleveland Basin towards the North Sea Basin continued throughout the Mesozoic and Tertiary periods.

3.3.2.5. Cretaceous and Tertiary Periods (144-2 Ma. BP)

At the close of the Jurassic era the Cleveland Basin became terrestrial and deposition halted. However, a change in sea-level covered the area by seas resulting in a period of chalk deposition. In the Boulby area no traces of these Cretaceous deposits are found, due to the subsequent period of erosion, which started 70 Ma BP and continues to today (Rawson and Wright, 2000).

3.3.3. Quaternary period (2-0 Ma. BP)

More recently, the research area was influenced by glacial presence. The present day landscape in the Boulby area was formed by ice sheets pushing in and out of the area

during three periods in the last 2 million years on the one hand and by the related sea level change on the other hand (Fig. 3.8) (Shennan, 1988).

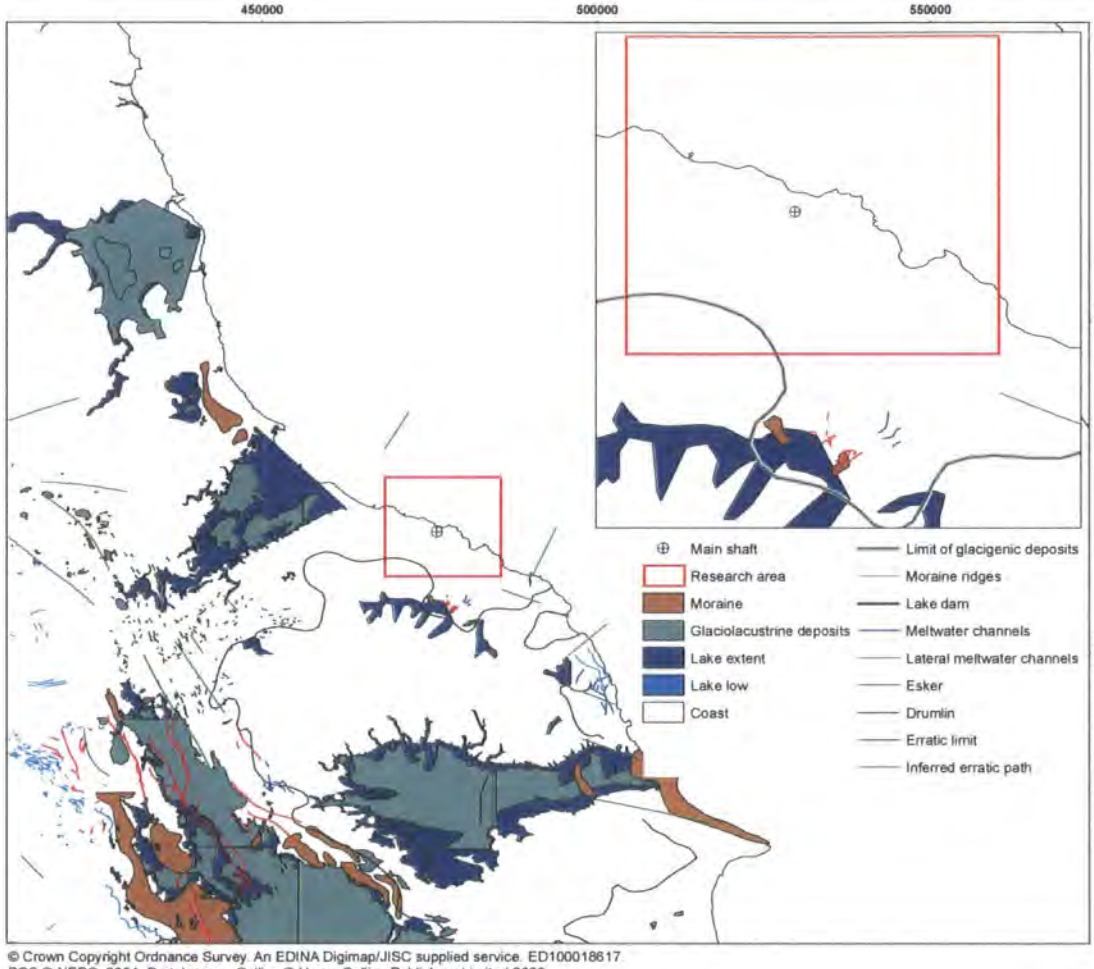

Figure 3.8: Glacial map showing Boulby research area in red (Clark et al., 2004).

During the Quaternary period the study area was repeatedly covered by ice sheets from the north. The ice deposited several units of glacial diamict across the area which locally reach thicknesses of 30 m or more. The last (Devensian) glaciation saw the extension of a lobe of ice southwards along the current North Yorkshire coast, with a moraine marking the western limit of the ice a short distance inland of the Boulby study area. This ice impounded several valleys which became flooded as a result. The retreat of this ice sheet resulted in the deposition of a locally variable sequence of glacial outwash deposits comprising sands and gravels that locally cap the glacial diamict on the Boulby cliffs.

Consequently, the inland part of the Boulby area has a northwards descending rolling topography with some steeper parts in the south east and steep cliffs along the coast (Fig. 3.9 and 3.10). Current marine erosion is a result of a sea level rise around 9000 BP and has

since been enhanced by human activities such as deforestation that may have started around the same period (Horton, 1979).

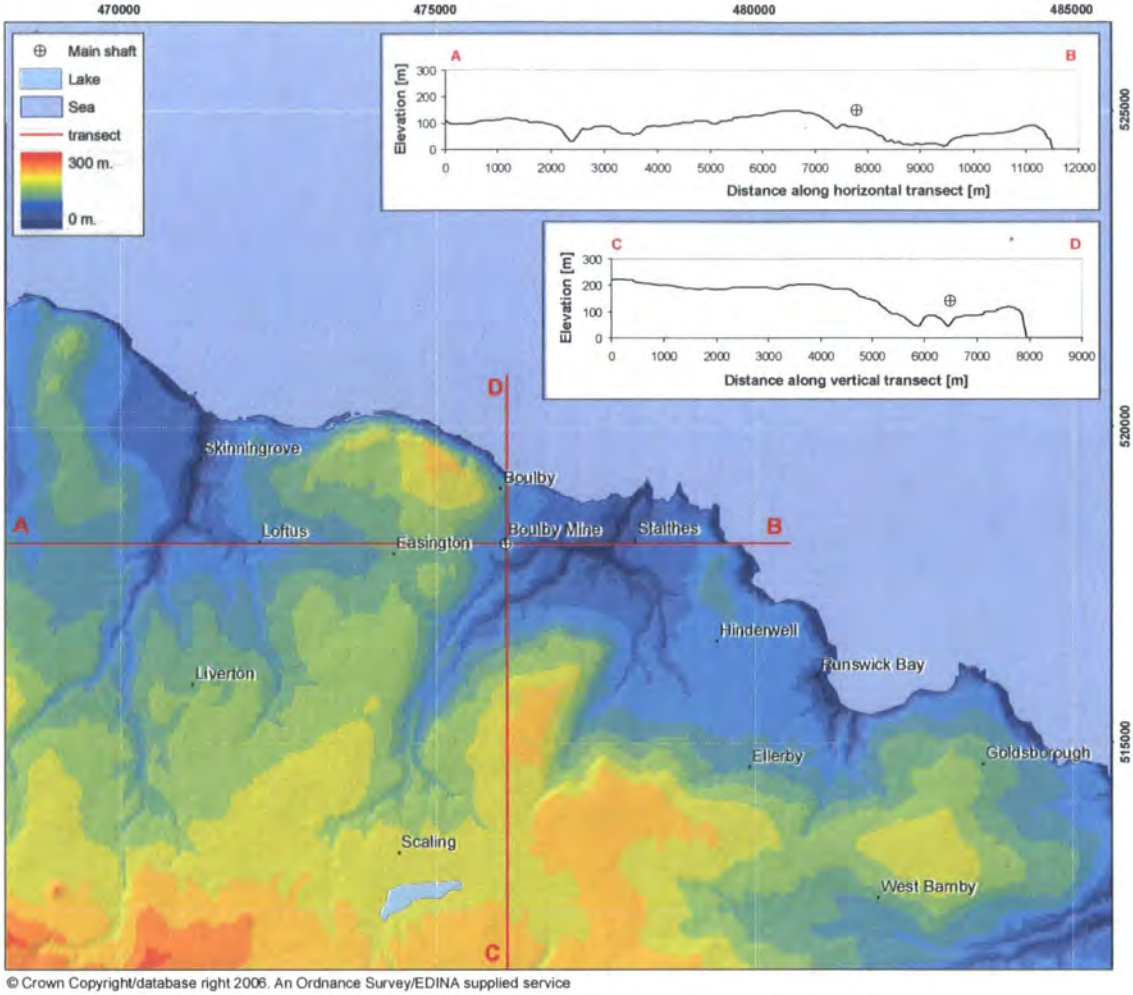

Figure 3.9: Digital elevation model (DEM), based on the Ordnance Survey Profile dataset

The elevation increases from sea level to a maximum of 272 metres OD in the south east. The mean elevation of the total inland area is 153 metres OD. Beacon Hill with an elevation of 301 metres OD is located approximately 1 km south of the Boulby area and gradually slopes down to the north where it forms the highest part of the Boulby area with an elevation of 272 metres OD. The lowest parts of the areas are the valleys of Skinningrove, Staithes and Runswick Bay.

Less than 9 km^2 of the area is below 67 metres OD, less than 14 km^2 is higher than 220 metres OD and the majority of the inland area (110 km^2 or 83%) ranges between 67 and 220 metres OD. The area is rolling with slopes under 10° in the majority of the inland area (124 km^2 or 93%). The south east corner of the Boulby area is oriented eastward and some

parts in the south face southward, but the dominating aspect of the area is north and north-east facing. Only 9 km^2 (7% of the inland area) has a south-west facing aspect. The general trend of the area is down sloping from the south west to the north east following three catchments formed in valleys draining into Skinningrove Beck and Staithes Beck and Runswick Bay.

The coastline consists of steep irregular and unstable dark Liassic shale and sandstone cliffs and small valleys (Fig. 3.10). Rock platforms along most of the coastline and some natural sandy beaches offer protection to the cliffs against wave impact. The rock platforms extend to approximately 300 metres into the sea just above sea level at low tide but largely covered at high tide. The main landscape forming process responsible for the steep cliffs is marine erosion (Spratt and Harrison, 1989).

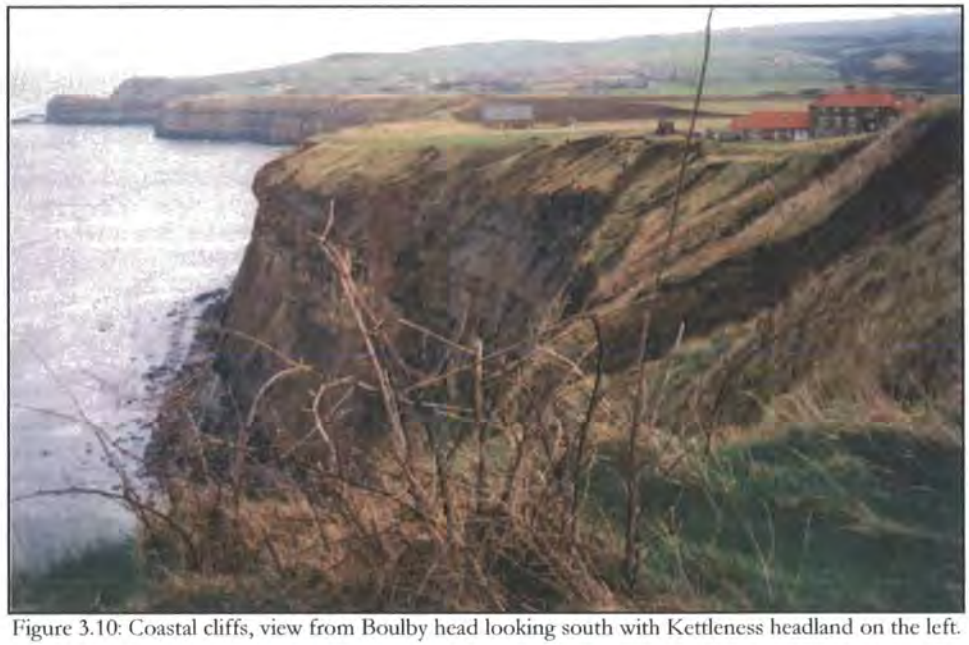

Figure 3.10: Coastal cliffs, view from Boulby head looking south with Kettleness headland on the left.

3.4. Land use in the 'Anthropocene'

Despite a long history of human influence, most dramatic changes have occurred since the 19th century in the 'Anthropocene' (Crutzen, 2002). Changes in vegetation and general land cover are caused by the changing economic and cultural value of the environment to the human settlers. While in past the biological succession of heath land into woodland was prevented by grazing of cattle, since around 1850 it has been prevented by controlled burning of pioneer vegetation to keep an open moor suitable for shooting grouse and

pheasants. Land cover of cultivated grasslands and arable land has changed considerably since the 1970s from low input agriculture to higher intensity monoculture. Since the 1920s forest plantations have replaced deciduous trees with softwood pine trees. The most important change in land cover was caused by the development of industrial activities such as mining and iron smelting in the area starting in the 1850s. As a consequence of these changes in land cover, erosion and sedimentation processes have intensified over the last few centuries. Burning of the moors and human disturbance of the surface destroys the natural protective vegetation and top layer of the soil leaving it prone to water and wind transportation.

3.4.1. Land cover, demographics and designated areas

The land cover of the United Kingdom has been classified by the Centre for Ecology and Hydrology (CEH) who produced the Land Cover Map 2000 (Fig. 3.11 and 3.12). According to their classification, approximately 49% of the land surface in the research area is covered by arable horticulture. These fields are bare in the winter and are used to grow cereals during the growing season. The second largest land cover type is grassland, which covers 23% of the land surface of the research area. The Land Cover Map (LCM) classification divides grassland into five subclasses all represented in the research area. These subclasses are: improved grassland, setaside grass, neutral grass, calcareous grass or acid grass. The shrub-like heath vegetation forms the third land cover class, which covers 12% of the land surface of the research area. In this class the following three LCM subclasses are merged: dense dwarf shrub heath, open dwarf shrub heath and bracken.

Woodland covers 9% of the land surface of the research area. The two woodland subclasses used by LCM are both represented in the research area: broad leaved / mixed woodland and Coniferous woodland, they are both mainly concentrated in the lower parts of the river valleys (see Fig. 3.11). Four of the LCM subclasses found in the research area can be merged into the urban and rock land cover class. These are littoral rock, littoral sediment, suburban/rural developed and continuous urban. In total these four subclasses cover 4% of the land surface of the research area. The final land cover class is named 'rest' and includes the subclasses fen, marsh, swamp and inland bare ground which cover 3% of the land surface of the research area.

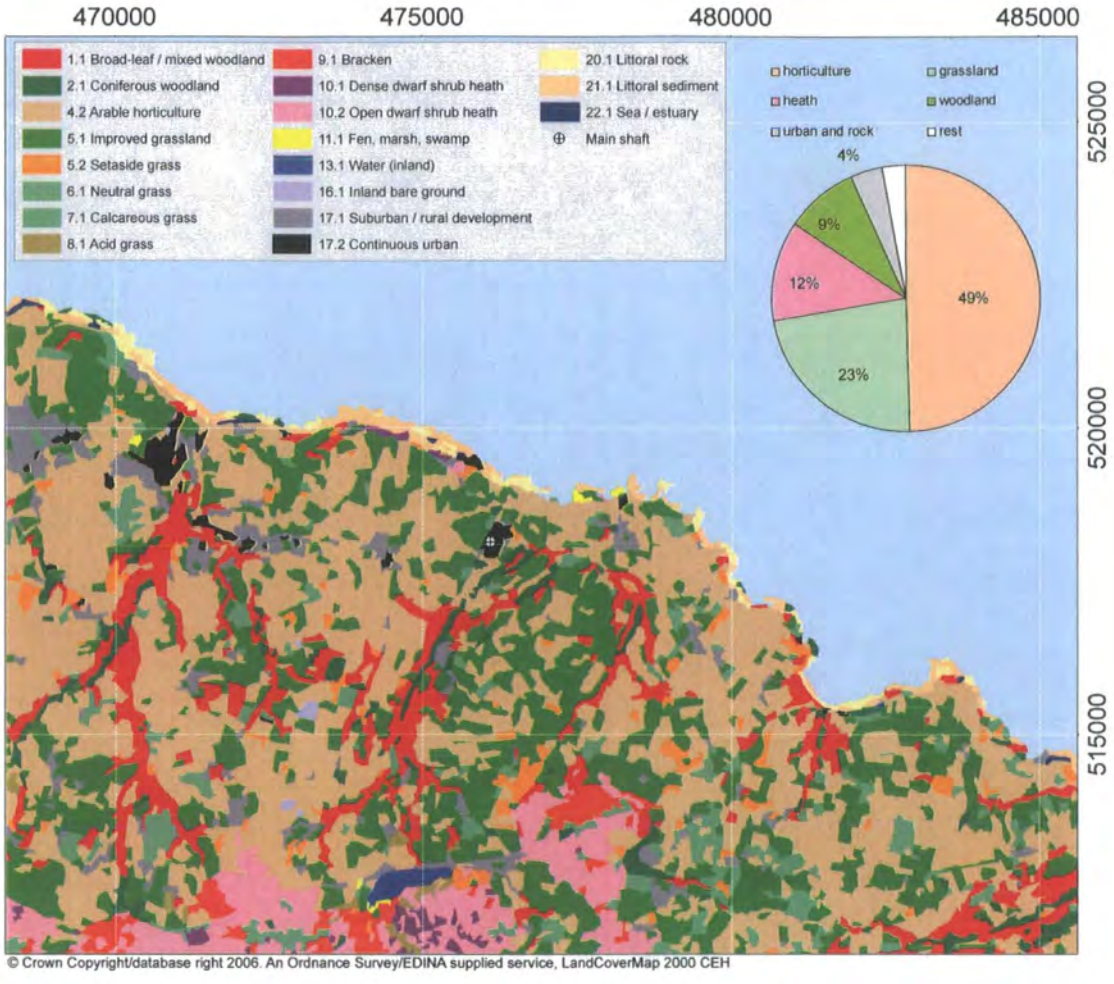

Figure 3.11: Designated areas in the Boulby area (OS, 2003).

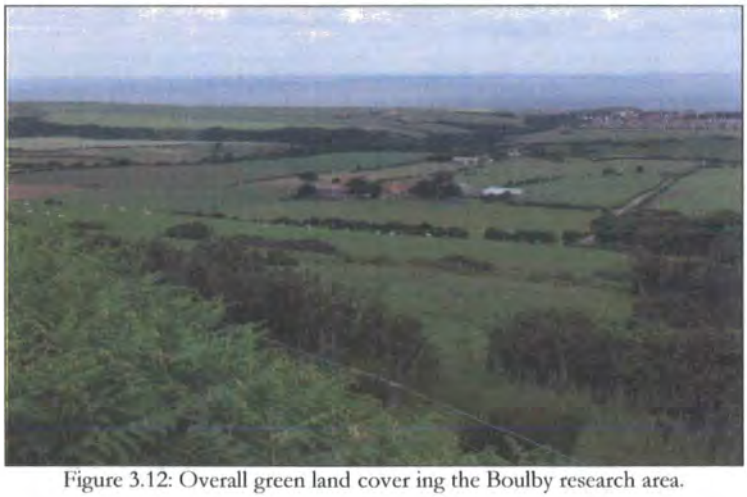

Figure 3.12: Overall green land cover ing the Boulby research area.

In the Boulby area there are twelve small villages: Brotton, Skinningrove, Loftus, Easington, Boulby, Staithes, Port Mulgrave, Hinderwell, Newton Mulgrave, Runswick Bay, Ellerby, Mickelby and East- and Wets Ellerby. The main concentration of population is in the north west of the area formed by Brotton village, Skinningrove harbour and village and

Loftus village, with a combined population of approximately 15000 persons (2001 Census). The total population in the Boulby area is less than 20,000, corresponding to approximately 1.5 persons per hectare.

Centrally located in the area is the shallow Scaling Reservoir, used for recreation such as fishing and water sports. A small section (4%) of The North York Moors National Park (NYMNP) falls within the Boulby area. The NYMNP was designated in 1952 mainly because of the upland heath land which is the largest single expanse in England (Rees et al., 2001). The semi-natural moor land habitats are of national and international relevance for many flora and fauna species and are therefore maintained. Management practices involve controlled burning and land use planning to avoid overgrowing and scattering of the moor land. It is important to realise that moor land vegetation is of high natural and aesthetic value, but it can only be maintained by human influences. The Boulby area has several national and international designated sites (Fig. 3.13).

The entire coastline of the Boulby area is classified as Heritage Coast except Skinningrove harbour. Patches of land are classified as Sites of Special Scientific Interest (SSSI) and patches of coastline are National Trust Holdings. The south west corner of the Boulby area is part of The North York Moors National Park classified as a Special Protection Area (Mouchel and Partners, 1996).

According to the Joint Characteristics Areas classification used by the English Nature and Countryside Agency (ENCA) the Boulby area is part of the 'North Yorkshire Moors and Cleveland Hills'. The coastline is part of sub cell 1D of the Scarborough Borough Council Shoreline Management plan, covering coastal process unit 1-8 (Mouchel and Partners, 1996). Mining is an important part of the industrial heritage of North East England. The region has been mined extensively for lead, copper, tin, limestone, coal, whinstone and gravel, but the Boulby area has mainly been mined for alum, iron, jet and cement (Spratt and Harrison, 1989).

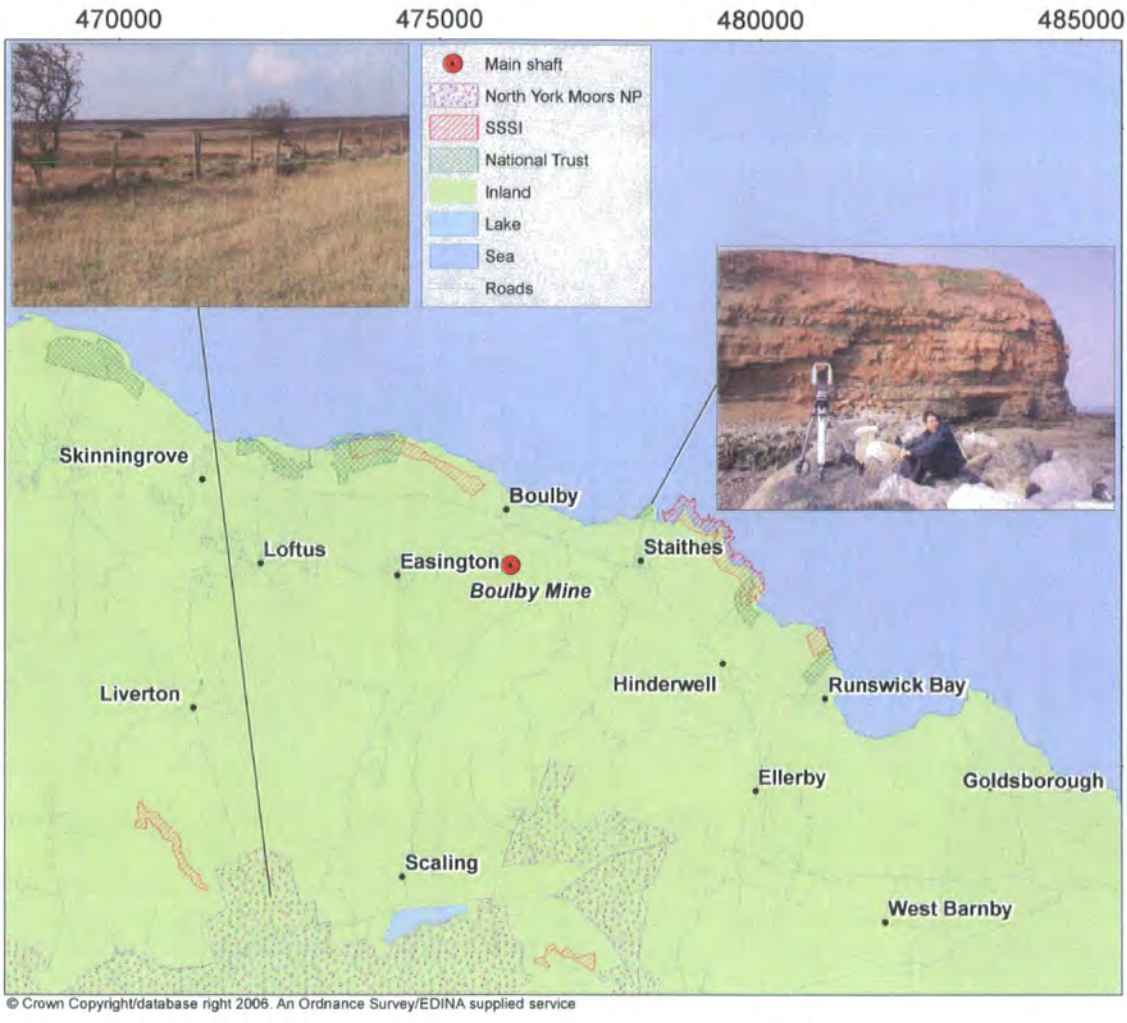

Figure 3.13: Designated areas in the Boulby area (OS, 2003).

3.4.2. Ironstone mining

Ironstone mining started in the research area approximately 2000 years BP, in the Iron Age. Archaeological evidence has been found of smelting of iron originating from Rosedale in the North York Moors. Also, evidence has been found of ironstone mining in the 12th century, which was mainly done under the direction of religious houses (Hemingway and Wilson, 1963). From around the late 1860s the Boulby area was part of the largest iron producing area in the world and the last ironstone mine in the area closed in 1964 (Fig. 3.14) (Spratt and Harrison, 1989). At its peak the area employed more then 8000 men and produced approximately 30% of the iron mined in the United Kingdom.

In total an estimated amount of 365.6 million tonne was mined between 1850 and 1964 in the Cleveland Basin. Initially ironstone was mined from Carboniferous shales of Westphalian age, but after 1850 intensive mining of Jurassic ores of Domerian age became dominant (Hemingway, 1974). The iron mines in the Cleveland basin can be divided into

three main areas of concentration. One of these groups is concentrated around the Skinningrove Beck and Huntcliffe area in the north west of the Boulby area (Fig. 3.15).

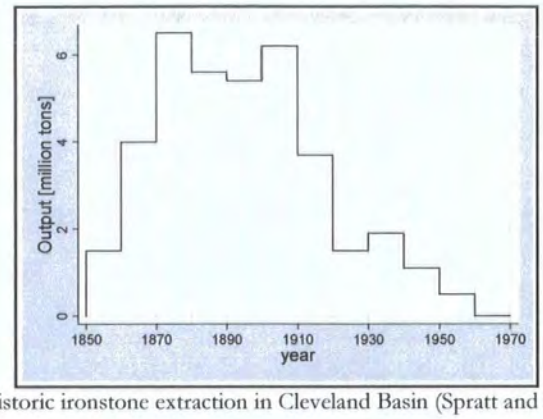

Figure 3.14: Historic ironstone extraction in Cleveland Basin (Spratt and Harrison, 1989)

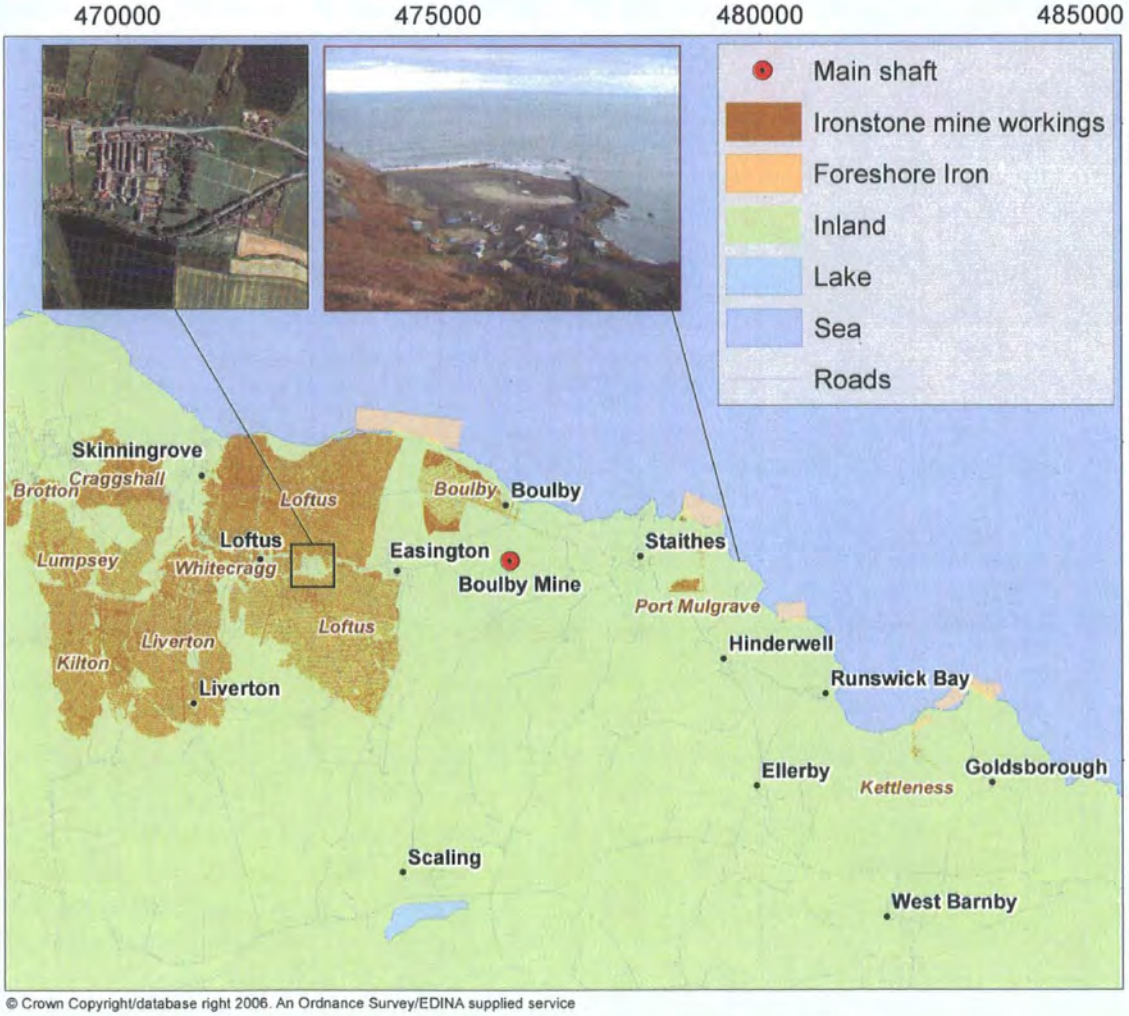

Figure 3.15: Extent of historic Iron mines in the Boulby research area.

Within the Boulby area 16 sites have been identified that have been mined for Jurassic ironstone. The depth of the main Jurassic Cleveland Ironstone Formation is up to 200 metres below the surface and it reaches the surface at the coastal cliffs and steeper valleys

in the area. Historic mines are found around these access points. The relatively deep location of the ironstone was a reason for the decline of the industry in the 1960's, when it became more economic to mine for ironstone elsewhere.

3.4.3. Alum mining

Large scale alum mining started in 1604, and by 1700 the Boulby area was part of the main centre for alum production of England (Spratt and Harrison, 1989). Alum mining occurred in the top 31 metres of the shale below the sandstone. Although almost unlimited supplies of suitable shale were available in the area, the activities were limited by practical and economic factors in relation to the processing of the raw shale to a marketable product. To produce 100 m^2 of alum, a large quantity of shale material was needed ranging between 3,000 and 10,000 m^2. Two major alum workings in the Boulby area were located directly on the coast at the headlands of Boulby and Kettleness, which were both intensely altered. A third quarry was located north-west of Sandsend. The alum working at Boulby headland reached 61 metres depth and 3.2 km in length.

Roman cement was mined from the same shale material that contains alum. This hydraulic cement had the ability to dry under water and was used in coastal protection works and piers. In the first half of the 19th century three locations were mined for cement in the Boulby area, east of Sandsend, Skinningrove and Runswick Bay. Although the quantity of shale material needed to produce 100 m^2 of marketable cement was comparable to the quantity needed to produce alum (7,000 m^2), the impact on the landscape was less visible as the mining took place in shafts into the cliff faces (Spratt and Harrison, 1989).

3.4.4. Jet mining

Jet stone, like coal and diamond, is fossilised wood and is mined in flattened planks. Whitby Jet has been a popular collectible, used for its ornamental value since the middle ages and mining has taken place in a wide area including the Boulby area. The Drift entrances have all collapsed but can sometimes be recognised by distinctive bare heaps of ore waste. More inland towards Guisborough shallow jet mines have caused subsidence in the form of sudden deep pits.

3.5. The Boulby potash mine

Potash is defined as rock that contains potassium chloride or sylvinite (KCl) valued for its potassium (K). The presence of potash in the North East of England was first discovered

near Ailslaby in 1939 by D'Arcy Petroleum Company (Milne, 1978). In 1952, a number of boreholes were drilled to determine the location and extent of the potash resources. The layer was regarded as uneconomic due to its deep location and the difficulty of sinking shafts into the water bearing Bunter Sandstone (Fig. 3.6) (Milne, 1978). In 1968 ICI in cooperation with Charter Consolidated Limited set up a new company Cleveland Potash Limited (CPL) and applied for a planning permission to mine 1.5 million ton of salt and potash per year in the Boulby area. In 1973 two 1100 metre shafts were sunk and CPL started excavating the Boulby potash mine. The surface installations comprise an 32.4 hectare site with the shaft entrances, an ore treatment plant and a rail loading facility (Milne, 1978).

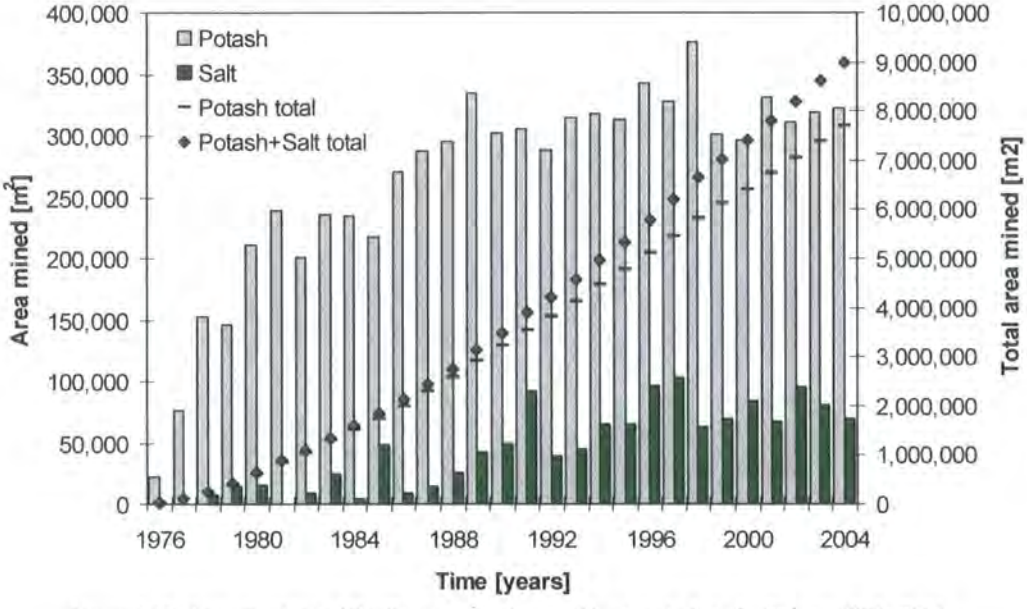

Figure 3.16: Annual extent of Boulby potash mine workings, potash and salt from 1976- 2004

The depth of the potash layer varies between 800 and 1,500 m below the surface with a seam ranging in thickness from 0–20 m but averaging 7 m. These deposits contain approximately 40% sylvinite and 50% sodium chloride. Since the excavations started in 1973 the mine has extended in a radial manner from the shafts. Since 1994, potash output has varied between 0.80 and 1.03 Mt a^{-1}, with salt production ranging from 0.38 Mt a^{-1} to 0.66 Mt. a^{-1}. In 2001, CPL produced 0.89 Mt of potash and 0.40 Mt of salt, but 2002 outputs measured to approximately 1 Mt of potash and 0.5 Mt of salt (CPL, 2002a). The progression of the total mined area is given in Figure 3.16. The Boulby potash mine is currently one of the deepest active mines in Western Europe (CPL, 2002a). Mine workings extend approximately 8 km inland and 7 km

offshore and the total extent of open seams is estimated at 1500 kilometres in the beginning of 2005 (Fig. 3.17).

3.5.1. Applied mining technique

The mining method applied in the Boulby potash mine is called 'room and pillar' mining (Kratzsch, 1983; Milne, 1978). Permanent pillars of potash are left behind and metal rods are inserted into the roof to control the closure rate in the mine workings. This way, rather than through sudden collapse, closure takes place gradually as a consequence of the crushing of the pillars by the overlying weight. It is essential that the overlying rock mass stabilises gradually without breaking.

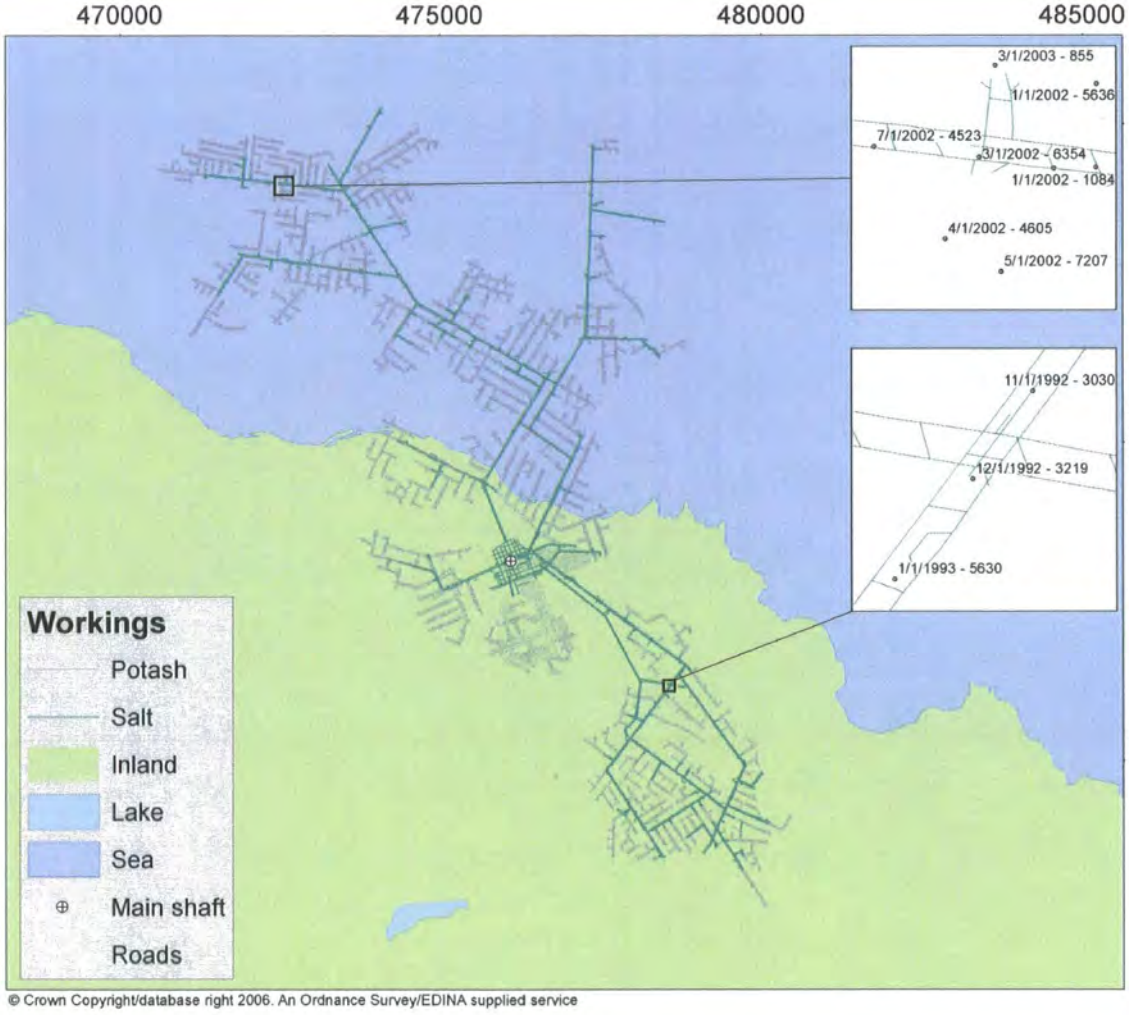

Figure 3.17: Map of mine workings CPL potash mine, Boulby area (OS, 2003)

Although closure is caused by gravity and the weight of the overlying rock mass, the deformation in the mine seam is not one dimensional. The mine roof bends downwards, the floor moves upwards and the walls move inwards almost simultaneously (Fig. 3.18) (Kratzsch, 1983).

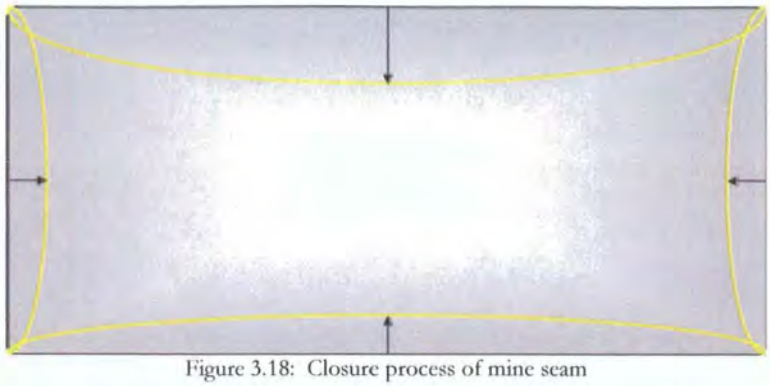

Figure 3.18: Closure process of mine seam

In the Boulby potash mine this process is closely monitored to enable safe access to the mining face. The combined horizontal closure tends to behave according to a standardised closure curve shown in the graph in Fig. 3.19.

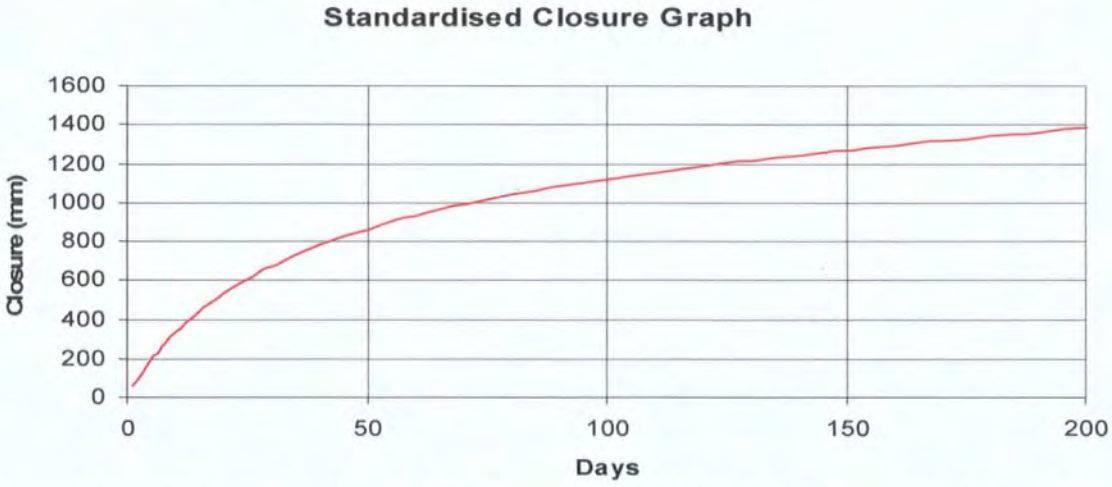

Figure 3.19: Standardised closure graph used by Boulby mining engineers (CPL, 2004), horizontal closure [mm] over time [days]

Equation 3.1:

$$y = 176 \times T^{0.4}$$

Allowing the rock to re-establish equilibrium over time following the partial removal of a rock layer can be compared to petroleum extraction from porous rock, where the granular framework is kept intact (Kratzsch, 1983). The closure of the mine workings is the driver of mining-related ground surface deformation. Therefore, the rate of closure and the control mechanism in place will affect the behaviour of the ground surface deformation. In the first years of mining explosive mining was applied occasionally, later only continuous mining using heavy machinery was applied allowing for a better control of the closure in the mine.

The mining takes place along two parallel roadways that are cut into the lower lying halite deposit, a brittle rock-salt mainly used for road gritting (Fig. 3.17 and 3.20). From the main roadways six parallel chambers are excavated into the overlying weaker sylvinite deposits, leaving 2.5 to 4 metre wide pillars between the chambers (Fig. 3.21) (CPL, 2004).

Figure 3.20: Boulby mine - limited closure in salt workings, kept open for transport.

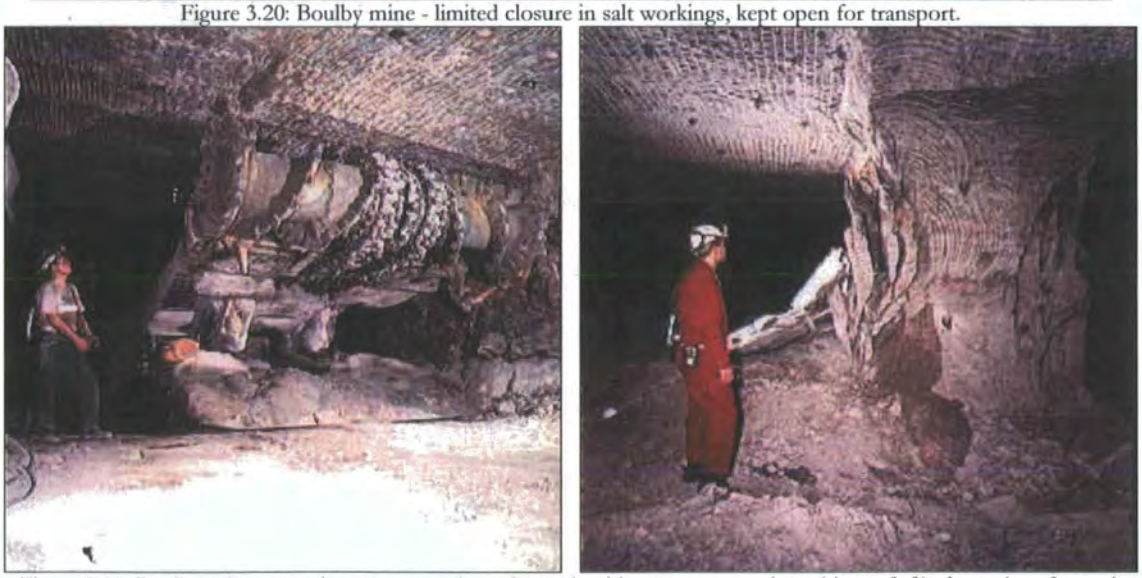

Figure 3.21: Boulby mine – continuous excavation of potash with remote control machinery (left), dynamics of potash safety pillars (right).

The potash is partially crushed underground and transported to the surface where it is further crushed and the sylvinite separated using a frath flotation technique. The generated waste is disposed of 1770 metres offshore using an underground tailings pipe. The sylvinite

is transported by rail to the CPL port facility on the river Tees, north of Boulby (Milne, 1978).

3.5.2. Levelling and excavation datasets of Boulby potash mine

The original datasets both collected and evaluated by CPL, are stored in Microsoft Access database files. To use the raw datasets as input to this research some pre-processing was required. In the following two sections the data analysis carried out in the initial phase of this research are described. In chapter four, the analysis of these datasets and the methodology of the subsequent development of an empirical prediction model will be discussed.

3.5.2.1. Levelling data collection

For the annual levelling surveys in the Boulby area a Sokkia SDL1 Digital Level, invar staff and ancillary equipment are used. The calibrated readout accuracy of this equipment is 0.001 millimetres (Kinder, 2001). The resulting dataset used in this research consists of 14036 unique records. Each record represents a measurement and is identified by a location and a date (Table 3.1). The elevation corresponds well with Ordnance Survey profile elevation data (Fig. 3.22).

The OSGB coordinates, in combination with the original elevation in metres OD indicate the three dimensional location of the station. The elevation is measured using levelling with an accuracy in the order of millimetres (Anderson and Mikhail, 1998). The date indicates the time of the elevation measurement.

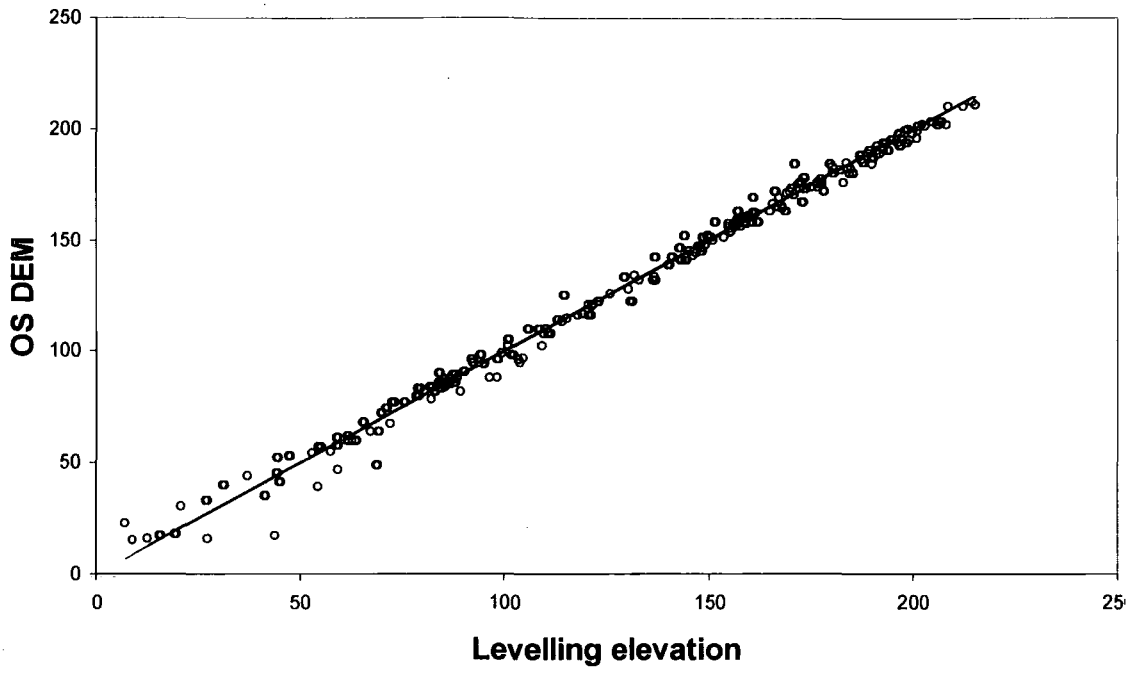

Figure 3.22: Plot of levelling data elevation against OS Profile elevation

Table 3.1: Levelling survey dataset, original attributes

Field name	Data type	Description	Example value
Measurement	Autonumber	Unique identifier	1
Station	Number	Identifier of measurement location	175
DayNumber	Number	Days after first measurement	360
OElevation	Number	Original elevation OD[m]	79.62178
Dates	Date/Time	Date of measurement	5/23/1977
LineNo	Number	Identifier of survey line	4
Easting	Number	OSGB X coordinate	476407.343
Northing	Number	OSGB Y coordinate	518690.747

To study the temporal and spatial behaviour of surface deformation, a unique identifier was required. Each dataset was converted to a set of measurements, where a measurement is the unique identifier, defined by a location (easting, and northing), a date (daynumber) and a deformation rate (Fig. 3.23). This was required because each location on the surface has several registration dates and on each registration date several locations on the surface are measured. The deformation rate (S) was calculated as the difference in elevation between two dates, with the time being taken as the midpoint of the two dates, as follows.

Equation 3.2:

$$\frac{elevation2 - elevation1}{day2 - day1} \cdot 1000 \cdot 365 = S\left[mm \cdot a^{-1}\right]$$

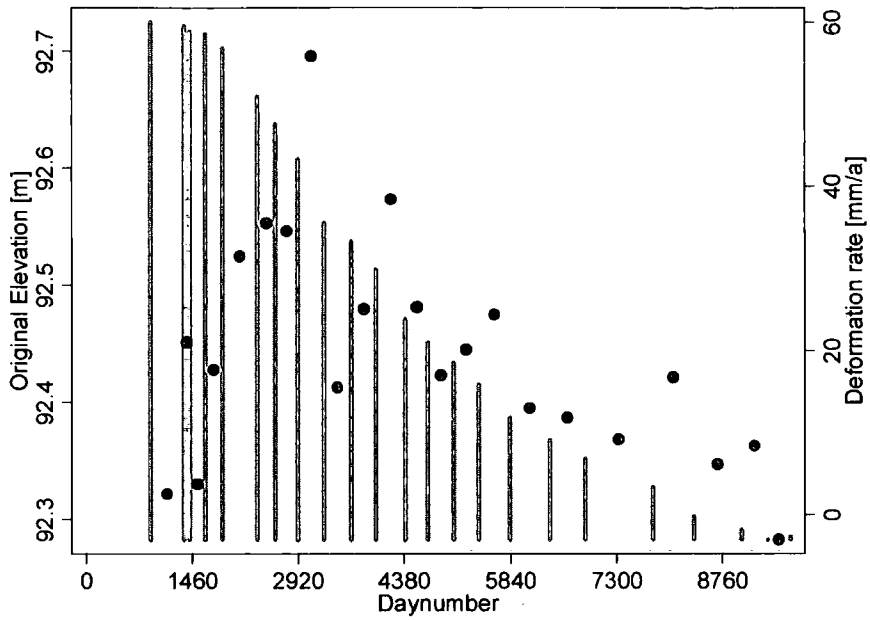

Figure 3.23: Original elevation measurements (left axis) over time at survey station 1053 (bars) and the associated deformation rate (right axis) between elevation measurements.

In Figure 3.23 the elevation at one randomly selected location on the surface, monitored by levelling is plotted over time, indicated by vertical bars. These elevation values were converted to deformation rate [mm a^{-1}] measurements, dated at the midpoint between these dates. The measurement values are indicated by black dots. The values of deformation rate range from - 3 (uplift) to a maximum of 63 millimetres per annum (see Fig. 3.24). Mapping the total deformation rate calculated over the 29.5 year interval of the levelling monitoring dataset shows spatial distribution of this variable (Fig. 3.25).

The map in Figure 3.25 shows that the highest present deformation rates are positioned above the potash mine workings, indicating a general correlation between the location of the mine workings and the deformation rate. In the research area deep underground excavation activities started in February 1976. From then onwards, the extent of the undermined area has grown to almost 90 km^2 in November 2005, over a period of thirty years. The total undermined area resembles a south-east to north-west oriented rectangular shape, measuring 15 km at its longest point and 6.5 km at its widest.

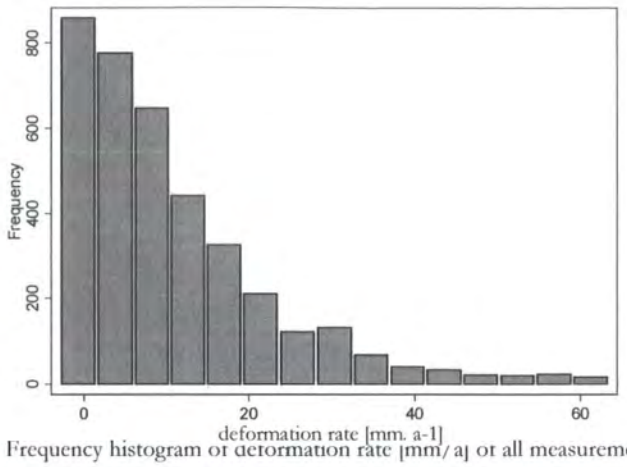

Figure 3.24: Frequency histogram of deformation rate [mm/ a] of all measurements to date

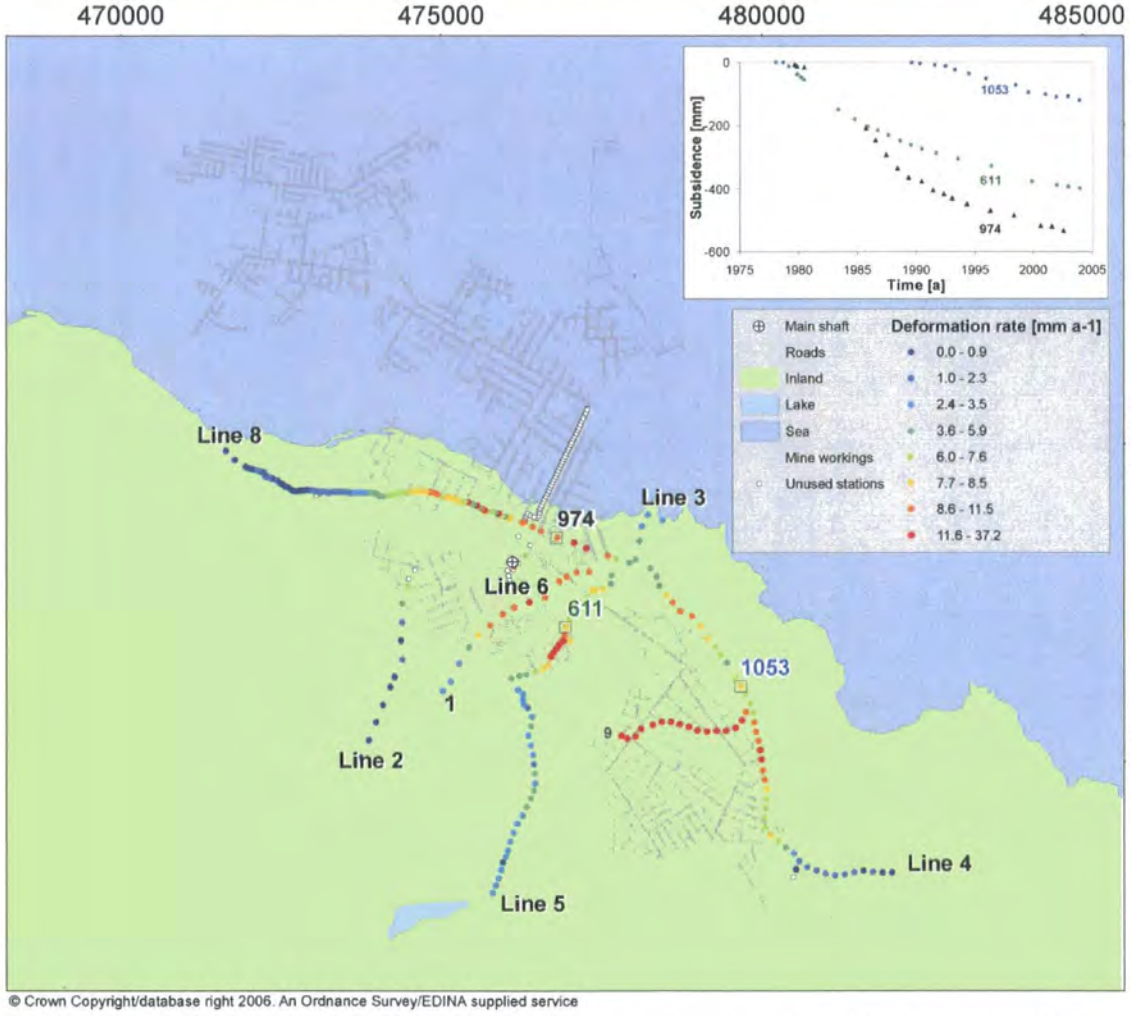

Figure 3.25: Total deformation rate in the Boulby area over 29.5 year interval measured with levelling surveys, with (in grey) the extent of the mining panels of the potash mine and (in blue) the high water mark coastline .

The maximum number of elevation measurements taken during one survey is 1511, of which 258 are taken at fixed points at the surface (Fig. 3.25). These fixed stations consist of a concrete structure located along roads and are assumed to be unaffected by any

deformation processes other than the mining related deformation that is monitored. Only these fixed stations are used to monitor elevation changes over time. The other non-fixed stations are used to calculate absolute heights at fixed stations from the surveyed relative height to the reference point (CPL, 2002b).

Annually, a part of the fixed stations is revisited and the absolute elevation at these stations is determined using standard levelling methods, described in chapter two. The number of stations and therefore the extent of the monitored area has grown and shifted to keep up with the expansion of the mining activities.

In the annual levelling surveys in The Boulby area, nine lines were used, numbered 1-6, 8, 9 and 11 (Fig. 3.25). Line 11 extends off the shore, following a tailings pipe tunnel. Lines 8 and 4 run from Skinningrove village in the north-west to Barnby village in the south-east. Line 8 intersects the excavation zone just west of easting gridline 474000 and line 4 intersects the excavation zone just west of easting gridline 478000, after which it continues along the east edge of the mine. Lines 5 and 3 run from Scaling dam in the south to Staithes harbour in the north. Line 5 intersects the excavation zone north of northing gridline 516000 and south of northing gridline 518000. The two transects formed by line 8 and 4 and line 3 and 5 are used in later sections of this chapter to demonstrate the spatial variation of the deformation.

3.5.2.2. Excavation data

The Boulby mine excavation dataset used in this research consists of 3484 unique records. Each record represents a mine block or mine panel section. A mine panel can consist of up to 58 mineblocks. Each mine panel has a number of attributes, given in the data table (Table 3.2). The most important attributes for this research are Easting, Northing, Area, Depth and MineDate. In the Boulby mine, potash and salt are mined. Despite evidence of a different closure rate between salt and potash, in this research, no distinction is made between the two materials. The majority of mine panels are potash, and salt and potash mine panels are almost evenly distributed throughout the mined area along two parallel roads (Fig. 3.17).

Table 3.2: Excavation dataset, original attributes

Field Name	Data Type	Description	Example value
BlockID	Autonumber	Unique identifier	60
Easting	Number	OSGB X coordinate	477325
Northing	Number	OSGB Y coordinate	517603
Elevation	Number	Elevation above -2000 MOD datum	940
Area	Number	Mining block surface area [m2]	5277.7
Depth	Number	Depth from surface [m]	1103.9
SorP	Text	(S)alt or (P)otash	S
PanName	Text	Panel name	9994
MineDate	Date/Time	Start date of mining	Jan-1989
Mperiod	Number	Year of mining	1989

The OSGB coordinates, as well as the depth from the surface indicate the three dimensional location of the centre of the completed mine panel. This was determined using a levelling method, measuring the relative position from the main shaft of the mine. The area of each mine panel is the size of the mine panel floor in squared metres. The height of a mine panel varies to some extent but is between 4 and 6 metres.

Mining activities started in 1976 in the centre of the mine and have gradually expanded outwards. Mining activities in one zone of influence are likely to have taken place in one mining period. The only area of the mine where mining activities have restarted after a long pause is located south of the mine centre, corresponding to the jump in the (blue) x,z projection of the graph in Figure 3.26. The time variable of measurements in this area will not reflect the average time after one mining period, but the average time after two mining periods.

Deformation behaviour at the monitoring stations can be determined based on the annual absolute elevation measurements with some reliability. The reliability of estimations at points located at some distance away from the monitoring stations depends on the used method. Interpolation of the measurements has been the generally approved method of estimating deformation beyond the monitoring stations. The location and distribution of monitoring station in the Boulby area is confined by the ability to place concrete structures in the ground. This was only possible along public roads and has lead to a non ideal point distribution.

The empirical cone model, developed in this research, employs both the measurements and the excavation variables to estimate the deformation beyond the monitoring stations. To compare the extent of the surface area disturbed by excavations and the surface area covered by annual levelling surveys, referred to as the excavation zone and the monitoring zone respectively, some of the cone model principles are used.

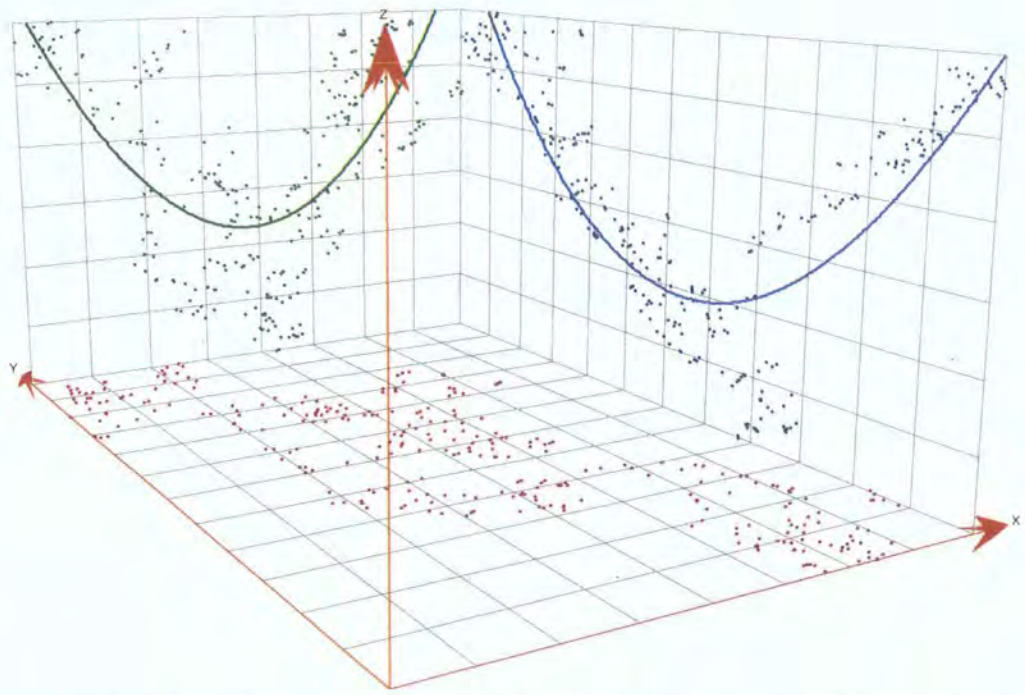

Figure 3.26: Spatial trend analysis of starting dates (z) in easting (x) and northing (z) directions.

Assuming that underground mining activities cause a cone shaped, or radially upwards and outwards growing zone of disturbance, the excavation zone at the surface must be larger that the actual squared metres of excavated material at seam level. Before estimating any rates of disturbance, the extent of the excavation zone can be estimated as a product of a chosen angle of draw of 45°, the depth of the mine panels and the coordinates of the centre of the mine panels. The 45° angle of draw is based on analysis described in chapter two. The final excavation zone for a certain year is the dissolved shape formed by all disturbance circles at the surface caused by mine panels started before or within that year.

The extent of the monitored area can be seen as a two dimensional shape on the surface, because each monitoring station can monitor excavation activities that occur at some distance away from the station. Adopting a similar method to the determination of the excavation zone, the distance around the survey station that is monitored is a product of the angle of draw of 45°, the depth of the mine panels and the location of the station. The most shallow mine panel in the Boulby area would have to be located a horizontal distance of 802 metres from a station to cause any measurable disturbance to that station, based on this method. The other mine panels are located at greater depth and are estimated to cause disturbance at horizontal distances further away. To include all mining activities, buffers of

802 metres radius around stations are used. The final extent of the monitored zone at a certain year is the dissolved shape formed by the circles of the stations included in the survey of that year.

In Figure 3.27 the development of the excavation zone and the section of this zone that is monitored at annual intervals are shown. The red shapes represent the extent of the excavation zone at the time of each annual levelling survey. The yellow shapes represent the monitoring zone at the time of each levelling survey. The orange shapes are the overlapping areas of both zones.

In the following figure, the relationship between the surveyed area and the undermined area is shown. Although the two areas have a similar extent from 1973 to 1988, they do not overlap completely. After 1989 the size of the excavation zone continues to grow beyond the monitoring zone. A large area in the north of the research area is not covered by the survey. This part of the mine is located under the sea and possible surface deformation can not be monitored using a levelling surveying technique.

Sub sea mining was initiated in 1981, now approximately 50% of the mined area lies offshore. Unfortunately, in this research only data for the deformation caused by the proportion of the mine under land can be used.

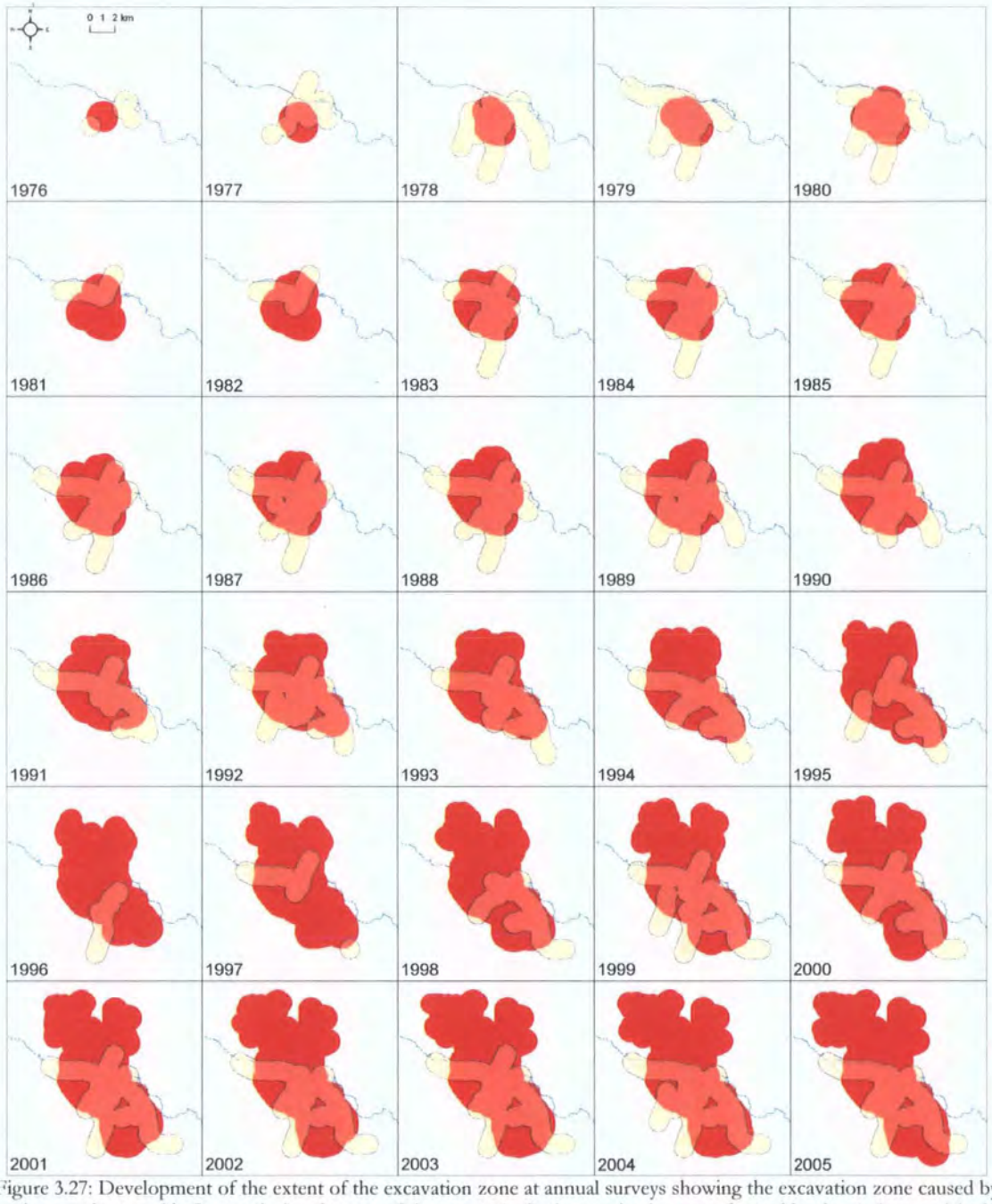

Figure 3.27: Development of the extent of the excavation zone at annual surveys showing the excavation zone caused by mine panels started before or during the year of the survey (red), the monitoring zone formed by the stations revisited during the year of the survey (yellow) and the overlap between the two zones (orange).

In Figure 3.28 the total extent of the excavation zone is plotted over time and compared to the extent of the section of the excavation zone that was monitored. In addition, the distance between the furthest mine panel and the monitoring stations is given (to give an idea of the suitability of the monitoring method).

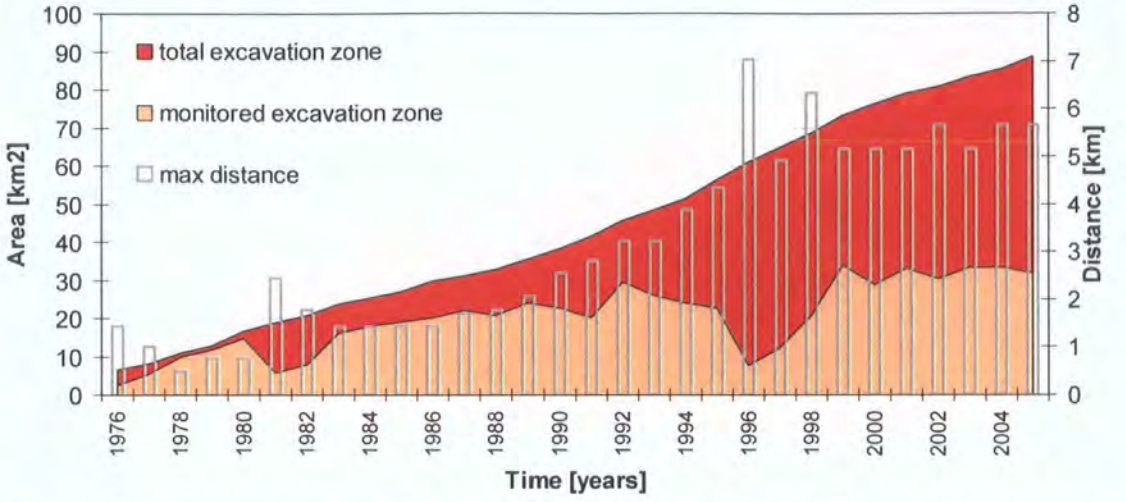

Figure 3.28: Size of the excavation zone (red and orange) and the monitored section of the zone (orange) over time, the grey columns indicate the maximum distance between mine panel and nearest survey station determined per annual survey.

In 1996 only a partial levelling survey was carried out and as a result the distance between mine panel and monitoring stations reached a maximum of 7 km. Between 1999 and 2005, this value fluctuates between 5 and 5.5 km.

3.6. Conclusion

Important considerations in the selection of the research area were the interesting surface dynamics caused by contemporary excavation. The Boulby area is an interesting location to test the feasibility of InSAR. In the Boulby area, the land use is rural and the climate temperate, which are conditions that have so far been considered unsuitable for conventional InSAR. In total only 4% of the area is classified as urban and rock (Fig. 3.29).

The climate in the Boulby area is maritime temperate and is likely to cause atmospheric distortion in radar imagery. The sedimentary geology is homogeneous in the research area and has experienced extended periods of subsidence and uplift throughout its development. The location of the potash mine workings in the Boulby area is partly under land, partly under sea and crosses a vulnerable eroding coastline. The maximum annual rate of deformation since the start of the potash mining activities in 1973 is 37.2 mm a^{-1} and the maximum deformation in that period was 63.0 mm. This can be considered to be gradual deformation. The ability to predict the impact of the mining activities on this coastline depends on the ability to accurately monitor and model the ground surface deformation.

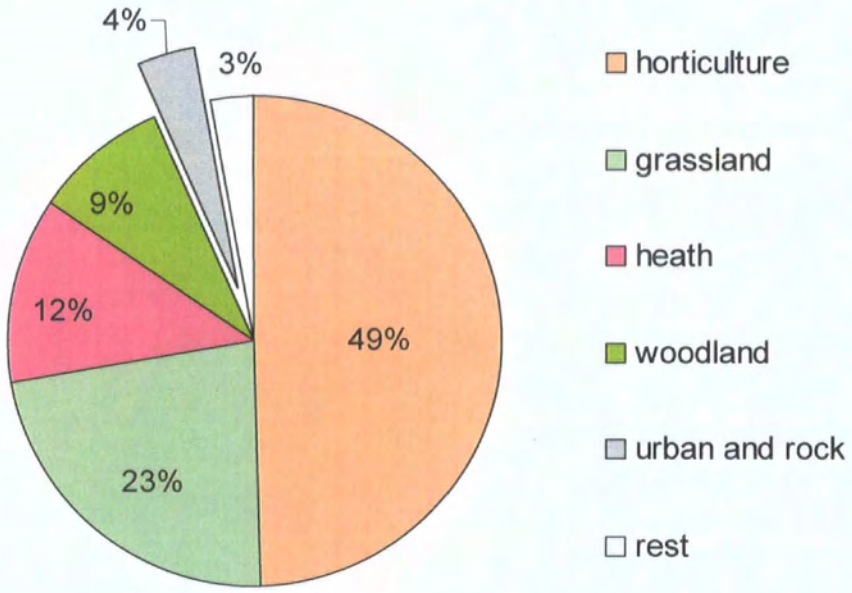

Figure 3.29: Land use classes based on LCM2000

CHAPTER 4. METHODOLOGY

'Equations are just the boring part of mathematics. I attempt to see things in terms of geometry.'

(Stephen Hawking, 1942-)

4.1. Introduction

This chapter describes the methodology used in this research. Different parts of this research were carried out in collaboration with scientists from other Universities, both in the USA and The Netherlands. The first part of the chapter will describe the InSAR analysis and the second part will discuss the development of the data-driven model. Both parts of the research can be split up into several steps.

In the first year of this research the writer of this thesis worked for one month with Mark Bulmer of the University of Maryland and the Nasa Goddard Institute in The USA. For one month the writer used the Atlantis-EV software to test the initial thirteen radar scenes of the research area. This was a valuable test period in which the writer could become familiar with the InSAR technique and test the potential for InSAR in the research area. The selection of radar scenes in this stage of the research was based on known requirements for conventional InSAR. The first dataset consisted of thirteen ERS1 and ERS2 scenes. The characteristics for these scenes were clear weather conditions at the date of registration and a perpendicular baseline of less than 200 m.

Results from this test analysis were the first deformation measurements over short timelines and a better understanding of the InSAR technique, and lead to clear ideas of the limitations of conventional InSAR in temperate areas with rural land use. In addition, the use of a closed-coded commercial software package such as Atlantis-EV was found to be unpractical for areas with low coherence.

Later in the first year of this research, the writer worked with Ramon Hanssen and his research team in Delft Technical University in The Netherlands for one month. They use an open-source software package which allows for parameter adjustment and can therefore be used in areas with a lower coherence. During my time at Delft the writer further developed my understanding of the InSAR technique. After ample experiments with conventional InSAR and parameter adjustments, it became clear that the coherence in the research area was too low to monitor the gradual mining related surface deformation that

occurs in the research area. At that time, the research team of Ramon Hanssen was developing a Matlab-DORIS application based on the Persistent Scatterer Technique published in 2001 (Ferretti et al., 2001). The PSI technique is better capable of generating continuous deformation monitoring datasets in areas with low coherence, as described in chapter two.

Following was period of collaboration with Delft University, where they would use the Boulby radar dataset in the development and evaluation of the Matlab-DORIS PSI application and where the writer examined the intermediate and final PSI estimates. During this period the writer was running different versions of the Matlab-DORIS PSI application in Durham to test different parameter settings as will be described in this chapter.

In conclusion, the four steps of the InSAR analysis of this research are (Fig 4.1):

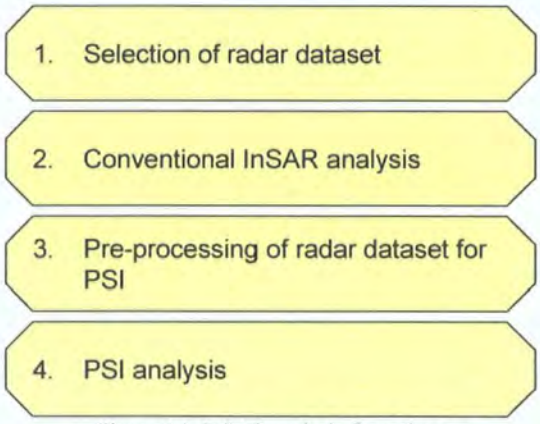

Figure 4.1: InSAR analysis flow-chart

In the second part of this chapter, the development of a data-driven cone model is described (Fig. 4.2). This part started with the evaluation and quantification of the input datasets. The second step consisted on a series of geo-spatial modelling exercises to understand the spatial and temporal complexity of the ground surface deformation. In the third step the data-driven cone model was developed as a method to set-up logical links between deformation and excavation dynamics. To generate the variables and in a later stage to generate the estimations of the ground surface deformation based on the excavation dataset, a cone model tool was developed. The cone model tool was used extensively to evaluate the algorithms and parameters in step five and six.

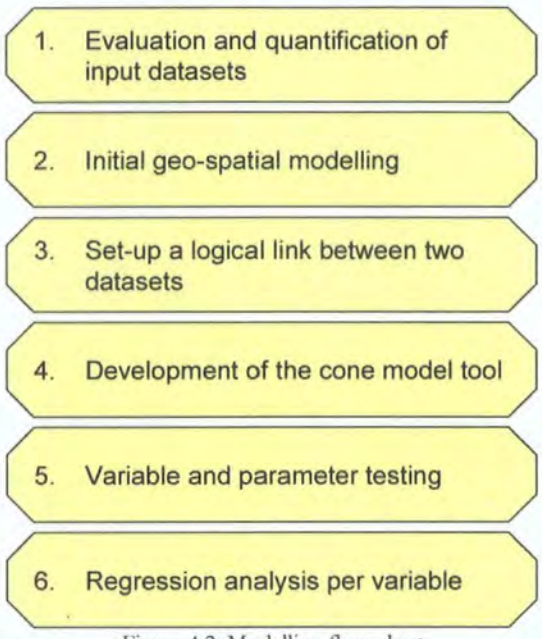

Figure 4.2: Modelling flow-chart

4.2. InSAR analysis

The ground surface deformation process considered in this research is a mining-induced deformation process with rates of vertical motion in the range of 0 - 50 mm a^{-1}. The conditions in the Boulby research area include a temperate climate, erratic atmospheric distortions and high temporal decorrelation due to agricultural land use (see chapter three). Recent developments in InSAR analysis are aimed at increasing the applicability of the technique to areas with unfavourable conditions.

Major improvements arose from the Persistent Scatterer InSAR (PSI) technique, developed by Ferretti and others, following research in 1997 (Usai, 1997; Usai and Hanssen, 1997) in which was recognised that areas with high temporal decorrelation often contain isolated points of high correlation, or persistent scatterers (Ferretti et al., 1999; Ferretti et al., 2000a; Ferretti et al., 2000b; Ferretti et al., 2001).

In both conventional InSAR and PSI analysis, interferograms are created by combining the phase values of two radar scenes. The difference between the two methods is the approach used for the removal of unwanted phase information and the unwrapping of the interferograms. In conventional InSAR the unwrapping takes place pixel by pixel for each interferogram. In PSI unwrapping is done simultaneously with the estimation of parameters of interest at randomly distributed 'persistent scatterer' points in the area using a large number of interferograms.

To calculate surface deformation the sources of unwanted information mentioned in section 2.4.3 need to be known as accurately as possible. Without reliable estimations of the atmospheric phase and the topographic phase successful unwrapping is problematic. Pixels that have a low interferometric coherence are excluded from the unwrapping process, creating isolating voids in the unwrapping procedure. In PSI the estimation of these phases is improved compared to the often problematic phase removal in conventional INSAR analysis and problems evolving from decorrelation are avoided by selecting the pixels with the highest probability to contain useful information.

In this chapter the methodology used to test InSAR and to generate a deformation monitoring dataset of the Boulby area is described. Two InSAR analysis stages are described during which both conventional InSAR and the more advanced PSI techniques were tested.

In the first InSAR analysis stage of this research, the viability of conventional InSAR in the Boulby research area was tested. This three month test took place in cooperation with and partly at the University of Maryland in the USA. Atlantis-Earth Viewer (Atlantis-EV), a licensed software programme was used (Annex I). With Atlantis-EV it was possible to do elevation and deformation analysis using ERS C-band radar scene pairs, with limited flexibility for the atonement of parameters.

The main objectives of this stage were to get a better understanding of the possibilities and limitations of the conventional repeat-pass InSAR and DInSAR technique, the software and the data. In this initial phase 13 radar scenes 3 ERS-1 and 10 ERS-2 were used, a subset of the final 36 scenes provided by the European Space Agency (ESA). All scenes have the same frame number 2511 and the same track number 366. The conclusions from this stage were used to focus the second stage of the InSAR to further explore the applicability of the InSAR technique to monitor gradual ground surface deformation.

4.2.1. Selection of the radar dataset

The process of selecting the radar scenes is an important step in InSAR analysis (Hanssen, 2001). The general characteristics of the used satellite, the specific characteristics of the radar sensor and the specific characteristics of the atmosphere and surface at the time of registration are all factors that can determine the success of the InSAR analysis. A certain level of coherence between and within scenes is required to successfully generate interferograms. The selection of the most appropriate radar scenes does not merely depend

on the environmental characteristics or the geometric and technical characteristics of the sensor, but also depends on the deformation process itself. The spatial and temporal rate and extent of each deformation process is unique and requires a different monitoring dataset.

The deformation process taking place in the Boulby area caused by deep underground mining has experienced deformation rates in the range of 0- 50 mm a^{-1}. The main process of deformation is concentrated in an area of 216 km^2 and has been continuously active since 1976 until present. The process can be classified as having a relatively small spatial extent, large temporal extent and a low deformation rate (Fig. 2.7). To generate the most appropriate deformation monitoring dataset, a long time interval with a high spatial resolution and medium temporal resolution would therefore be ideal.

The first step in this selection process is to determine which satellite and which scene provider to use. At the time of this research a limited number of options existed (Table 2.2). The most important factors to consider in this step are the wavelength and pixel resolution of the radar sensor, the extent of the mission and the revisiting time of the research area.

The three civilian satellite types currently providing a long monitoring period are ERS, JERS and RADARSAT (Table 2.1). Both the European ERS satellites and the Canadian RADARSAT satellite use a C-band sensor, while the Japanese JERS satellite uses an L-band sensor. The longest monitoring period is covered by the two compatible ERS satellites operated by the European Space Agency covering a period of 15 years from 1991 to 2005. The revisiting time for these satellites is 24 days for RADARSAT, 44 days for JERS and 35 days for the ERS-1/ERS-2 satellites. The latter satellite pair was directed into a tandem orbit from April 1995 for one year, resulting in scenes taken 24 hours apart.

Despite the fact that the ERS satellites use a C-band sensor instead of the more ideal L-band sensor (Chang et al., 2004), it is currently the most popular satellite used for InSAR applications and research (Table 2.3). The ERS satellites cover the longest mission period and they provide tandem scenes for DEM generation. Most importantly, highly accurate positioning data for the satellite at the time of registration is available for the ERS satellites. This is essential for successful calibration of the radar scenes as described below. The limited accuracy of the positioning data available for the JERS satellite is the most important limitation for wide use of this satellite (Massonnet and Feigl, 1998).

The satellites selected for this research are the ERS satellites, rather than the equally suitable RADARSAT satellite. The main reason for this choice is that the European Space Agency, who operates the ERS satellites, encourages scientific use of the radar scenes and the development of InSAR applications and has provided 30 scenes for this research, free of charge. The total mission extent of the ERS-1 satellite was from 25 July 1991 till 10 March 2000 and that of ERS-2 from 21 April 1995 till 31 December 2005. Although ERS-2 is currently still in orbit, scenes are no longer suitable for InSAR analysis due to breakage of the precise positioning instrument.

To preview the coverage of a specific location and to select the required scenes an open source software programme was used. The DESCW programme has been created by Eurscene in collaboration with ESA/ESRIN (Biasutti et al., 2004). With the use of DESCW, track number 366 and frame number 2511 in ascending swath was selected as the frame consistently covering the Boulby research area (Fig. 4.3).

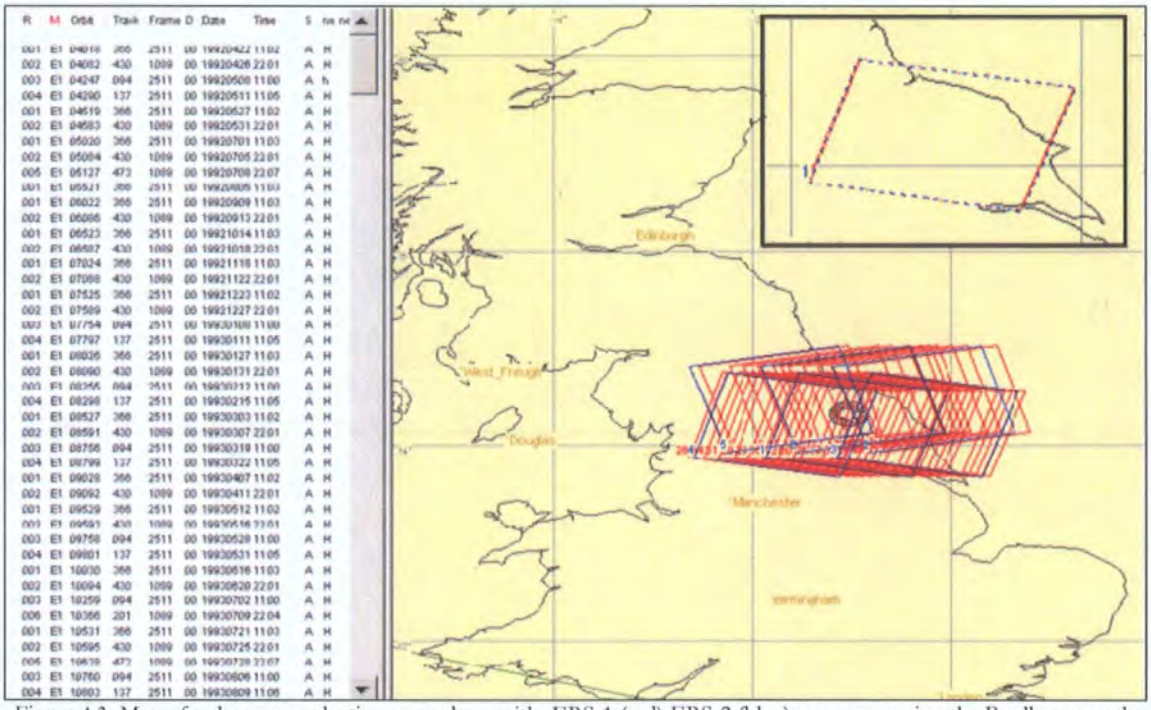

Figure 4.3: Map of radar scene selection procedure, with ERS-1 (red) ERS-2 (blue) scenes covering the Boulby research area (ellipse) in the top right inset the selected frame 2511.

As can be seen in Figure 4.3 several frames overlap with frame 2511. The total number of ERS scenes covering this exact area is 119. For the purpose of InSAR it is best to select scenes from a single frame (Hanssen, 2001). Of the 119 existing scenes, a total of 36 were selected, to include two tandem pairs and for the rest scenes with a perpendicular baseline between -500 and 500. Eventually only 33 scenes were used in the analysis as three scenes

had to be dropped in a later stage of the analysis (Fig. 4.4 and Table 4.1). This was due to the Doppler shift, a phenomenon which causes a small change in wavelength due to the relative movement of the satellite and Earth's surface during the registration.

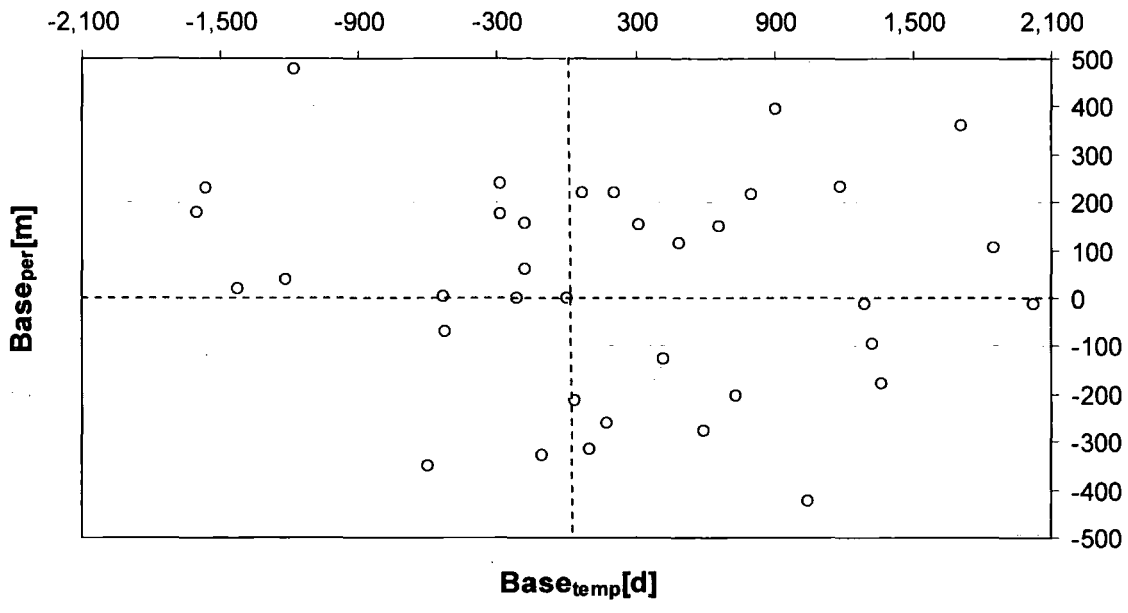

Figure 4.4: Baseline plot of the 36 selected radar scenes

The acquisition dates of the selected 36 scenes are between 9 September 1992 and 17 August 2002 and cover a potential monitoring period of almost ten years. The initial thirteen scenes are marked with a 1 in the 'set' column, the scenes that were later added and are included in second phase of the analysis are marked 2. The scenes are delivered as single look complex (SLC) scenes by ESA, containing both amplitude backscatter and phase data.

Table 4.1: Characteristics of the selected radar scenes

Nr	Date	Orbit	$Base_{par}$	$Base_{per}$	$Base_{temp}$	Set	Mission
1	19920909	6022	164	178	-1599	1	E1
2	19921014	6523	144	228	-1564	1	E1
3	19930303	8527	52	20	-1424	1	E1
4	19930929	11533	75	38	-1214	1	E1
5	19931103	12034	221	477	-1179	2	E1
6	19950609	20394	-17	-349	-596	2	E1
7	19950818	21396	112	4	-526	1	E1
8	19950819	1723	76	-70	-525	1	E2
9	19960419	24903	162	240	-281	1	E1
10	19960420	5230	130	176	-280	1	E2
11	19960628	25905	128	-1	-211	1	E1
12	19960802	26406	163	155	-176	1	E1
13	19960803	6733	121	61	-175	1	E2
14	19961012	7735	-97	-329	-105	1	E2
15	19970125	9238	0	0	0	1	E2
16	19970301	9739	-38	-212	35	1	E2
17	19970405	10240	121	219	70	1	E2
18	19970510	10741	-37	-314	105	1	E2
19	19970719	11743	3	-260	175	1	E2
20	19970823	12244	170	220	210	1	E2
21	19971206	13747	63	152	315	1	E2
22	19980321	15250	1	-128	420	2	E2
23	19980530	16252	132	114	490	1	E2
24	19980912	17755	-18	-277	595	1	E2
25	19981121	18757	86	151	665	1	E2
26	19990130	19759	-73	-203	735	2	E2
27	19990410	20761	139	216	805	1	E2
28	19990724	22264	254	394	910	2	E2
29	19991211	24268	-277	-425	1050	2	E2
30	20000429	26272	218	231	1190	1	E2
31	20000812	27775	79	-13	1295	2	E2
32	20000916	28276	-21	-96	1330	2	E2
33	20001021	28777	-18	-179	1365	2	E2
34	20010901	33286	289	502	1680	1	E2
35	20011006	33787	117	361	1715	1	E2
36	20020223	35791	70	105	1855	2	E2
37	20020817	38296	280	-13	2030	1	E2

4.2.2. Conventional InSAR analysis

4.2.2.1. Creation of Digital Elevation Models from tandem pairs

In the first dataset of 13 selected radar scenes, two tandem pairs were included, orbits 24903 and 1723 forming the April-96 tandem pair and orbits 26406 and 6733 forming the August-96 tandem pair, both from year 1996. Each pair consists of two data scenes one from ERS-1 one from ERS-2, taken only one day apart. The surface deformation expected over one day is negligible, so all three dimensional information collected is static and can be used to create a DEM.

A benefit of the tandem pairs is that surface characteristics remain approximately the same over one day and result in a high coherence between the two data scenes. The first DEM was created using the April-96 tandem pair. The perpendicular baseline between these data

scenes was -64 m and the altitude of ambiguity was 147 m. The second DEM was created using the August-96 tandem pair. This pair has a perpendicular baseline of -94 m. and an altitude of ambiguity of -100 m.

For the April-96 tandem pair, two scenes were selected a master scene (orbit 24903) and a slave scene (orbit 1723). Atlantis-EV has the option to subset the large SLC scene to a region of interest. This was done using the master scene. The process runtime decreased from approximately 60 minutes to approximately 10 minutes by creating a subset.

The slave scene was co-registered and re-projected to the master scene. A new slave scene was created with the data from the old slave scene in a raster identical to the raster of the master scene. In order to do this re-projection, a polynomial transformation was carried out, calculated from master and slave tie points. Coarse tie points are generated based on relative x and y locations in the two scenes. The tie points are further refined by shifting the slave tie point to a location with amplitude backscattering comparable to amplitude backscattering at the master tie point location.

After successful adjustment of the slave scene, the interferogram was created representing the phase difference between the two scenes at each pixel in the output raster. The output raster is the interferogram with clear fringes shown in Figure 4.5. The removal of a residual phase caused by an error in the position of the satellites at the time of registration was required. A perpendicular baseline correction of 7 meters was found to improve the later unwrapping results.

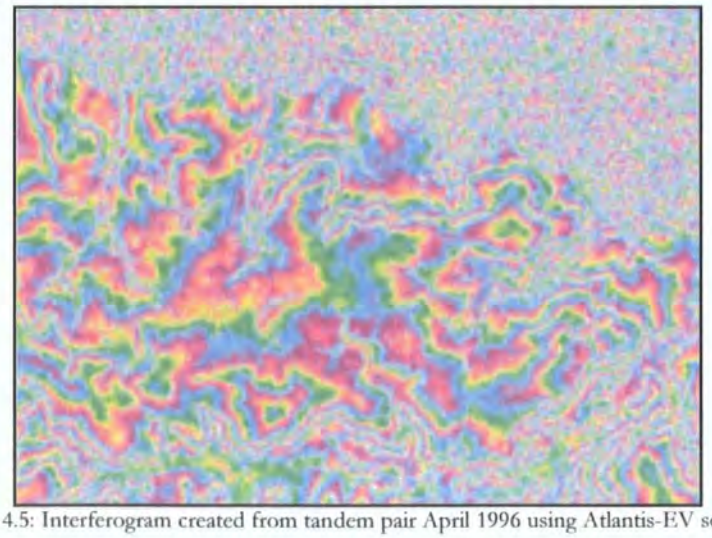

Figure 4.5: Interferogram created from tandem pair April 1996 using Atlantis-EV software

Phase unwrapping of the interferogram converted the phase change colour circles (fringes) into actual height data (Fig. 4.6). The same procedure was done for the August-96 tandem

pair with orbit 26406 as master and orbit 6733 as slave scene. The altitude of ambiguity of the April interferogram equals 147 metres and that of the August interferogram equals 100 metres, calculated using equation 2.5. Initially the height difference in slant range direction is calculated and than converted to terrain corrected or geocoded projection, resulting in a DEM of the surface. To make the DEM most compatible to other dataset, the two DEMs were created in a (geocoded) UTM ellipsoid 12 projection with a wgs84 co-ordinate system (Fig. 4.6 and 4.7).

The effect of the pre-processing procedure for the PSI analysis described below is a higher quality of interferograms. Still the difference between the two DEMs from two tandem pairs is large. The tandem pairs resulted in the following interferograms (mixed with magnitude) (Fig. 4.8 and 4.9).

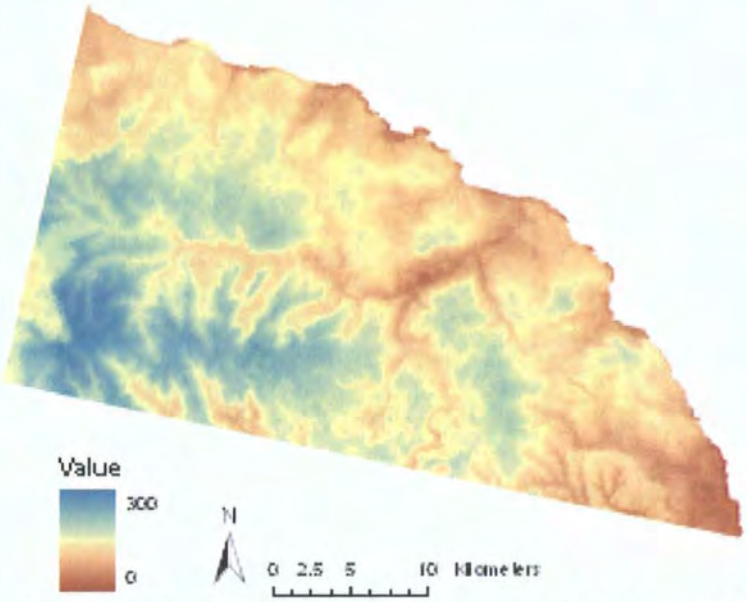

Figure 4.6: DEM created from the April 1996 tandem pair values represent elevation [m], area is the Boulby research area.

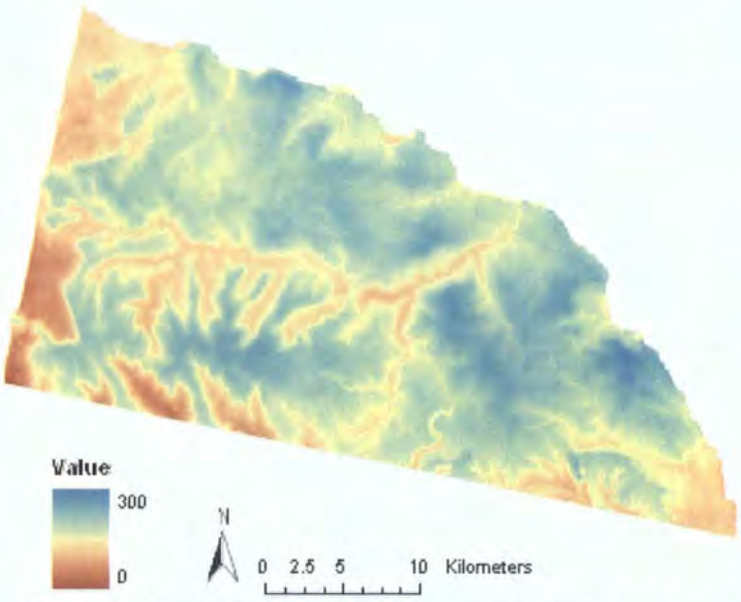

Figure 4.7: DEM created from the August 1996 tandem pair values represent elevation [m], area is the Boulby research area.

Although both interferograms look correct, after unwrapping, the height values are different. The scale of the first DEM (April 1996) ranges between 0 and 400 metres while the scale of the second DEM (April 1996) ranges between 0 and 250 metres. The height range in reality for this area is from 0 to 272 as described in chapter three. To evaluate the spatial distribution of errors the created InSAR DEMs were compared to the OS Profile DEM (Fig. 4.10).

The deformation and temporal decorrelation at the surface was found to be low for the two tandem interferograms. However, when the results of the two DEMS are compared to OS-profile, a considerable inaccuracy is detected (Fig. 4.10). For the August tandem pair, this inaccuracy is likely to be the affect of geometrical decorrelation. In the last days of the tandem mission, the ERS-1 spacecraft was operating in an unstable condition and Delft scientists were not able to calculate it's precise orbit path for the scene of 2-August. Geometrical decorrelation would explain also the diagonal trend in off-set which can be seen in Figure 4.10. The April DEM has a more homogeneous off-set throughout the research area. This inaccuracy is likely to have been caused by atmospheric decorrelation.

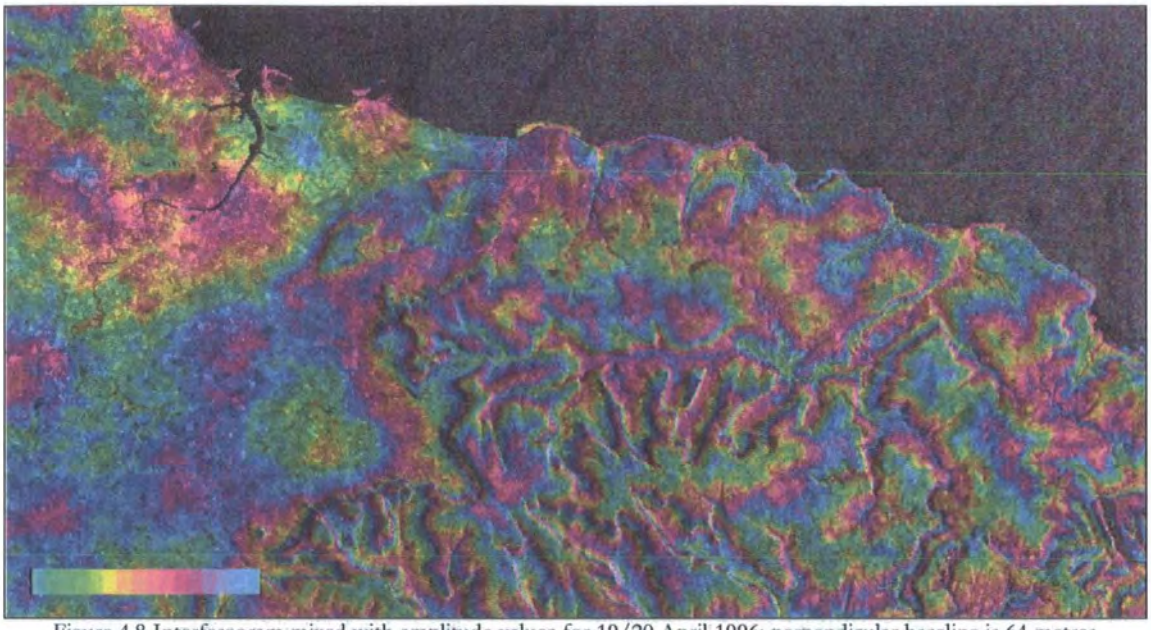

Figure 4.8 Interferogram mixed with amplitude values for 19/20 April 1996: perpendicular baseline is 64 metres

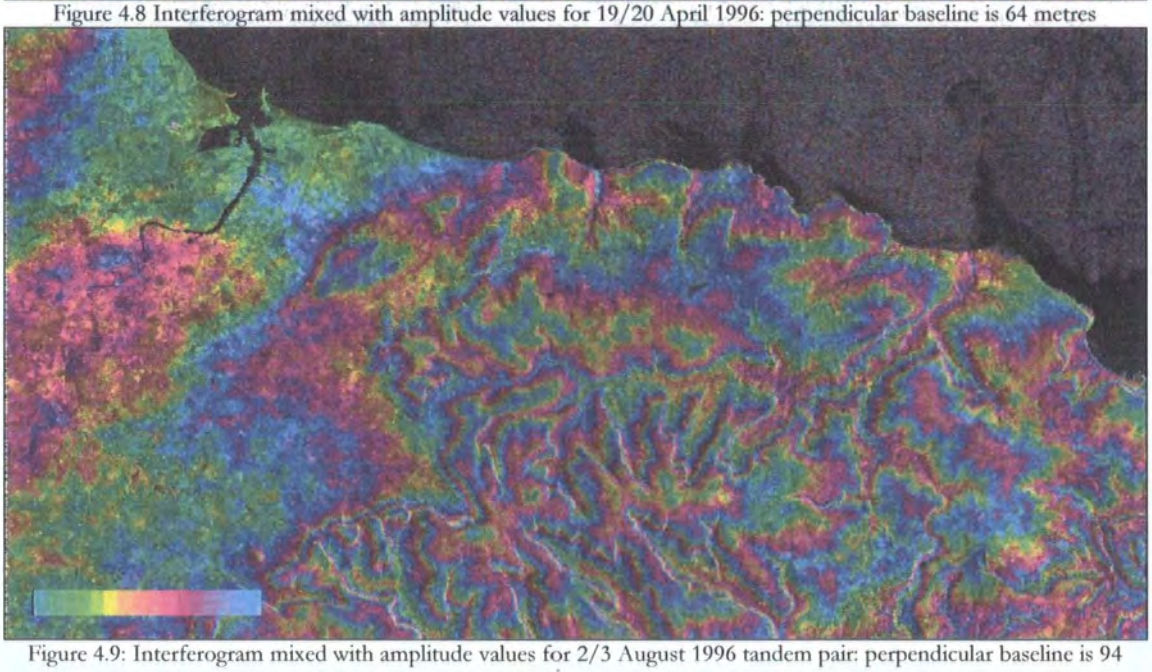

Figure 4.9: Interferogram mixed with amplitude values for 2/3 August 1996 tandem pair: perpendicular baseline is 94 metres

A divide can be made between the higher and steeper areas that are relatively underestimated by the InSAR DEM and the lower and flatter areas that are generally overestimated by the InSAR DEM.

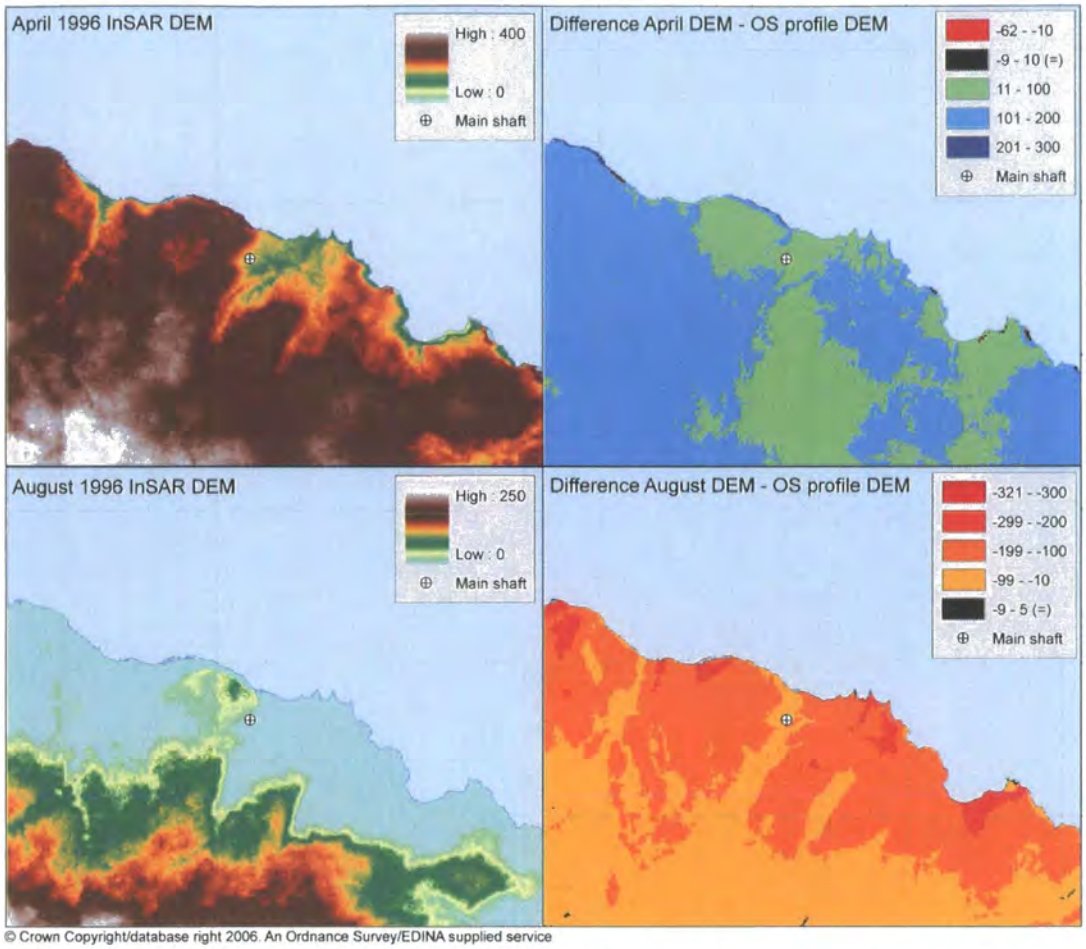

Figure 4.10: DEM comparison, left InSAR generated DEM's, right difference with OS Profile DEM data.

In the first stages of the InSAR analysis the DEMs derived from the tandem pairs were used, however due to inaccuracies mentioned above, it was necessary to find an alternative DEM to estimate the topographic phase. The DORIS software, used in the later stages of this research, has an integrated conversion method to use a DEM from the SRTM mission. The use of the higher resolution OS Profile (1:10,000 scale) DEM product may result in a better estimate of the topographic phase. However for the purpose of this research, the readily available SRTM estimate was considered to be of sufficient quality. Due to time constraint, the OS Profile dataset was not used as this would have required the conversion and precise co-registration of this dataset.

4.2.2.2. Differential InSAR (DInSAR)

The first attempt to calculate ground surface deformation was done using three-pass DInSAR (Fig. 2.13). Using both the April in the August a tandem pairs, the interferometric phase for eleven other scenes was calculated. With the standard CEOS positioning data provided with the SLC scenes, no deformation results were found. Considerable improvement was achieved by replacing the CEOS positioning orbits with Delft precision orbit data (Scharroo and Visser, 1998) .

For the April-96 tandem pair this resulted in eleven interferograms and an equal number of deformation maps. Pixels with low coherence (<0.3) were masked out, because the information contained in these pixels can be regarded as noise (chapter two). The coherence maps that are created as output products of the runs give information on the potential of the data scenes. The unwrapping was problematic and only resulted in small islands of deformation data (Fig. 4.11).

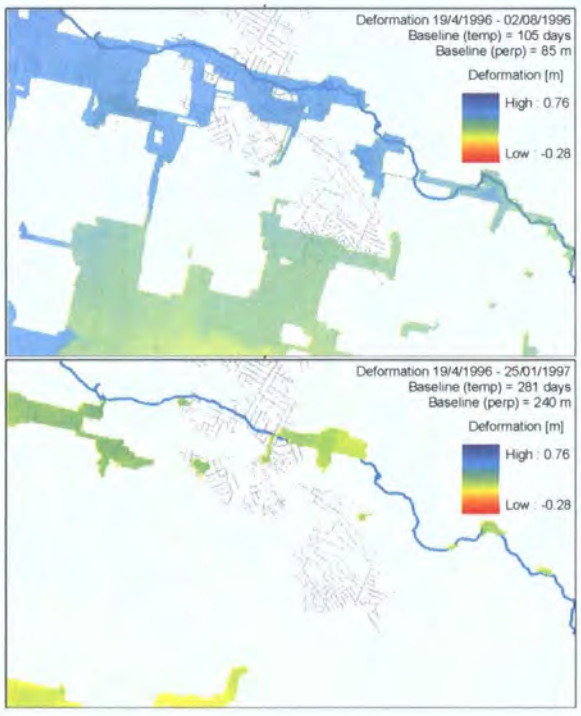

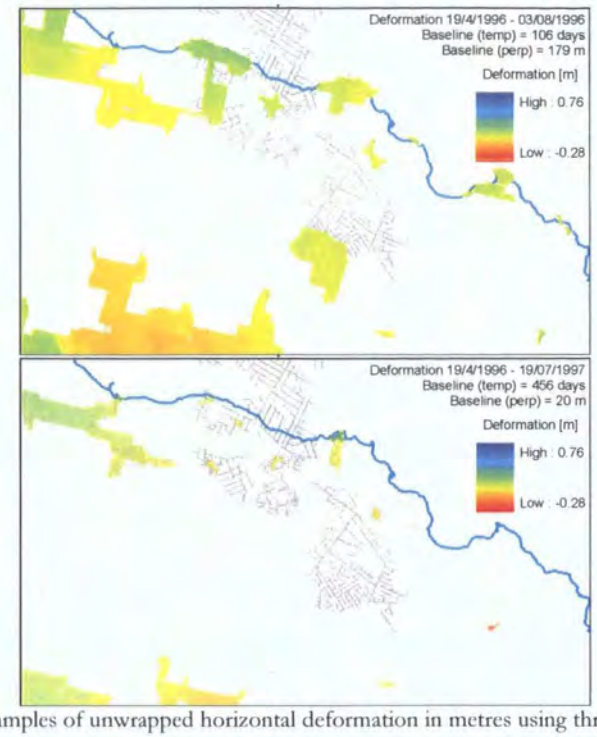

Figure 4.11: Examples of unwrapped horizontal deformation in metres using three-pass DInSAR.

Next, a four pass DInSAR trial was carried out, in which a tandem pair was used as a DEM while an independent scene pair was used to determine the deformation (see Fig. 2.13). This means that the DEM created from a tandem pair was used to subtract the height information from the differential interferogram. This resulted in more interferograms, despite increased atmospheric distortion. Instead of dealing with different atmospheric conditions on two or three days, with four-pass InSAR four days are involved.

A reason for a better result is probably the timing of the scenes used for the differential interferogram. The scenes forming part of the tandem pairs are in or just before the growing season, which resulted in low coherence over longer time intervals. The best deformation dataset was generated from a four-pass differential run using the orbit 9238 (January 1997) scene and the obit 9739 (March 1997) scene and the April-96 tandem pair as DEM (Fig. 4.12).

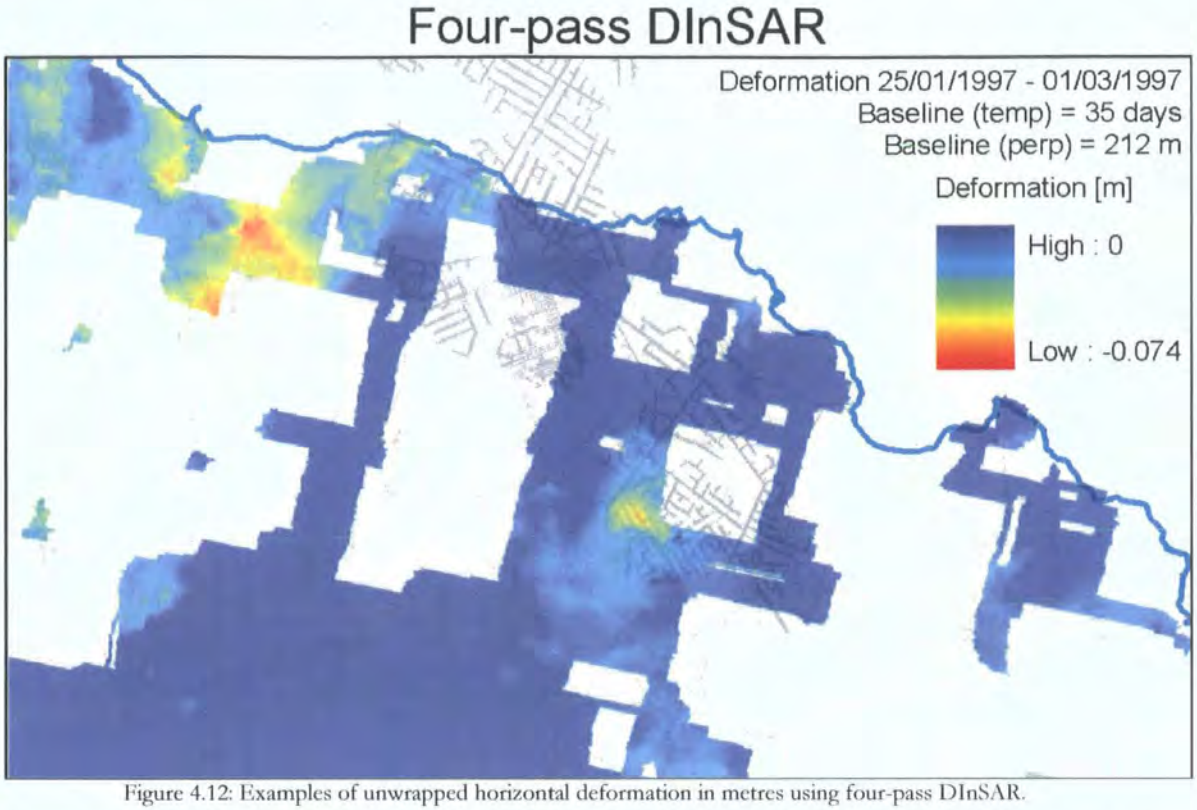

Figure 4.12: Examples of unwrapped horizontal deformation in metres using four-pass DInSAR.

The south section of the mine was undermined during the time period covered by the interferogram. The measured deformation is therefore likely to be genuine. The time period covered is only 35 days in the winter period and shows a maximum subsidence of 7.4 mm. This would correspond with a deformation rate of 77 mmm a^{-1}.

To eliminate the extra atmospheric distortion caused by using four scenes, the use of an external DEM was tested. The external DEM was derived from the Shuttle Radar Topography Mission (SRTM) which was conducted in February 2000. This space shuttle mission resulted in almost world wide DEM coverage with a resolution of approximately 90 metres. The technique used was single pass C-band radar InSAR. The reliability is unknown, as this DEM was pre-released by the USGD without being tested. This did not result in better differential interferograms, due to the difficulties associated with co-registration of a DEM which has a different spatial resolution and projection.

In this stage of the InSAR analysis, the open source software programme DORIS (Delft object-oriented radar interferometric software) was used. DORIS is developed by Delft Institute of Earth Observation and Space Systems of Delft University of Technology (Kampes and Usai, 1999). This programme can be used licence-free for academic purposes. This method offers more flexibility for the atonement of both the parameters and the

actual code. In this stage of the analysis the DORIS programme was used in combination with the licensed software programme Matlab to test PSI (Sigmon, 1998).

To test conventional InSAR with the DORIS software, a small subset covering the city of Middlesbrough approximately 30 miles from the Boulby research area, but still within the extent of the used radar scenes (Fig. 4.13). This location was chosen because the land cover is urban and the coherence was good. Also the deformation was expected to be zero. This hypothesis was tested.

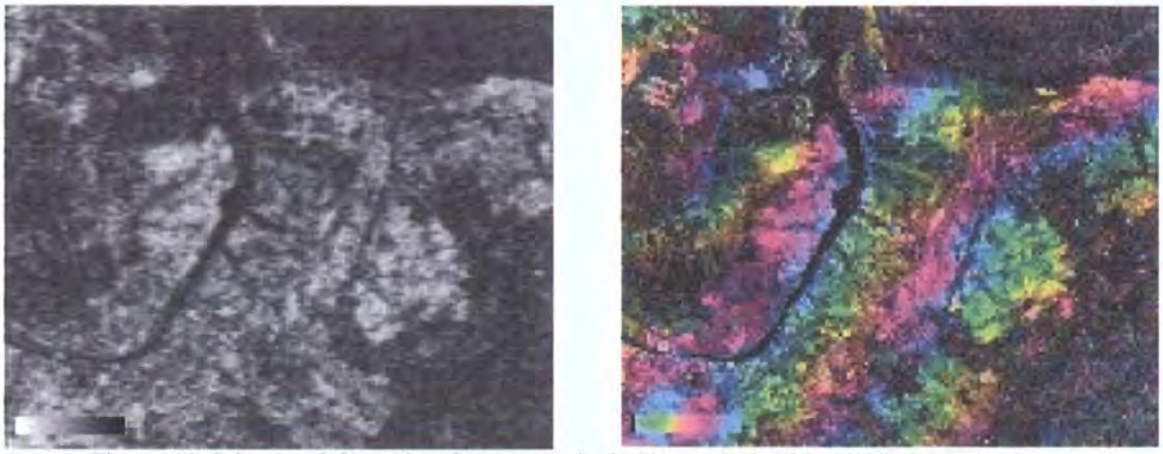

Figure 4.13: Coherence (left) and interfererogram mixed with magnitude of the Middlesborough subset

The test was done using all 36 radar scenes. First the scenes were numbered from 1 to 36, chronologically (Table 4.1). Then interferograms were created from all (n)-(n+2) scene pairs, resulting in 26 interferograms, allowing for an overlap in time between each interferogram. The interferograms were corrected for both reference phases, caused by the curvature of the Earth and height phase, caused by the topography of the area. The reference phases were calculated by DORIS based on the perpendicular and parallel baselines. The height phases were calculated by DORIS based on an external SRTM-3 DEM. The output of DORIS is 26 interferograms. By subtracting the median value of each interferogram, estimation was made of the deformation range in each scene which proved to be close to zero, which confirmed the initial hypothesis.

A similar conventional InSAR analysis with the DORIS software was tried for the research area. The resulting interferograms (appendix 4) show low coherence but are later used for the PSI analysis. Using the conventional pixel-by-pixel unwrapping method as used successfully in the Middlesbrough area did not result in deformation measurements.

To test the results of the InSAR analysis, the deformation measurements were compared to the levelling deformation measurements. In this research, the expected area and rate of

deformation was known and could be used to estimate the quality of the found InSAR measurements. If the deformation found in the undermined area did not exceed the deformation found elsewhere in the research are, the deformation estimate was considered unsuccessful.

4.2.3. PSI analysis

4.2.3.1. Pre-processing of radar scenes

In PSI analysis, radar scenes require pre-processing to limit the amount of distortion. The pre-processing consists of four main steps: conversion, cropping, over-sampling and calibration (Cassee, 2004; Cho et al., 2005; ESA, 2002). The methodology used to take these pre-processing steps was developed by DEOS and consists of a Matlab script that was frequently tested and improved using amongst others the Boulby research area datasets. Eventually eight steps were required for successful pre-processing of the scenes (Tab. 4.2).

Table 4.2: Pre-processing steps for PSI analysis

Conversion and cropping
Create patches of limited size
Over-sampling of the scenes
Calculate ESA calibration vector per imag
Calculate power loss correction
Calibrate the over-sampled amplitude data per patch
Create DORIS'.raw' files
Create new master '.res' files.

After pre-processing, a so called multi-look scene comparing the total amplitude value of all 36 radar scenes, was created demonstrating successful conversion, cropping, over-sampling and calibration. Each pixel represents the amplitude measured at the same area at the surface, resulting in a smooth un-speckled black and white scene of the area (Fig. 4.14).

Figure 4.14: Multi-look amplitude scene of 36 calibrated radar scenes of the Boulby research area

The scene in Figure 4.14 shows the average amplitude for each pixel based on 36 scenes covering a period of 8.6 years. The lighter pixels have high average amplitude values. This does not necessarily correspond with persistent amplitude values over time and could be affected by a single high value in one radar scene. The selection of potential persistent scatterers is based on an algorithm that looks at the variation from the average value for each scene. This is described below.

4.2.3.2. PSI processing

The pre-processing steps resulted in the definition of one master scene and 26 slave scenes with the required input files for each scene. Approximately 50 runs were tried using different parameters to optimise the PSI results, following is an example of some of the runs (Table 4.3).

Table 4.3: Parameters, required for the PSI analysis test runs.

parameter name	description	run1	run2	run3	run4	run5	run6
max_mem_buffer	250 MB, maximal memory size of buffer	5.0E+08	5.0E+08	5.0E+08	5.0E+08	5.0E+08	5.0E+08
input_filename	text file with input file names	input_file	input_file	input_file	input_file	input_file	input_file
Fig.	counter of Figures	0	0	0	0	0	0
lambda	wavelength [m]	5.7E-02	5.7E-02	5.7E-02	5.7E-02	5.7E-02	5.7E-02
m2ph	meters to phase constant	4*pi/ lambda	4*pi/ lambda	4*pi/ lambda	4*pi/ lambda	4*pi/ lambda	4*pi/ lambda
num_lines	number of lines (azimuth direction)	5001	5001	5001	5001	5001	5001
num_pixels	number of pixels (range direction)	1428	1428	1428	1428	1428	1428
az_spacing	[m], azimuth spacing, factor 2 for oversampling	4/2	4/2	4/2	4/2	4/2	4/2
r_spacing	[m], range spacing, factor 2 for oversampling	20/2	20/2	20/2	20/2	20/2	20/2
psc_selection_method	1 = threshold, 2 = number, 3 = grid	1	1	1	1	1	1
psc_selection_gridsize	[m], grid size for psc selection	250	250	250	250	250	250
psc_threshold	threshold for amplitude dispersion	0.25	0.3	0.25	0.25	0.25	0.28
ens_coh_threshold	ensemble coherence threshold	0.7	0.7	0.6	0.6	0.6	0.6
psp_threshold1	ps potential threshold, recommendation = 0.65	0.65	0.65	0.65	0.6	0.5	0.6
psp_threshold2	[dB], ps potential threshold, recommendation = -2 dB	-2	-2	-2	-2	-2	-2
ps_eval_method	1 = ps potential, 2 = whole scene	1	1	1	1	1	1
ps_perc	percentage of pixels analyzed for PS	100	100	100	100	100	100
atm_corr_length	[m]	1000	1000	1000	1000	1000	1000
reference_selection	Choose man (manual, using plot) or auto (automatic)	man	man	man	man	man	man
*azimuth coordinate	reference point	1248	1248	1248	1248	1248	1248
*range coordinate	reference point	876	876	876	876	876	876
std_H	[m], standard deviation of the DEM used (x2)	20	20	20	20	20	20
std_v	[m], measure of the expected linear deformation (x2)	0.2	0.2	0.2	0.2	0.2	0.2
filter_length	[year], for low-pass non-linear defo filtering	1	1	1	1	1	1
APS_doplot	APS plots	n	n	n	n	n	n
model	APS kriging model	nug., ex.cov.	nug., ex.cov.	nug., ex.cov.	nug., ex.cov.	nug., ex.cov.	nug., ex.cov.
range	APS kriging range	375	375	375	375	375	2000
itype	APS kriging interpolation type	universal, drift	universal, drift	universal, drift	universal, drift	universal, drift	universal, drift
nk	number of	30	30	30	30	30	30

script name		23nov.mat	24nov.mat	7dec.mat	8dec.mat	9dec.mat	10dec.mat
psc	number of persistent scatterer candidates	1883	5316	1883	1883	1883	3332
edges	number of edges	5134	15331	4999	4999	4999	9091
psp	number of potential persistent scatterers	14684	14684	14684	17622	26388	17622
ps	number of persistent scatterers	2577	2748	11097	13515	20716	13075

The script used in Matlab to test the different parameters is given in Appendix 1.

4.2.3.3. Potential Persistent Scatterers (PPS's) selection from amplitude scenes

The first processing step is the selection of potential persistent scatterers (PPS) from the scenes, based on high and consistent amplitude sequence in all scenes. The phase value is sensitive to decorrelation factors. Amplitude however is less sensitive and can therefore be used to select the PPS's. Different methods exist for the selection of PPS's from amplitude values and in this research the amplitude dispersion is used to determine the level of persistence (Feretti, 2001). Values from 0.3 to 0.2 have been tested, this resulted in respectively a higher number of less reliable PPS's or a lower number of more reliable PPS's in the Boulby research area. The most optimal value for allowed amplitude dispersion was found to be 0.27.

To ensure a homogeneous spatial distribution of PPS's a grid was placed over the scenes and one pixel in each grid cell with the lowest dispersion value, under the threshold value was selected as PPS (Fig. 4.15). Testing showed that the most optimal grid spacing was found to be 150 metres. The selection of pixels is done in several runs and the grid position on the scenes is shifted half a grid size each time both horizontally and vertically to avoid selecting neighbouring pixels.

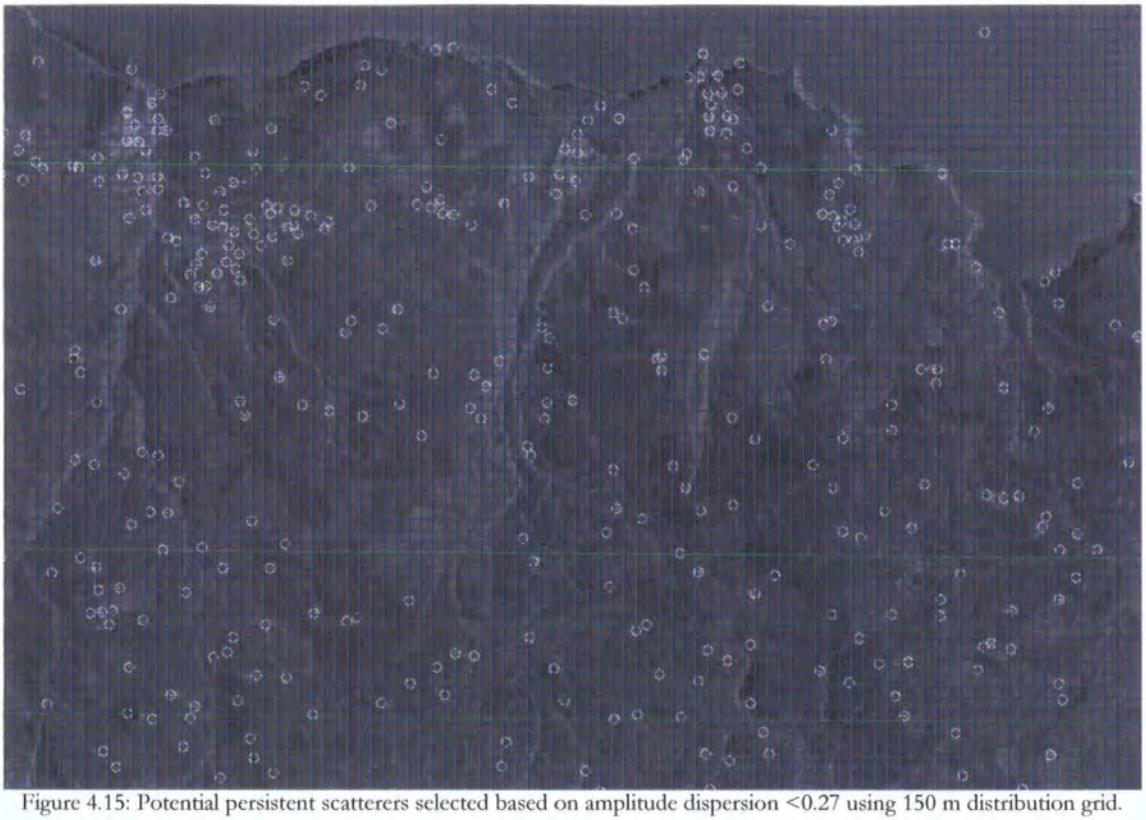

Figure 4.15: Potential persistent scatterers selected based on amplitude dispersion <0.27 using 150 m distribution grid.

4.2.3.4. Generation of interferograms using DORIS

The second step is the creation of interferograms using the DORIS open software programme. The selected master scene for this analysis is scene number 13 with registration date 25 January 1997 (Table 4.1). The temporal baseline of interferograms ranges between 35 days and 2030 days. The overall coherence of most interferogram is extremely low and are proven in stage 1 of this research not to be suitable for conventional InSAR.

4.2.3.5. Subtraction of the topographic phase from interferograms

In the conventional InSAR approach two methods are used to calculate the topographic phase of an interferogram. The first method uses a scene pair from the ESA tandem mission to determine the topographic phase. The main problems with this method are the presence of a unique path delay phase in both interferograms. In cases where the atmosphere is likely to contain variable amounts of condensed water as in temperate coastal areas this method is not preferable. A solution suggested by Ferretti et al. is to stack multiple tandem pairs to minimise the effect of differences in path delay. This method requires several good quality tandem pairs.

A different method to calculate the topographic phase is through the use of an external Digital Elevation Model (DEM). Depending on the quality of the external DEM the elevation can be estimated with a higher accuracy and free of atmospheric distortion. However, because SAR can penetrate some objects at the surface but not all, using a DEM created with another measuring technique can cause relative inaccuracies.

In this PSI analysis a DEM from the SRTM-3 was used. To test the viability of the SRTM DEM to remove the topographic phase some tests were done with the Boulby research area dataset, such as the Middlesbrough test described above.

4.2.3.6. Derive and unwrap phase data for PPS's from all 26 interferograms

In the fourth step the PPS's are connected with a Delauney triangulation network of arcs (Kampes and Hanssen, 2004). Between PPS's arcs are drawn, connecting the PPS's in space. The optimum maximum arc length was found to be 2 kilometres. The arcs are the new unique identifiers for the next steps in the analysis. Each arc is connected to a series of relative phase change values derived from the 26 interferograms. Using the ambiguity function (equation 2.5) the arcs can be unwrapped and relative height difference can be determined per arc (Ferretti et al., 2001).

4.2.3.7. Estimation and removal of atmospheric phase screen (APS)

Based on the initial differential interferometric phase values estimated using the PPS points, interpolations of the outlier values are made. These interpolations are used as estimation of the atmospheric phase. Further research at the accuracy of this method is currently undertaken (Hanssen and Ferretti, 2002).

4.2.3.8. Selection of PS's

In this step, the initial unwrapped height difference estimations are used to evaluate the reliability of each PPS and to determine which PPS's are persistent scatterers (PS's). First the PPS's with the lowest temporal coherence and PPS's that are connected to less than three arcs are dropped. The relative height differences found for each PS over time still include the atmospheric and topographic delay phase. A number of filtering steps is taken to determine which part of the value is the actual deformation value.

4.2.3.9. Final generation of the PSI deformation values

After a final unwrapping of the filtered relative phase values for the final PS's, an average deformation rate value is found for each PS. PSI deformation measurements are initially in slant range which is converted to a vertical and a horizontal component. At this stage, the vertical component equals the average annual deformation rate for the complete 8.6 years of monitoring between December 1992 and August 2002. In addition to the annual deformation rate, a residual value for each PSI measurement is calculated from the separate interferograms (Ferretti et al., 2001; Kampes, 2006).

4.3. Modelling ground surface deformation

'Study the past if you would define the future.' (Confucius)

The relationship between excavated material and surface deformation is complex, partly due to the differences in capacity of strain absorption by the ground layers between mining seam and surface and the interactions between these layers. Layers can act as brittle plastics, elastics or fluids and this has essential impact on the spatial and temporal behaviour of surface deformation. Following is a methodology used to develop a data-driven model. The main hypothesis is that the complexity of the mechanical behaviour of the surface is contained in the data and that future deformation can be estimated based on past behaviour.

4.3.1. Evaluation and quantification of input datasets

The two main input datasets for this part of the research are the relative elevation measurements from the levelling surveys and the excavation records, both datasets from CPL. The format, extent and amount of spatial and temporal overlap between these datasets is discussed in chapter three. In this chapter the methodology to determine and apply the correlation between the two input datasets will be discussed. The quality of the input datasets determines the quality of the outputs of any data-driven model (Waveren et al., 1999). The cone model is therefore dependent on the quality and compatibility of the two datasets. There are three factors to consider, the relative elevation, the accuracy in OSGB location (or horizontal position) and the time measurement represented in the two datasets.

In the case of levelling surveying, elevation is measured against the first point or reference datum (Fig. 4.16). The selection of the reference datum is important. To measure

deformation over time, the reference datum should be selected in an area that can be expected to be stable relative to the observed deformation process. The elevation at each point is calculated by adding the accumulative vertical distances to the reference point (Fig. 4.16).

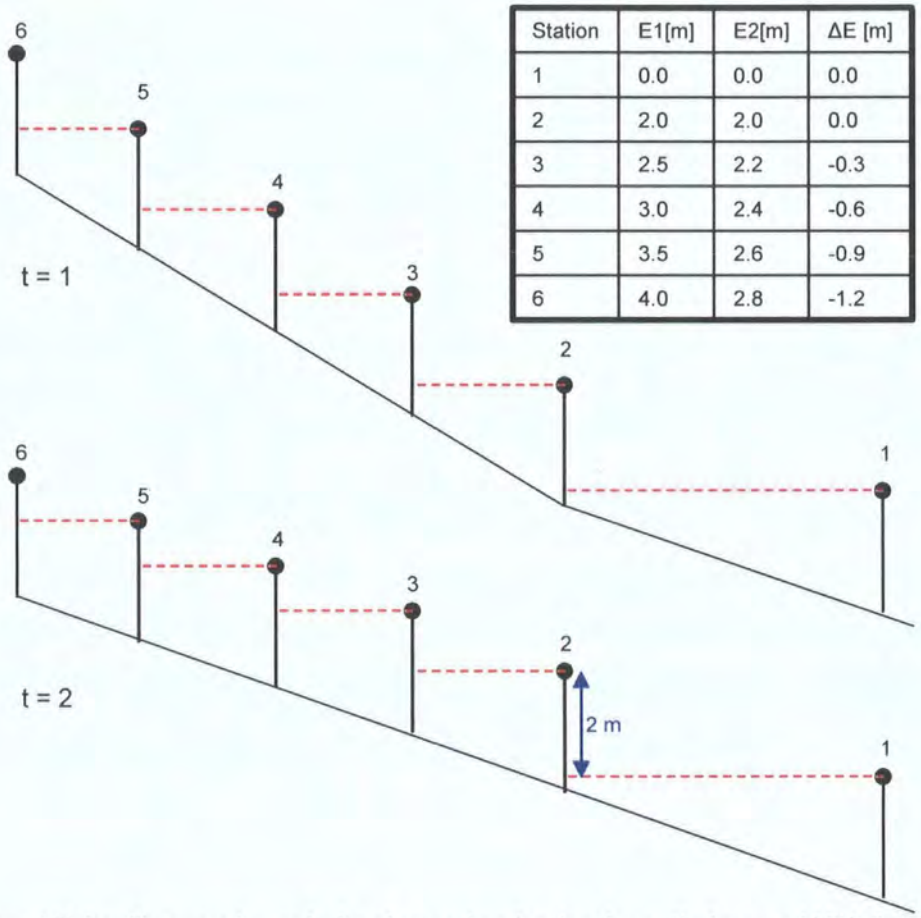

Station	E1[m]	E2[m]	ΔE [m]
1	0.0	0.0	0.0
2	2.0	2.0	0.0
3	2.5	2.2	-0.3
4	3.0	2.4	-0.6
5	3.5	2.6	-0.9
6	4.0	2.8	-1.2

Figure 4.16: Levelling surveying method used to monitor elevation change (Anderson and Mikhail, 1998)

The accuracy maintained in the levelling procedure is 0.2 mm per step. If the difference between two readings of the same steps exceeds 0.2 mm the reading is repeated and re-tested (Kinder, 2001). The stations used in the following analysis are the fixed stations, represented by a concrete fixture. The average number of levelling steps between the stations ranges between 1.1 on line six and 4.6 on line eight (Fig. 3.25). Consequently, the average maximum error between two stations ranges between 0.22 and 0.93 mm (Tab 4.4).

Table 4.4: Maximum elevation error in levelling dataset, based on number of steps between fixed stations

LineNo	steps	stations	avg	error [mm]
1	1268	953	1.33	0.27
2	570	415	1.37	0.27
3	391	292	1.34	0.27
4	2700	1994	1.35	0.27
5	2339	1403	1.67	0.33
6	394	359	1.10	0.22
8	2710	585	4.63	0.93
9	798	608	1.31	0.26

The accuracy of the given OSGB coordinate of the surface stations is of a high order and the actual location of the used benchmarks was confirmed using levelling surveys to the OS benchmark in the Boulby area and by using Digital GPS (Kinder, 2001; Rosser, 2003).

The accuracy of the given OSGB coordinate of the centre of the mine panel depends on the applied underground surveying technique. The method used is a triangulation method which measures the relative position from the mine shaft, based on angular measurements. Due to the difficulties of levelling underground, the accuracy is likely to be several centimetres. However, this accuracy is less important as it will be used to determine the angle between the station at the surface and the location of the mining panel. For example, a horizontal shift of one metre represents a shift in angle of 0.057° if the depth of the mining panel is 1000 metres.

Finally, the time factor is represented by the time of levelling and the starting time of mining, which are both of a different level of accuracy. In the levelling dataset the used time unit is 'day' (Tab. 3.3). Because the deformation is converted to annual deformation rate, this is a high level of data accuracy. The excavation dataset does not give closure data per day; instead it provides a date in which it started to be mined and the unit is 'month' (Tab. 3.3). The time variable that will be used to compare these two datasets is the number of days between mining and the mid point between two surveys. Consequently, the accuracy of this variable is one month which will also be the maximum accuracy of estimates based on this dataset.

4.3.2. Initial geo-spatial modelling

In 1998, an initial study was carried out to determine the amount of ground surface deformation taking place around the Boulby mine, on behalf of Cleveland Potash Limited

(CPL, 1999). Based on the levelling datasets, an empirical model of the estimated ground surface deformation caused by mining activities was made. This model is given in equation 4.1.

Equation 4.1 (CPL, 1999):

$$Y = -753.63 \times \ln(x) - 677.33$$

Where Y is the distance from the central entrance shaft of the mine in metres and x is the ground surface deformation rate in mm a^{-1}. To calculate the ground surface deformation rate based on this logarithmic equation, a raster file was generated with straight line distance values from the main entrance shaft. Using the spatial analysis tool of ArcGIS, a conversion of the original algorithm was used to calculate the ground surface deformation rate for each raster pixel, given in equation 4.2.

Equation 4.2:

$$x = e^{\frac{Y + 6.77.33}{-753.63}}$$

The result of this algorithm is mapped in Figure 4.17, showing the spatial correlation between the mine workings and the deformation rate estimated by the model.

The only input variable used in the 1998-model is the distance from the main entrance. In the area around the entrance shaft, the estimated deformation rates correspond well with the measured values on which the model is based (Fig. 4.18). However, the shape of the mine is not circular around the main entrance and the effect of the southern and northern parts of the mine are not included in the estimations.

In the two graphs in Figure 4.5, the deformation rate at the levelling stations, derived from the CPL dataset is compared to the estimated values from the 1998-model. Because of its simplicity, this model can be used for a quick analysis of the impact of a mine. However, because it does not take into account the actual location of the mine panels around the shaft nor the progressive expansion of the mine, the model can not be used to make any conclusions about the impact of the mining activities on the surface.

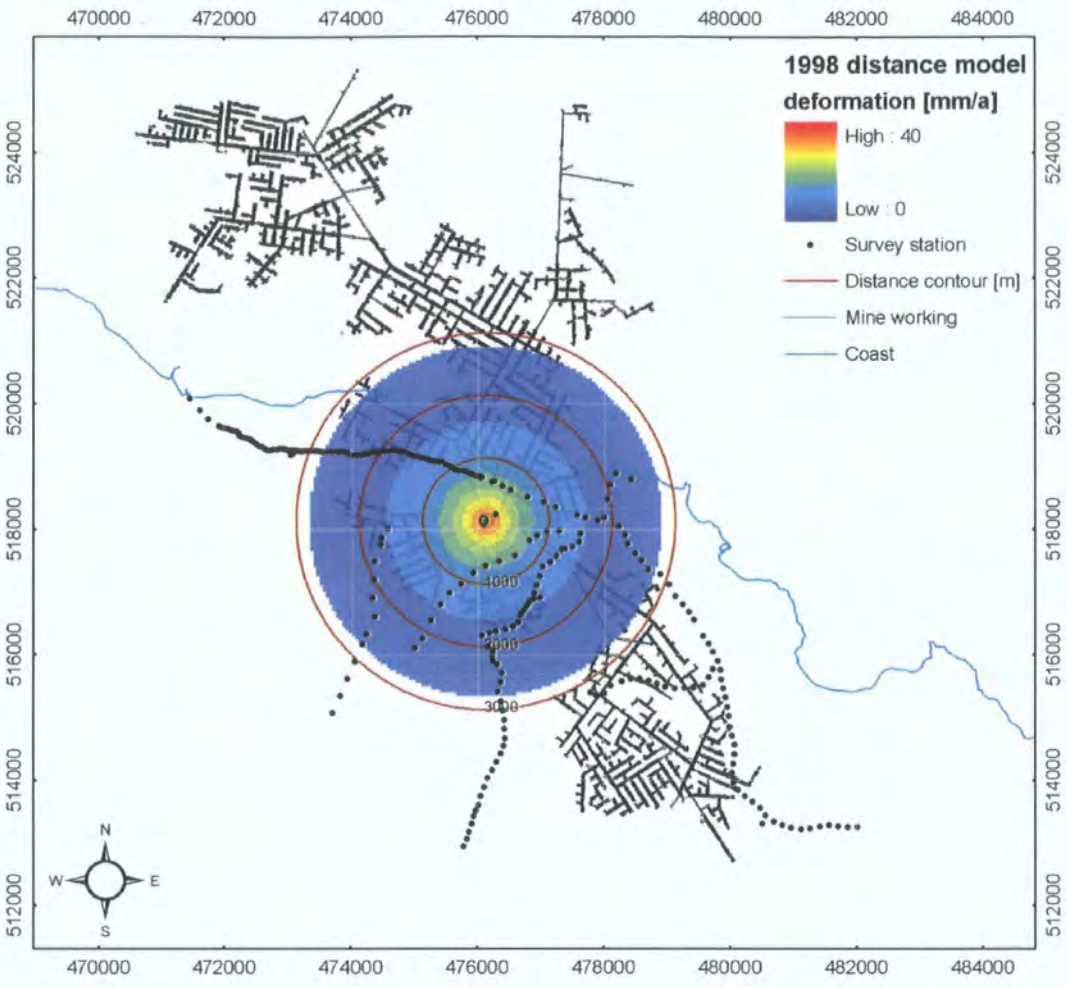

Figure 4.17: Estimated total deformation rate in the Boulby area over 22 year interval around the main entrance shaft of the Boulby mine.

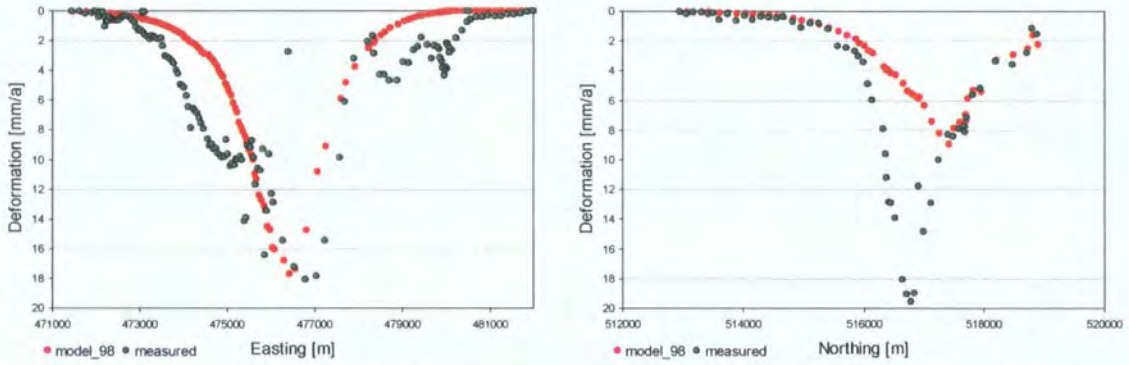

Figure 4.18: transect comparison model 1998 and measured deformation rate: line 8/4 against easting; line 3/5 against northing.

Another method to determine the rate of deformation at points away from the survey stations is by means of interpolation. Several types of interpolation can be carried out to estimate the extent of the disturbed area. Following is the result of an inverse distance

weighted interpolation (Fig. 4.19). The number of values included in the estimation is 12 and the maximum distance is 1500 metres.

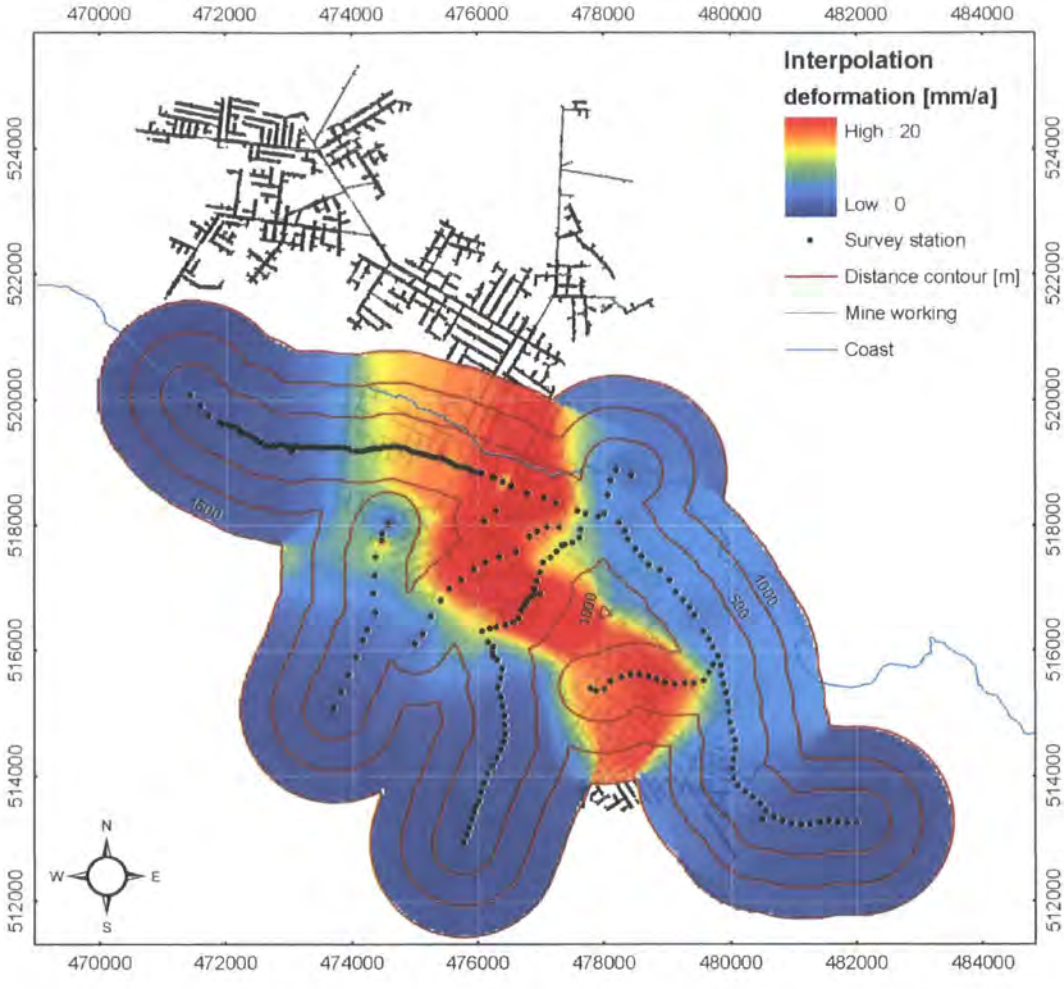

Figure 4.19: Interpolation of total deformation rate after 29.5 years of monitoring.

The result of this interpolation is a raster file where the pixel values represent the estimated rate of deformation based on the nearest 12 measured values. The estimated value is the weighted product of these 12 values. In Figure 4.19 the interpolation raster is mapped on top of the mine. The distance contours indicate the distance from the survey stations. The limited overlap of the levelling stations and the extent of the mine workings is discussed in chapter three. The deformation taking place at a distance more than 1500 m. away from the levelling stations can not be reliably estimated.

Like the geospatial model, interpolation to analyse correlation between the mining activities and the deformation rate at the surface have demonstrated that refinement and complexity is required. These experiments confirm that a larger number of variables, including spatial and temporal variables of the mining

activities to estimate the ground surface deformation. As a consequence the cone model was developed, integrating existing modelling concepts with large dataset, a geographical information system and a relational database.

4.3.3. The cone model - Principles

The area of land on the surface affected by underground mining due to the settlement of ground layers is defined as the 'area of disturbance' and will exceed the undermined area (Kratzsch, 1983; Whittaker and Reddish, 1989). The amount of disturbance outside the area of disturbance should approach zero. In influence function modelling, the circular or ellipsoidal extent of this area on the surface is formed by extending a cone from the centre of the mine to the surface (Figure 4.20) (Kratzsch, 1983; Whittaker and Reddish, 1989). The angle of the outer edge of this cone to the vertical line from the centre of the mine to the surface is defined as the 'angle of draw'. Typically the angle lies between 31 and 54° (Kratzsch, 1983). A larger angle of draw results in a larger area of disturbance.

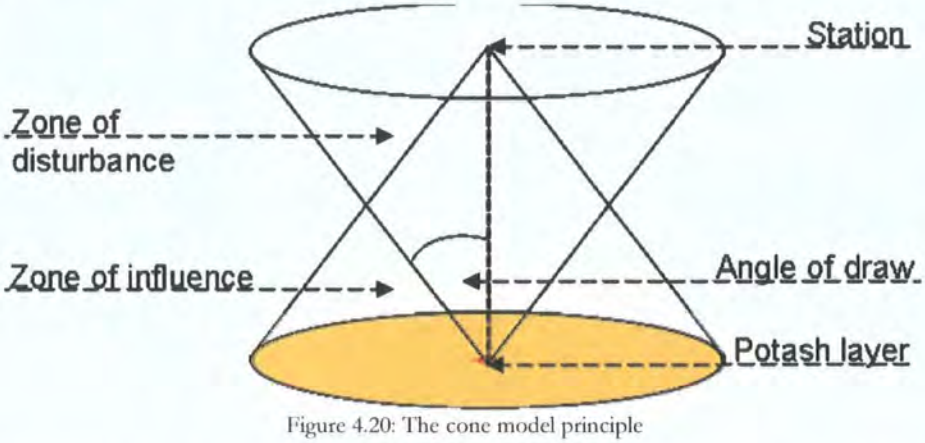

Figure 4.20: The cone model principle

Adding the excavation dynamics will make this simple model somewhat more complicated. Instead of taking one point to represent the entire mine, a number of points can be used representing the centre of individual excavation panels. Each excavation panel has a central x-, y- and z-coordinate as well as a starting date of excavation. The actual area of disturbance at the surface will be formed by the resulting overlapping shape of the different cones and will change according to the excavation dynamics.

By reversing the cone, any given point on the ground forms the pivot to a cone shaped zone of influence (Figure 4.21). Mining activity located within the volume of the cone would be likely to cause deformation at that point. Using this concept, it becomes possible to correlate several characteristics of mining activity within a volume to the deformation process at the surface. Ground surface deformation rates [mm a^{-1}] at a given point on the

surface can be related to variables such as the number and size of the mining panels within the zone of influence and their location in relation to the centre of the circle. Using the cone model principles a relationship between excavation dynamics and surface deformation can be made. The two layers in Figure 4.21 represent the ground surface (green) and the potash seam (blue).

The main unit used in influence function methods is the elementary trough, a zone of disturbance for each excavation unit that can be added to estimate the total zone of disturbance (Chapter two). Instead of using elementary curves caused by individual excavation units as done in the influence function method, the CSM method uses the combined effect of all excavation taking place in the zone of influence. Variables are determined for all excavation units influencing a surface point in space and time, grouping them together to quantify a specific correlation between the excavation data and the survey data The relationship between these variables and the measured deformation can be used to predict deformation.

The size and shape of the perimeter of the deformation bowl at the surface are determined by one parameter and two variables: the angle of draw, the average depth of the excavation units and the relief at the surface. If the angle of draw is accurate known, it can be used as the maximum nearest mine panel angle (β) to determine which mine panels and which stations should be linked to each other. Because the extent of the mine workings grows, the number of mine panels that will be linked to a station will change over time.

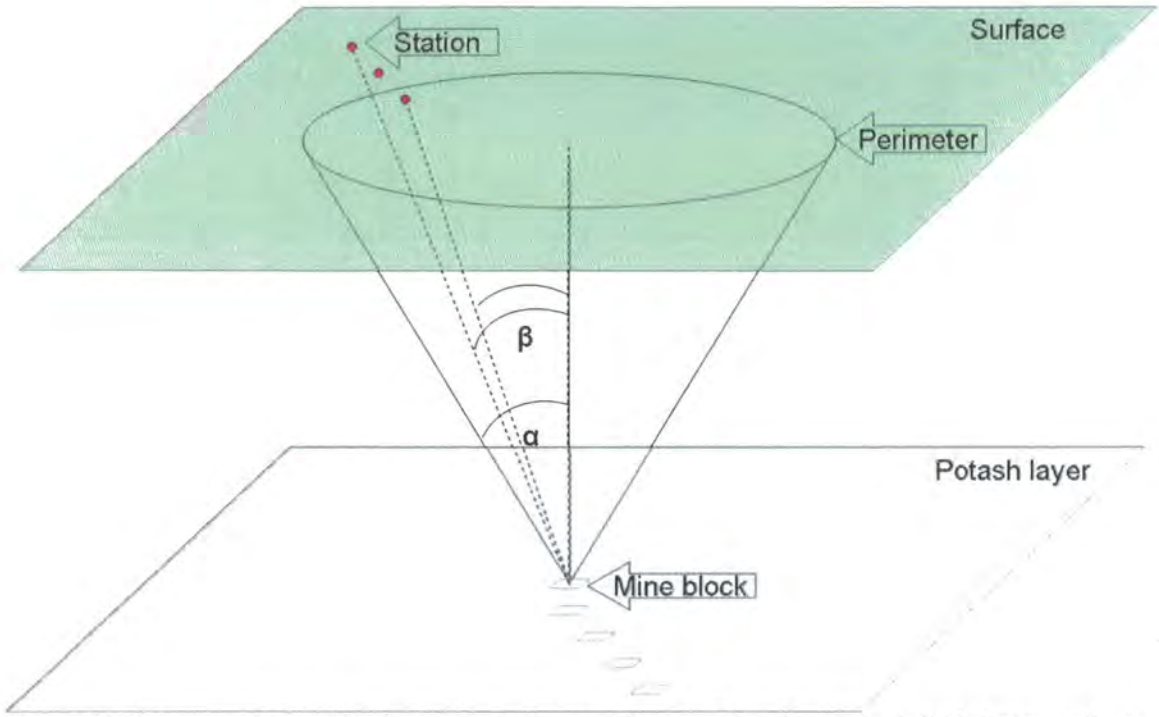

Figure 4.21: The cone model principle, showing the perimeter of the zone of disturbance of an individual mine panel, α is the angle of draw and β is the nearest mine panel angle.

4.3.4. The cone model – Tool

In the following section the development of a data-driven subsidence-forecast model is described. This model is loosely based on existing theory of influence function models, but is mostly a new model developed as part of this research and in close co-operation with CPL. Computational power in the form of a relational database is employed to make the connection between the different variables derived from the two dynamics. Microsoft © SQL software in combination with Microsoft © Access Project interfaces enabled the set-up of a tool to relate these datasets. In Figure 4.22 a diagram is given of the function of the relational database, based on the cone concept.

Initially, the relational database is used to determine the algorithms that explain the correlation between the excavated volume, the spatial distribution and the temporal variation of the mining panels and the ground surface deformation. Eventually this functionality was turned around and the ground surface deformation could be estimated using the algorithms and the excavation dynamics as input. The manual for this tool is given in Appendix 2.

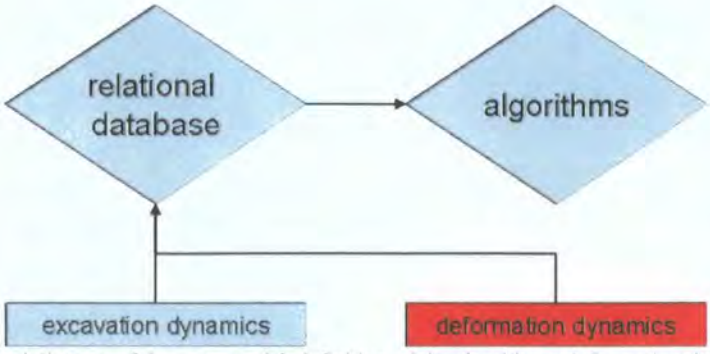

Figure 4.22: Conceptual diagram of the cone model, definition of the algorithms: deformation dynamics are measured.

The building blocks of a relational database are tables containing the input datasets, new intermediate tables and output tables that contain the results of data queries. The queries ore stored procedures that take data from one Table to generate a new Table are capable of parameter-based selection and the use of mathematical and geometrical functions. Based on all tables and queries a diagram can be built to visualise the data stream (Fig. 4.23).

The process of finding the best way to join the tables and to generate the best variables to quantify the different situations in the zone of disturbance included many trial and error tests. The diagram in Figure 4.23 has looked considerably different at times. Following is an explanation of the procedures in the final diagram used to generate the variables.

The SQL scripts written for this model are given in Appendix 3. In procedure one a measurements Table is generated, from the levelling dataset. A unique id number is given to each measurement record, which represents a levelling station with known OSGB coordinates and a day-number, at the midpoint between two elevation measurements. In procedure two the radius of the zone of disturbance at seam level is calculated based on the angle of draw, a given parameter and the Depth variable of the mining panels. A radius for each mine panel is calculated. In the third procedure the mine panels are linked to each other to generate a 'near mine panels'-table. This table gives for each mine panel all mine panels within their zone of disturbance. The input tables are the excavation dataset and the radius table generated in the second procedure. In the fourth procedure a summary of the 'near mine panels' table generated in the previous procedure is made, based on the date of mining of each mine panel and the selected prediction period. For each mine panel and at each unique point in time the average distance to all mine panels in the zone of disturbance is calculated. The input tables are the 'near mine panels'-table and the periods-table, which contains periods by year.

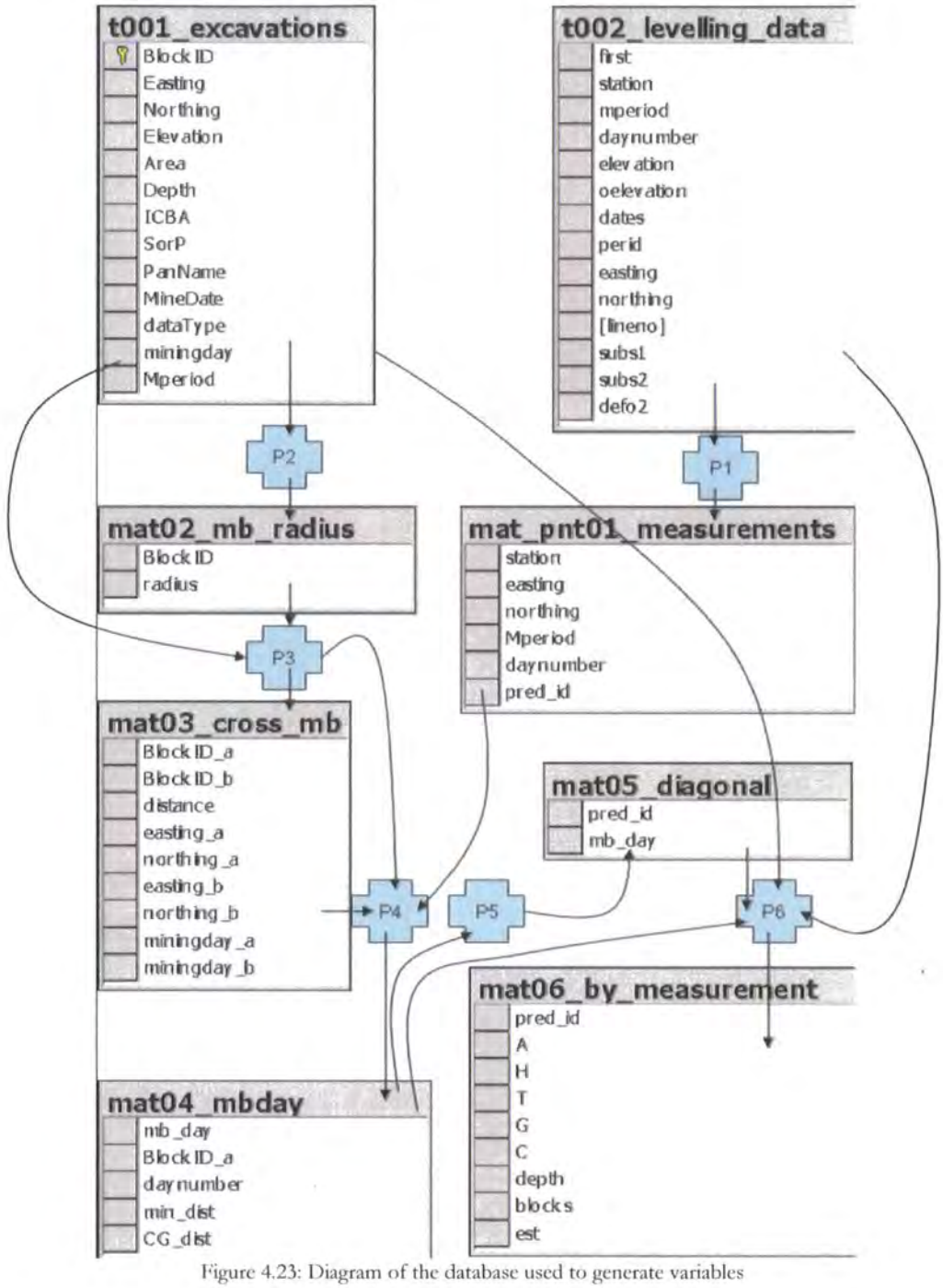

Figure 4.23: Diagram of the database used to generate variables

In procedure five the prediction records generated in the first procedure are joined to the summarized mine panel table generated in the fourth procedure. This join is controlled by the angle of draw parameter, because only mine panels within the zone of distance of a prediction point are joined to that prediction point. The new table consists of unique diagonals, each representing a prediction point at the surface, a mine panel and a point in time. In the final sixth step the variables are calculated, based on inclusion of all those panels that fall in a zone of disturbance of a prediction point at a point in time:

A = the sum of the area of the mine panels

H = the average horizontal distance between all panels and a prediction point

T = the average time difference between the mining dates and the prediction date

G = the average of the 'near mine panel' distance

4.3.5. The cone model - Variable and parameter testing

This section describes the development of four optimal regression-algorithms that forecast deformation rate (dependent variable), each based on one of four (independent) variables, i.e. mined area (A), horizontal distance (H), mine panel distance (G), and time difference (T). These regression algorithms were integrated into the cone model tool. The 'Labfit' software package was used to return all possible curves in order of the highest coefficient of determination, based on standard least squares methods. For this research, those ten algorithms with the highest R^2 for each variable were tested in different combinations with regression algorithms for the other variables using the cone model tool described above. Only after a lengthy iterative process, which integrated the individual algorithms for each variable into one estimation algorithm, the best curve for each variable was chosen. The R^2 of each selected algorithm had a p-value less than 0.01 and was therefore statistically significant at the 99% confidence interval.

4.3.5.1. The Angle of draw based on the β-ratio

In section 2.5.3, the angle of draw (or limit-angle) principle (Fig. 2.18) is introduced. In the cone model, the angle of draw parameter determines the size of the zone of influence. The angle of draw determines which mine panels affect which stations, both in the regression analysis and the final model. The angle of draw for the Boulby area was calculated based on the β-ratio, a parameter created for this research based on the measurable deformation at variable horizontal distances from the mine panel (Fig. 4.21).

The β-ratio is a dimensionless ratio of the number of measurements lower than a certain deformation rate as a percentage of the total number of measurements. The stations are grouped based on the β angle between surface stations and mine panels. All measurements were divided into thirty equally sized lags. The β angle is the angle between the vertical and a line from the centre of a mine panel to a monitoring station. If the grouped measurements at a certain β angle are close to or exactly zero, this means that β equals or

exceeds the angle of draw. Or differently stated if the surface stations are out with the zone of influence, the measured deformation rate at the station should approach zero.

By plotting the β-ratio for each of the thirty lags over the mean β angle for that lag, an estimate of the angle of draw can be made. In Figure 4.24 the β-ratio's for the threshold values 0, 2, 4, 6, 8 and 10 mm a^{-1} are plotted over the β angle.

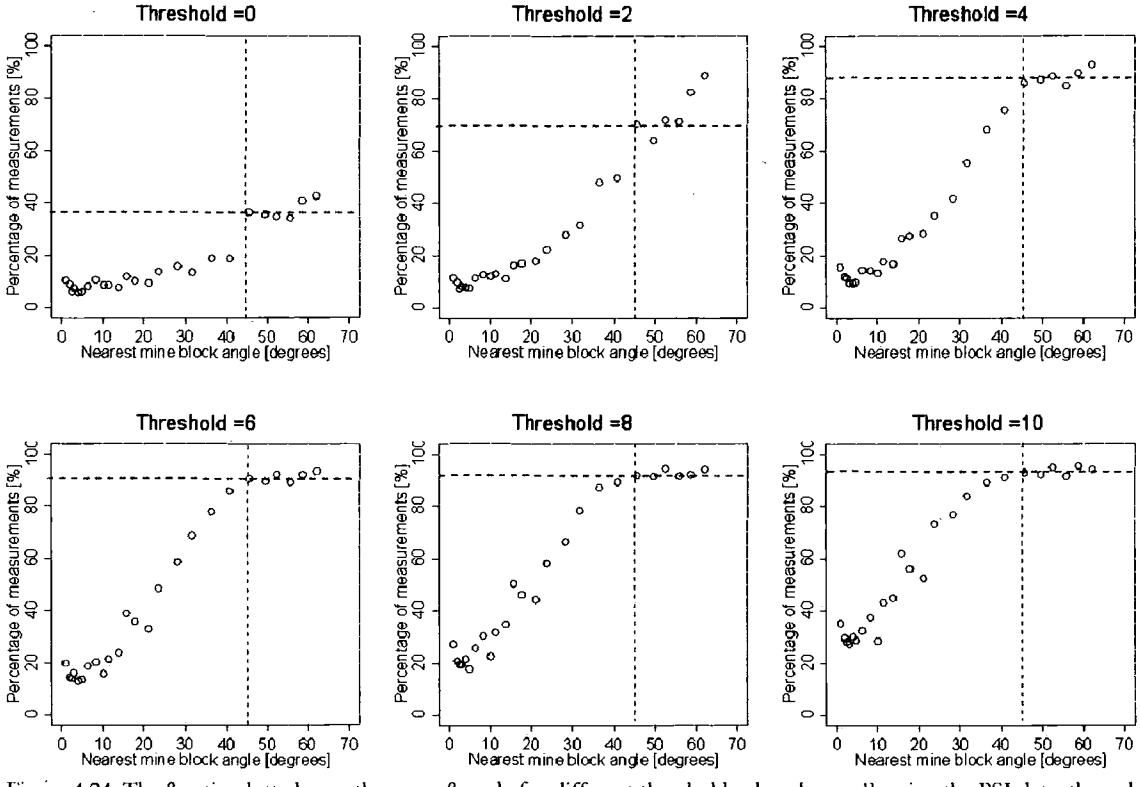

Figure 4.24: The β-ratio plotted over the mean β angle for different threshold values [mm a^{-1}], using the PSI data, the red and blue lines represent the 45° angle and the measurement at that angle respectively.

The graphs in Figure 4.24 consistently show that the β-ratio reaches a stable high value for lags with at an angle of 45°. Measurements at stations located inside the zone of influence above an excavation unit delimited by angle β have a considerably higher probability to show deformation than stations located outside that cone. Based on the recurring pattern in the above graphs, the assumption can be made that the angle of draw for the Boulby area is 45°.

In Figure 4.25 an impression of the extent of the projection of a cone delimited by a 45° angle of draw is given for monitoring station 1053 in the south east of the research area. The green circle is the projection or slice of the cone at potash seam level (ca. 1200 m. below the surface).

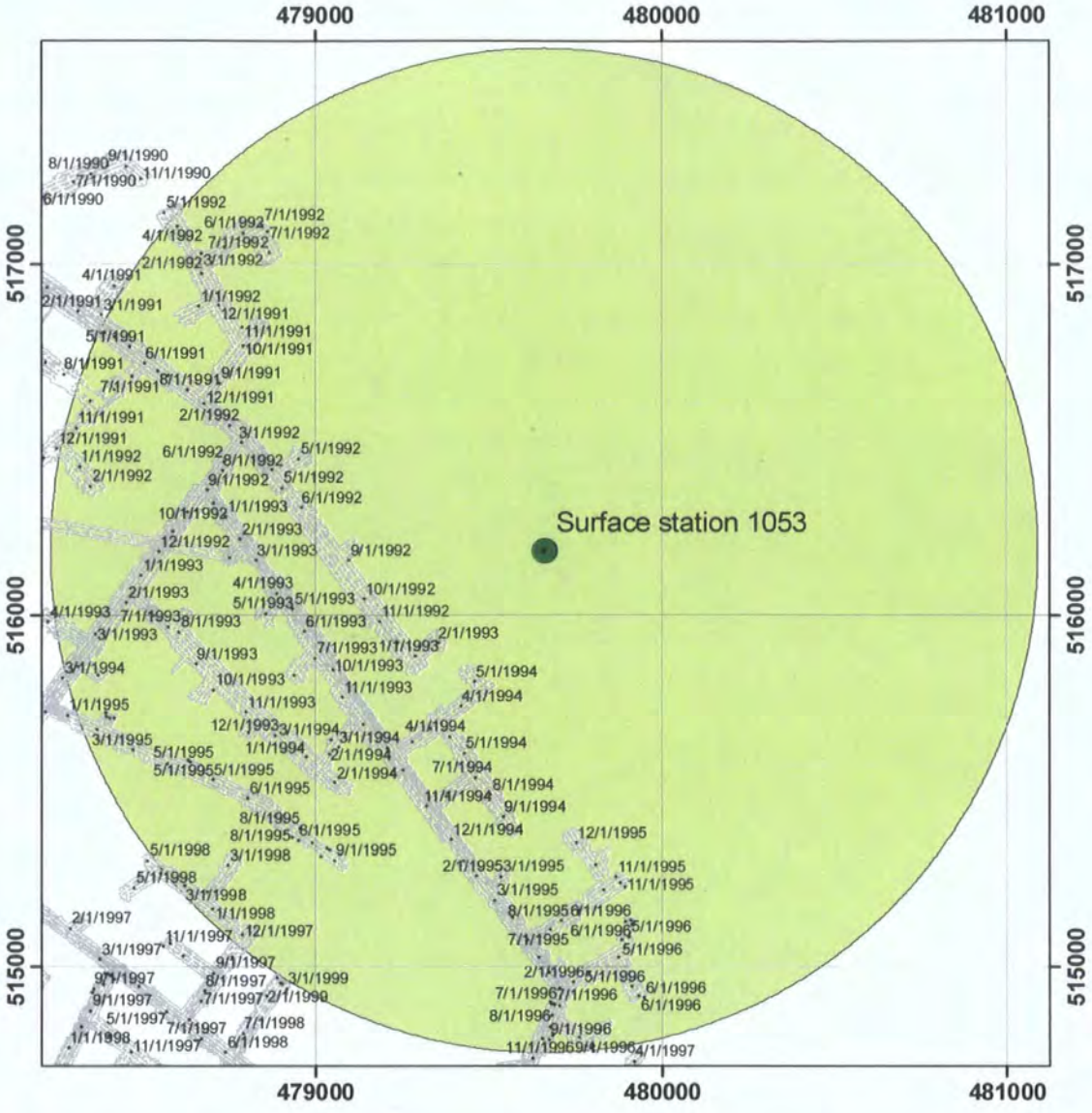

Figure 4.25: Projected cone of monitoring station 1053 delimited by 45° angle of draw.

The cone delimited by the angle of draw is one of the main principles of the cone model and is used in the following sections to further explain the correlation between mining activities and ground surface deformation.

4.3.5.2. Mined area

Correlation between surface deformation and mining can imply that deformation at the surface results from the sum of the disturbances of the excavation units in a certain area (Kratzsch, 1983). In mining models such as influence function methods, total volume of deformation i.e. the volume of the ground surface deformation 'bowl' equals the total

excavation volume. The assumption that the surface will deform by forming a ground surface deformation bowl with the same volume as the total volume of the excavated material does not stand in more recent models and becomes less valid in the case of deep mining (Whittaker and Reddish, 1989) and (Chrzanowski et al., 1997).

To determine the statistical relationship between the volume of extraction and ground surface deformation, the size and number of the mine panels had to be quantified. The variable in the excavation dataset that represents the size of the mine panel is the mined area. As a consequence, the volume of excavation was expressed as the two-dimensional squared area of the mine panel floor. The height of the mine panels has a constant value of 6 metres, because of practical factors such as the proximity of water bearing sandstone in the overlying seams and the capacity of the equipment (CPL, 2002a). If a specific mine panel exceeds 6 metres height, this would result in an underestimation of the total volume of extraction.

The SEH- model, discussed in section 2.5 is based on the assumption that the seam height rather than the mined volume is a controlling factor in the ground surface deformation (NCB, 1966). However, if this factor is indeed constant throughout all mine panels, the effect of the panel height will automatically be included in the regression later in this analysis. It should be noted that the closure rate is estimated to be 1400 mm in 200 days after which it slows down to 200 mm in 100 days. A closure of 6 meters would take approximately 20 years (Fig. 3.19 and 4.26).

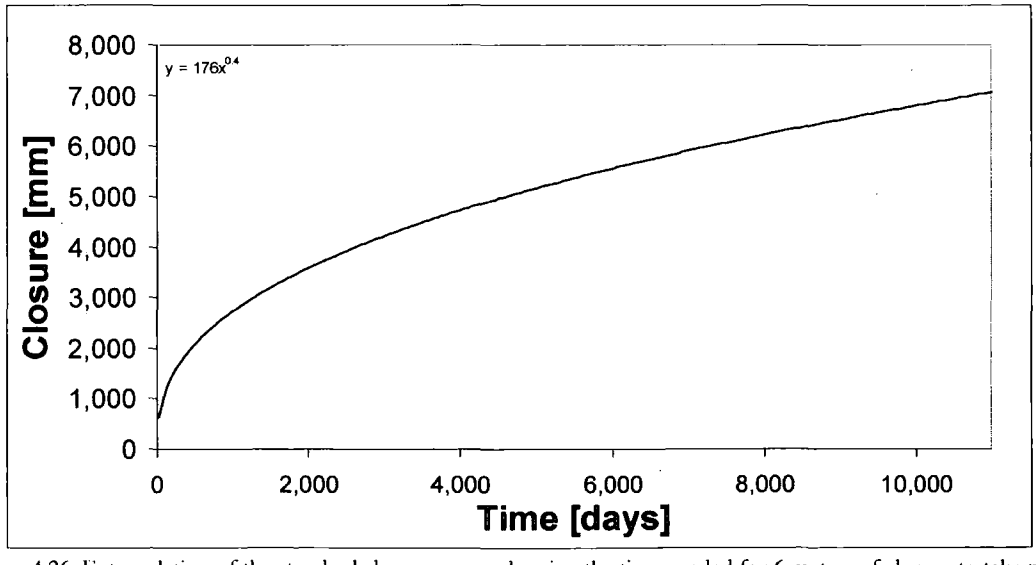

Figure 4.26: Extrapolation of the standard closure curve, showing the time needed for 6 metres of closure to take place (CPL, 2004).

The first variable that was examined in this analysis was therefore mined area. The development of this variable over time is either stable of progressive. Initially only the effect of this variable is examined, later the algorithm found best fitting for this relationship is used for multivariate regression, integrating the effect of all variables. In Figure 4.27 the situation four points in time at one hypothetical survey station is considered.

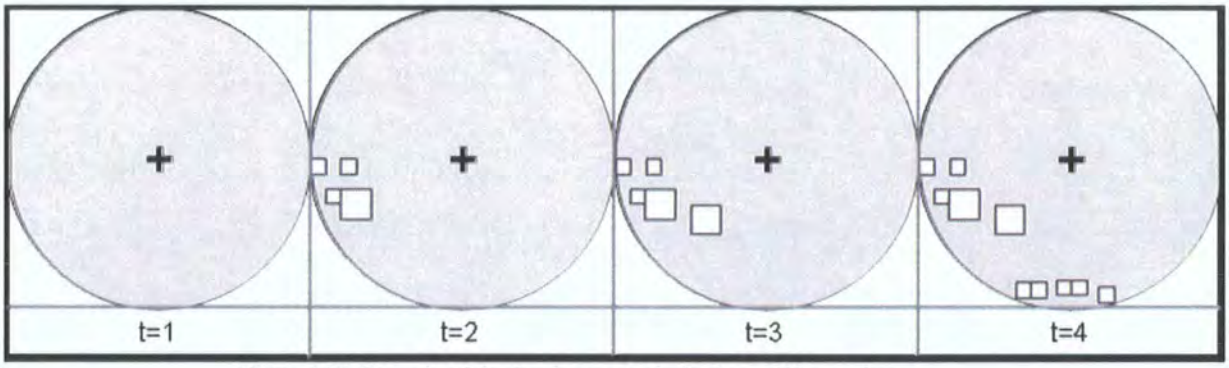

Figure 4.27: Example of the development of mined area (A) over time.

The circles represent the zone of disturbance, which dimensions are determined by the average depth of the mine panels and the angle of draw (see above). The blocks represent mine panels of varying sizes and appearing at irregular intervals. Mine panels affect deformation at the survey station if they fall inside the cone shaped area under the station. At t=1 the mined area is zero. Over the following days, a total of 10 mine panels appear in the cone. To determine the impact of the total mined area at each point in time, initially the sum of all mine panels is examined. The measured rate of deformation is plotted against the mined area for a selected subset of the dataset, as a remaining subset was reserved for the evaluation. This graph is a point cloud with a high standard variation (Fig. 4.28). At this stage there is not much trend to be found in this relationship.

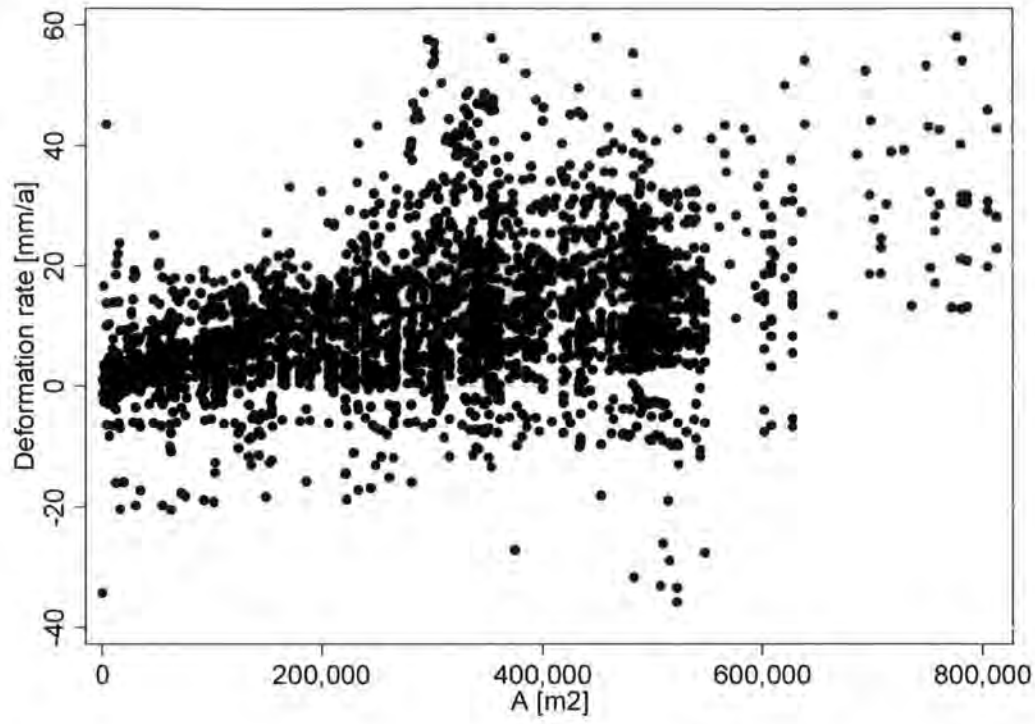

Figure 4.28: Deformation rate [mm a $^{-1}$] plotted against mined area [m2]

The next step was to summarise the deformation rate values by bins of the variable A. The median value (or 50% percentile) can be a powerful representation of the dataset. The size of the bins depends on the value density, and the number of values in each bin is approximately 155. Therefore, the median value over each bin is based on an equal number of values. The associated value for A for each bin is again the median of the interval of the bin. For example if there are 155 situations in which the total mined area in the zone of disturbance is between 200,000 and 210,000, these values are then summarised into one. The summarised value has a deformation rate and a mined-area value that equal the medians of these 155 values. The summary of all values can be plotted and show a much clearer correlation (Fig. 4.29).

In this graph the last value is removed, which represents the median of the final bin, containing less values than the other bins and forming an outlier. There is almost a linear relationship between the measured rates of deformation and the mined area, with a median rate of 20 mm a^{-1} if 600,000 m^2 is mined in the zone of disturbance.

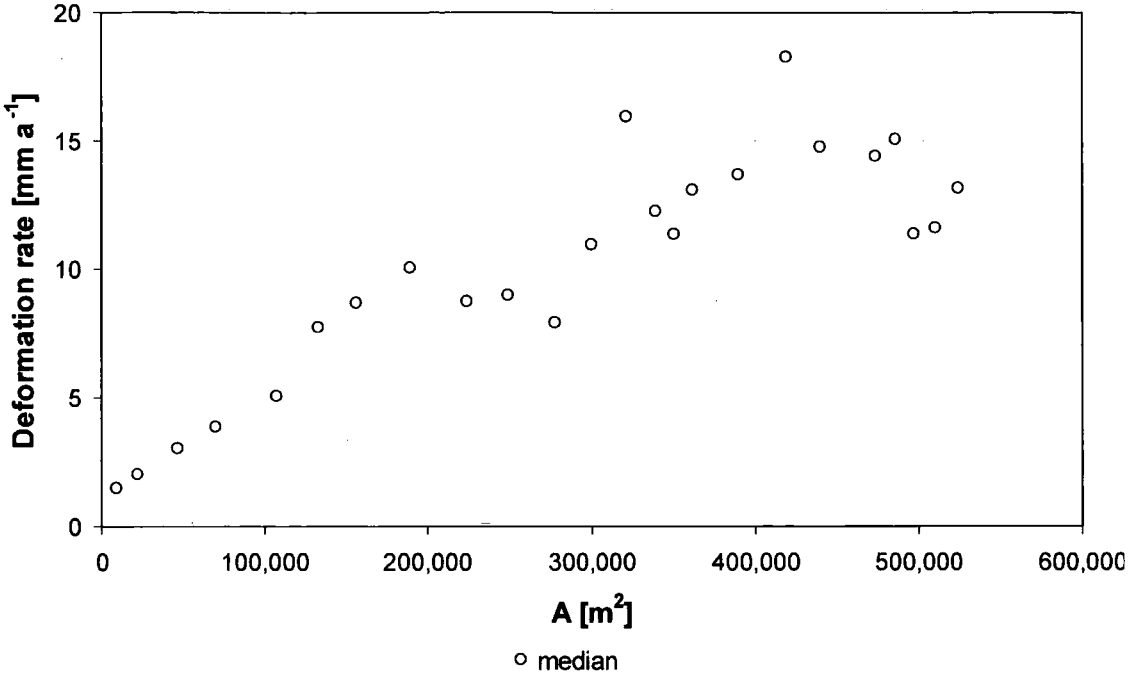

Figure 4.29: Deformation rate [mm a $^{-1}$] plotted against mined area [m2], using medians

In the final algorithm of the cone model, the contribution of all mine panels is summarised. It is therefore necessary to plot this variable against the deformation rate divided by the number of mine panels that fall inside the zone of influence at a station at a point in time. Equation 4.1 describes the curve fitted through the median deformation rate over deformation factor values (Fig. 4.30).

The R^2 value for this function is 0.78 and the p-value <0.01. Although $\hat{S}_A$ seems to correlate well with the median measure deformation rate, the actual measured values show a degree of freedom around the medians, indicating variations other than mined area.

Equation 4.3: $$\hat{S}_A = \frac{1}{4.48 \times \log(A_d)}$$

Where: A_d is the total mined area per d

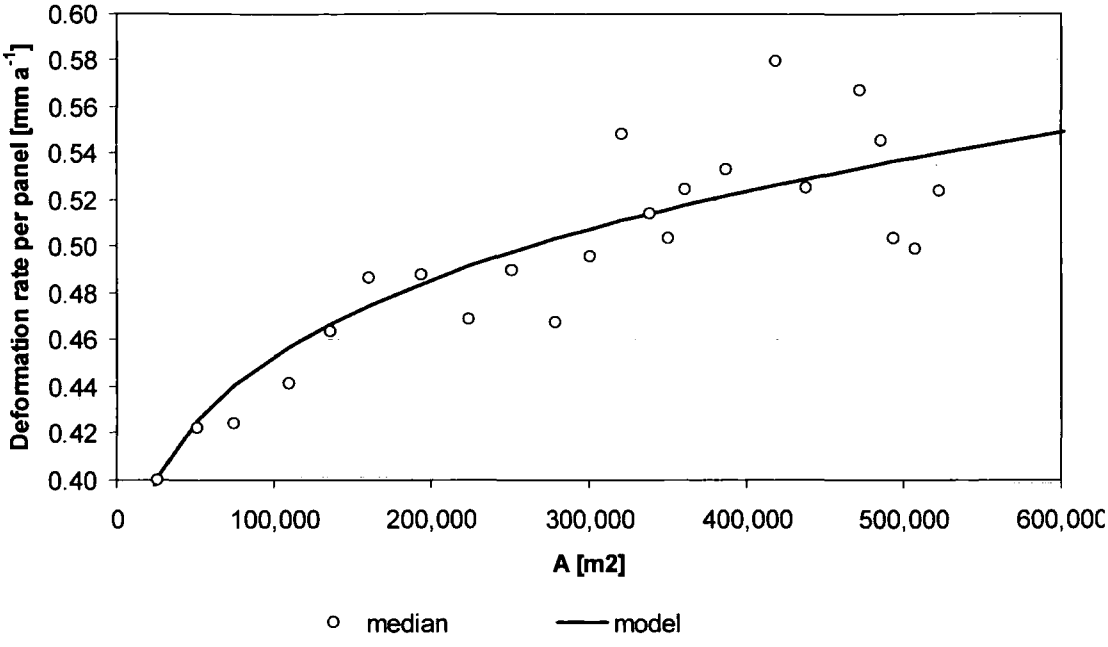

Figure 4.30: Deformation rate [mm a $^{-1}$] plotted against mining density [%], using medians from the levelling dataset, with fitted curve.

In Figure 4.30 the domain of A starts at 9,000 m^2, which is the minimum total mined area for a zone of influence of a surface station, a situation where only one mine panel falls within the zone of influence. In this situation the related deformation rate is 0.40 mm a^{-1}. The maximum mined area is 602,000 m^2 and would cause a deformation rate of 0.54 mm a^{-1} per mine panel.

4.3.5.3. Spatial distribution

At a monitoring station deformation may occur if a critical volume of excavation occurs in its vicinity. However, apart from the quantity of material removed from the cone shaped area, the position of the mine panels in the cone is relevant to the amount of deformation rate measured at the station. The two hypotheses that were behind this part of the analysis are:

1. The horizontal distance between a mine panel and a monitoring station is negatively related to the deformation rate.
2. Mine panels in close proximity of other mine panels cause relatively higher deformation rates.

The average horizontal distance is calculated from the OSGB coordinates of the levelling stations and the mine panels. Again the selected mine panels are those that fall inside the cone of a survey station at the time of the measurement. Over time, changing average horizontal distance is a result of new mine panels that appear in the cone shaped area (see Fig. 4.31), causing a shift in the location of the centre of gravity. This value can decrease and increase for one survey station over time.

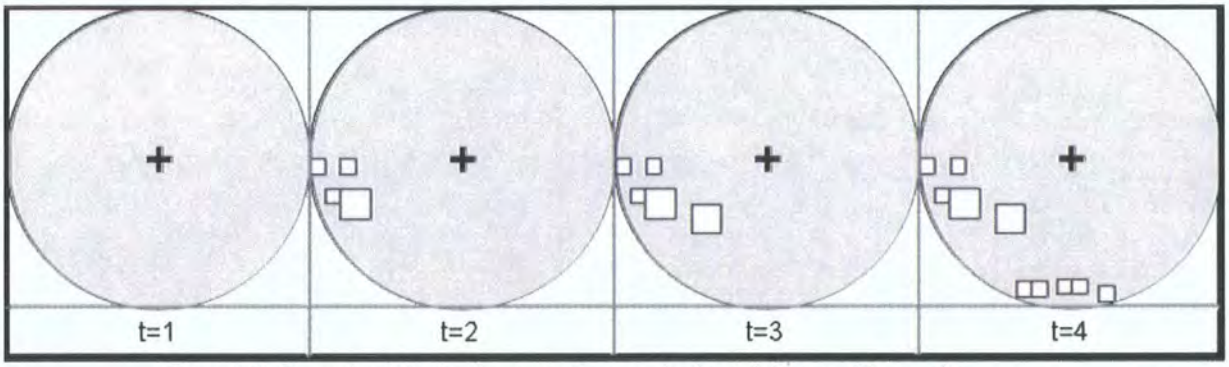

Figure 4.31: Example of the development of average horizontal distance (H) over time.

In above diagram, the average horizontal distance equals the radius of the zone of disturbance in the first circle. The average distance decreases in the two circles at times two and three, where mine panels gradually approach the station. At time four the average horizontal distance has dropped a small fraction, due to the appearance of new mine panels at the rim of the zone of disturbance. To test the first hypothesis, the average horizontal distance of all mine panels in the zone of disturbance is plotted against the measured deformation rate (Fig. 4.32).

The point cloud shows little trend due to the degree of freedom, or trends in other variables. However, to determine the relationship between horizontal distance and deformation rate, the values are summarised in a similar way as explained for the mined area variable above. The bins of horizontal distance are based on the value density and the number of values summarised are again approximately 155. The summarised values are the have a deformation rate and an average horizontal distance value that equal the medians of 155 values (Fig. 4.33).

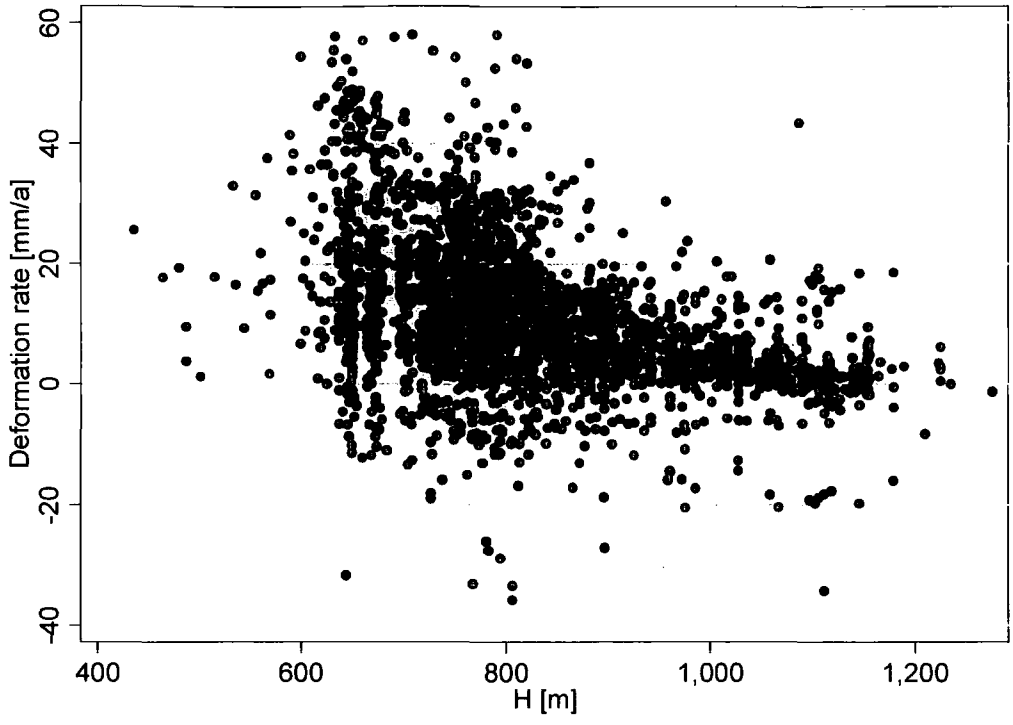

Figure 4.32: Deformation rate [mm a $^{-1}$] plotted against mined area [m2]

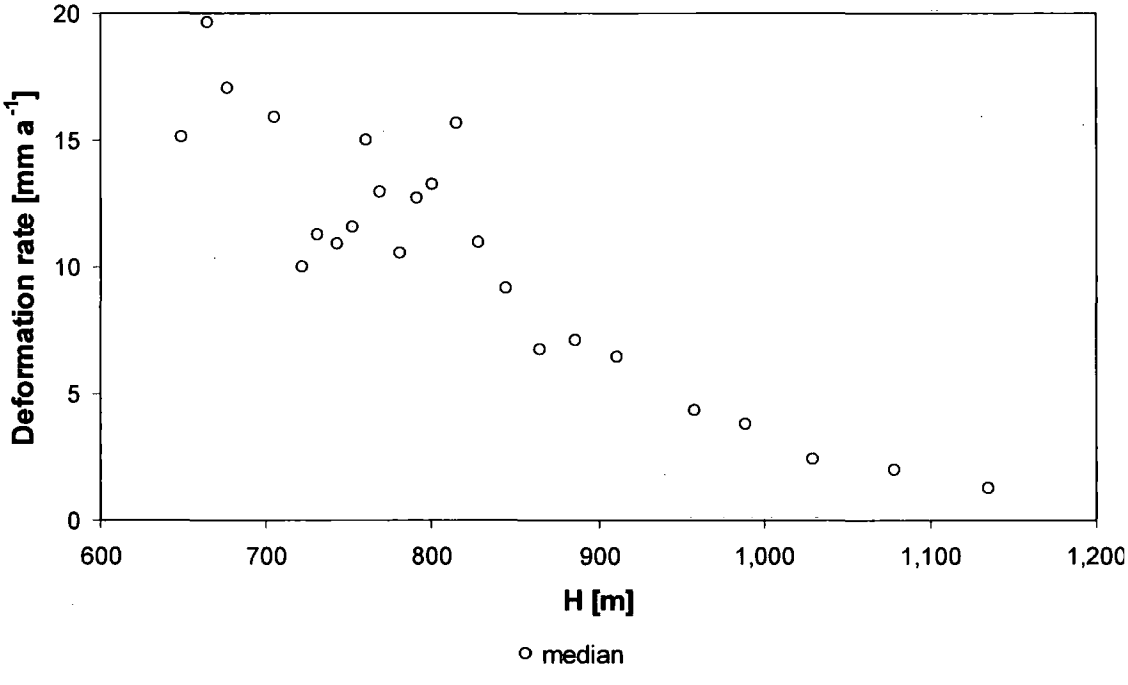

Figure 4.33: Deformation rate [mm a $^{-1}$] plotted against mined area [m2], using medians

The trend in the summarised graph is clear and seems to confirm the first hypothesis. The further from a surface station the mine panels are located, the lower the measured deformation rate is. The minimum value of 600 can be explained by the fact that mine panels grow progressively and don't often suddenly pop up right underneath a monitoring

station. If mine panels are located right underneath a station, more panels will be located throughout the zone of disturbance. This is the reason why the average horizontal distance will not reach 600 m.

Application of the reversibility of the model, the horizontal distance can be interpreted as the average distance of stations to an excavation unit (Fig. 4.34). The values in Figure 4.34 appear to confirm the assumption of a shallow-saucer shaped deformation bowl. Equation 5.3 describes the curve fitted through the median deformation rate over deformation factor values.

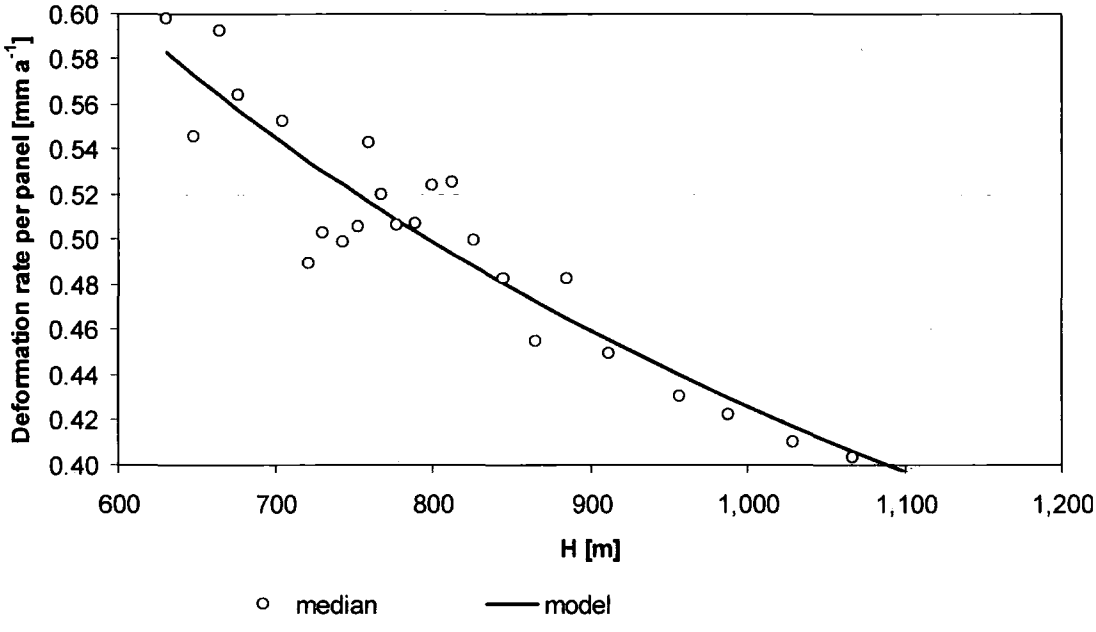

Figure 4.34: Deformation rate [mm a -1] over average horizontal distance [m], medians from levelling dataset, with fitted curve.

The R^2 value for this function is 0.84. and the p-value<0.01.

Equation 4.4: $$\frac{1}{1.71 \cdot 10^{-3} \times H_d + 6.34}$$

Where:

H_d is the horizontal distance between mine unit and surface station per d

The second hypothesis considers the distance between a mine panel and the mine panels that surround it, or the amount of clustering inside the zone of disturbance. To quantify the effect of other mine panels, the average distance between mine panels is plotted against the deformation rate. New circles are drawn around each mine panel that equal the size of

a zone of disturbance. This new circle is used to select the mine panels that could have an effect on the mine panel in question (Fig. 4.35).

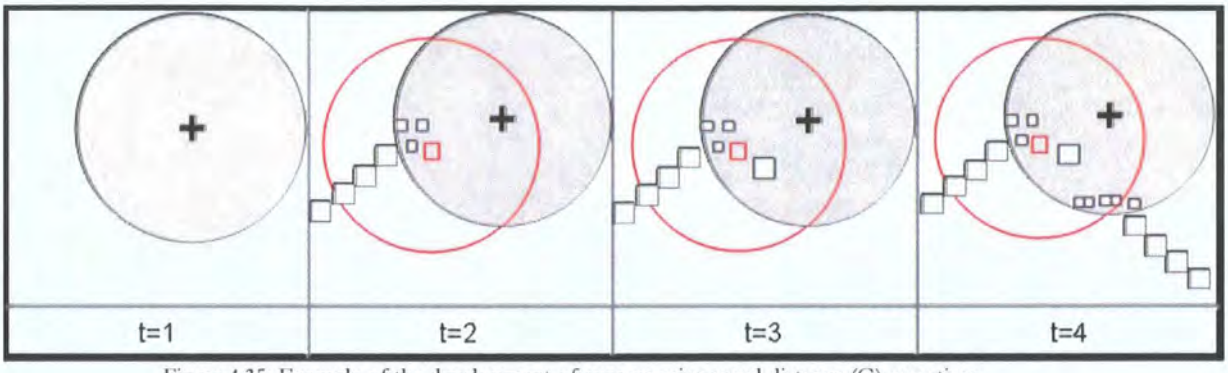

Figure 4.35: Example of the development of average mine panel distance (G) over time.

If the red mine panel is considered, the average distance to other mine panels equals the average distance to the mine panels that are in the red circle. This can include mine panels that are outside the zone of influence. In the first circle, the value equals the radius although no mine panels are inside the zone of disturbance. At time two, the mine panels are somewhat clustered, which will result in a low average distance value for each mine panel. This clustering is even more at time three, where another large mine panel is built close to the red mine panel.

However, at time four the value for the average distance between mine panels will increase, due to the construction of new mine panel away from the red mine panel. Although it is likely that these new mine panels increase the amount of deformation rate, the hypothesis is that this increase would have been more if the mine panels were built closer to the existing mine panels. In Figure 4.36 the total average distance between mine panels for all mine panels in the zone of disturbance is plotted against the rate of deformation (Fig. 4.36).

The trend in this plot is unclear and again a summary is made per bin. The number of values in each bin is approximately 155. The summarised values are the deformation rate and the average distance to near mine panels that equal the medians of 155 values (Fig. 4.37).

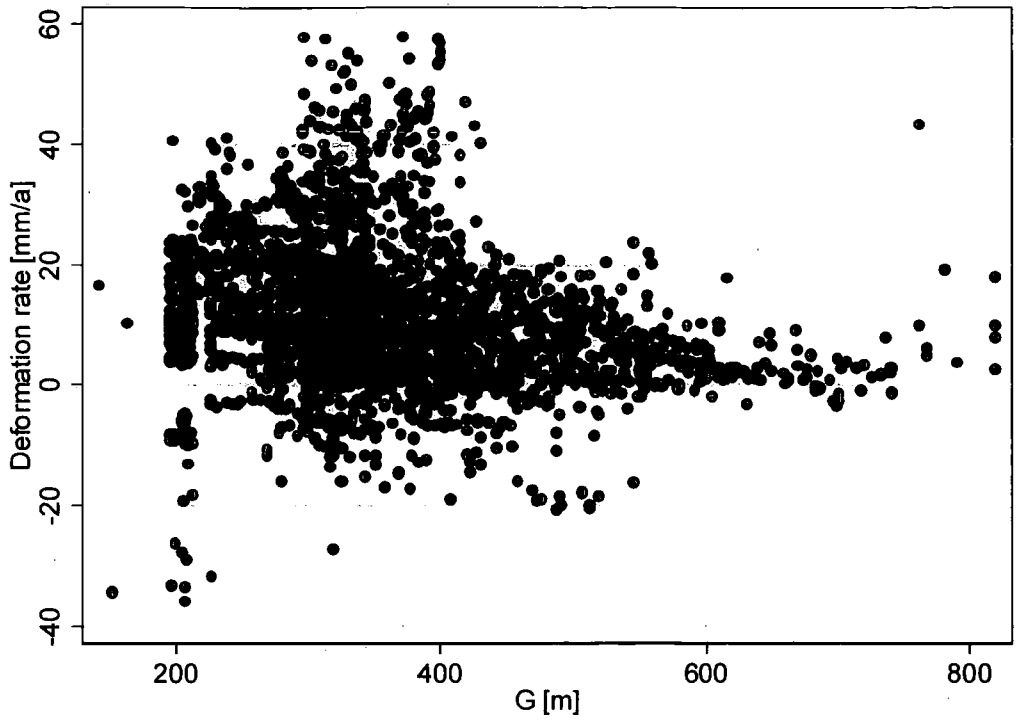

Figure 4.36: Deformation rate [mm a $^{-1}$] plotted against average distance between mine panels [m2]

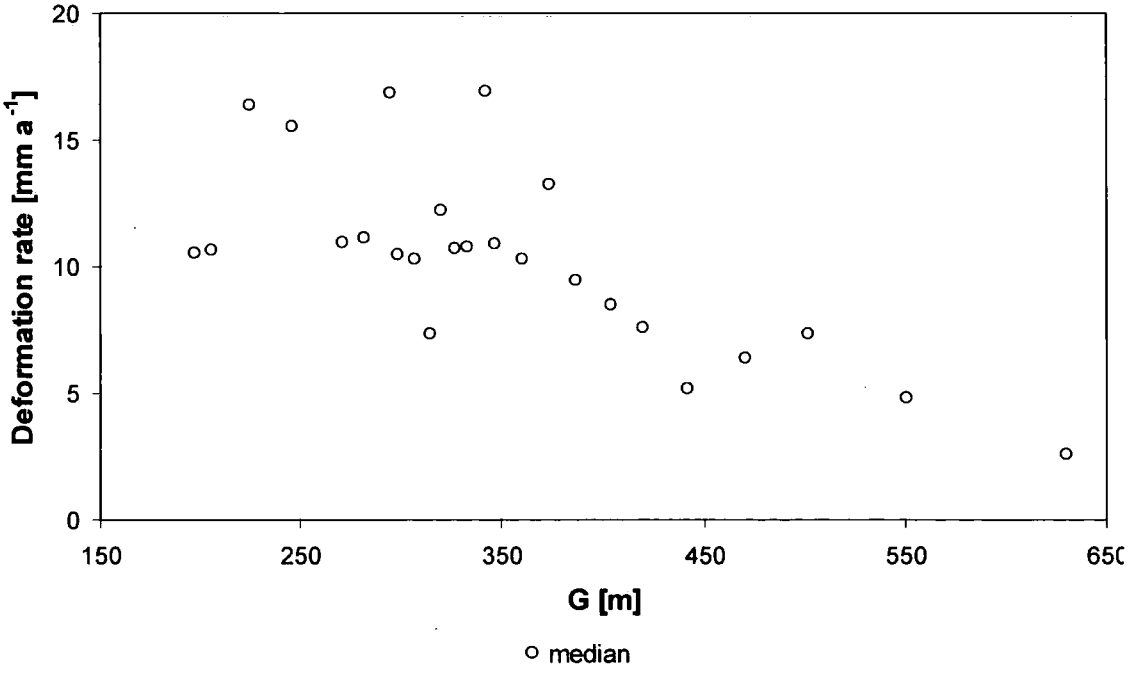

Figure 4.37: Deformation rate [mm a $^{-1}$] plotted against average distance between mine panels [m2], using medians

This time only a weak trend is found. However, it is clear that mine panel that are clustered and constructed near other mine panels will cause a relatively higher rate of deformation than mine panels constructed away from existing mine panels. If the mine panels that are

located in the zone of disturbance are well distributed they cause relatively less deformation. If the mine panels are clustered, the relative deformation rate will be higher.

From the graph the deformation appears to be higher if the distribution is less evenly distributed and the mean distance between mine units and the surrounding mine units becomes larger (Fig. 4.38).

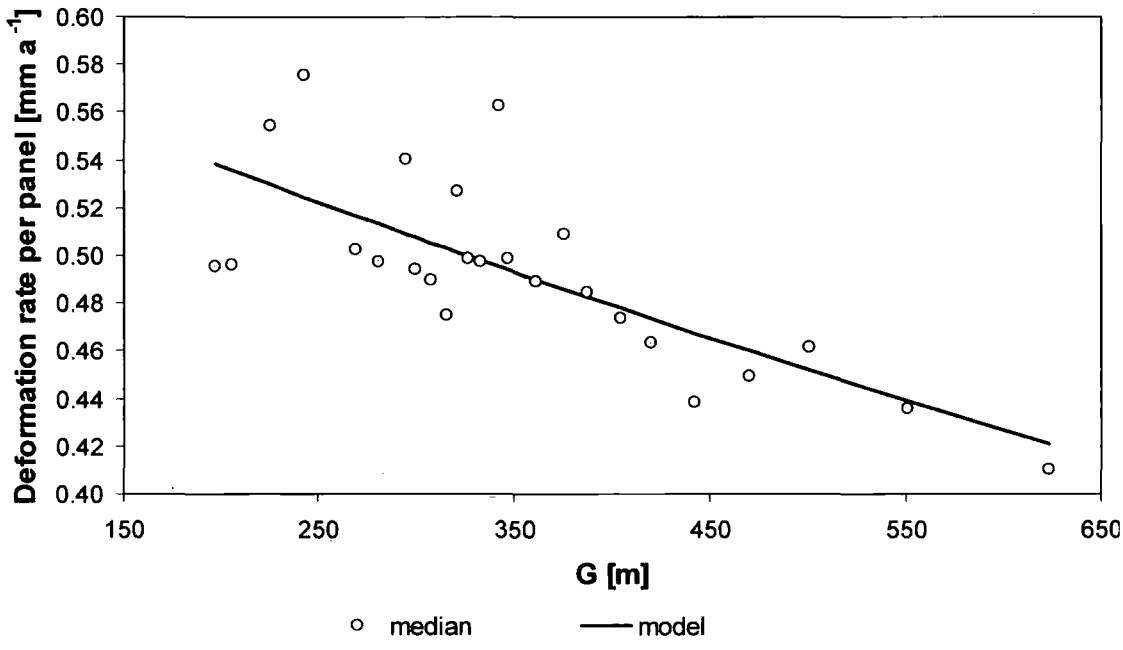

Figure 4.38: Deformation rate [mm a $^{-1}$] over distribution factor [%], medians from levelling dataset, with fitted curve.

Equation 4.5 describes the curve fitted through the median deformation rate over deformation factor values. The R^2 value for this function is 0.79 and the p-value<0.01.

Equation 4.5: $6.04 \times e^{-5.78 \cdot 10^{-4} \times G_d}$

Where:

G_d is the horizontal distance between mine unit and gravitational centre of surrounding mine units per d

4.3.5.4. Temporal distribution

The temporal progression of excavation activities in mining is often a gradual process in which excavation units are opened next to recently abandoned units. This stepwise expansion of excavation activities is seen in the Boulby mine (Fig. 3.26 and 3.28). The effect of an excavation unit on the surface unit forms a profile over time (Rees et al.). This profile will continue to develop when a second excavation unit is opened next to the first.

According to the influence function principle of equivalence, the profiles of the two units develop identically and are not affected by each other.

The expected temporal behaviour of deformation after mining has taken place is often described by three main characteristics. The first is the peak deformation rate occurring at a relatively short time after mining has taken place. The second is the gradual decline in deformation rate approaching a stable situation at relatively long time after mining has taken place (CPL, 1999). And finally the third characteristic is the total recovery period, or the amount of time after mining it takes for an area to re-establish a stable situation.

To examine the influence of the time that has elapsed after mining, initially the average time for all selected mine panels was considered as an independent variable. In a later stage the variable time is considered as a variable influencing the impact of each independent variable in the final regression function to estimate deformation. This means that over time the impact of each mine panel on the measured deformation rate varies. The impact of the amount of excavated material and the location and distribution of the excavations changes over time. However, to determine the extent of the variation of these variables over time, the initial analysis of time as an independent variable was used.

This variable was quantified as the average time between the starting date of the selected mine panels and the time of measurement. The selected mine panels are the mine panels that fall inside the cone shaped area at the time of measurement. Also this variable can increase and decrease over time and depends on the appearance of new mine panels in the cone shaped area. In Figure 4.39 four situations are drawn of one selected survey station at four moments in time.

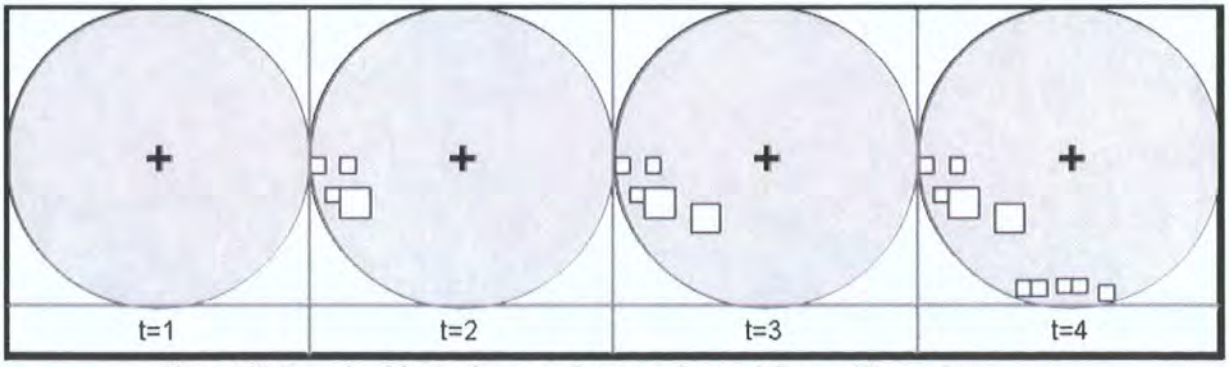

Figure 4.39: Example of the development of average mine panel distance (G) over time.

In the above situation at time one, the average number of days between mining and measuring will be zero, as mining activities have not yet started. At time two, mine panel

were constructed at some point between time one and two. The period between time one and two can be one year and the mine panels can have been constructed over a period of four months at the end of this year. The average number of days difference will be low. At time three, which may be one year later, the number of days will have increased with 365 days but may have been reduced by the construction of new mine panel at some point in the last year. At time four again a year has passed, and the number of days difference will have been increased for the old panels, but will have been reduced due to the construction of new panels. Plotting the deformation rate against the difference in days gives a point-cloud graph (Fig. 4.40).

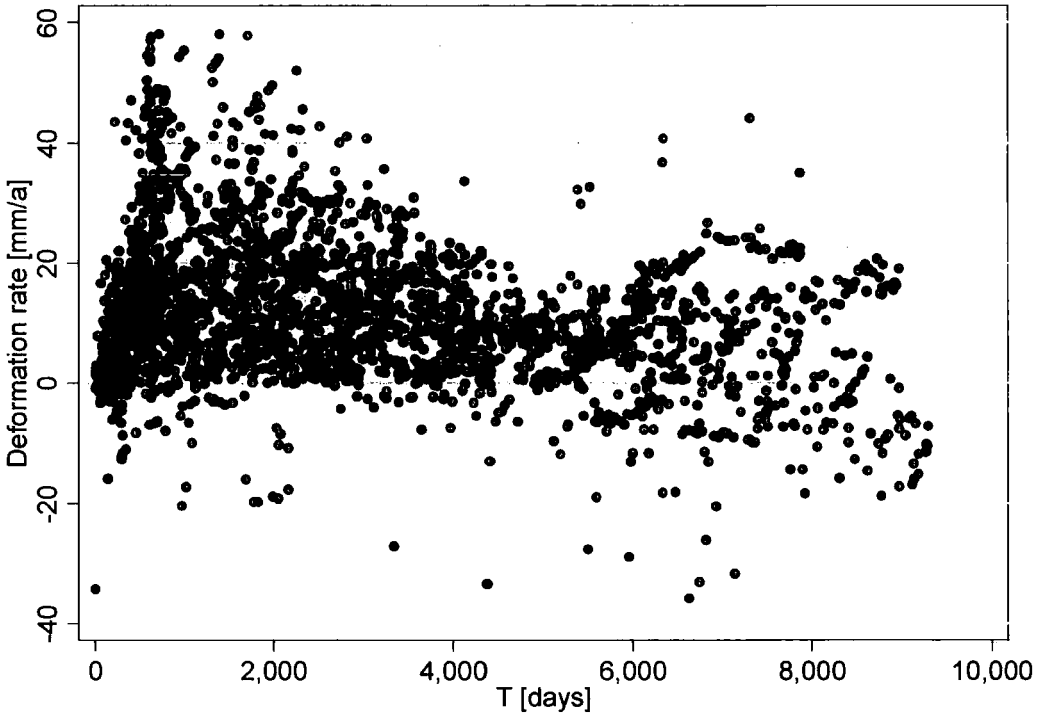

Figure 4.40: Deformation rate [mm a $^{-1}$] plotted against average time difference between mining and measuring [m2]

The trend in this plot is unclear and again a summary is made per bin. The number of values in each bin is approximately 155. The summarised values are the deformation rate and the average time difference that equal the medians of 155 values (Fig. 4.41).

This time, a trend can be seen in the relationship between time difference and deformation rate. A certain peak value is formed roughly between one and two thousand days (2.7 and 5.5 years), where the maximum rate takes place after which gradually decreases over time. Equation 4.6 describes the curve fitted through the median deformation rate over deformation factor values (Fig. 4.42).

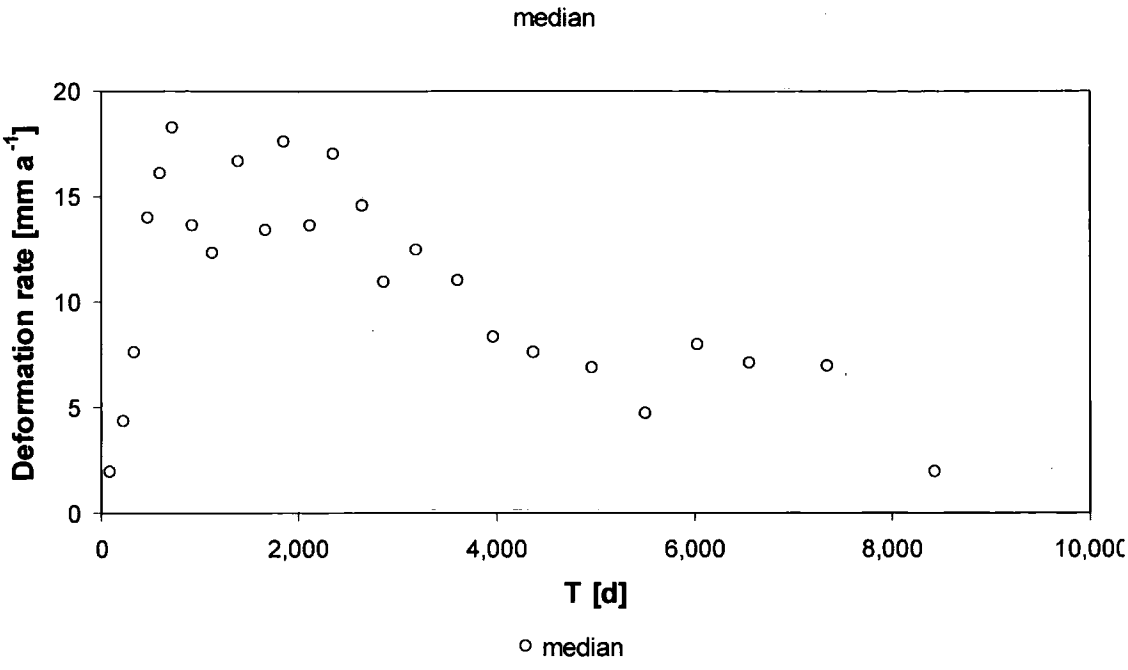

Figure 4.41: Deformation rate [mm a $^{-1}$] plotted against average time difference between mining and measuring [m2], using medians.

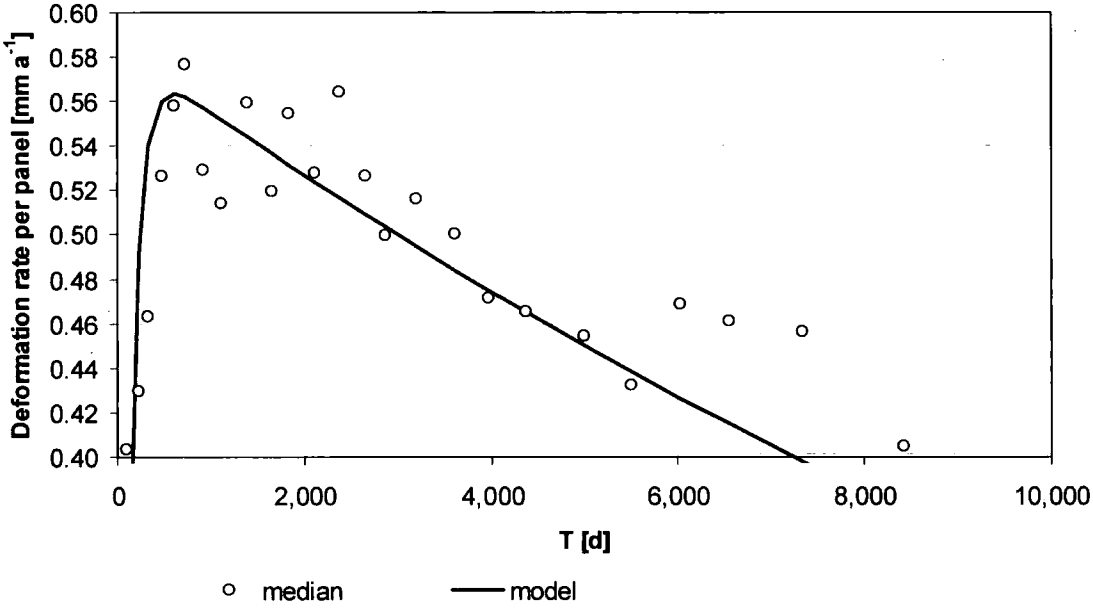

Figure 4.42: Deformation rate [mm a $^{-1}$] over distribution factor [%], medians from levelling dataset, with fitted curve.

The R^2 value for this function is 0.87 and the p-value<0.01. A peak in deformation is found 608 days or 20 months after mining. After this peak the deformation rate gradually decreases. Based on equation 4.4, deformation caused by one mine panel will range between 0.4 and 0.57 mm a^{-1}. If the curve is extrapolated, the deformation rate will cross the zero after 274 years. This value is likely to be an overestimation, but based on the

existing data a best estimate. In reality it is more likely that the deformation rate will gradually reach a stable state. This will be discussed in chapters five and six.

Equation 4.6: $-5.86 \times \left(e^{-8.39 \cdot 10^{-3} \times T_d} - e^{-5.27 \cdot 10^{-5} \times T_d}\right)$

Where:

T_d is the time difference between starting date of mine unit and measurement date of surface station per *d*.

4.4. Conclusion

In this chapter the methodology used to test InSAR and to develop a data driven deformation model in the Boulby research area is described. Increasing scientific interest and progress in the development of techniques have led to a large variety of InSAR applications. Until recently, it has been assumed that InSAR applications were limited to urban areas, as a consequence of coherence loss in rural areas (Kampes, 2006; Strozzi et al., 1999). In this research, methods have been tested to extract useful information from low quality interferograms. As described in chapters two and three, conditions found in the Boulby area are not ideal for the use of InSAR.

The spatial resolution of the Boulby levelling dataset is 13.5 survey points per km^2 of undermined area and the temporal resolution is 0.56 survey measurements per station per year. In contrast, radar scenes from the European Space Agency (ESA) have a potential spatial resolution of 12500 measurement points per km^2 and a potential temporal resolution of 10.4 measurements per point per year. More important than the number of observations is the spatial and temporal distribution of observations.

Testing of conventional InSAR both with a commercially available 'off-the-shelf' and an 'open source' software programme, found that it is impossible to use conventional InSAR to generate a valuable monitoring dataset of a slow deformation process in the area. This was due to high temporal decorrelation and significant topographic and atmospheric distortion. Almost 95 percent of the Boulby area comprises land use suffering from high temporal decorrelation. With conventional DInSAR the majority of the Boulby area is unsuitable for unwrapping at temporal baselines of 75 days or more. The estimated deformation values in small patches ranged between 13 mm a^{-1} and 15 mm a^{-1} in areas where the deformation was approximately 5 mm a^{-1} according to the levelling survey.

During the analysis as described above, some difficulties where encountered. Co-registration failed in the case of two data scenes, most probably because Delft orbits were not available. The 2 August 1996 scene and the 28 June 1996 scene had an acquisition date at a period that the ERS-1 spacecraft was operating at an uncontrolled path. This occured in the last days of the tandem mission and Delft has not been able to calculate its precise orbits over that period.

The Atlantis-EV software programme was powerful and suitable to test InSAR. Unfortunately, the software code was not accessible and operates as a black box. Therefore sometimes errors could not be solved and runs would fail due to unknown causes. For research areas with non-ideal characteristics such as the Boulby research area, this software offers great limitations and did not lead to successful dataset generation.

The methodology used in the second stage of the analysis using PSI, was much more successful. Thanks to a more effective way of removing atmospheric and topographic decorrelation, the quality of the interferograms was improved. The use of persistent scatterers proved to be an effective way of avoiding large patches of low coherence values, making unwrapping of the high value pixels impossible. Objects that can be persistent scatterers are artificial or bare structures, such as buildings or coastal defence walls. Buildings are partly clustered in villages but farm houses are evenly distributed based on farm sizes. In Western Europe, even sparsely populated rural areas such as the Boulby area contain a considerable number of evenly distributed farm houses.

Despite a promising outcome from the PSI analysis, the distribution of the PS monitoring points was limited. Consequently, the development of the data-driven model was based on a subset of the levelling data. By examining the behaviour of the median ground surface deformation value over the bins of each variable, the influence of outliers has been minimised. The outliers can occur as a result of errors in data collection or processing; poor data coverage; inadequate data density; or they can represent other ground surface deformation processes not considered in this analysis.

The cone method has been demonstrated to be a useful approach for the organisation of the data and has allowed the determination of correlations between the input variables and the ground surface deformation. By interpolation of the estimations, maps can be created showing the behaviour of ground surface deformation as a consequence of mining activities.

Four input variables have been selected for this model based on data availability, coverage, consistency, and influence in the regression analysis. These are mined area (A), horizontal distance between the mining panel and the survey point (H), spread of the mining panels within the zone of influence (G) and time after mining panel extraction (T).

An important finding on the spatial behaviour of ground surface deformation in the Boulby area is the angle of draw of approximately 45°. This Figure, which suggests that a mining panel at a depth of 1000 m will cause a zone of disturbance with a horizontal radius of 1000 m, is an essential tool for future mine planning. The behaviour of ground surface deformation rate over time seems to reach a peak, approximately 20 months after mining, after which the deformation rate declines almost linearly over time. The trends found in the individual variables were used to generate algorithms to estimate deformation based on the excavation dynamics. The result of these algorithms summarised per zone of influence, will be discussed in the next chapter.

CHAPTER 5. RESULTS

"Not everything that can be counted counts, and not everything that counts can be counted." (Albert Einstein)

5.1. Introduction

The gradual local ground surface deformation process in the Boulby research area has been monitored using ground-based and space-borne techniques. The dynamics of the mining activities that have taken place over the last thirty years and continue today have been linked to this deformation process based on the ground-based levelling dataset. Four main variables were found to show clear correlation with the measured deformation values. These are the total undermined area, the average horizontal distance, the proximity of other mine panels and the time difference between mining and measuring. To enable the estimation of future rates of deformation and the five key indicators determined in chapter two, these variables are used in a multivariate regression analysis integrated with the cone model tool.

An independent deformation dataset has been generated based on information derived from space-borne radar scenes of the same area using the Persistent Scatterer InSAR technique. In this chapter the results from both the data-driven modelling analysis and the InSAR analysis are presented and compared to each other.

5.2. Results of the PSI analysis

The results of the PSI analysis steps, described in chapter four is a dataset with 29 elevation measurements at persistent scatterer points in the Boulby research area. In this research space borne C-band radar was used, operating at a height of approximately 800 kilometres above the Earths' surface at a wavelength of 5.6 mm, collected by the imaging radar sensor on board the ERS1 and ERS2 satellites both from the European Space Agency (ESA).

Initially the selection of radar scenes was an essential step in the analysis in order to limit the temporal and geometric decorrelation and to increase the chance of a high quantity of reliable measurements from the conventional InSAR (chapter four). In Figure 5.1 the baselines of the scenes selected for this research are plotted.

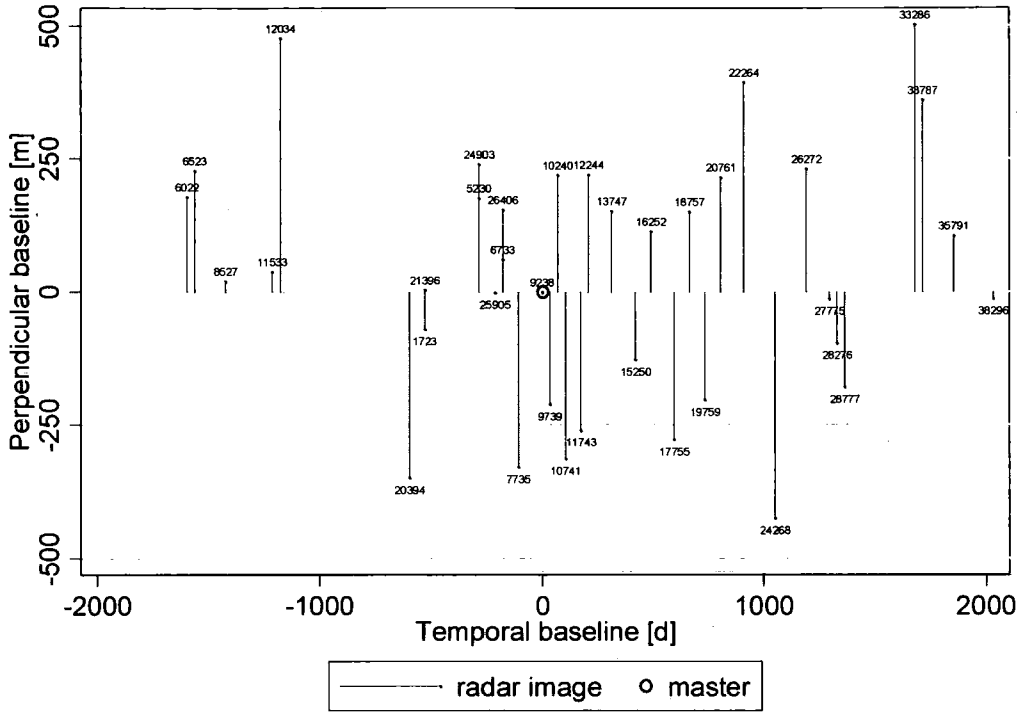

Figure 5.1: Baseline plot of the used radar scenes, showing the temporal and spatial (perpendicular) baseline relative to the master scene for each scene. The label represents the orbit number of the scene.

The selected master scene is the scene registered on 25 January 1997 with orbit number 09238. The selection of the initial thirteen scenes was based on their relative baselines to this master scene, and the recommended maximum perpendicular baseline is 200 m (Hanssen, 2001). The relationship between the perpendicular and temporal baseline and the coherence in an interferogram is discussed in more detail in chapter six. For the PSI analysis, the baselines were less relevant and all scenes available for the research area were used, exceeding the baseline restrictions of conventional InSAR (Kampes, 2006).

Interferograms derived from coherent multiplicative interferometry are visualisations of the phase difference between two scenes (Goldstein et al., 1985). The colours indicate the relative difference in phase change between neighbouring pixels. Ideally, a rainbow-like pattern is formed by bands of similar colours referred to as interferometric fringes. The transition from one colour to the next corresponds to a step in elevation in slant direction of the radar (Hanssen, 2001). In Figure 5.2 the interferograms for eight of the 29 radar scenes versus the master scene are given, the rest of the interferograms are given in Appendix 4.

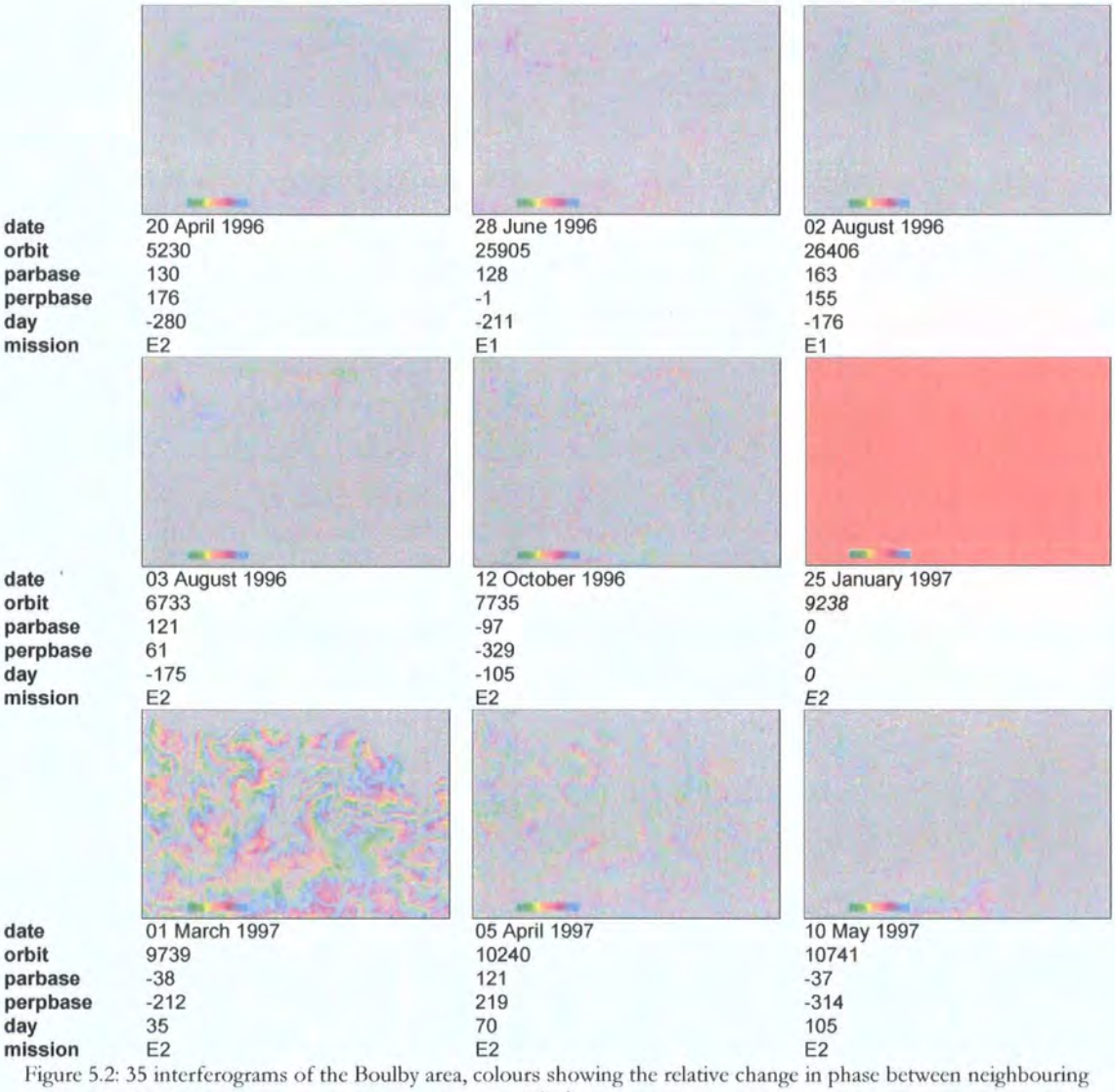

Figure 5.2: 35 interferograms of the Boulby area, colours showing the relative change in phase between neighbouring pixels.

The interferogram resulting from comparing the scene registered on 1 March 1997 to the master scene registered on 25 January 1997 shows a rainbow-like pattern. The other 35 interferograms seem highly decorrelated and show only small patches of smooth patterns at most. To sift useful information on deformation from the vast amount of data collected by imaging radar, a method was used to determine which conditions could lead to the least disturbed signal. This method has led to the selection of persistent scatterer candidates (PSCs) and finally the selection of persistent scatterers (PSs). The persistent scatterers can be used as 'natural' deformation monitoring stations or reflectors were selected using the amplitude dispersion method (Ferretti et al., 2000a; Ferretti et al., 2001).

To determine the persistent scatterer candidates, the radar amplitude scenes are multiplied and pixels showing high amplitude are selected. If the ensemble coherence of such PSC's is found to be consistently high over time, such pixels are selected as PS's (Abernethy, 2000;

Kampes, 2006; Leijen and Hanssen, 2003). The ensemble coherence of all selected PSC's is given in Figure 5.3.

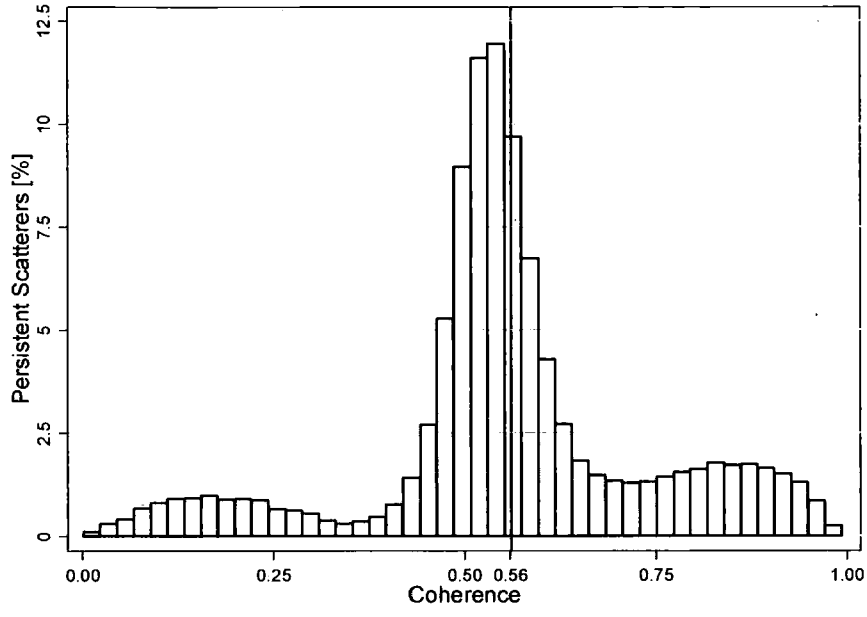

Figure 5.3: Histogram of coherence values of selected PSC's in the Boulby area

The mean ensemble coherence for all PSC's in the Boulby research area is 0.56. The area has a dominantly rural land use, but man made objects such as industrial buildings and farm houses are found around the area and in theory can function as PS's. However, the even if an object should function as a point scatterer, the amount of scattering is not necessarily consistent enough throughout the complete period of observation.

To determine the threshold ensemble coherence value a ground-thruthing process was carried out a method of visually comparing the location of PSC's with objects on an aerial photograph. In Figure 5.4 all PS's with an ensemble coherence of more than 0.7 are plotted.

A correlation between build up areas and PS's can be seen. Man-made objects often display high amplitude values in radar scenes (Hanssen, 2001). The high amplitude pixels with a coherence value higher than 0.7 were plotted on aerial photographs of the Boulby area. Based on visual selection, the PSC's with an ensemble coherence of more than 0.8 were selected.

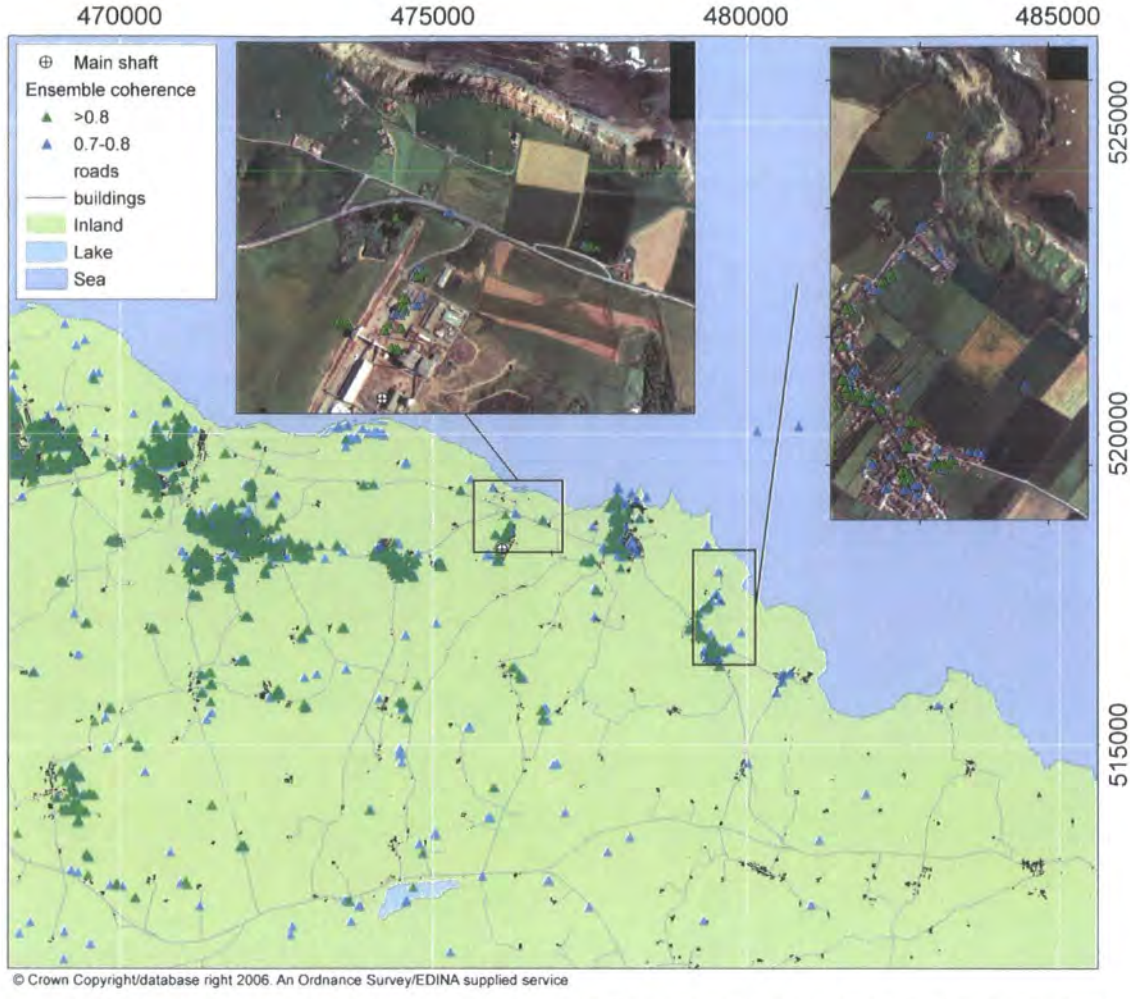

Figure 5.4: Persistent scatterers with an ensemble coherence of 0.7-0.8 in blue and 0.8 or higher plotted on topographical data. Subsets showing the Boulby mine buildings and main shaft with PS's plotted on aerial photographs.

The PS's plotted in Figure 5.4 show a small spatial displacement. This spatial displacement is due to the horizontal inaccuracy inherent to radar observation (Hanssen, 2001). The relative elevation difference between slave scenes and their collective master scene was used to generate a deformation profile over time for each selected PS. The dataset includes the relative elevation change at 1583 persistent scatterers unevenly distributed in the research area (Fig. 5.5) and 29 points in time for a period of 8.6 years. The measurements describe the deformation between 9 September 1992 and 21 October 2000.

For the selected PS's a measurement of elevation relative to the elevation at the registration date of the master scene is given at all registration dates of the used radar scenes. The distribution of the selected PS's is limited and they are clustered around villages in the area. In Figure 5.5, those PS's that are located in the potentially disturbed area, within the 45° angle zone are plotted and classified by cluster.

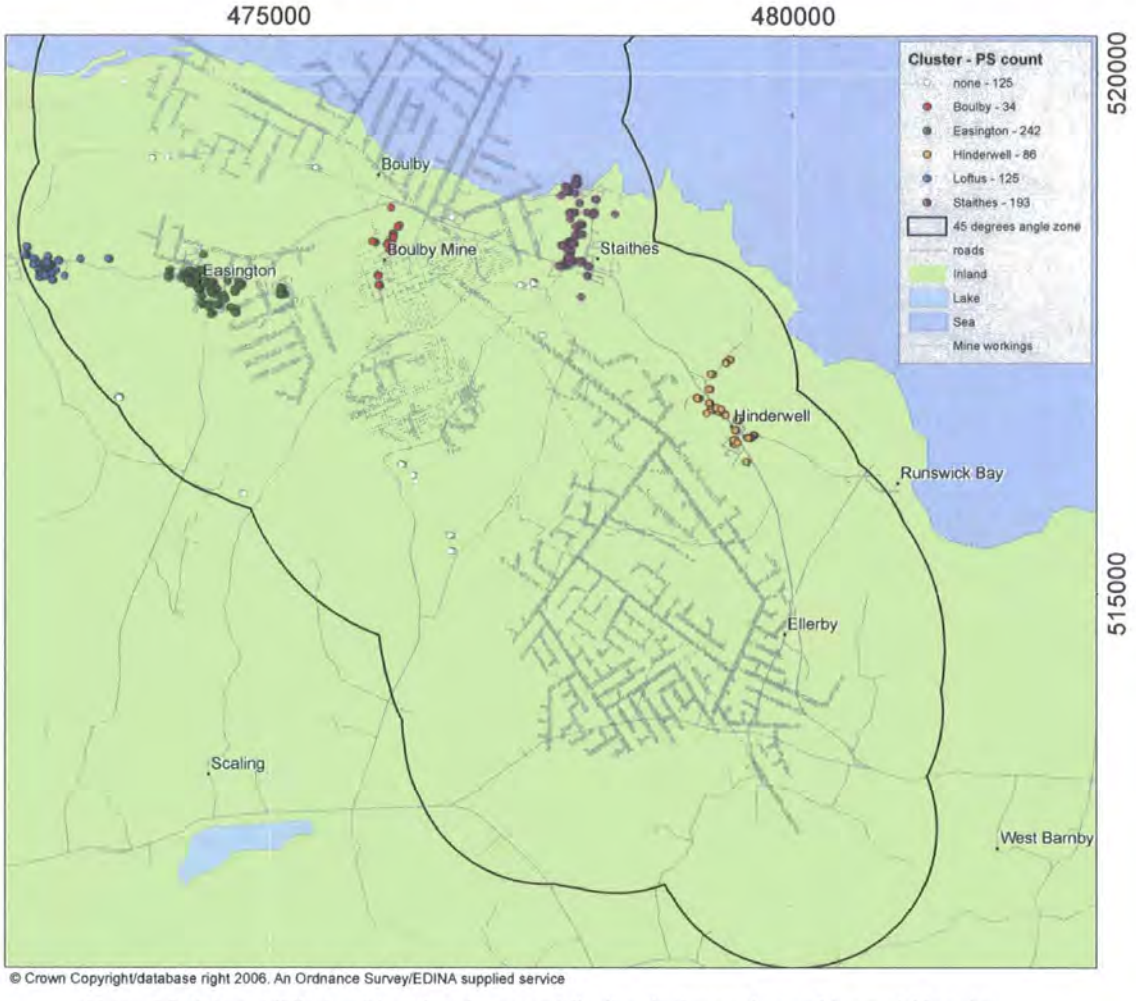

Figure 5.5: Selected PS's that fall within the potentially disturbed area, clustered by spatial location

The large industrial buildings of the Boulby potash mine that are located around the main shaft function as a cluster of 34 PS's. This area has been undermined from the start of the potash mining activities in February 1976. The most recent excavations in that area are dated August 2003. Approximately one kilometre west of the main shaft is the largest group of PS's within the 45° angle zone clustered around Easington (242). This area was actively undermined between January 1979 and May 1986.

Three more clusters are located within the potentially disturbed area, but have not actually been undermined. One is located around Hinderwell (86), where mine panels were constructed within reach between August 1991 and September 2002. Mine panels near Staithes (193) were constructed between September 1983 and December 1988. The final cluster is near Loftus (125), which has not been undermined either but is likely to be affected by the mine panels under Easington. Another 125 PS's are distributed around the

area. The total density of PS's per km^2 is 6.4 while in urban areas this value ranges between 100 and 300 (Colesanti et al., 2003).

The development of the potentially disturbed surface area over time was discussed in chapter three. In the period that was covered by the PSI analysis, the progression of the mine panels took place in the north and south of the mine (Fig. 5.6).

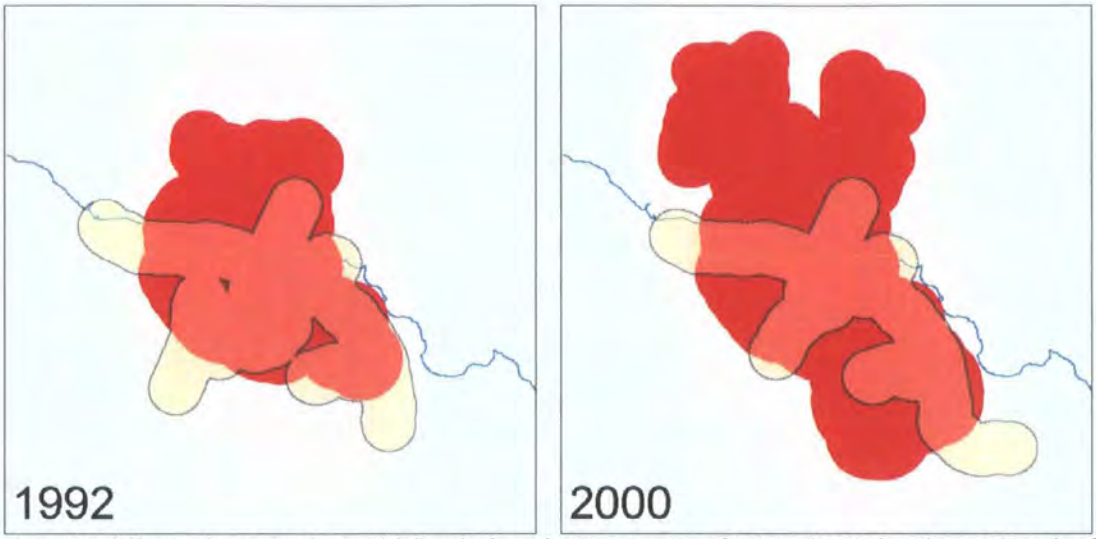

Figure 5.6: difference in extent of potential disturbed area between January of 1992 and 2000, based on a 45° angle of draw around the mine panels.

Deformation profiles over time for the five PS clusters are given in Figure 5.7. Although deformation seems to take place in all five clusters during this period, there is a clear difference in rate and variance per cluster. In the PS cluster around the Boulby main shaft, the mean deformation shows a linear gradual deformation pattern accumulating from zero to 74 millimetres in the monitoring period. In the Easington, Hinderwell, Loftus and Staithes areas the mean value reaches 61, 92, 7 and 61 millimetres respectively. The box represents the window in which all values within the 25^{th} percentile and 75^{th} percentile fall per two-year lag. The whiskers show the reach of adjacent values (all values within 1.5 times the inter-quartile range), while the markers show outliers. Variance is present in the five graphs, indicating variance in deformation in the five locations. The deformation data summarised in the box plots shows there is an uncertainty associated with each of the five PS clusters.

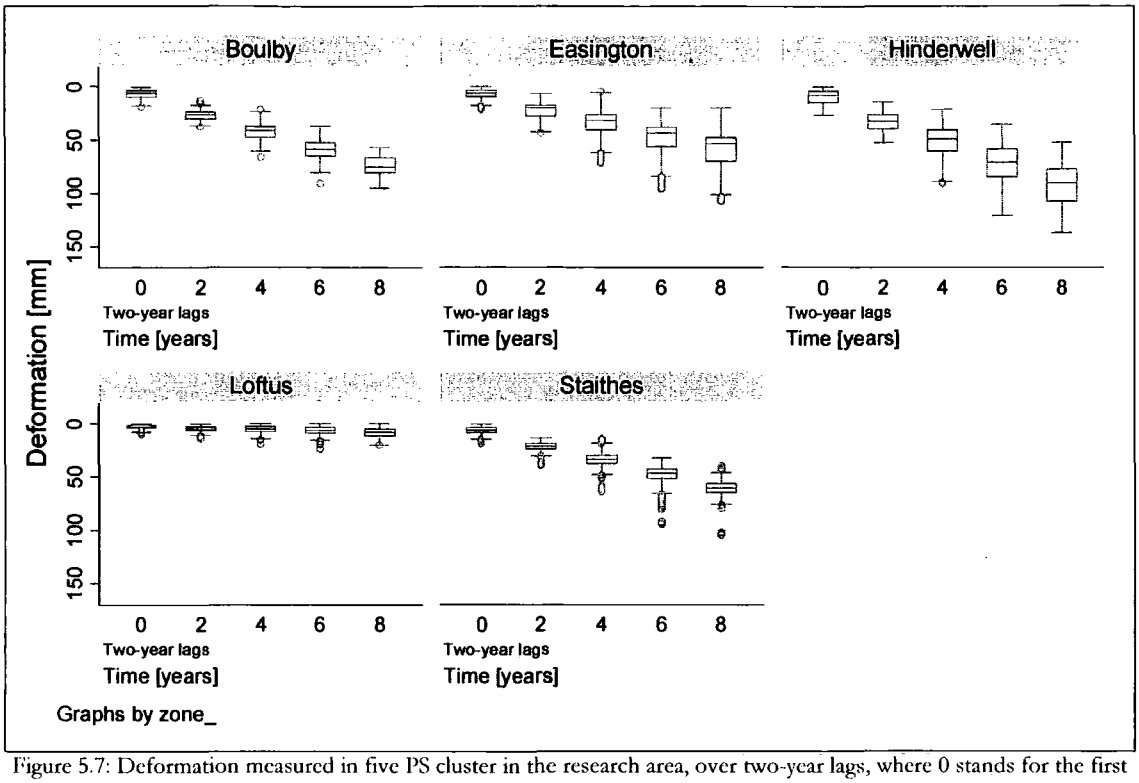

Figure 5.7: Deformation measured in five PS cluster in the research area, over two-year lags, where 0 stands for the first two years of PSI monitoring etc.

Excavation of the Boulby main shaft area started in 1976 and restarted only in 2003. The cluster in Easington is located at the edge of the workings and experiences somewhat lower rates of deformation. This part of the undermined area will have experienced the peak deformation before the PSI monitoring period.

The mean deformation is highest in the Hinderwell area, which is also the cluster with the largest variance. This result corresponds with the development of the mining activities as explained in Figure 5.6. At the start of the PSI monitoring area, deformation was already taking place at a steady rate in Easington and Boulby and to a lesser extent in the Loftus area. In the Hinderwell area, no deformation was taking place followed by the peak deformation wave progressing through the area, reflected in the high variance and large total mean deformation.

The Loftus area has not been included in the annual levelling survey carried out by CPL to monitor the deformation caused by the potash mine. However, the PSI analysis seems to have detected a small deformation trend in that area. This may be due to the proximity of the mine panels under Easington. An alternative explanation could be the presence of extensive iron mines in that area. This will be discussed in chapter six.

The area around Staithes, has not been undermined and mining has only taken place in the proximity of Staithes till December 1988, approximately four years before the start of the PSI monitoring period. The monitoring data collected during the annual levelling surveys does not suggest this much deformation in this area over this period (Fig. 5.8).

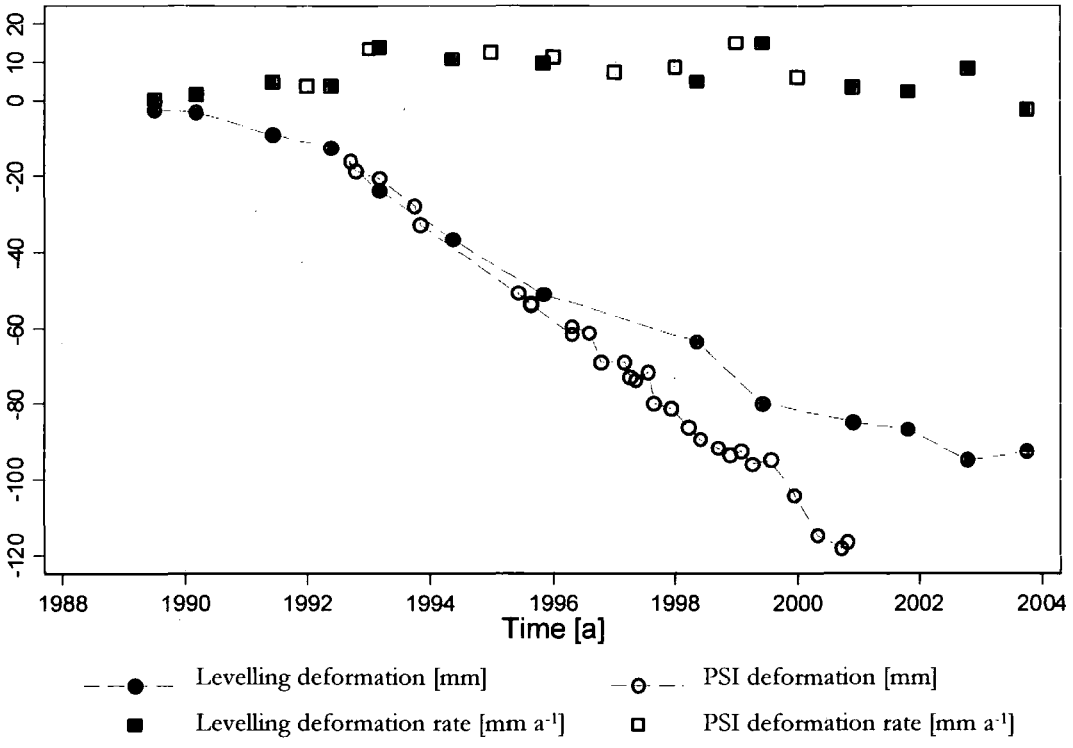

Figure 5.8: Deformation measured with levelling survey in Staithes, data from one monitoring station.

The deformation measured over time seems to show a linear trend in all five clusters. The average deformation rate for the period between 9 September 1992 and 21 October 2000 measured at the PS locations is given in Figure 5.9.

On the map, a cluster of PS's in the area of Hinderwell has deformation values between 10 and 20 mm a-1. This cluster is in an area that is expected to experience peak rates of deformation. In the west side of the Boulby research area, PS's that are at some distance away from the mine workings show no deformation. The reference point used in the PSI analysis is located in the Middlesbrough area further to the west. The area east of the mine workings does not have any selected PS's.

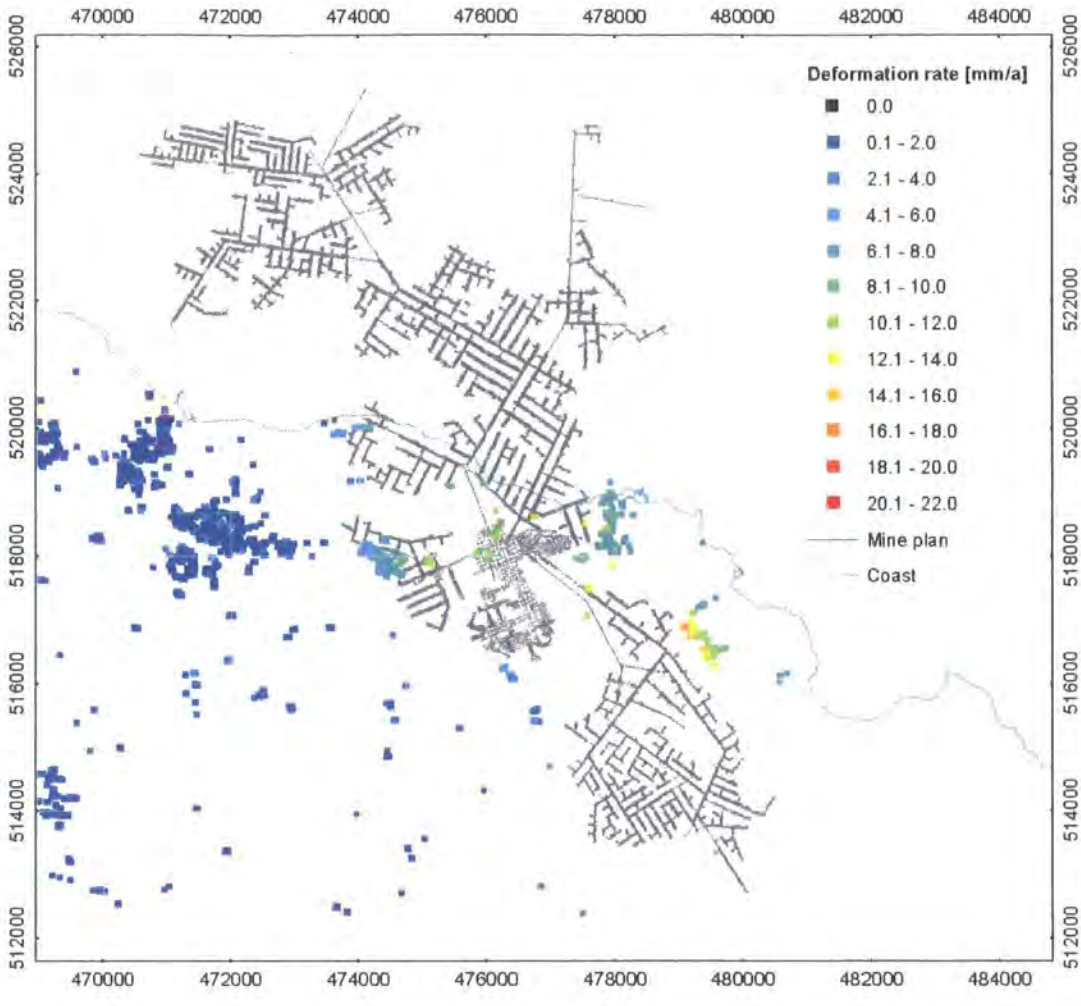

Figure 5.9: Total deformation rate in the Boulby area over 8.6 year interval measured with PSI.

There are some PSC's in the east side of the area (Fig. 5.9), but no PSC's with an ensemble coherence more than 0.8. This is due to the failure to find edges, or network links between PSC's in this area. The maximum spatial distance between two PSC's is one of the parameters set in the PSI analysis. If the distance between PSC's is too low, the unwrapping of the phase difference to determine the atmospheric distortion between two PSC's becomes difficult (Kampes, 2006). The set maximum distance used is 2 km.

5.2.1. Analysis of PSI results

To determine the relationship between excavation and the PSI deformation monitoring dataset, a spatial analysis was carried out. The PS's were used as monitoring stations and used as input for the cone model. First the deformation rate per PS measurement was calculated based on the linear deformation value for each interferogram plus the residual values.

The β-ratio, used to determine the angle of draw in section 4.3.5 was also used to compare the PSI measurements to the levelling measurements. Again, the β-ratio is calculated as a dimensionless ratio of the number of measurements lower than a certain deformation rate as a percentage of the total number of measurements. The PS stations are grouped based on the β angle between PS stations and mine panels. All measurements were divided into thirty equally sized lags. Higher β-ratio percentages indicate a larger percentage of measurements in a certain lag that are under the threshold value (Fig. 5.10).

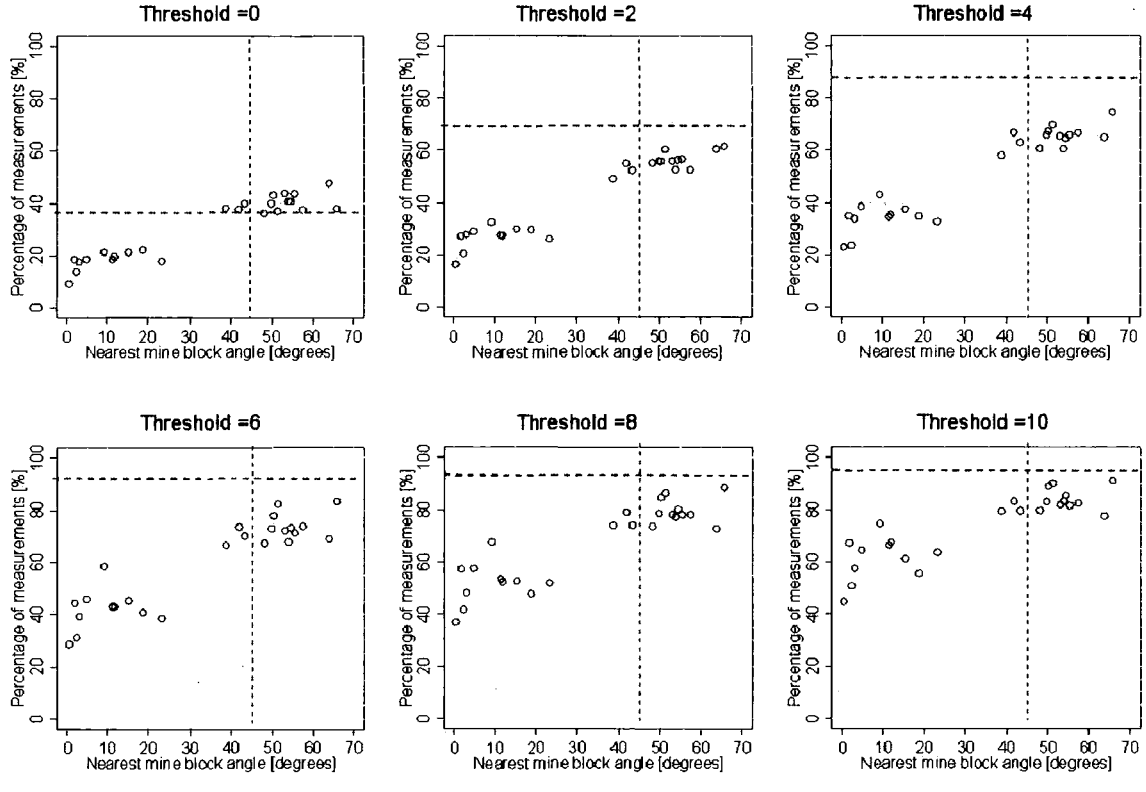

Figure 5.10: The β-ratio plotted over the mean β angle for different threshold values [mm a-1], using the PSI data, the red and blue lines represent the 45° angle and the levelling measurement at that angle respectively.

By plotting the β-ratio for each of the thirty lags over the mean β angle for that lag, an estimate of the angle of draw was made. In Figure 5.10 the β-ratio's for the threshold values 0, 2, 4, 6, 8 and 10 mm a^{-1} are plotted over the β angle. To compare the PSI measurements with the levelling measurements, the β-ratio value at the angle of draw of 45° are indicated with the red and blue lines.

In general, the same pattern is found in the PSI dataset as in the levelling survey dataset. The PSI dataset has a lower percentage of values under the threshold values than the levelling dataset. This is due to the spatial distribution of the PS dataset, which is both clustered in built up areas and includes a much larger area which is not affected by recent

mining activities than the levelling dataset. Relatively, there is a higher percentage of values lower than the threshold if the angle exceeds 40°.

The deformation measured by PSI and levelling is compared in more detail for each PS station cluster, as described above. A total of 34 persistent scatterers are found with a coherence of more than 0.8 in the built up industrial site owned by CPL, which accommodates the main entrance shaft to the underground workings and several on the ground processing plants (Fig. 5.11). The measurements at these 34 PS stations are compared to the measurements at two levelling stations, located in the proximity in Figures 5.10 and 5.12.

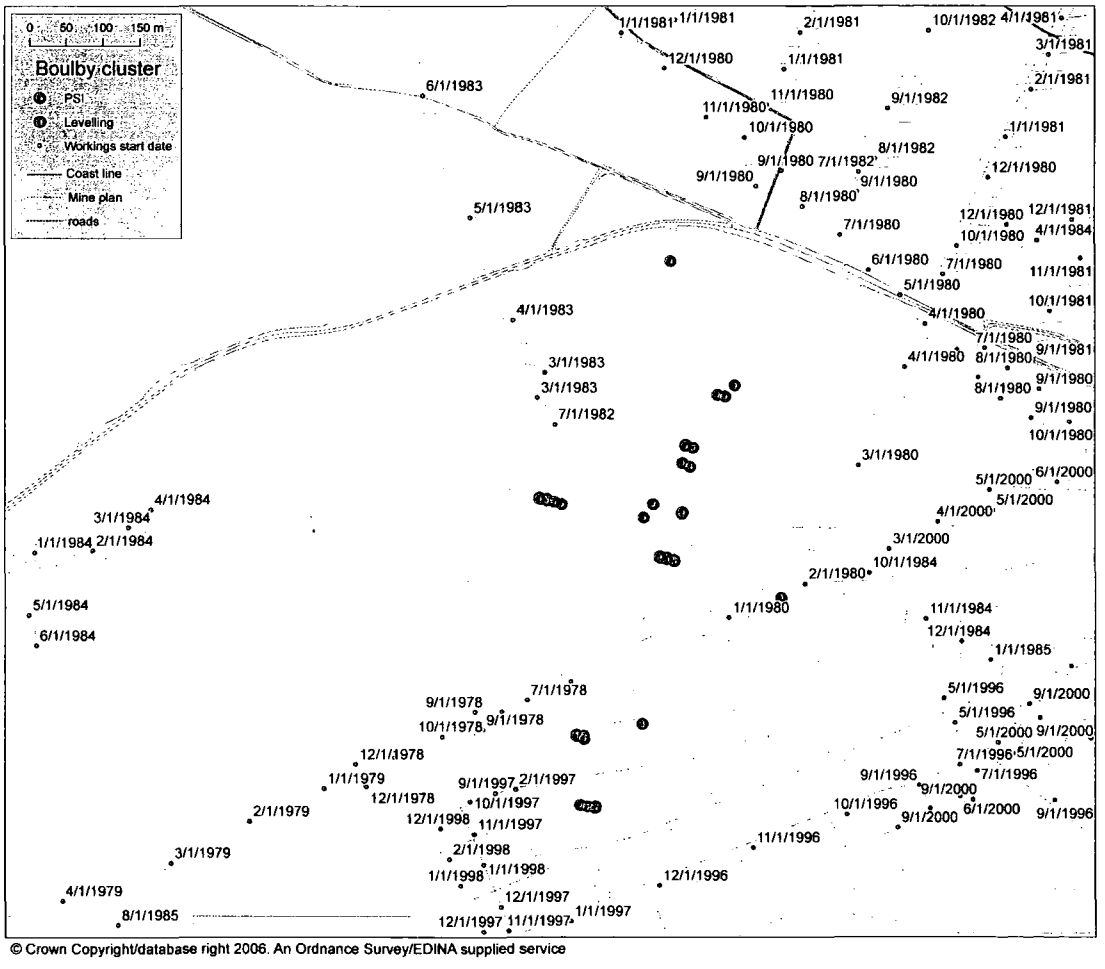

Figure 5.11: Levelling station (red) and PSI (stations) in the PS cluster located around the Boulby mine main shaft.

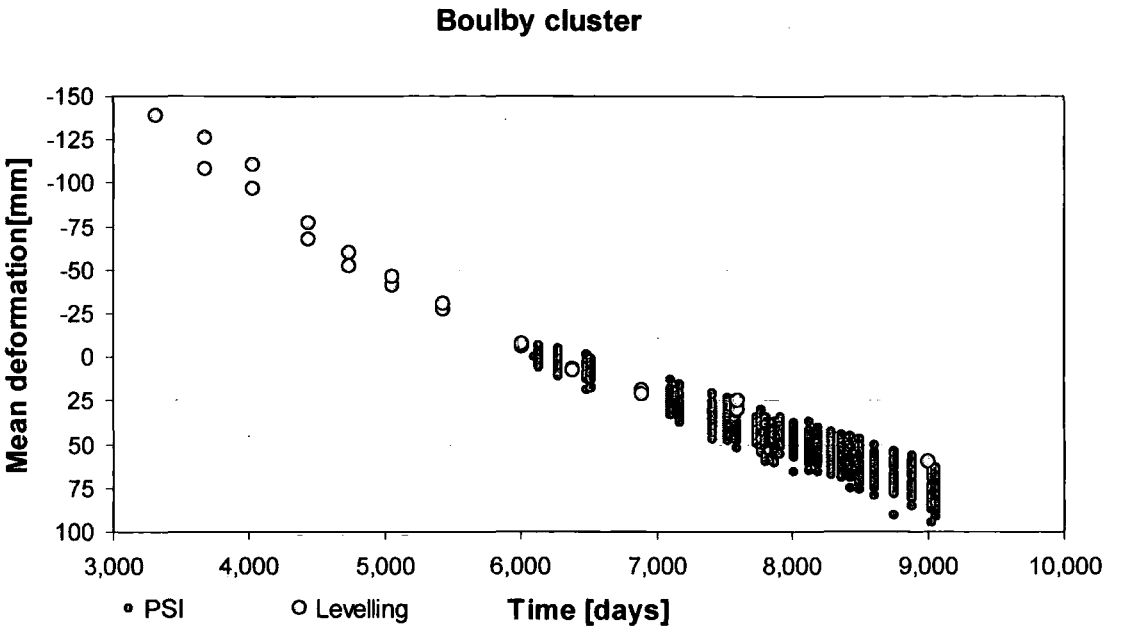

Figure 5.12: Deformation [mm] plotted over time measured by PSI and levelling, around the Boulby mine main shaft.

The mean deformation measured at the PS stations exceeds the deformation measured at the levelling stations. Also, a larger variance between the values found at the 34 stations is found compared to the variance between the two levelling stations. This may be due to the extent of the area covered by the 34 PS stations, which is larger than that of the two levelling stations and may therefore be a genuine variance in deformation pattern found in this area. However, it is also possible that this variance is a sign of the inaccuracy of the PSI measurements. The maximum difference between the maximum deformation value measured by PSI and the maximum deformation value measured by levelling is 35 millimetres.

About two kilometres west of the Boulby main shaft is the village of Easington, which has been undermined in the past for ironstone and is currently undermined by CPL. In Easington a total of 242 persistent scatterers were found (Fig. 5.13). In Figures 5.10 and 5.14 the measurements at these 242 PS stations are compared to the measurements at four levelling stations, located in the proximity.

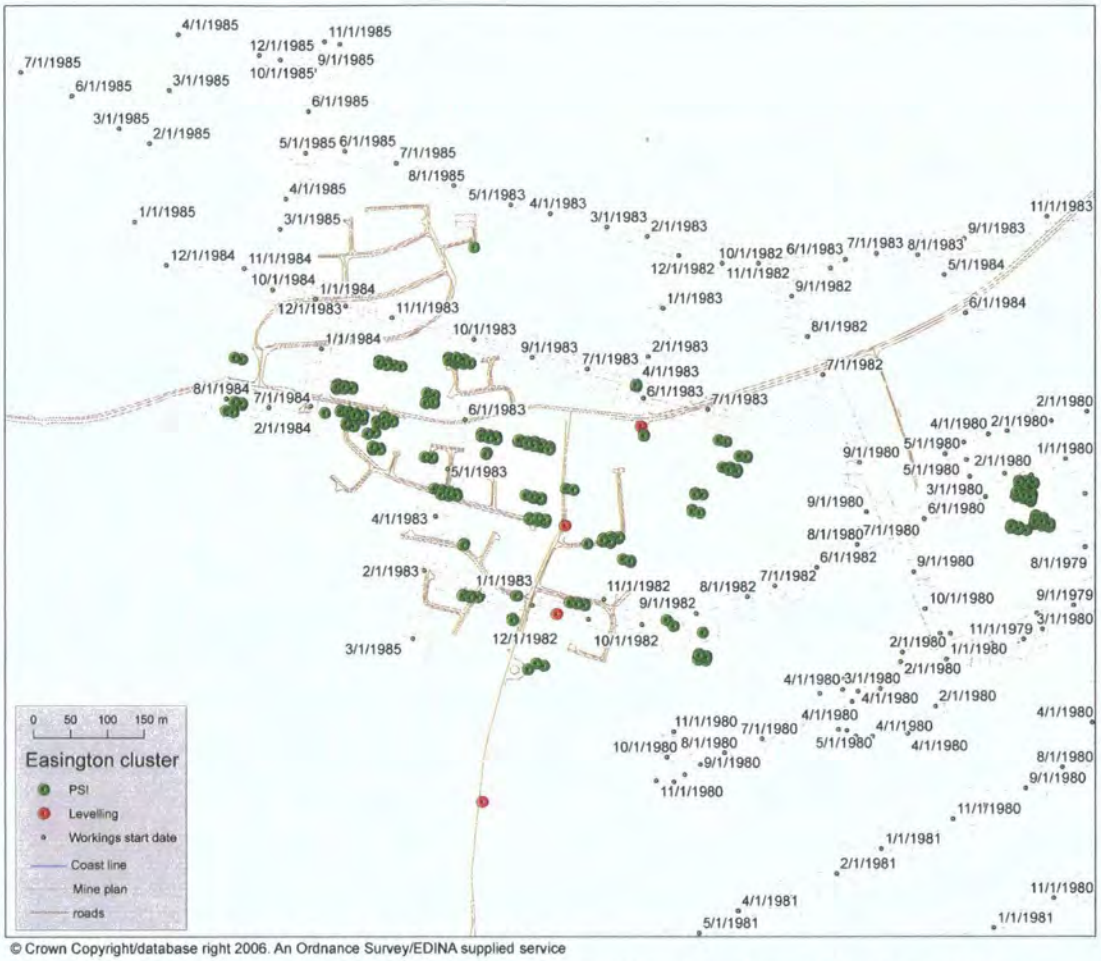

Figure 5.13: Levelling station (red) and PSI (stations) in the PS cluster located around the village of Easington.

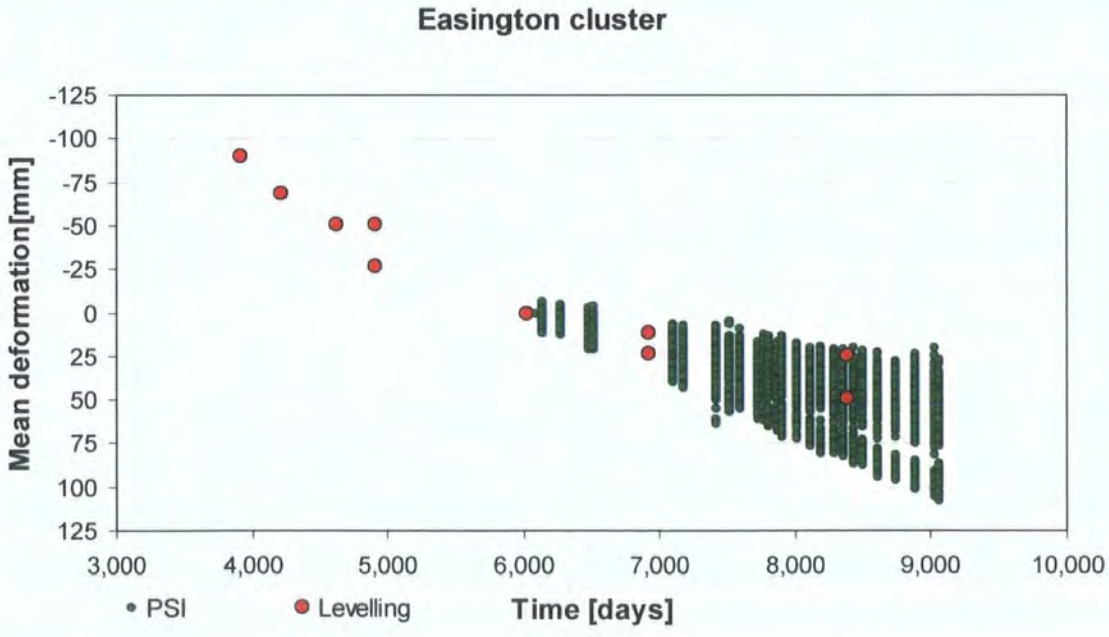

Figure 5.14: Deformation [mm] plotted over time measured by PSI and levelling, around the village of Easington.

Again the mean deformation measured at the PS stations exceeds the deformation measured at the levelling stations. The greater variance found at the 242 PS stations may also be a genuine variance in deformation pattern found in this area or an indication of accuracy loss. The difference between the maximum deformation value measured by PSI and the maximum deformation value measured by levelling is 30 millimetres.

Hinderwell, another village in the research area is located approximately three and a half kilometres south-east of the main shaft. In Hinderwell a total of 86 persistent scatterers were found (Fig. 5.15). In Figures 5.10 and 5.16 the measurements at these 86 PS stations are compared to the measurements at four levelling stations, located in the proximity.

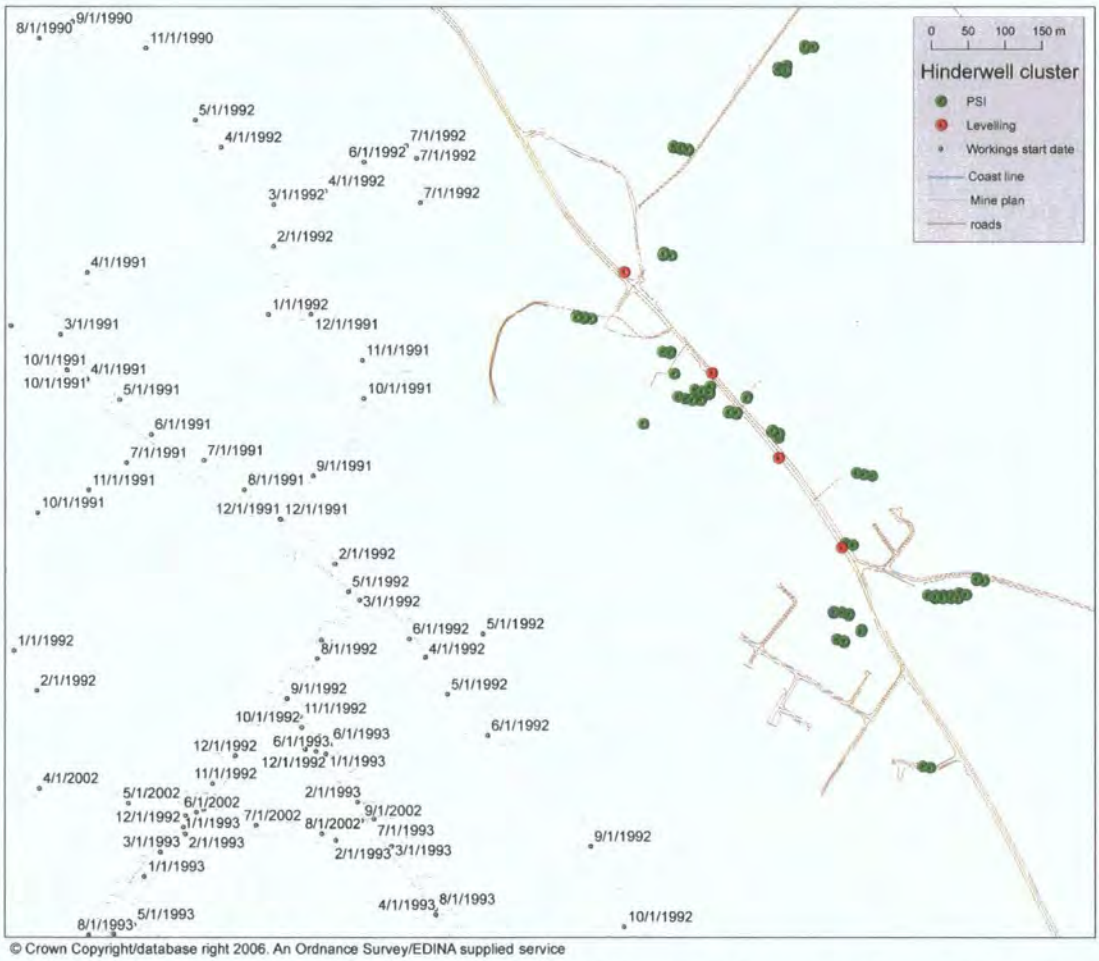

© Crown Copyright/database right 2006. An Ordnance Survey/EDINA supplied service

Figure 5.15: Levelling station (red) and PSI (stations) in the PS cluster located around the village of Hinderwell.

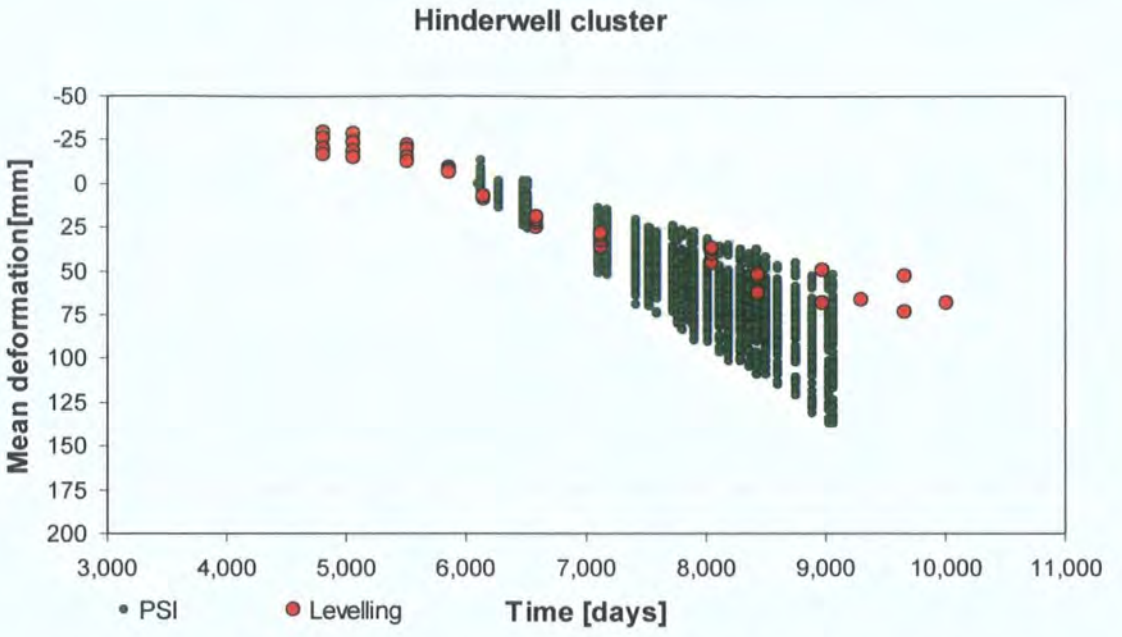

Figure 5.16: Deformation [mm] plotted over time measured by PSI and levelling, around the village of Hinderwell.

In the case of Hinderwell it is clear that the mean deformation measured at the PS stations exceeds the deformation measured at the levelling stations. In this case, it is unlikely that the large variance is evidence of a genuine variance in deformation pattern found in the covered area. The village of Hinderwell is built up in a narrow strip along the main road, which is also used for the levelling surveys. The four levelling stations in Hinderwell have a spatial distribution comparable to that of the 86 persistent scatterers in the area, with an exception of the ten PS stations in the north-east of Hinderwell. The difference between the maximum deformation value measured by PSI and the maximum deformation value measured by levelling is 60 millimetres.

At about one and a half kilometres further west from Easington another cluster of 125 persistent scatterers was found just east of the village of Loftus (Fig 5.17). This area was also undermined for ironstone but is out-with the zone of influence of the CPL potash mine. There are no levelling stations in the Loftus area and the deformation rate is expected to be close to zero and unrelated to the location of the potash mine.

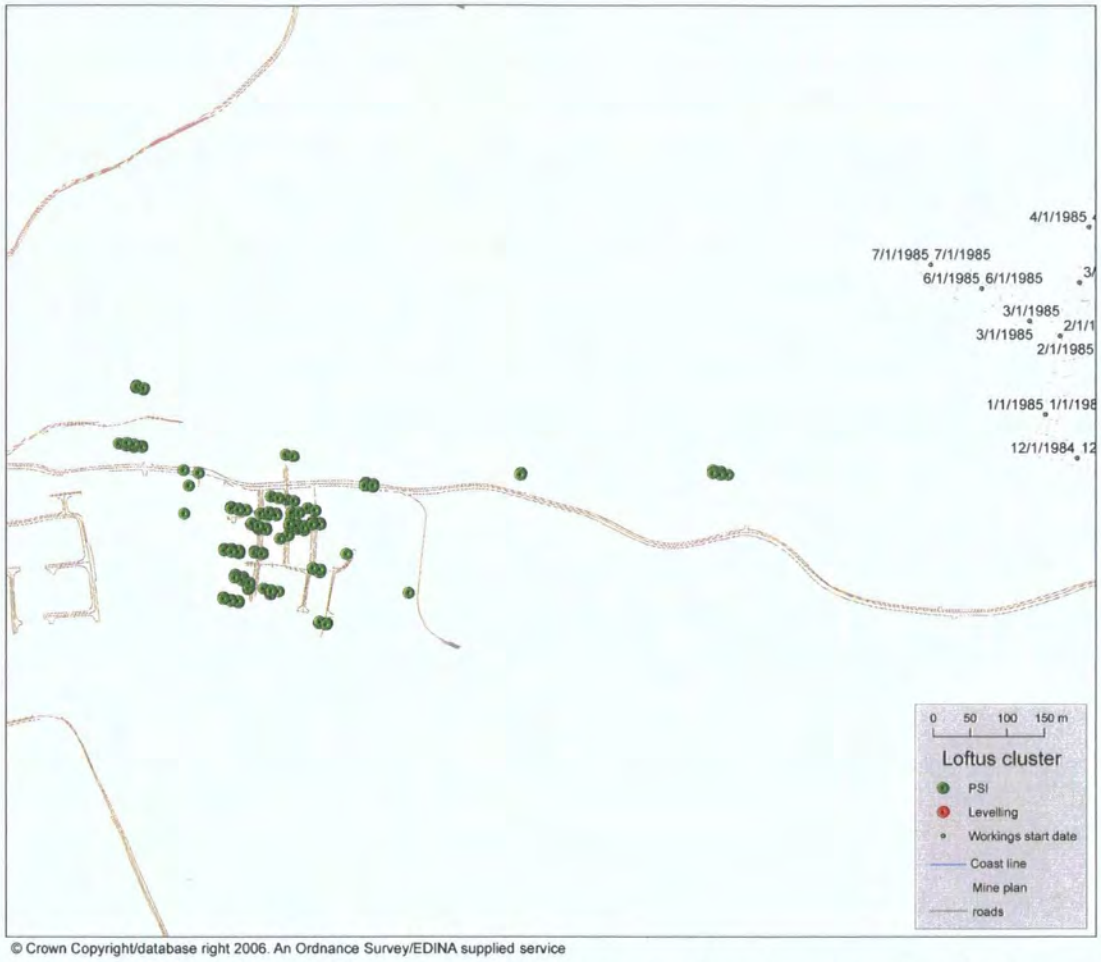

Figure 5.17: Levelling station (red) and PSI (stations) in the PS cluster located east of the village of Loftus.

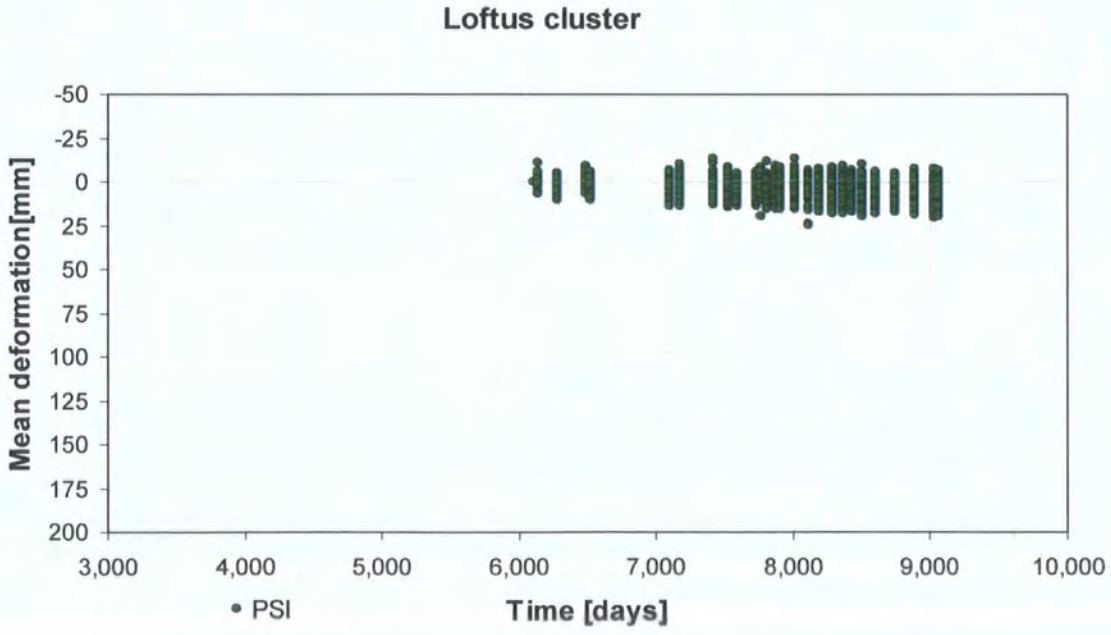

Figure 5.18: Deformation [mm] plotted over time measured by PSI and levelling, east of the village of Loftus.

The deformation measured near Loftus is close to zero, but still demonstrates a variance which ranges from 9 at the second measurement to 32 millimetres at the last day (Fig 5.18). The variance shows a linear relationship with time. This may be an indication of cumulative inaccuracy over time.

The fifth and final cluster of persistent scatterers was found around the harbour and village of Staithes, a seaside resort close to the edge of the CPL potash mine workings (Fig. 5.19). The levelling data from eight levelling stations have shown a gradual deformation in this area. This deformation is compared to the measurements found at 193 PS stations in Figures 5.10 and 5.20.

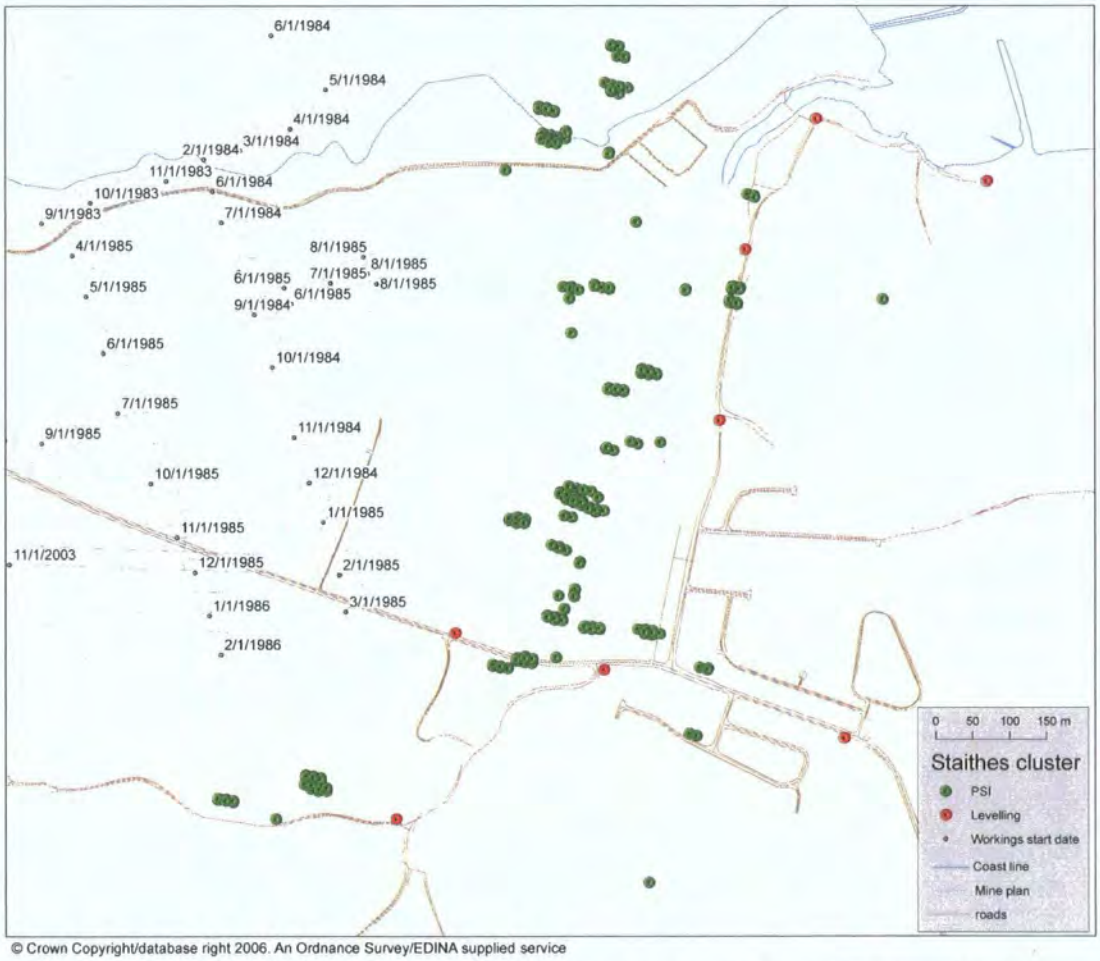

Figure 5.19: Levelling station (red) and PSI (stations) in the PS cluster located around the village of Staithes.

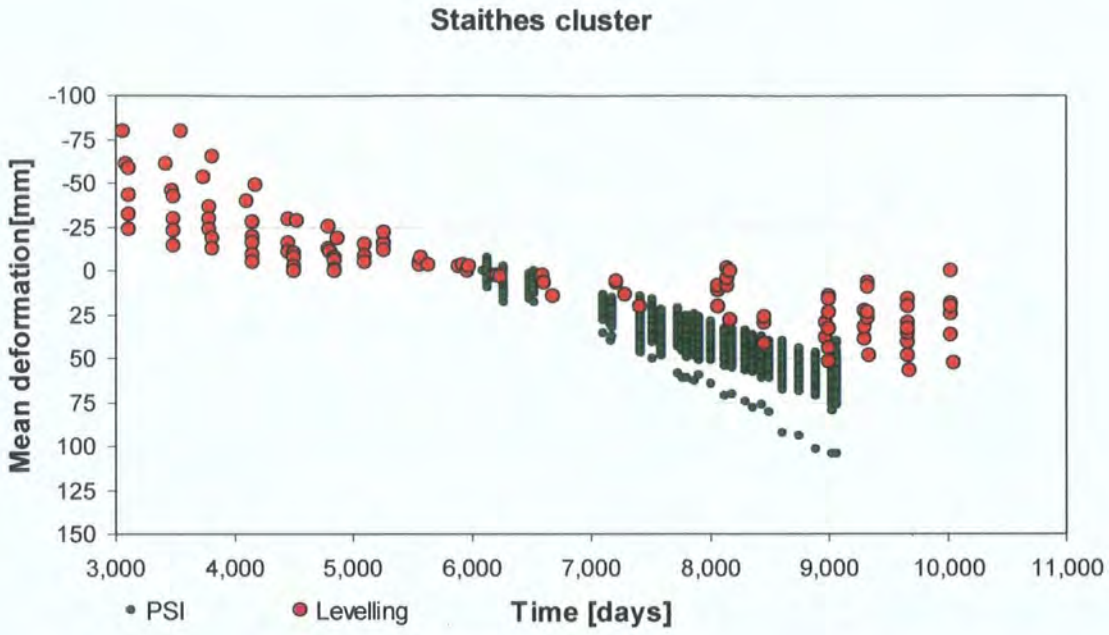

Figure 5.20: Deformation [mm] plotted over time measured by PSI and levelling, around the village of Staithes.

The measurements at the PSI stations around Staithes do not show the same pattern as the measurements at the levelling stations. The variance is comparable and in the range of 50 millimetres for both datasets, which both cover a similar area. The mean deformation in both datasets is hard to compare and indicates a large over-estimation of deformation in the PSI dataset.

5.3. The cone subsidence model

To relate a mine unit located in the potash seam to the surface stations located on the surface, a cone shaped zone of disturbance delimited by the angle of draw (α) and the depth of the mine panel (Fig. 5.21) is applied. The angle of draw has been estimated to be 45° for the Boulby area, based on the β-ratio or the distance between mining activity and the nearest point on the surface approaching zero deformation (chapter four).

The cone delimited by the angle of draw is one of the main principles of the cone subsidence model and is used to explain the correlation between mining activities and ground surface deformation. The correlation between mining activity and surface deformation can be explained by the fact that the pattern of deformation at the surface results from the sum of the disturbances of the excavation units in a certain area. Applying the cone model, the amount of deformation at a surface station is estimated as a function of the mining units falling into a cone at a certain time.

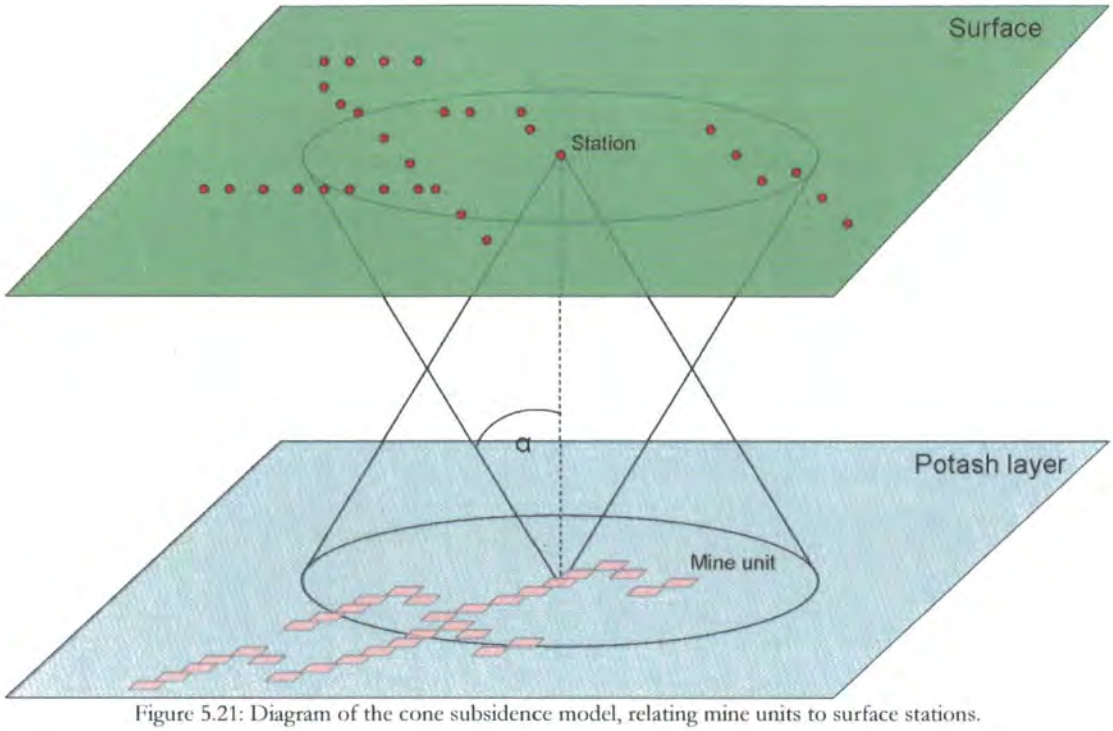

Figure 5.21: Diagram of the cone subsidence model, relating mine units to surface stations.

Deformation rate in millimetres per year can be estimated using equations 5.1. A deformation fraction (d) is the deformation connected to one station-mine unit combination. A deformation fraction can also be visualised as a diagonal vector between mine unit and surface station along which a certain one dimensional weight is pulled. If the cone under station x encloses 12 mine units, deformation at station x is a sum of 12 deformation fractions.

In equation 4.2 through 4.5 the deformation factor per individual diagonal (*d*) caused by four separate variables is calculated. Equation 5.1 is the concluding summary of all deformation fractions, resulting in an estimated deformation rate at the surface.

Equation 5.1: $$\hat{S} = \sum_{d=1}^{n} \hat{S}_A \times \hat{S}_H \times \hat{S}_G \times \hat{S}_T$$

Where:

$\hat{S}_A$ = Deformation factor caused by variable A - Total mined area

$\hat{S}_H$ = Deformation factor caused by variable H - Average horizontal distance

$\hat{S}_G$ = Deformation factor caused by variable G - Average distance between mine panels

$\hat{S}_T$ = Deformation factor caused by variable T - Average difference in time

The quality of the estimations can be tested by assessing the difference between the estimated ground surface deformation and the measured ground surface deformation for the test subset (40%) of the data. The test subset of the data was not used for the development of the model. The total difference between measured and estimated deformation rate is showing in the box-plot diagram in Figure 5.22. The box represents the window in which all values within the 25th percentile and 75th percentile fall per two-millimetre lag. The whiskers on the box plot show the reach of the adjacent values (all values within 1.5 times the inter-quartile range), while the markers show outliers.

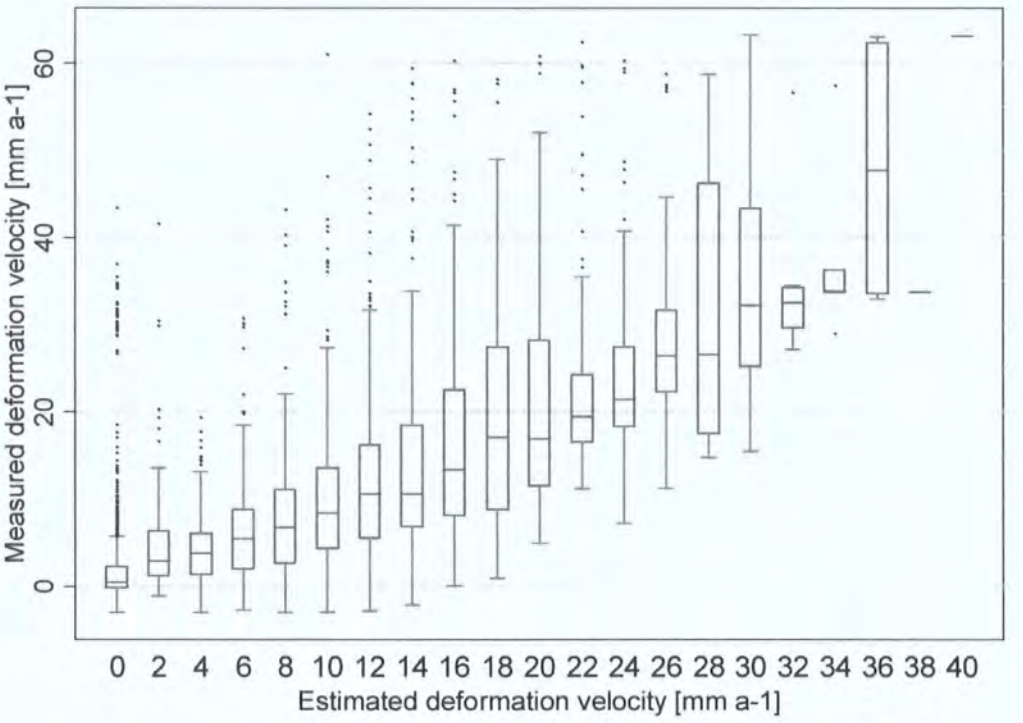

Figure 5.22: Box plot showing measured values over equal bins of estimated values. Box shows 25%-75% percentile and median of values in each bin.

A histogram of the difference between estimated and observed values of ground surface deformation rate is given in Figure 5.23. This shows that 89 % of the estimations are between -1.65 and +1.40 mm a $^{-1}$ of the actual ground surface deformation value and 51 % of the estimations are between -0.6 and 0.4 mm a $^{-1}$ of the actual ground surface deformation value. From the scatter plot of the estimated ground surface deformation versus the observed ground surface deformation it seems that the estimations for lower ground surface deformation values are better than estimations for higher ground surface deformation values, the overall adjusted R^2 of the model is 0.53, based on all data and not the mean values that were used to develop the cone model.

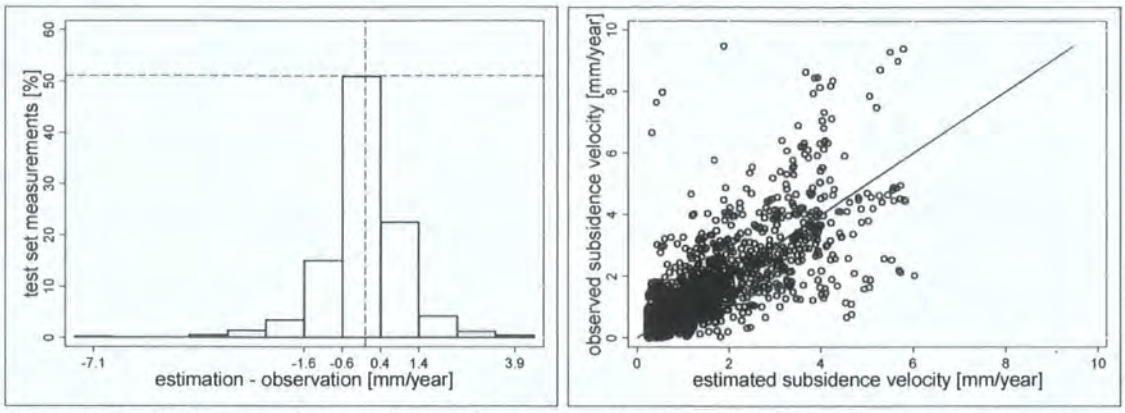

Figure 5.23: Left: Histogram of estimated minus observed ground surface deformation. Right: Scatter plot of estimated versus observed ground surface deformation

The cone model is able to estimate the five key indicators discussed in chapter two. Following is first the estimated key indicators for the whole Boulby area. These key indicators are based on the current extent of the mine workings. The total subsidence is based on the settlement of the mine workings as they were in 2004.

To evaluate the estimations to existing levelling data, intermediate estimations are made. The estimations made by the cone model are done by prediction record. As explained in the previous chapter, each prediction record has a unique location at the surface and a point in time. From this format, the five indicators can be derived. In addition, the feasibility of the cone model to estimate the potential gradual ground surface deformation caused by mining activities is tested in an area outside the currently undermined area.

5.3.1. Ground surface deformation in the Boulby area

5.3.1.1. The moment of recovery

In the previous section, the relationship between the median deformation rate values and the time difference between mining and measuring has been determined. The relation of the time variable and the deformation rate per mine panel was used to fit a curve. This curve was found to lead to the best long-term estimations of ground surface deformation. In reality it is likely that the deformation rate approaches zero but not actually reaches zero. In theory the moment of recovery estimated by the cone model is therefore infinite (Eq. 5.2).

However, an acceptable rate of deformation can be chosen based on the accuracy of the relative elevation measurements of the used levelling technique. The found curve can be

extrapolated until it crosses a 0.2 mm a-1 threshold (Fig. 5.24). This occurs at approximately 19,994 days, where the estimated deformation rate is 0.2001 mm a-1.

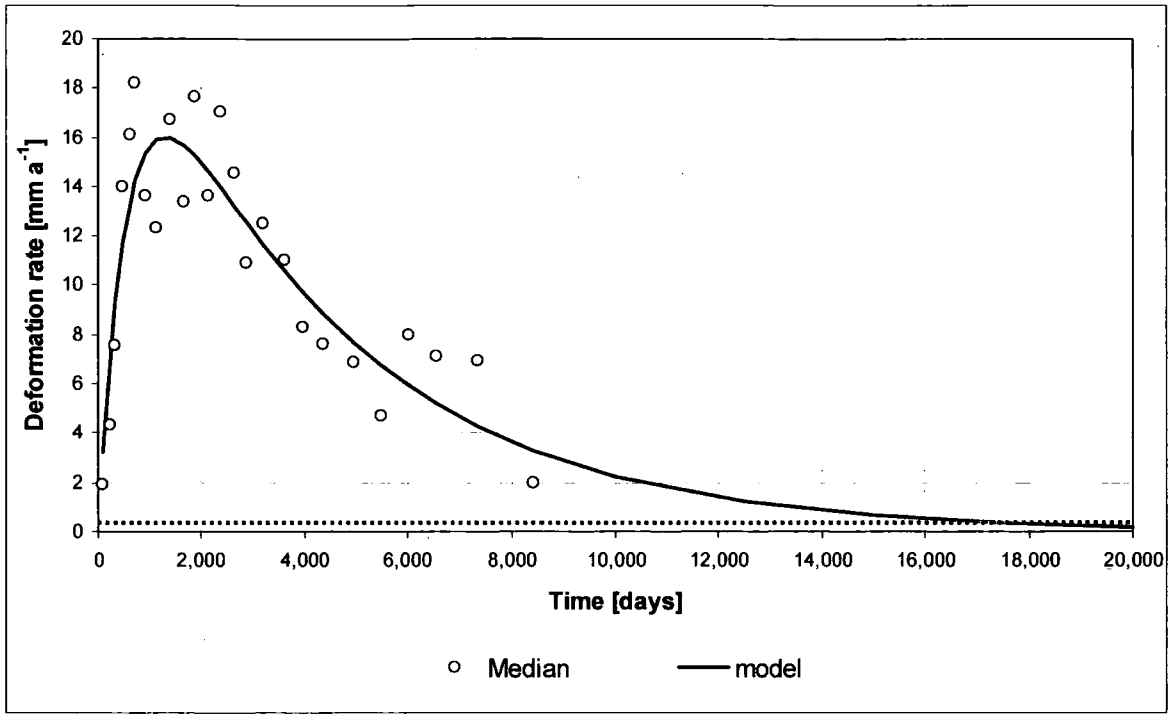

Figure 5.24: Deformation rate [mm a $^{-1}$] over average time after mining [d], medians from levelling dataset, with extrapolated fitted curve.

Equation 5.1: Alternative curve through deformation rate over average time after mining

$$\hat{S}_T = -25.55 \times \left(e^{\left(-1.750 \cdot 10^{-3} \times T_d\right)} - e^{\left(-2.426 \cdot 10^{-4} \times T_d\right)} \right)$$

The R^2 of this equation is 0.76.

The long-term estimation of the deformation at levelling stations around the area, demonstrates a certain flattening in the deformation after 19,990 days or 54.7 years. At this point the settlement is likely to approach completion. Unfortunately, this can not yet be confirmed by measured rates of deformation, the oldest part of the mine is currently 33 years old.

The algorithms used in the cone model were based on a subset of the levelling stations. This development subset includes 60% of the stations, while the other randomly selected 40% is used as an evaluation subset. Following is the comparison between the estimations based on the cone model and the levelling measurements, both at the evaluation stations (Fig. 5.25). The graphs of the all 60 plots are given in Appendix 5.

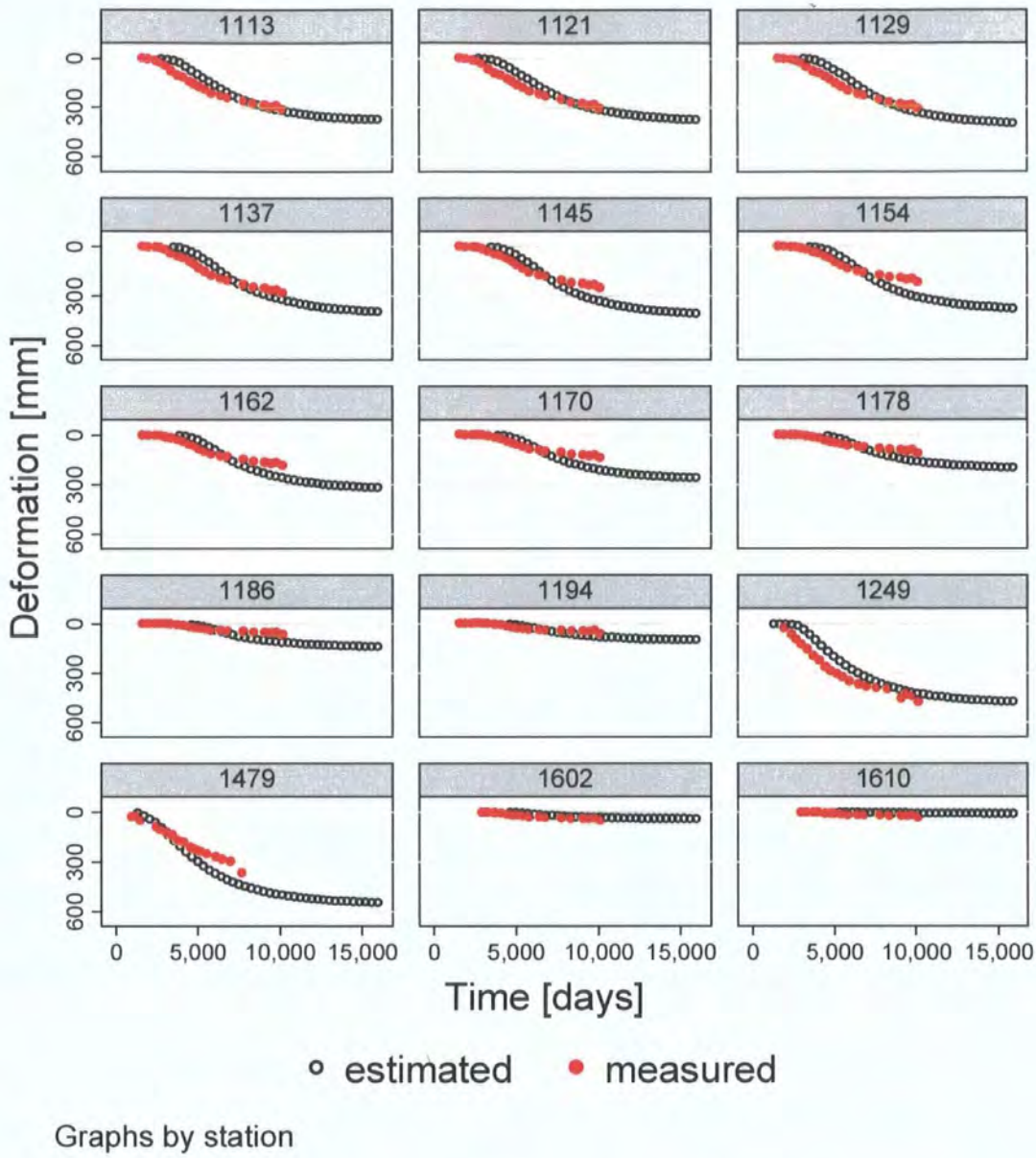

Figure 5.25: Subset of the evaluation levelling stations, used to evaluate the cone model estimations.

The graphs give the estimated curve together with the monitored curve at the selected evaluation stations. Of the selected evaluation stations, three show a clear under-estimation over time. At these stations, the estimated deformation remains too low although the difference between estimation and measured deformation does decrease over time. At fourteen stations the estimation is more than the measured values, resulting in over-estimation. At the remaining forty-three stations the monitored deformation seems to follow a comparable pattern over time to the estimated deformation. It is noteworthy though that the monitored deformation seems to start sooner than estimated.

5.3.1.2. The outside shape of the subsidence area

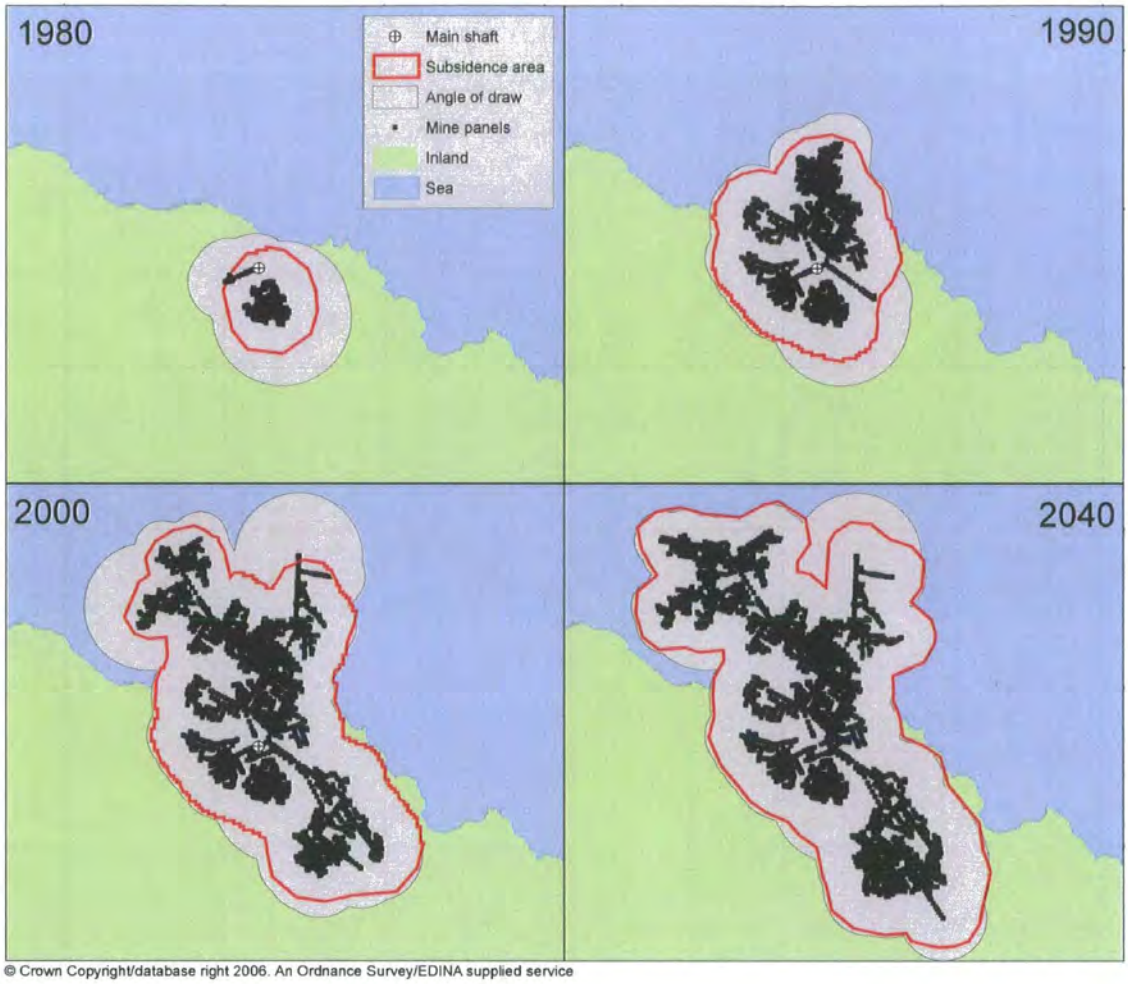

Figure 5.26: The outside shape or 'zero' contour of the estimated area of deformation based on the cone model

The outside shape of the area that is affected by the mining activities and is experiencing a measurable level of subsidence is the second of the five key indicators. An acceptable rate of deformation can be chosen based on the accuracy of the relative elevation measurements of the used levelling technique. The relative accuracy between levelling stations is between 0.22 and 0.93 mm (Table 4.4). The acceptable rate of measurable ground surface deformation is 0.2 mm a-1. The found curve can be extrapolated until it crosses the 0.2 mm a-1 threshold (Fig. 5.26). If the measurable amount of deformation is assumed to be 2 mm, a contour can be drawn to indicate the outside shape.

5.3.1.3. The total subsidence profile

The survey transects are divided into 9 individual lines. Four of these survey lines can be combined to form two transects crossing the research area (Fig. 5.27).

Figure 5.27: Levelling stations on lines 3, 4, 5 and 8 crossing the Boulby area

One transect runs from Skinningrove harbour in the north west to West Barnby village in the south east and is formed by survey lines 4 and 8. The second transect runs from Scaling dam in the south to Staithes harbour in the north and is formed by survey lines 5 and 3. The deformation measured at the fixed stations along these lines is given in Figures 5.28, 5.29 and 5.30 showing total deformation at three points in time, 1980, 1990 and 2000.

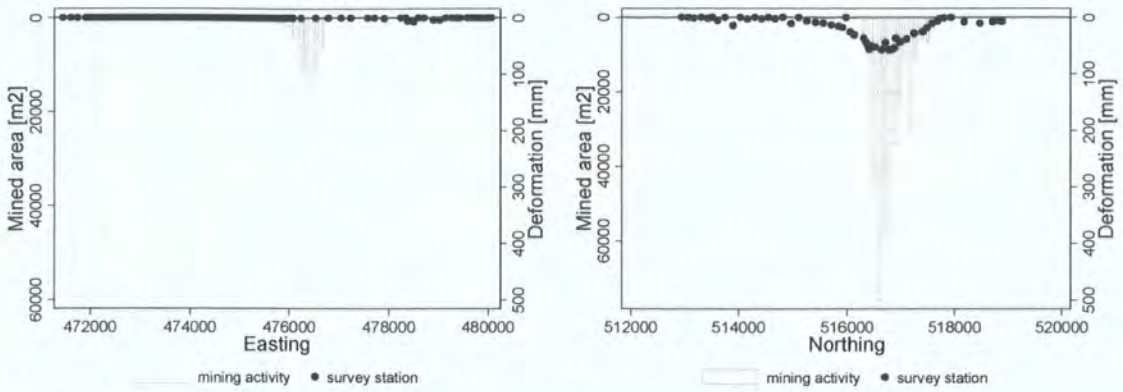

Figure 5.28: Transect 8-4 (left) and 5-3 (right) for year 1980, showing mined area (m2) in proximity of transects and measured deformation along transects.

The maximum measured deformation on transect 8-4 in 1980 was 7 millimetres and was probably not related to the mining activities taking place to the south of the transect.

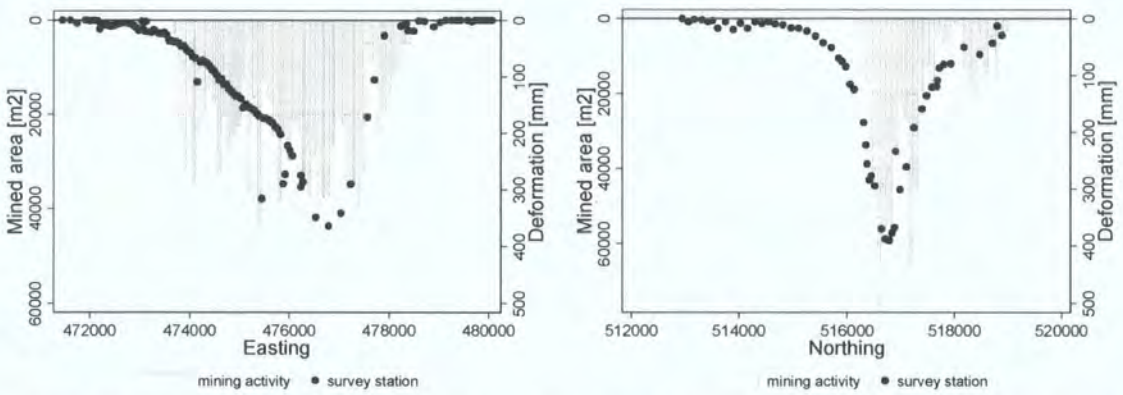

Figure 5.29: Transect 8-4 (left) and 5-3 (right) for year 1990, showing mined area (m2) in proximity of transects and measured deformation along transects.

In 1990 the mine was almost developed under transect 8-4 to its current extent. The transects in Figure 5.29 intersect the excavation zone north of northing gridline 516000 and south of northing gridline 518000. Transect 8-4 intersects the excavation zone just west of easting gridline 474000 and just west of easting gridline 478000, after which they continue along the east edge of the mine.

The spatial pattern initially forms a saucer shape (1980), progresses into a cone shape (1990) and gradually forms a more complex shape (2000 and 2005). The development over time and the location and shape of the deformation is clearly correlated to the mining activities.

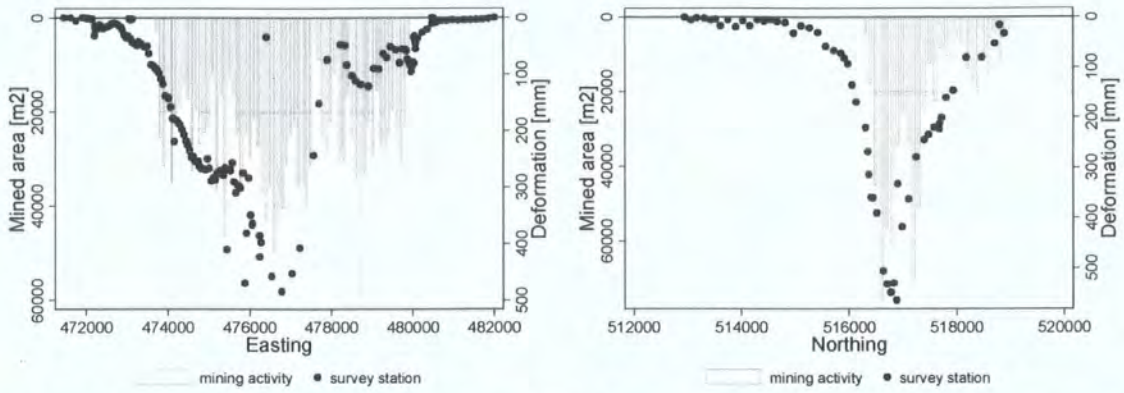

Figure 5.30: Transect 8-4 (left) and 5-3 (right) for year 2000, showing mined area (m2) in proximity of transects and measured deformation along transects.

Based on the cone model estimation can be made of the spatial pattern of ground surface deformation through time based upon mining activities to date (Figure 5.31). The ground surface deformation values on the map in Figure 5.32 are derived from 100 metres pixel based estimations of the total ground surface deformation from the regression analysis. The Figure clearly demonstrates the development of the ground surface deformation bowl as it follows the expansion of the mine. The general shape of the mine plan is mirrored by the shape of the zone of deformation or subsidence bowl at the surface.

Deformation is overestimated in the earlier profiles up to approximately 1993. After 2001 a bias occurs, where estimates in the west appear too high and estimates in the east end of the transect appear to underestimate the deformation.

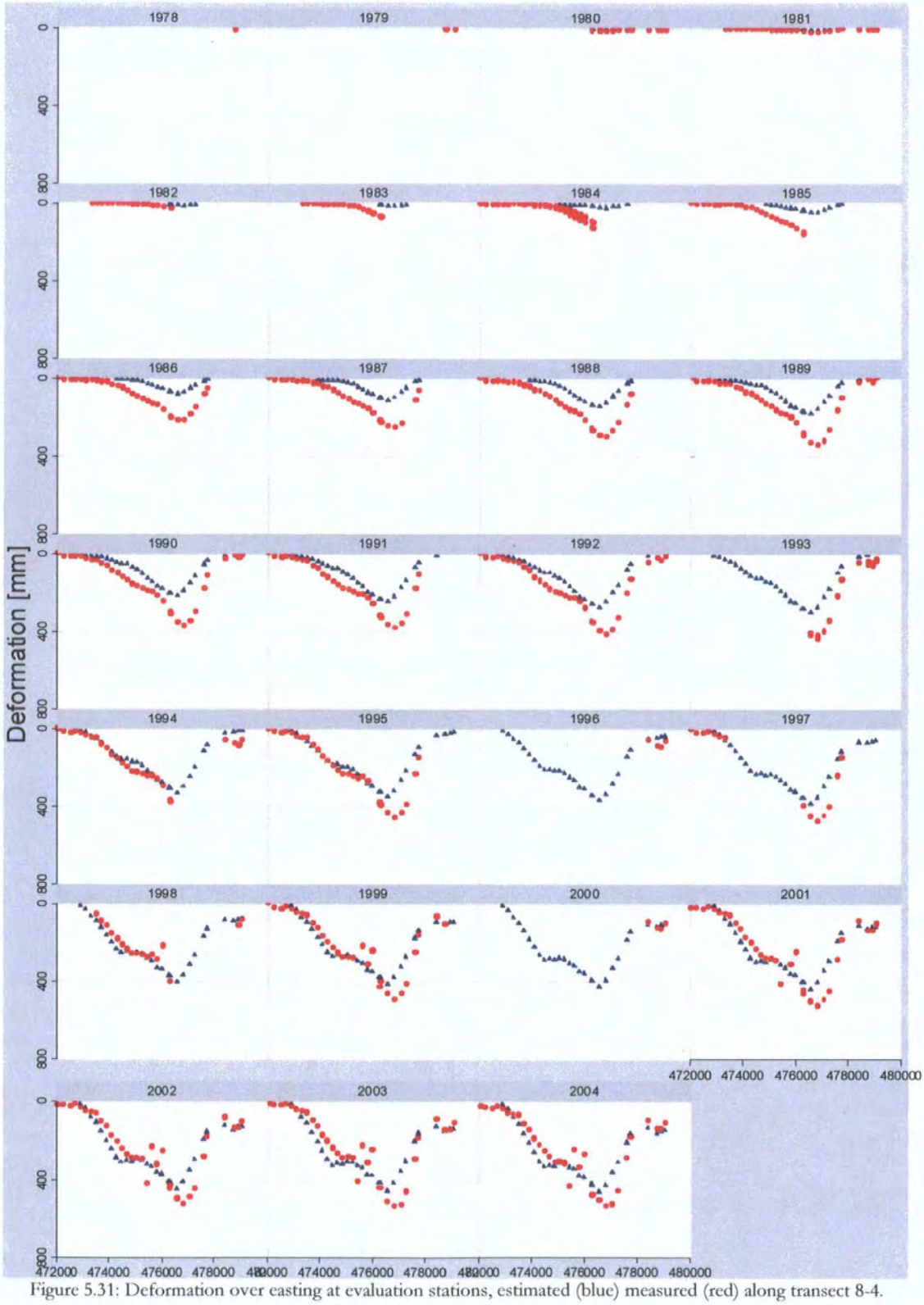

Figure 5.31: Deformation over easting at evaluation stations, estimated (blue) measured (red) along transect 8-4.

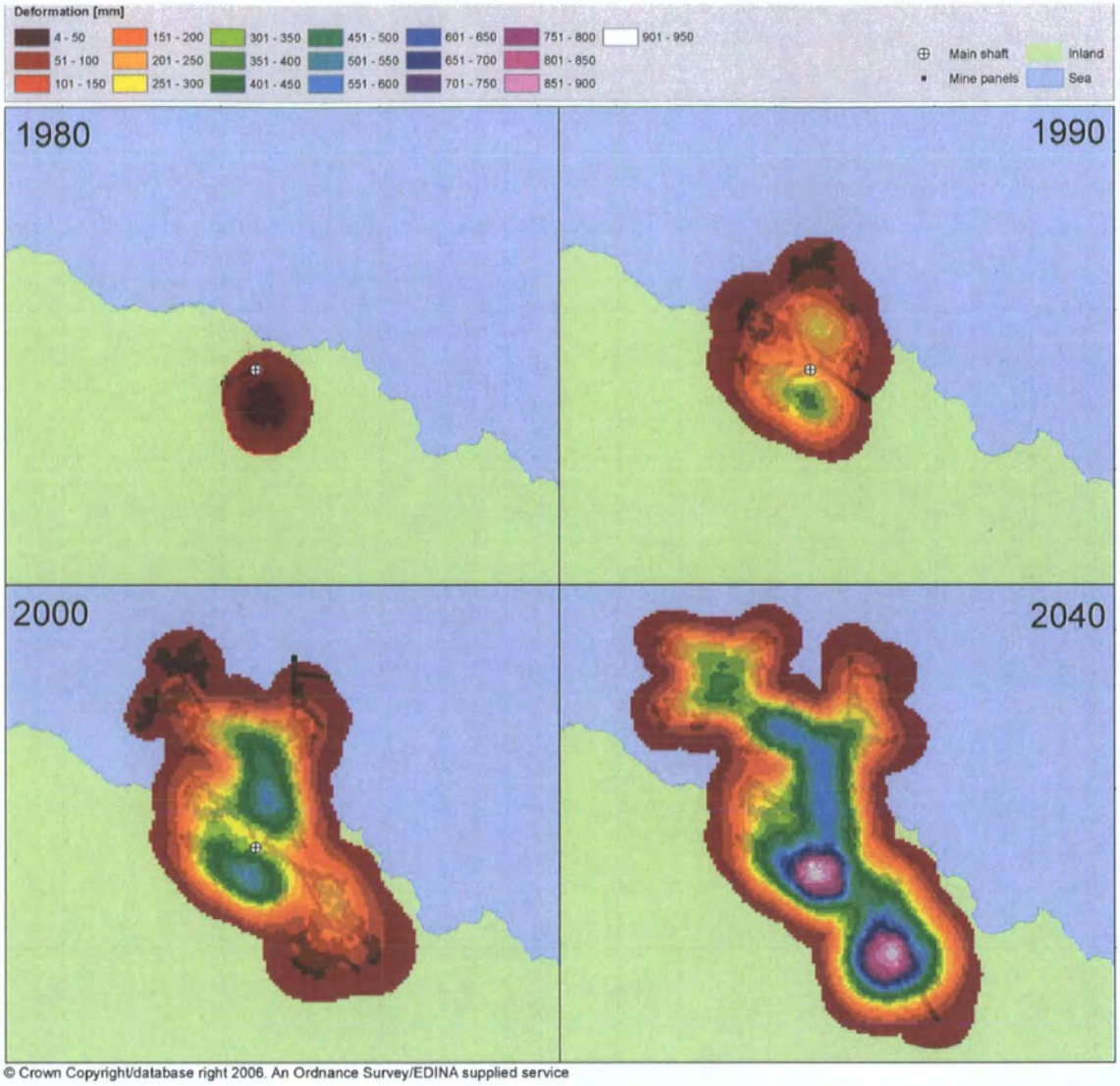

Figure 5.32: Estimated total deformation at four points in time

5.3.1.4. The maximum rate and the moment of maximum rate

Estimations of the development of surface deformation over time are given in Figure 5.33 plotting the estimations at selected existing surface stations.

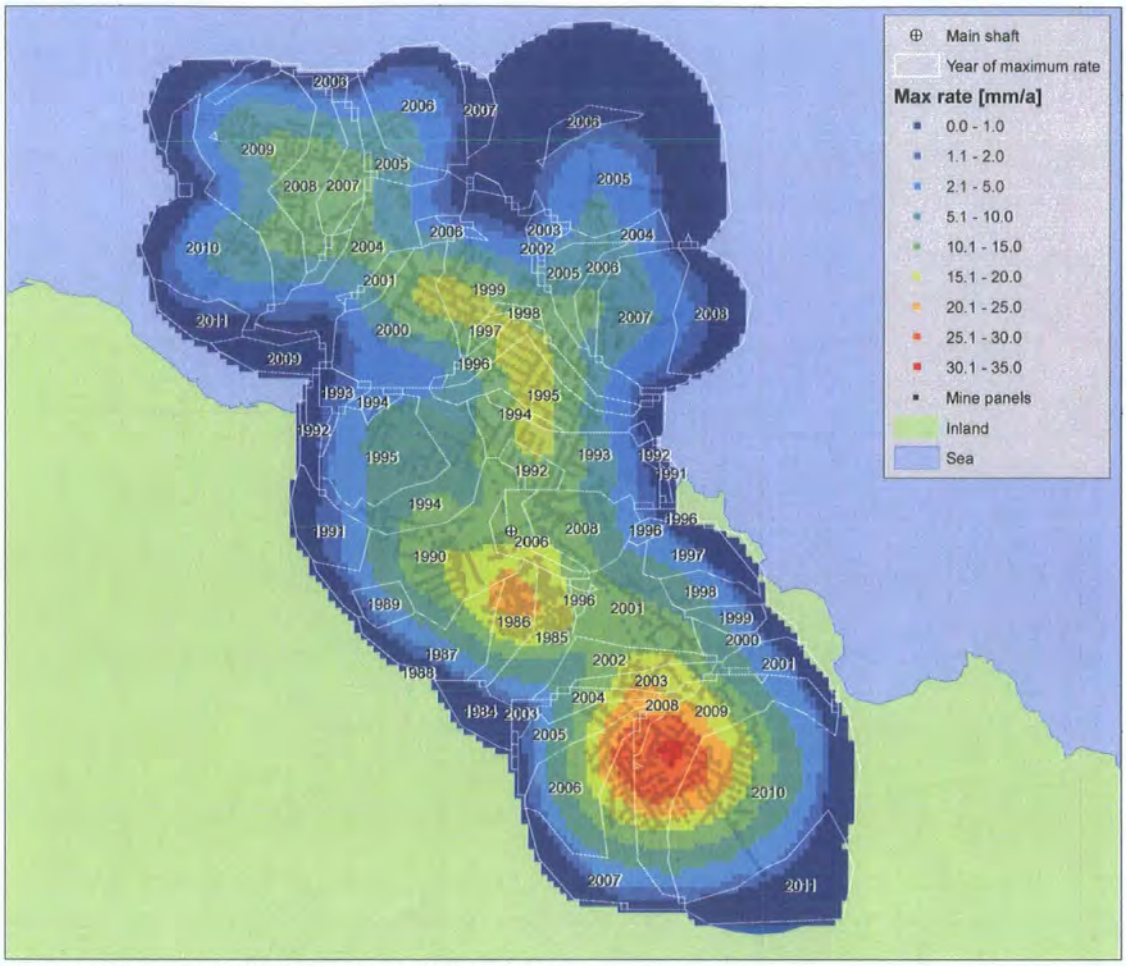

Figure 5.33: The estimate maximum rate of deformation and the period in which this rate was reached.

5.3.2. Scenarios - surface deformation in the Scaling area

The cone model is a tool that enables the study of surface deformation, based on a better understanding of the variables controlling the rate and extent of surface deformation caused by deep underground mining. The cone model can also be used as a planning tool, by predicting subsidence caused by different mining scenarios.

The effect of different mining scenarios on the surface can be predicted. The differences in response between different mining scenarios can be considered in the planning of future mining activities. To illustrate this, some mining scenarios are tested in the Scaling area, a small section of the Boulby research area (see chapter three). This area does not contain any potash or other materials suitable for commercial mining and this example is therefore purely hypothetic. The area is located at approximately 2 kilometres to the south west of the current workings and is dissected by the A171 road (Fig. 5.34).

Figure 5.34: Location of Scaling village and Scaling dam south west of Boulby mine.

The area around Scaling village has the typical rural land use found in the Boulby area and holds the Scaling dam, now mainly used for recreation. A more detailed description of this part of the research area is given in chapter three. On the aerial photograph, the artificial protection wall at the north side of the dam is visible.

There are 6 levelling survey stations located in the Scaling area. Thus far, there has not been measured any deformation in the area. The cone model will be used to test the effect of three different mining scenarios on the estimated deformation in the area:

- Concentrated, gradual mining
- Concentrated, sudden mining
- Well distributed, sudden mining

Figure 5.35: Aerial photo of year 2000 showing Scaling area

In the first scenario, the mining activities take place in over a short time interval and concentrated in the centre of the research area (Fig. 5.36). The eight black squared shapes are the hypothetical mine units located within 100 metres of the centre of the Scaling area. The mine units are started within a period of eight months after each other between 1 January 2006 and 1 August 2006.

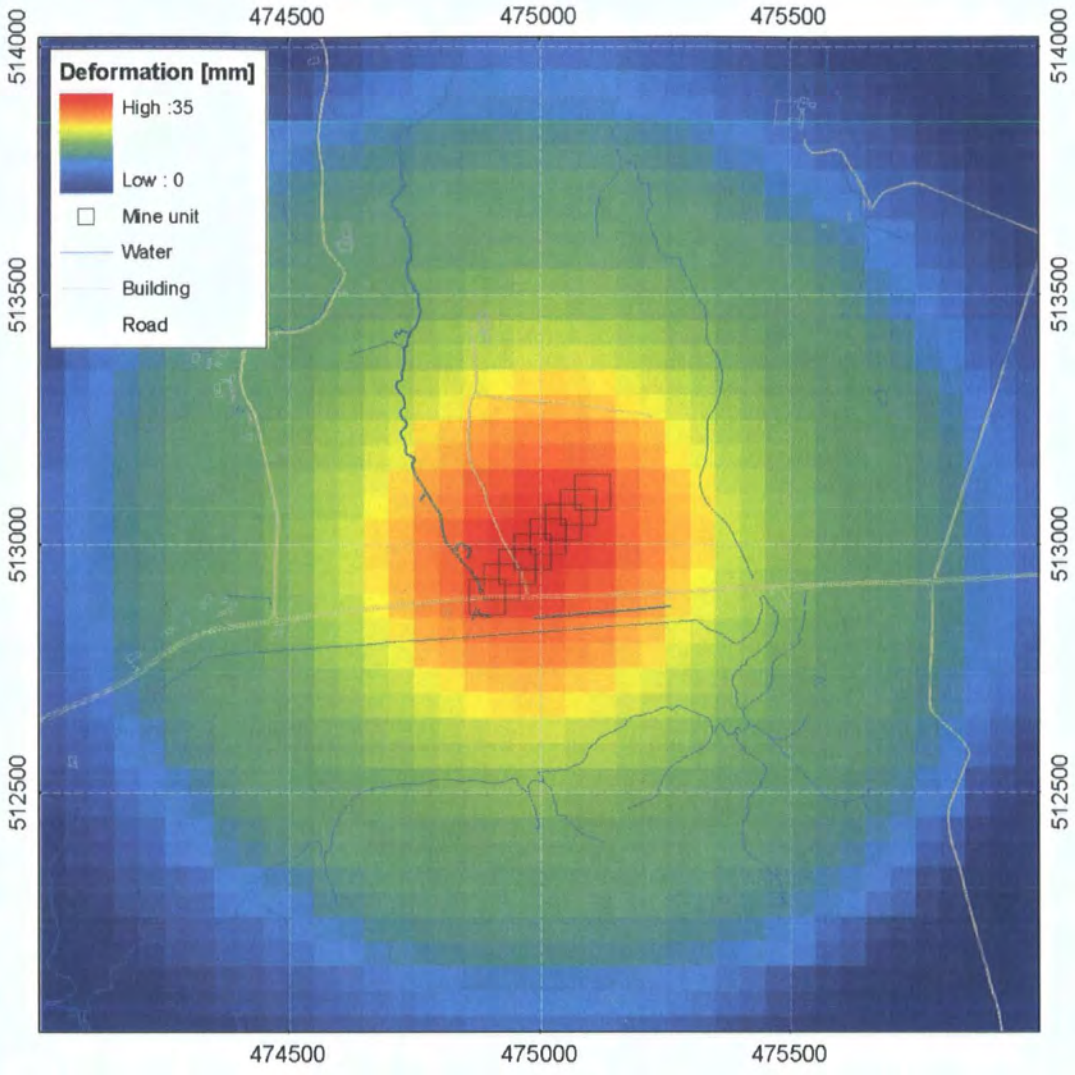

Figure 5.36: Hypothetical total deformation [mm] in January 2021 caused by mining scenario 1.

The effect of this mining scenario on the surface is an almost circular saucer shape reaching 60 millimetres in the centre of the Scaling area gradually flattening to 0 millimetres outwards over a 1000 metres distance. In the second scenario, the eight mine units are located in the same place as in the first scenario, within 100 metres of the centre of the Scaling area (Fig. 5.37).

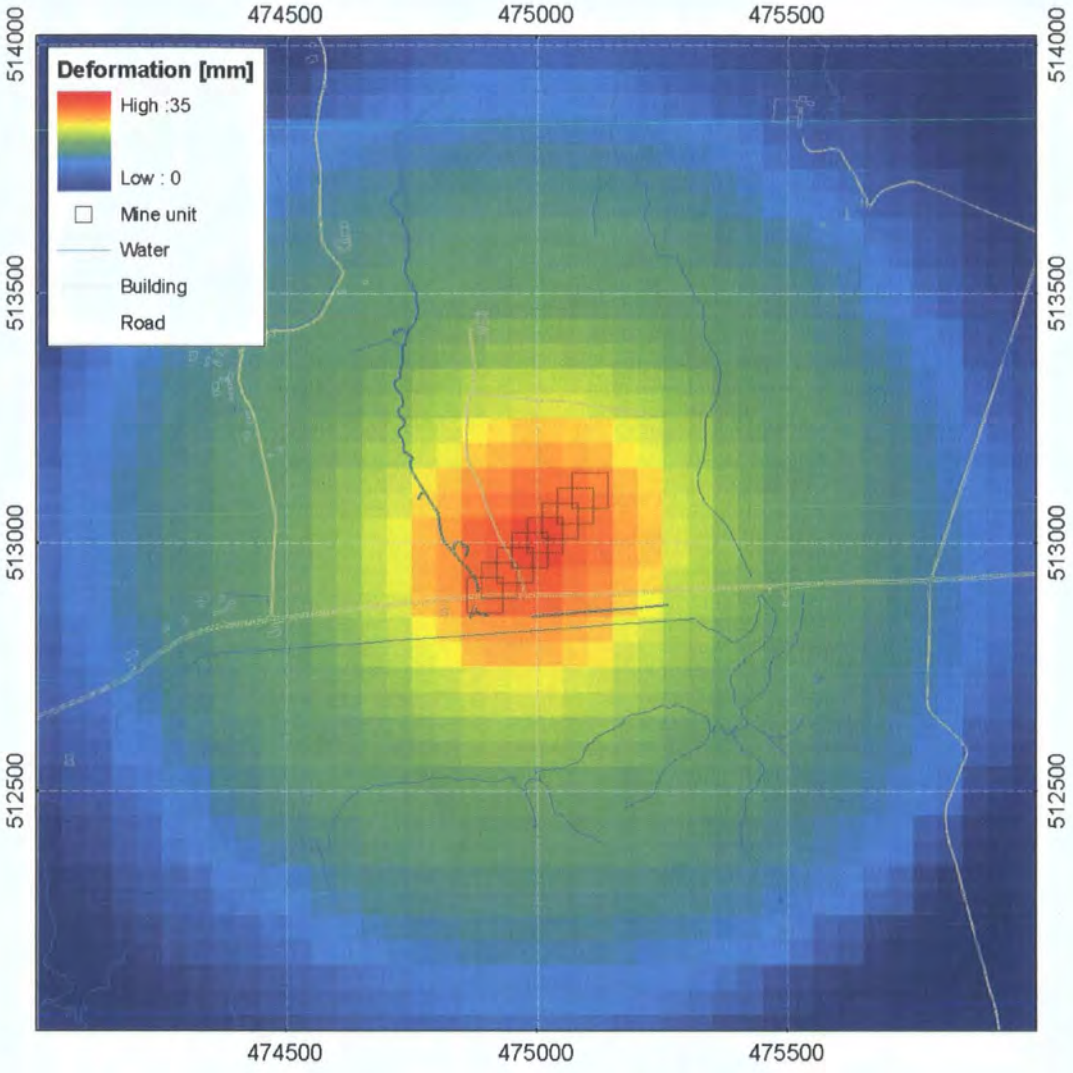

Figure 5.37: Hypothetical total deformation [mm] in January 2021 caused by mining scenario 2.

Instead of the sudden mining activities in the first scenario, the mining activities in scenario 2 are distributed over a period of eight years. The starting dates of the eight mine units are between 1 January 2006 and 1 January 2013.

The effect of this second mining scenario on the surface is again an almost circular saucer shape reaching 60 millimetres in the centre of the Scaling area gradually flattening to 0 millimetres outwards over a 1000 metres distance. The subsidence bowl is shallower although the affected area is similar in extent and circular shape.

The third and final scenario tested in the Scaling area tests a pattern of with well distributed mining activities, but started within a short time interval (Fig. 5.38).

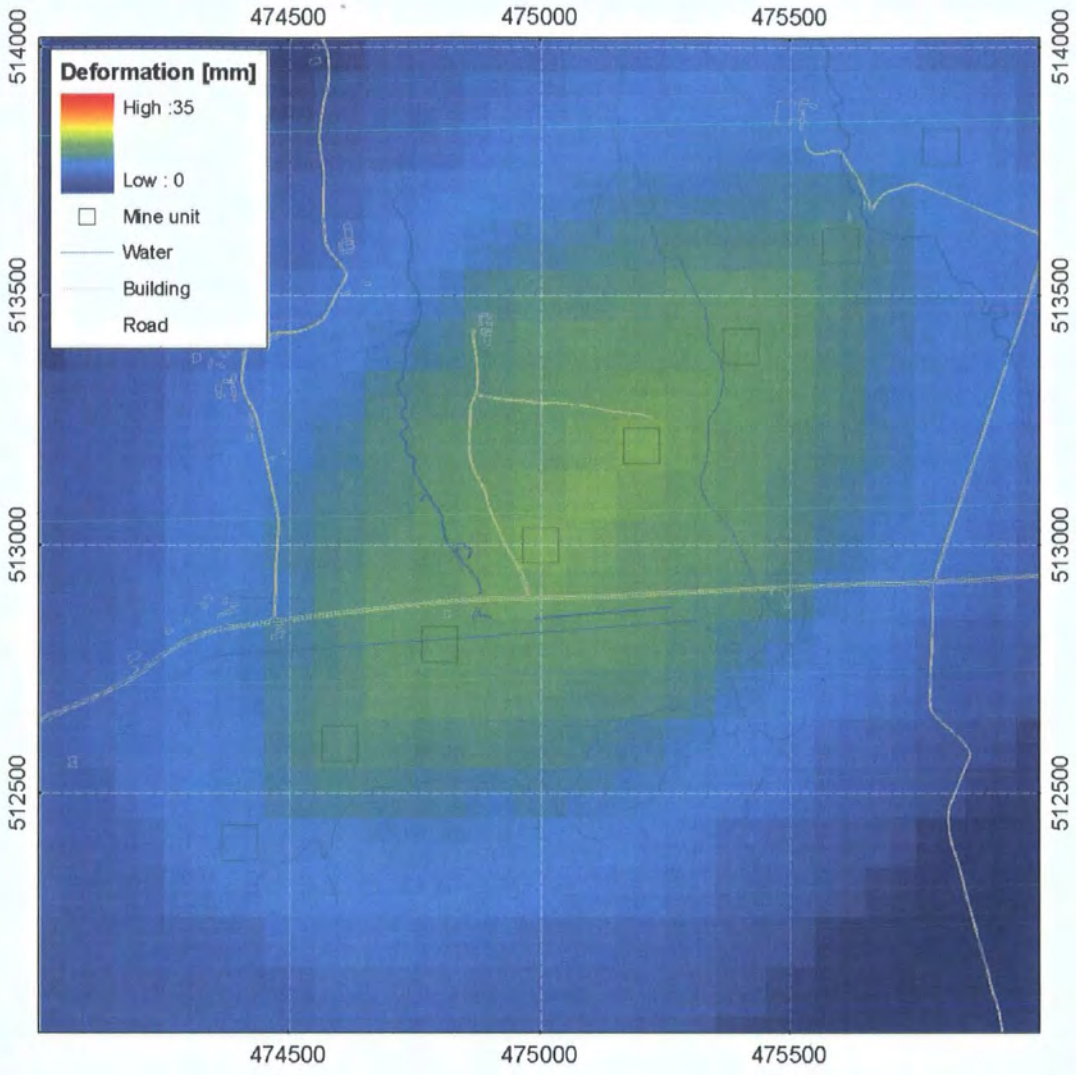

Figure 5.38: Hypothetical total deformation [mm] in January 2021 caused by mining scenario 3.

The shape and extent of the surface deformation is considerably different from scenarios 1 and 2. In each of the three scenarios, the mining activities took place in eight identical mine units, the effects of the mining activities on the surface are different. In Figure 5.39 a comparison is made of the deformation pattern over time for the three scenarios.

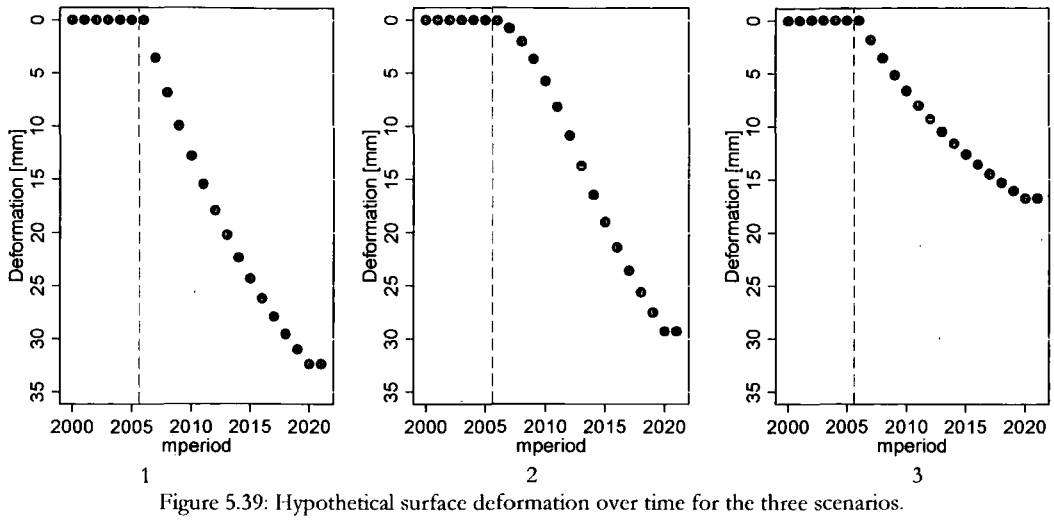

Figure 5.39: Hypothetical surface deformation over time for the three scenarios.

Distribution of mining activities over space has a considerably stronger impact on the deformation pattern than distribution over time. Clustered mine panels that are mined in short period of time have almost exactly the same impact on the surface as clustered mine panels that are mined over a longer period of time. Mine panels that are well distributed have a considerable smaller effect on the amount of surface deformation. This demonstrated one of the possible applications of the cone model tool as a planning tool of different mining scenarios.

5.4. Conclusion

This chapter has presented a ground surface deformation monitoring dataset generated by PSI analysis, as described in chapter four. The dataset includes the relative elevation change at 1583 persistent scatterers unevenly distributed in the research area at a density of 6.4 PS's km^{-2}. Compared to other PSI research findings this is a low density of PS's. The final PSI deformation datasets comprises the total deformation over a period of 8.6 years and a time series of 29 measurements at variable time intervals. The measurements describe gradual ground surface deformation of the Boulby research area between 9 September 1992 and 21 October 2000.

The main result of the data-driven modelling analysis described in chapter four is the cone model and the cone model tool. This tool enabled the testing of different mining scenarios and their effect on the ground surface deformation. As deformation measured over the oldest part of the mine has not yet reached zero, the cone model was not able to find a definite moment of recovery based on the existing dataset. However, based on an

alternative equation an annual deformation rate of 0.2 mm a^{-1} is reached after 54.7 years. This can be regarded as a stable rate of deformation, since it close to the accuracy of the levelling survey technique used. In future the dataset will cover areas that have reached a stable situation which can then be used to improve the algorithms of the behaviour over time.

The outside shape of the area of deformation, the peak deformation rate and the spatial distribution of the peak deformation rate can be estimated with the cone model tool. Since the period of recovery can not yet be estimated based on the existing dataset, the profile of the final deformation could not be estimated. The intermediate deformation profile at certain points in time can be estimated and give a clear idea of the long-term effect of current mining activities. The main advantage of the cone model tool is its ability to compare the effect of different mining scenarios. An example is given in this chapter of a hypothetical situation of mine panel in a previously un-mined area.

CHAPTER 6. DISCUSSION

'The important thing in science is not so much to obtain new facts as to discover new ways of thinking about them.' (Sir William Bragg, 1862-1942)

6.1. Introduction

This research has produced interesting findings on both the InSAR analysis and the data-driven modelling. In this chapter these findings will be discussed in a wider context. The increased applicability of different InSAR techniques to monitor ground surface deformation entails that an increased number of large datasets is generated. These datasets will give information about the dynamics of the deformation process at the surface.

In cases with well documented driver dynamics, these large datasets can be used as input in a data-driven model to understand the correlation between driver dynamics and the ground surface deformation dynamics. In this research proof has been found that gradual ground surface deformation can be predicted accurately, using a data-driven approach. In the case of gradual ground surface deformation related to mining, the dynamics of the driver causing deformation are well documented and can be used as variables in a model. In the Boulby area, the amount of deformation as a result of different mining scenarios could be estimated. In other situations where ground surface deformation is caused by spatially distributed drivers, this approach can lead to accurate estimations if they are based on large high quality datasets.

6.2. Feasibility of conventional InSAR

Temperate climates are variable over both long periods (months) and short periods (hours) and weather conditions are hard to predict. The difference in path delay between two registration dates is therefore likely to be high. If this difference is constant for the whole scene it can be corrected. However, in the case of spatial variation within the radar scenes this becomes difficult (Hanssen, 2001). In areas with some relief, such as the Boulby research area, the spatial variation of the atmospheric phase can be considerable. In Figure 6.1 the difference between an InSAR based DEM created from a tandem pair and an independent DEM from OS Profile data, is shown.

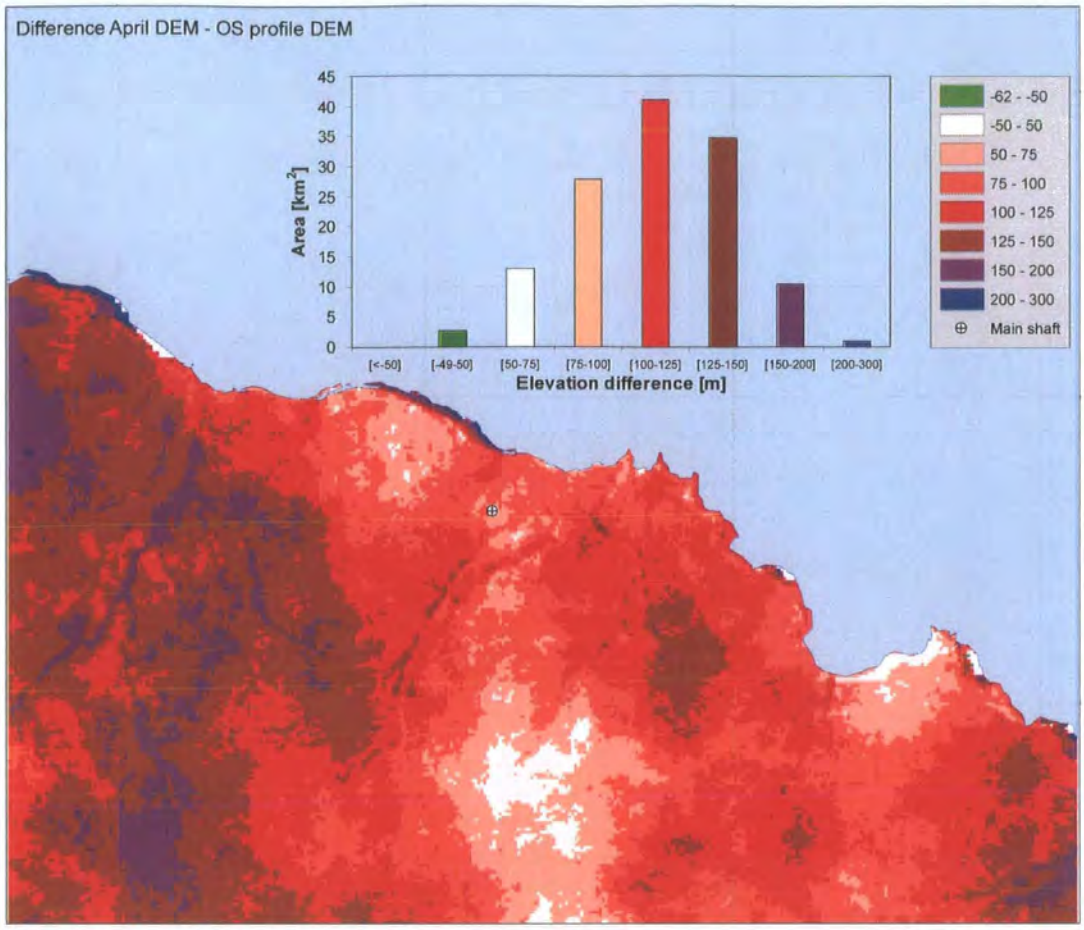

Figure 6.1: The difference between the April-96 InSAR DEM and the OS Profile DEM

A relative longer travel time between the two input radar scenes has caused an overestimation of the topographic height. The phase difference of the tandem interferogram does not contain a (φ_{defo}) and the (φ_{topo}) has been removed by subtraction of the OS DEM. Consequently, the overall difference is due to a difference in atmospheric conditions between the two days. More local variations such as those found along the river valleys and the coast line are likely to be the result of shadowing and layover, an effect of the radar viewing geometry (Woodhouse, 2006).

After removal of the topographic phase (φ_{topo}) and the path delay phase (φ_{path}) successful unwrapping of interferogram depends on the amount of coherence or decorrelation (φ_{noise}) in an interferogram (Hanssen, 2001). In conventional InSAR the removal of the topographic phase is generally straightforward. The topographic phase can be estimated based on an independent DEM of the area, such as the OS Profile data (OS, 2005). Alternatively, the topographic phase can be estimated based on an interferogram made with

radar scenes that are taken at a short time interval, for example during the ERS1/ERS2 tandem mission.

The decorrelation phase (φ_{noise}) is not a phase that can be estimated or subtracted in any way. To estimate whether a pixel contains an unacceptable amount of decorrelation a dimensionless index is calculated referred to as the coherence value. Some objects at the surface have a low coherence. Pixels that contain such objects cannot be used to generate any measurements and return a low coherence value even over single day temporal baselines (Fig. 6.2 and 6.3). In general there are three main sources of decorrelation which limit the feasibility of differential InSAR (Ferretti et al., 2000b).

1. Decorrelation due to temporal change of the scatterers.

2. Decorrelation due to the different looking angle.

3. Decorrelation due to volume scattering.

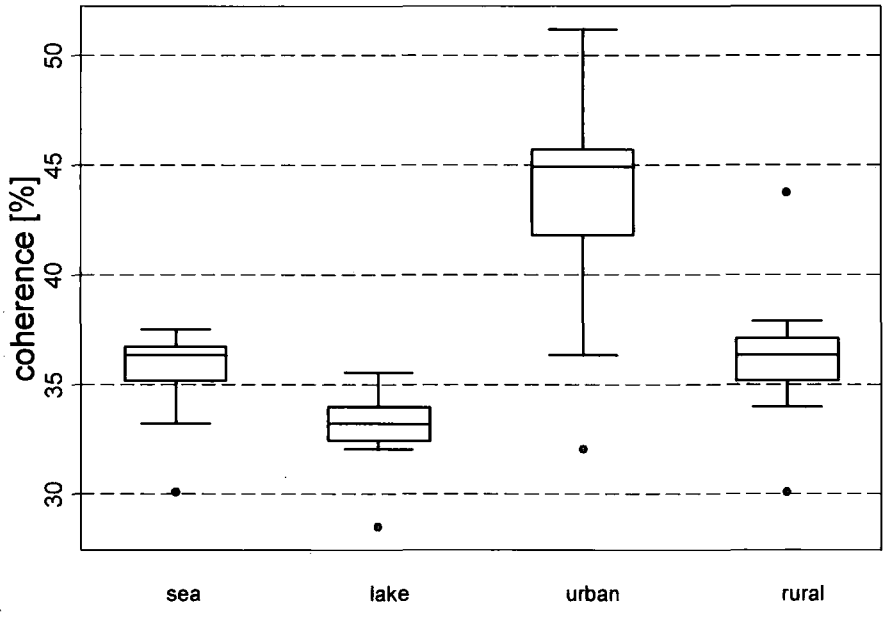

Figure 6.2: Box plot of the median coherence [%] four polygons in the Boulby area, the boxes represent the 25%-75% occurrence window with the horizontal line indicating the mean value.

In Figure 6.2 a comparison was made between four land-cover types, sea, lake, 'rural' and 'urban'. For each of these land-cover types coherence values of a tandem interferogram were extracted, based on small subsets (Fig. 6.3). In the Boulby area 'urban' land-cover is only found in small villages.

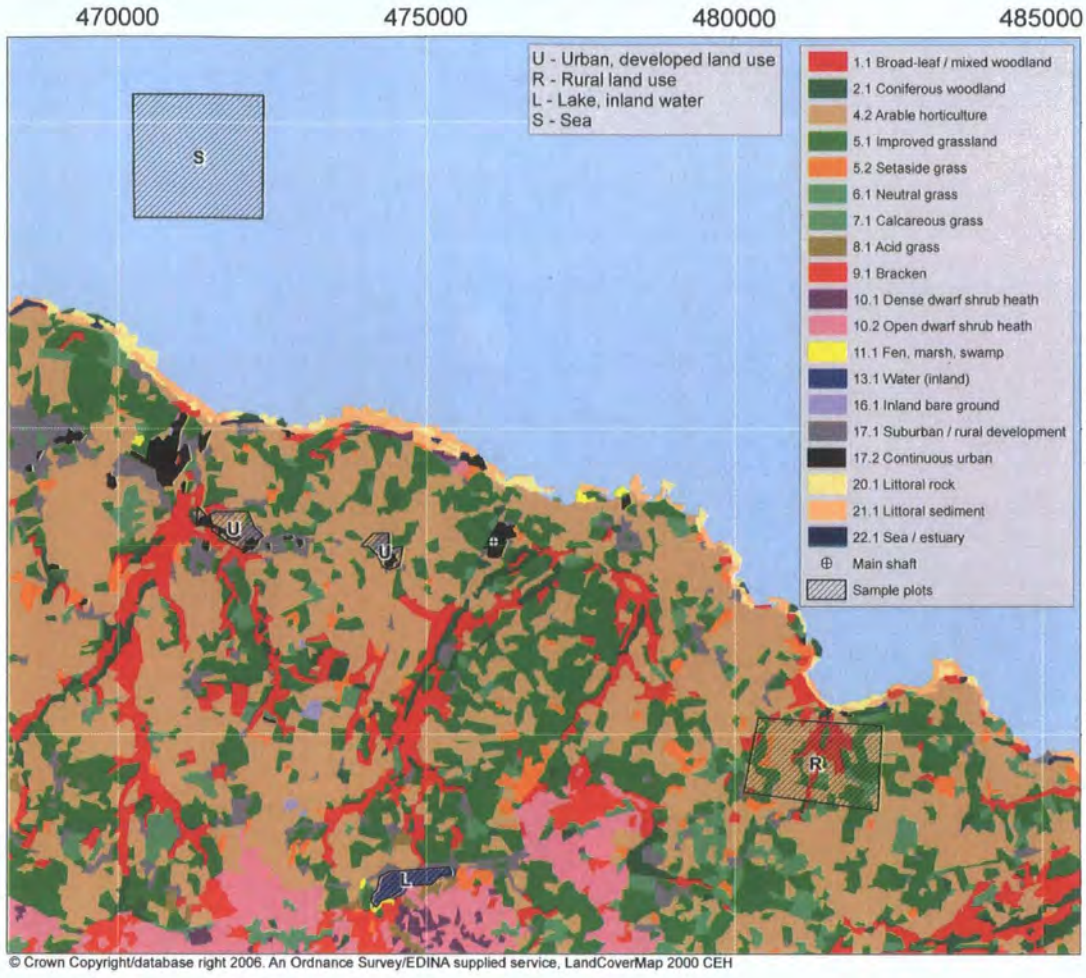

Figure 6.3: Location of the sample plots used to compare land-use classes, background LCM 2000.

In Figure 6.3, the selected sample plots used for the coherence comparison in Figure 6.2 are superimposed on the land cover map introduced in chapter three. The land use in the selected sample plots does not correspond to a homogeneous land cover type. The two plots selected as U (Urban, developed land use) in fact comprise of a mixture of continuous urban, suburban/rural development, arable horticulture, improved grassland and broad leaved/mixed woodland. The location and extent of the sample plots were selected based on the known boundaries of the settlements and represent a mixture of land cover types found in an average rural settlement. The large sample plot selected as R also includes a mixture of land cover types, arable horticulture, setaside grass, improved grassland and broad leaved/mixed woodland. The last two classes are L (Lake, inland water) and S (Sea). The sample plot chosen for L includes the Scaling dam located in the centre of the research area. For the sample plot for sea, a large plot is selected approximately one kilometre off shore.

From Figure 6.4 and 6.6 it is clear that with a one-day temporal baseline the coherence of inland or sea water is low. The signal-noise ratio is low for water because the amount of signal, which is based on the amount of backscatter of water is low. Interestingly, the coherence of rural land-cover is only marginally less than that of urban 'land-cover'. The coherence for urban polygon was considerably higher than for the other three polygons.

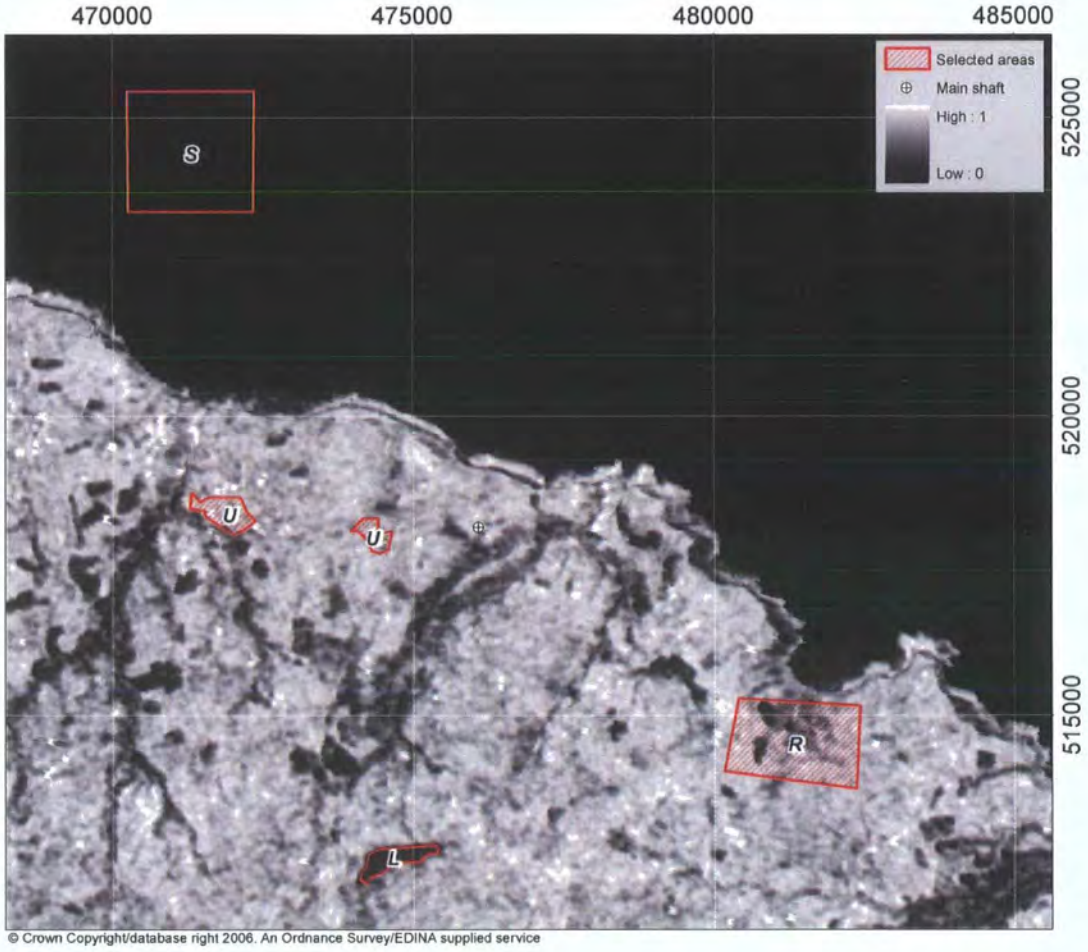

Figure 6.4: Location of the subset areas used to compare land-cover classes, plotted on the coherence image of the interferogram made with the April 1996 tandem pair, showing the highest possible coherence

The patches of low coherence in Figure 6.4 correspond with the highest over and under estimations in Figure 6.2. This is an indication that these errors are not caused by inaccuracies of the OS DEM, but are most likely to be caused by the radar viewing geometry or the vegetation.

To measure ground surface deformation the temporal baseline has to be long enough for some deformation to occur. Rural land-cover has a large seasonal variation, especially arable land, which experiences development of vegetation cover followed by harvest. In

Figure 6.5 the mean coherence for the whole interferogram is compared to the coherence of a tandem interferogram, for ten interferograms of the Boulby area. The steep drop in coherence is mainly due to the loss of coherence in the rural land-cover areas. In Figure 6.5 the coherence in the four land-cover subsets is plotted over the temporal baseline.

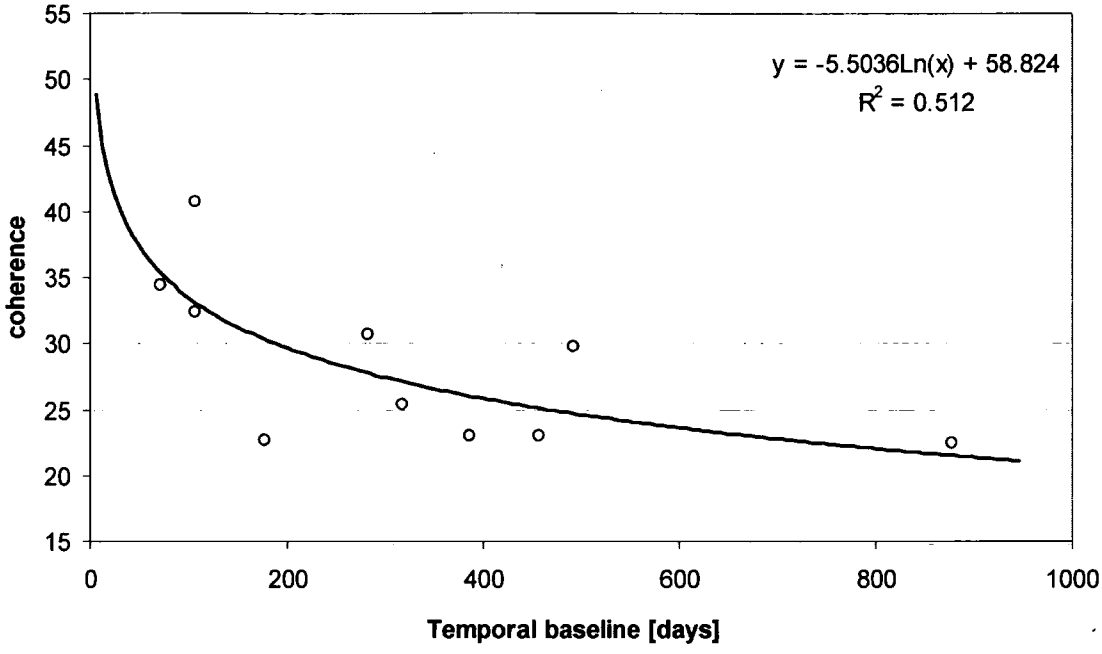

Figure 6.5: Distribution of (dimensionless) coher ence values for ten interferograms, where a pixel value of 256 equals a coherence of 1.

The dimensionless interferometric coherence index (Fig. 6.6) is converted to percentages, where 100% equals the total coherence for the April-96 tandem pair, regarded as the highest achievable value for coherence in the Boulby research area. At 35 days the coherence of both the rural and the urban polygon are significantly higher than the two other polygons. When the temporal baseline exceeds 70 days, the coherence found in the polygon with rural land cover equals the coherence found in the polygon covered by sea water. The relative coherence in the research area seems to decrease over time. This confirms a negative relationship between the temporal baseline in days between the two registrations and the relative interferometric coherence of the result (Fig. 6.7).

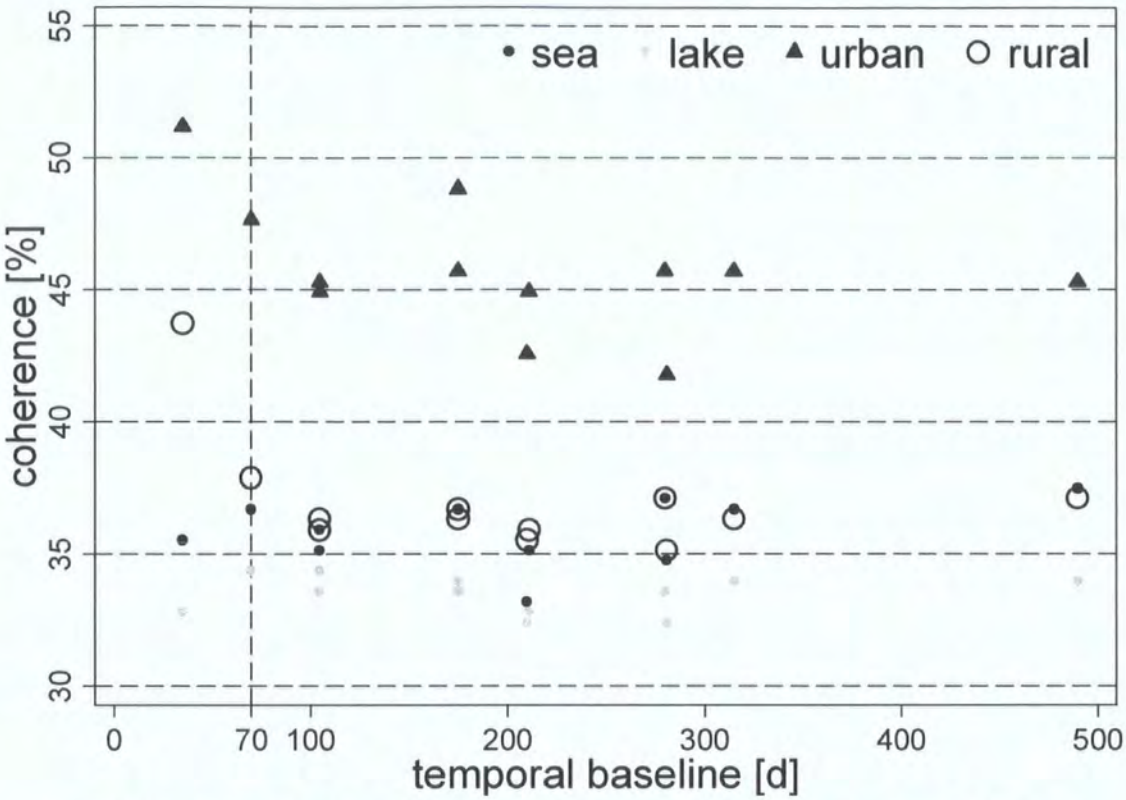

Figure 6.6: Development of coherence [%] over temporal baseline for different polygons within the Boulby area

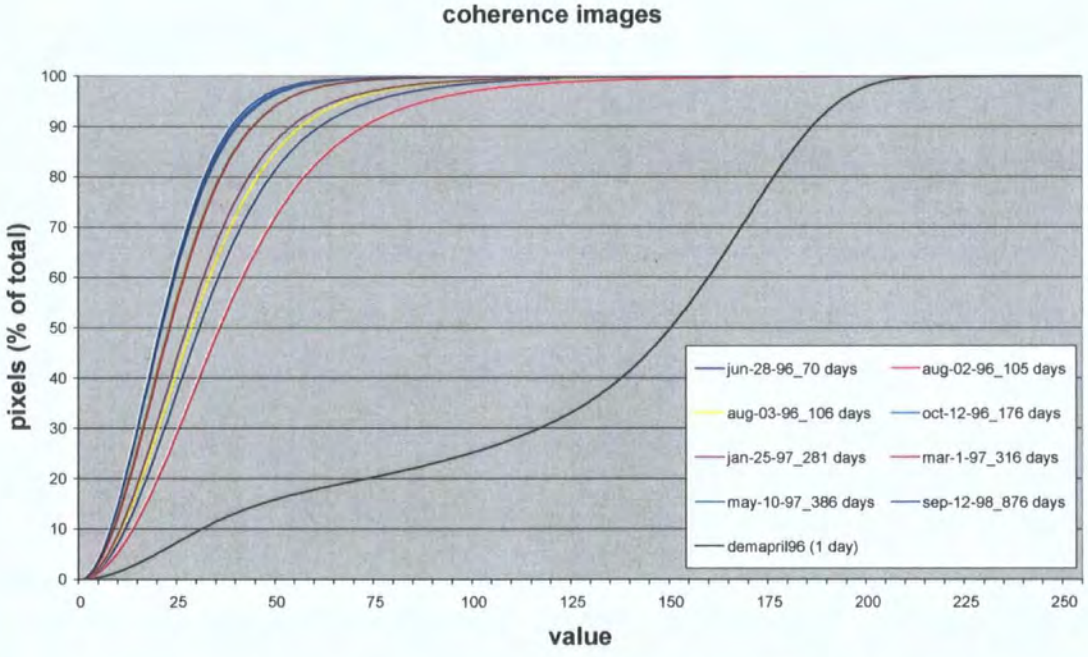

Figure 6.7: Coherence versus temporal baseline for the three pass DInSAR runs.

Coherence loss due to temporal decorrelation forms the most important limitation to the feasibility of conventional InSAR. The land use in the Boulby research area is mainly rural

with large seasonal changes in land cover. The presence of fixed structures offering coherent backscattering is scattered and causes a disturbed and patched interferogram, unsuitable for unwrapping.

In conventional InSAR one reference point is used to unwrap a complete scene. Vertical deformation is determined from pixel to pixel using the value at the reference point and scene parameters such as the perpendicular base line. Pixels that have a low coherence are excluded from the unwrapping process. As a consequence, a number of pixels with high coherence are excluded because they are surrounded by pixels with low coherence.

High coherence patches are present in the area and seem to correspond with buildings mapped by Ordnance Survey topographical data. For the PSI technique to be feasible, sufficient objects functioning as persistent scatterers have to be present in the research area and a sufficient number of scenes have to be available.

Alteration of land surface characteristics between pairs of radar images is likely to result in image decorrelation. This effect is exacerbated by the length of the period between radar image acquisitions because environmental processes change the nature of the land surface. The focus of this research is gradual deformation in the order of centimetres per year. In the case of such gradual surface deformation decorrelation can be caused by surface processes, such as vegetation growth, ploughing of fields and burning of moors to a degree that conventional InSAR is unfeasible.

In cases where deformation is sudden and of a large magnitude, decorrelation is less of a limitation. An example is the 2003 Earthquake in the city of Bam in Iran. This shallow-slip rupture earthquake had a magnitude of 6.5 and caused both vertical and horizontal deformation, at some places measuring two metres (Fialko et al., 2005). The deformation took place over a very limited time span and monitoring with InSAR was carried out using a before and after ASAR image. ASAR is the Advanced Synthetic Aperture RADAR sensor onboard the ENVISAT satellite launched in 2002. There are small differences between SAR and ASAR, such as the wavelength range and inclination angle. However, ASAR images can be used for InSAR analysis in a similar way to the SAR images used in this research.

In the BAM study, the temporal baseline was 70 days for both interferograms that were made. This would be too short to measure a gradual deformation process, such as found in the Boulby research area. In the case of an earthquake, a short temporal baseline is

sufficient. The overall coherence of the interferograms is high, because of the arid climate in Iran, urban land use and a short temporal baseline. Despite the high overall coherence in the two interferograms, there are some areas that can not be included in the unwrapping process, due to the high level of destruction. Despite the exclusion of these areas, this is the first large shallow earthquake with sufficient high coherence to allow for measurements of surface displacements across the earthquake rupture, which has lead to insights into the shallow slip deficit.

6.3. *Persistent scatterer InSAR analysis*

6.3.1. Selection of the persistence scatterers based on ensemble coherence

The main parameter used to select the initial potential persistent scatterers (PPS's) in this research is the amplitude dispersion index threshold. This parameter is based on the consistency of the backscatter value over time and is calculated as the standard deviation of the amplitude value in relation to the temporal mean for that pixel (Kampes, 2006). The amplitude dispersion index threshold used for the final PSI analysis in the research was 0.27. In other studies thresholds between 0.25 and 0.4 have been used (Colesanti et al., 2003; Ferretti et al., 2001).

There are two advantages of selecting PPS's based on the amplitude, rather than directly excluding pixels with a low coherence for each individual interferogram. First, a pixel with low amplitude will have a relatively high coherence, as a consequence of the signal-to-noise ratio. Second, in coherence estimates the values of neighbouring pixels are included. Individual isolated PS' can therefore be excluded due to low coherence in the area.

Only after the estimation and removal of the atmospheric phase based on the PPS values, the complex ensemble coherence is calculated for each PPS. This ensemble coherence index can be used to estimate the reliability of the PS measurements. Instead of estimating the signal-to-noise ratio for each interferogram pixel, based on the phase difference in a window of neighbouring pixels, this coherence is based on the phase consistency over time (Kampes, 2006).

The accuracy of the deformation value measured at each PPS will be related to the ensemble coherence, because coherence is an indicator for the signal-to-noise ratio. In Figure 6.8 this relationship is demonstrated. The measured deformation values are plotted over ensemble coherence values of the corresponding PPS's. The graph shows that the

variance of the deformation measurements is high for PPS's with low ensemble coherence. The line in the graph represents the inter-quartile range, which is the difference between the 25th percentile and the 75th percentile values over each lag. The lags in this graph are steps of 0.01 on the ensemble coherence axis.

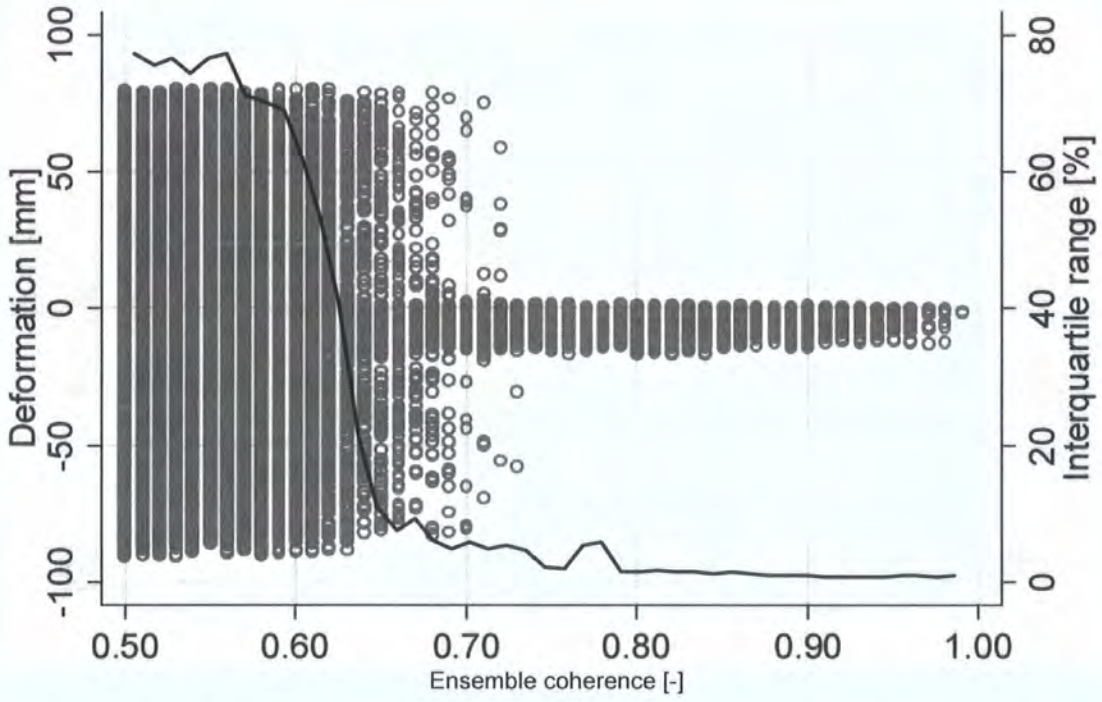

Figure 6.8: PSI measurements deformation plotted over ensemble coherence, showing range and variance.

Based on this relationship and the spatial correlation between the PPS's and the land cover at the surface, an ensemble coherence threshold of 0.8 was selected. All PPS's with an ensemble coherence of more than 0.8 were selected as PS's. More valuable deformation information is present in the PPS's with lower ensemble coherence, but for this research they were excluded.

6.3.2. Density and distribution of persistent scatterers

Pixels that are excluded from unwrapping in conventional InSAR due to low coherence values of neighbouring pixels can contain valuable information. In PSI these pixels are selected and initially used to estimate the topographic phase and the path delay phase and finally to estimate the deformation phase. Unwrapping is not done pixel by pixel, but by connecting the persistent scatterers in space and time. The feasibility of PSI to measure gradual ground surface deformation in a temperate rural area depends on the density and spatial distribution of individual isolated man-made structures or exposed rocks (Colesanti

et al., 2003). The density of PS's in urban areas is found to be between 100 and 300 PS/km^2 (Colesanti et al., 2003). In the Boulby research area the density is 6.4 PS/km^2 (Fig.6.9).

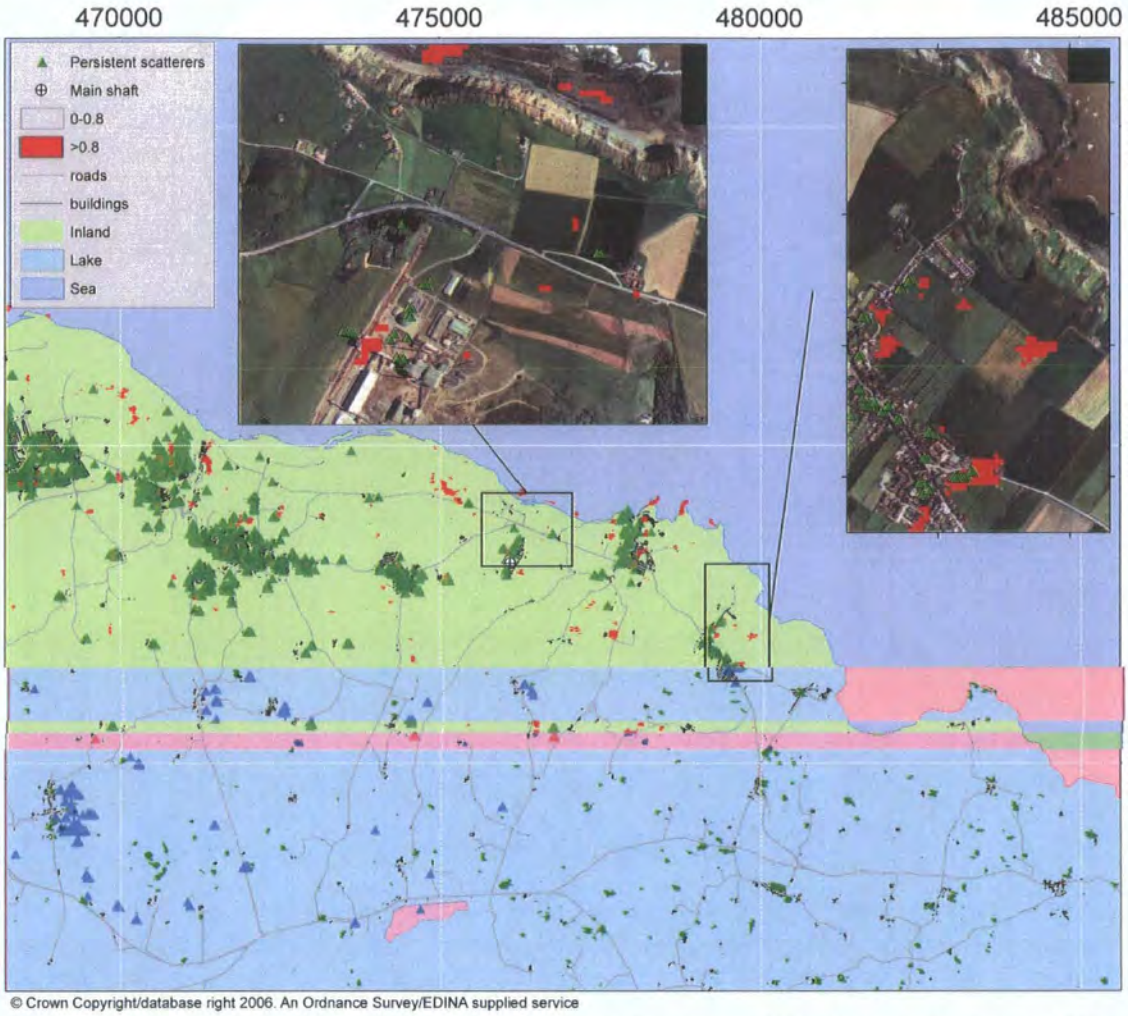

Figure 6.9: Pixels with coherence>0.8 based on the April tandem interferogram and PS's with ensemble coherence>0.8.

In Figure 6.9 the difference between coherence based on one tandem interferogram is compared to the location of PPS pixels with an ensemble coherence of more than 0.8. The miss-match between the two types of pixels is visible. While pixels with a high coherence based on one interferogram are clustered, the PPS's with high ensemble coherence are frequently located in isolated locations.

The PPS's can be spatially joined to the LCM land cover classes as described in chapter three. The join with this land cover classification allows for the statistical analysis of ensemble coherence values found in the different land cover classes (Fig. 6.10).

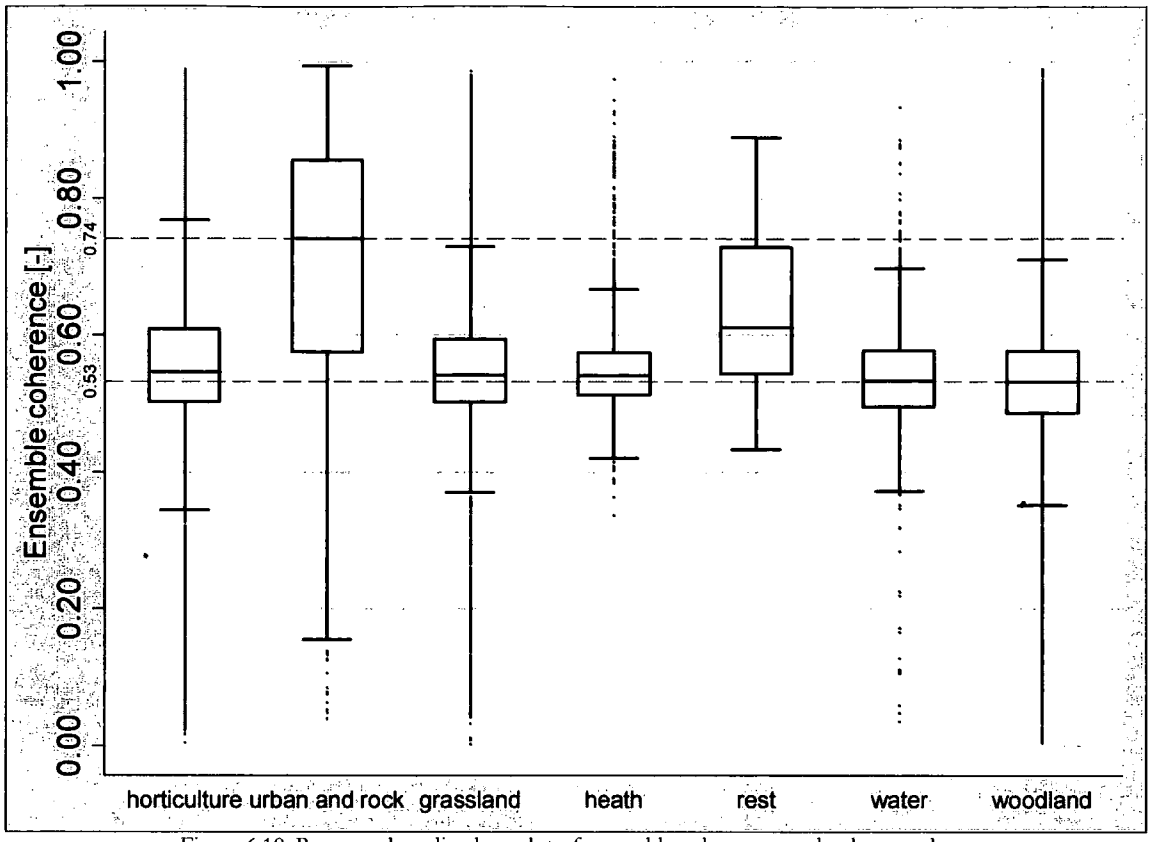

Figure 6.10: Range and median box plot of ensemble coherence per land cover class.

The PPS's located in an area classified as 'urban and rock' have a median ensemble coherence of 0.74. Unfortunately only 4% of the research area is classified as urban or rock. The PPS's located in area classified as 'rest' have a median ensemble coherence of 0.64. This class includes areas covered by fen, marsh, swamp and inland bare ground and comprises 3% of the research area. The remaining 93% of the area is covered by the other five classes. The ensemble coherence of PPS's that are located in these land cover classes ranges between 0 and 1, but the median values are all close to 0.53.

The variance found in these values is partly a genuine variance indicating the presence of potential persistent scatterers next to pure noise values in most classes. However part of the variance is likely to be caused by spatial inaccuracy of the PPS's when projected on the OSGB grid, inherent to radar data (Woodhouse, 2006). As a consequence, some of the PPS's may have been missclassified.

6.3.3. PSI versus levelling measurements

The total deformation values in Figure 6.11 represent deformation measured in the research area by levelling surveys. From the levelling dataset, the expected amount of deformation in the PSI interval should be approximately [8.6/29.5] times the total

deformation corresponding to a total maximum deformation of 187 mm and a total mean deformation of 54.8 mm In Figure 6.12 the deformation measured by the PSI analysis is given.

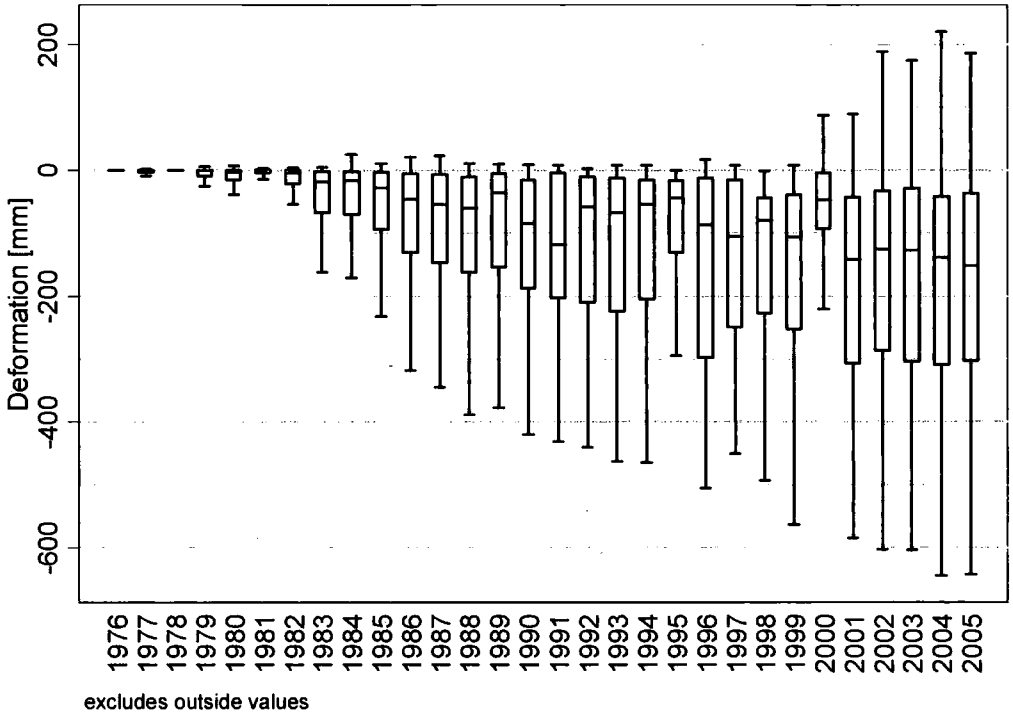

Figure 6.11: Graph showing all levelling deformation data, grouped by year where a box represents the 25 percentile, 75 percentile and median values, lines represent the 5 percentile and 95 percentile values, outliers are excluded.

Both the total mean (27 mm) and total maximum deformation (144 mm) measured by PSI in the research area are less than the measured values. Underestimation of deformation has been found by other PSI feasibility studies (Walter et al., 2004), but can not be proven in this research. Although the mean of all PSI measurements suggests an underestimation, this may be caused by the use of a disproportionate number of measurements in areas not affected by deformation. The maximum deformation may have taken place in a part of the research area where no PS was located.

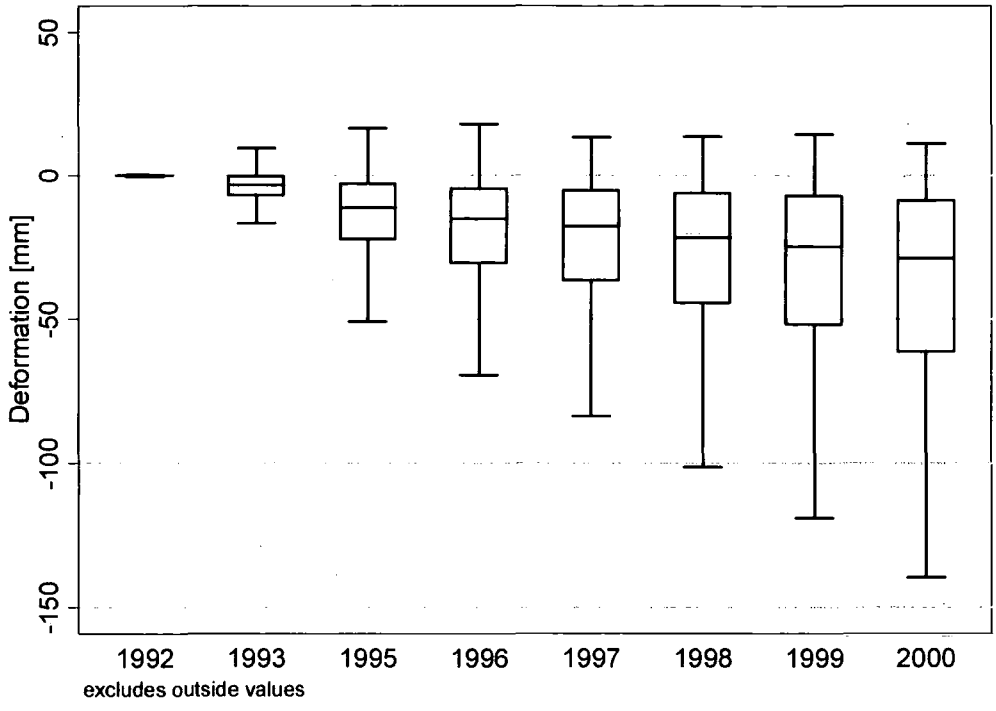

Figure 6.12: Graph showing all PSI deformation data, grouped by year where a box represents the 25 percentile, 75 percentile and mean values, lines represent the 5 percentile and 95 percentile values, outliers are excluded.

Notable though in Figure 6.12 is the linear trend in the PSI dataset, also found in other publications of PSI analysis (Kircher et al., 2003; Walter et al., 2004). Since the interferometric phase values have a range of 56 mm, the actual relative deformation between two PS's is based on pre-existing knowledge on the deformation process. Currently, the unwrapping process of the PSI edges is based on a uni-variable linear model.

Relative phase difference within one interferogram that varies from the trend throughout all interferograms is considered as atmospheric distortion. The expected trend over time is entered as *a priori* input for the PSI analysis and can be a non-linear uni-variate model. In many actual ground surface deformation processes the deformation is non-linear and multi-variate over time and space. This makes the separation between atmospheric distortion and ground surface deformation a complex and possibly weak step in the PSI technique.

To compare the two datasets, deformation is converted to annual deformation rate over the two monitoring intervals. In Figures 6.13 and 6.14 the total deformation rate measurements are plotted over a shape of the current mine plan.

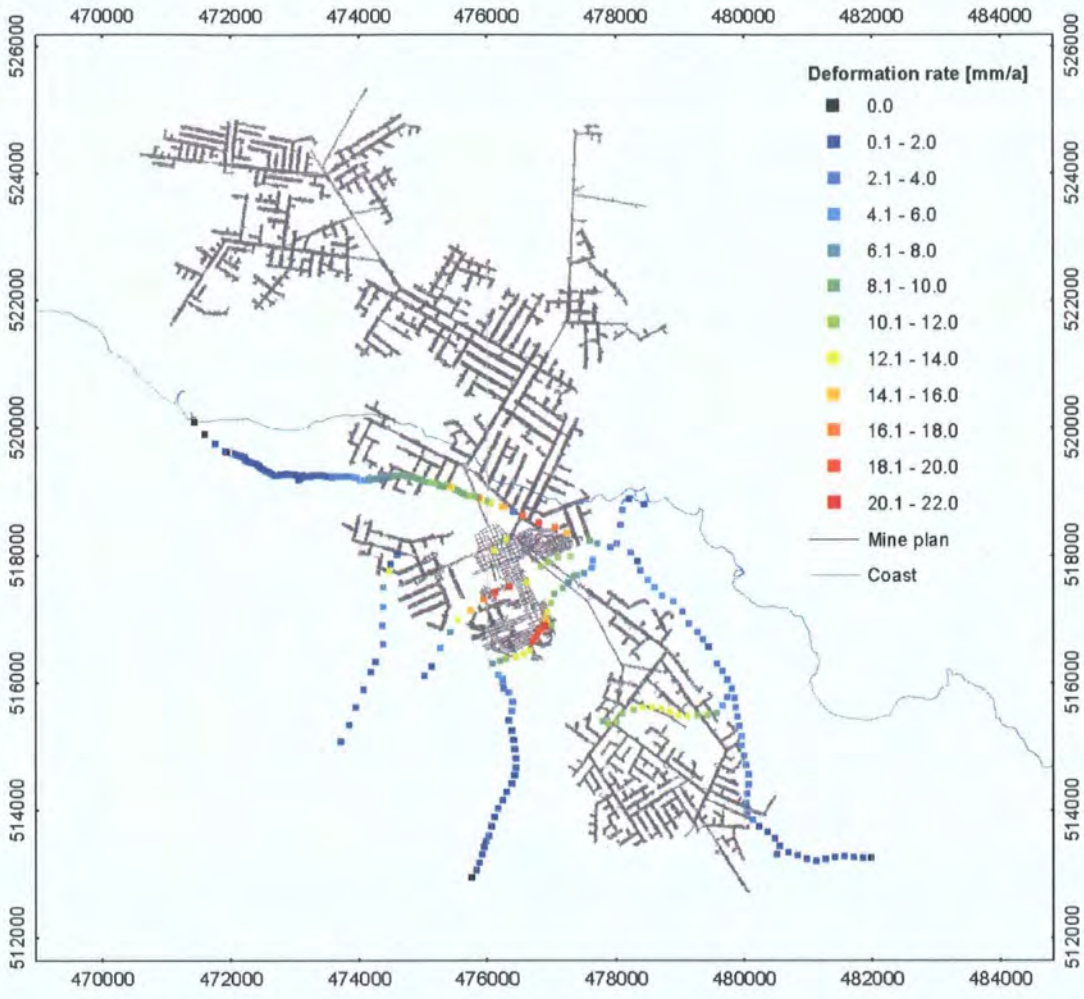

Figure 6.13: Total deformation rate in the Boulby area over 29.5 year interval measured with levelling surveys, with (in grey) the extent of the mining panels of the potash mine and (in blue) the high water mark coastline.

The coloured markers in Figure 6.13 represent deformation monitoring stations used in the annual levelling surveys. Maximum deformation rates measured with levelling surveys exceeding 21 millimetres per year appears to occur in the centre of the mine, the area where the density of mining activities is highest and the time after mining is longest. A second dip in the deformation pattern is found, located over the concentration of mining units in the south of the research area. Deformation gradually approaches zero moving outwards and beyond the extent of the undermined area.

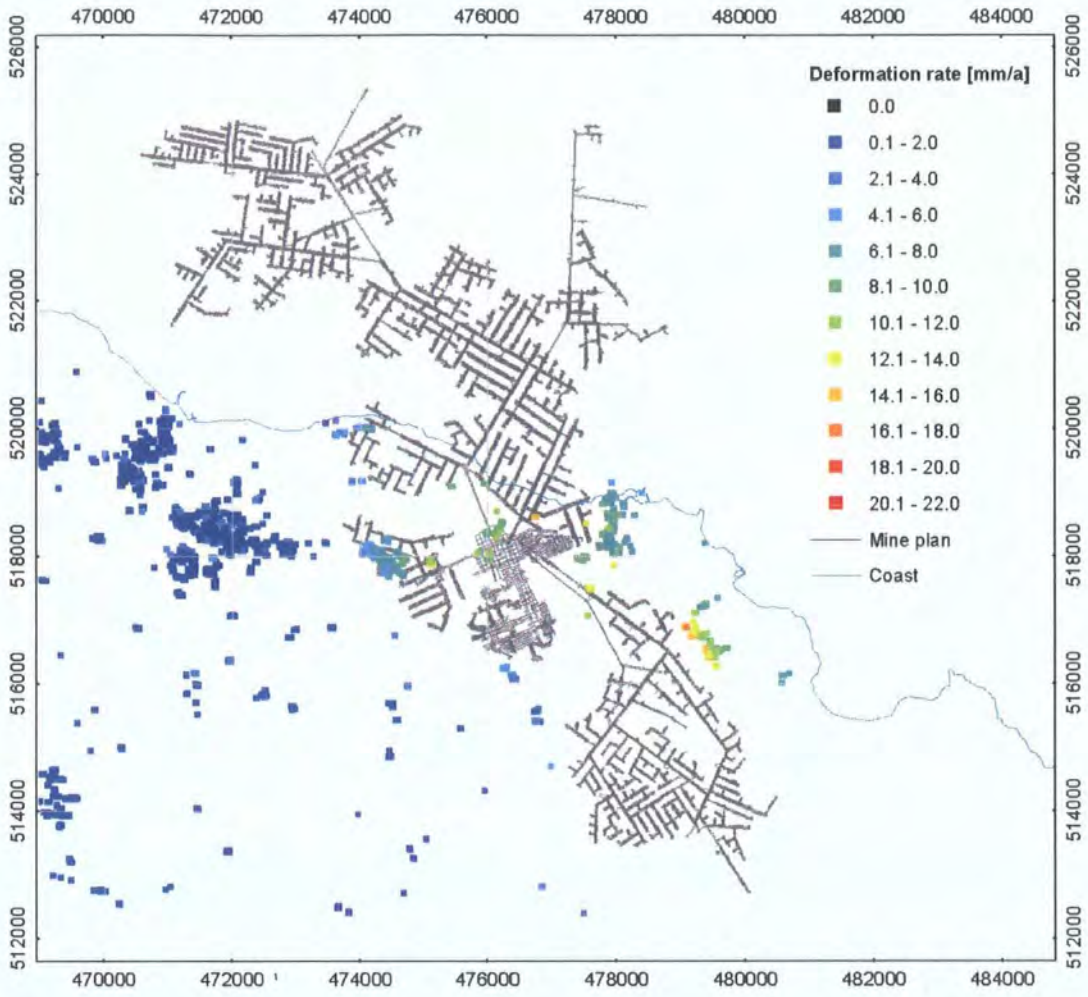

Figure 6.14: Total deformation rate in the Boulby area over 8.6 year interval measured with PSI, with (in grey) the extent of the mining panels of the potash mine and (in blue) the high water mark coastline.

With PSI, the highest deformation values were measured in the area around Hinderwell village in the east of the research area. In the period 1992-2000, the time interval covered by the PSI dataset, this was an area experiencing active undermining. On the eastern edge of the undermined area, the shape of the affected area corresponds closely with the deformation measured in the levelling survey. The PSI measurements indicate a total deformation between 50 and 130 millimetres in the Hinderwell area (Fig. 6.15).

The levelling measurements in that area over that period indicate a total deformation between 50 and 75 millimetres. There is an overestimation of the deformation in a large proportion of the persistent scatterers in the Hinderwell area.

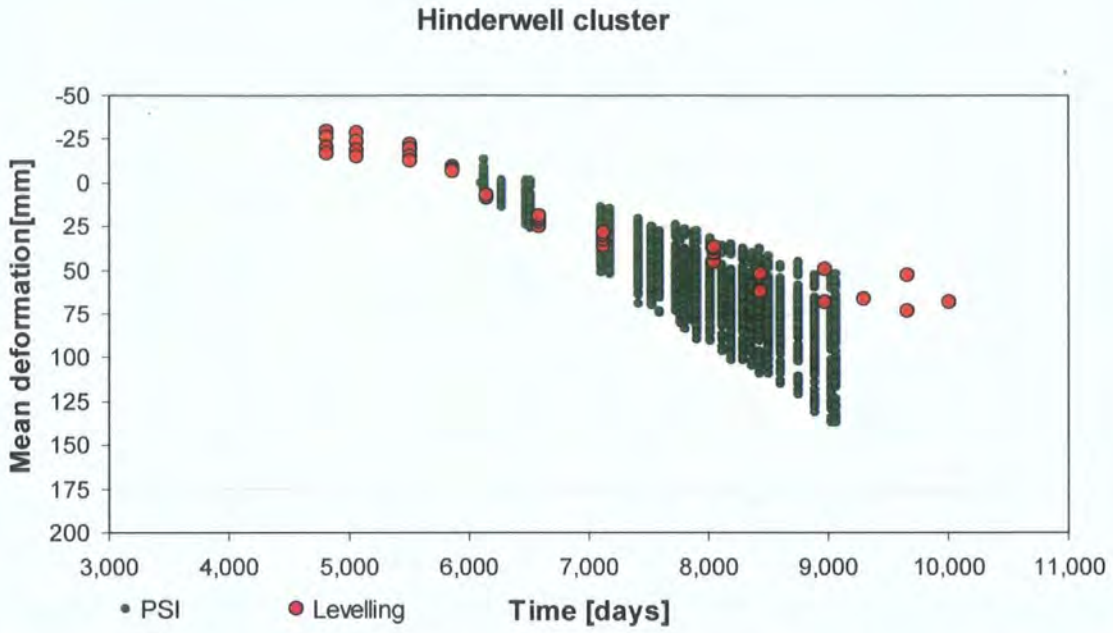

Figure 6.15: Deformation [mm] plotted over time measured by PSI and levelling, around the village of Hinderwell.

The levelling dataset describes the measured behaviour of the surface from the beginning of the potash mining in May 1976 until today a period of 29.5 years. The InSAR dataset only describes the behaviour at an 8.6 year time interval, from 9 September 1992 till 21 October 2000. The accuracy of the PSI measurements has a theoretical limit of approximately 1 mm (Colesanti et al., 2003). The maximum deformation in the research area increased gradually from zero in May 1976 to 643 mm in November 2005, according to the levelling dataset (Fig. 6.15). The total mean deformation reached a value of 188 mm.

6.4. Data-driven modelling

6.4.1. Advantages over other modelling types

The advantages of a data-driven model over other models are its relative simplicity in the calculations and at the same time its ability to estimate deformation in a four dimensional space. As a result of its simplicity, a data-driven model is pragmatic and universally applicable. Empirical models, such as the SEH- model offer a similar simplicity and universality (NCB, 1966). The fact that they are used extensively despite clear discrepancies between the model and the measured deformation is a sign that there is a need in industry for easily applicable models. However, the problem with such models is that they are based on one or more actual datasets and are subsequently used elsewhere.

Deterministic and numerical models are useful tools to determine the impact of specific phenomena in the mining process, such as brine inflow or inclination of the seam. The ability of such models to estimate the deformation at the surface depends on the detail in which deformation is migrated from seam to surface. This requires a great detail of information on the actual layers in the ground. In addition to this, the actual behaviour of the ground layers under great stress is often unknown.

In a data-driven model such as the cone model, the estimations are based on specific local conditions. Although most of these conditions are unknown, they will be reflected in the found algorithms. In this research, the data-driven cone model was applied to deep potash excavation and as a consequence is able to calculate future deformation rates. In a similar way, this cone model could be applied to mine workings in a different area or even to the location of tunnel segments or limestone dilution chambers in combination with data on the deformation of the ground surface. In each new situation a complete new set of algorithms has to be produced, based on multivariate regression. The cone model sets up the link between the datasets and can generate the four variables and median values that form the input to the regression. For the cone model to be able to find these variables the two datasets need to contain x, y, z and t values.

6.4.2. Use of median values

In data-driven modelling, the variation in large datasets is applied to understand and predict the dynamics of a process. In the data-driven cone model, the initial graphs that plotted the deformation rate over the variables was considerably scattered and did not contain much information. To subtract this information, a representative summary of the data had to be made. By using the median or 50^{th} percentile value, outliers did not have any affect on the used values and the correlation between deformation arte and variable was based on the most common values.

The medians were taken over bins with a flexible interval. The interval was based on the number of values found. This was to make sure that a relative small number of deformation values occurring at an odd variable value would influence the trend. Again this was done to ensure that the regression analysis was based on the most common values.

6.4.3. Boundaries of ground surface deformation

In the influence function method, the extent of the deformation area is determined by the angle of draw parameter (Whittaker and Reddish, 1989). In the data-driven cone model this parameter is also used to determine the zone of influence. In the case of deep underground mining, with excavations located at 1000 m below the surface, an error in angle of draw of will result into a considerable error in estimation of the zone of influence. The angle of draw for the Boulby site has been determined by assessing the measured rate of deformation in relation to the lowest angle between the survey point and the nearest mining panel (Fig. 6.16).

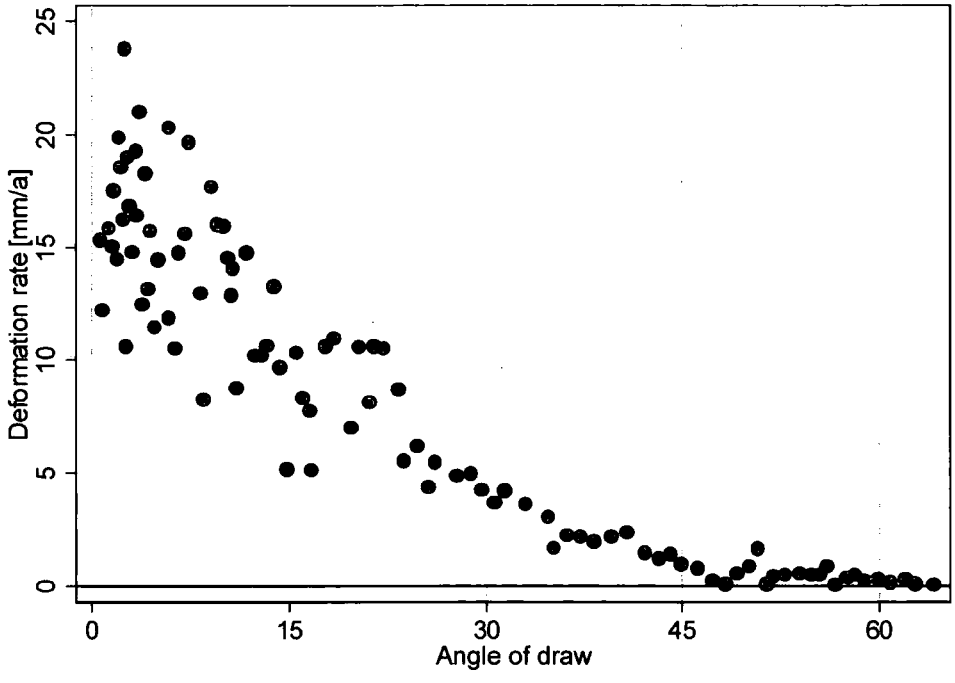

Figure 6.16: Deformation rate over angle of draw

It is clear that ground surface deformation rate decreases with increasing minimum angle values. Although statistically there appears to be a small measurable effect in terms of ground surface deformation at angles as high as 60°, this effect tends to 0 after minimum angles greater than 45°. In the Soma coal basin in Turkey, underground mining at a depth of 100 metres in has caused the ground surface to subside up to six metres. Coal mining has taken place there for more than 100 years based on a non-mechanised longwall method (Aksoy et al., 2003). The angle of draw that was found based on numerical modelling and laboratory tests is 50 degrees (Aksoy et al., 2003). Typically the angle lies between 31 and 54° (Kratzsch, 1983).

The gradual trend towards zero in Fig. 6.16 is an illustration of the fact that ground surface deformation does not have a fixed boundary. The first key indicator of ground surface deformation, as defined in section 2.2, is 'the outside shape of the subsidence area: a shape along the outside of the disturbed surface area, where the ground surface is unaffected'. With the term unaffected a state is meant where the experienced deformation is regarded stable. This is subjective and will vary in different parts of the world. In the Boulby area ground surface that experiences a total deformation of 2 mm or less and a deformation rate of 0.2 mm a^{-1} or less is regarded as stable. The threshold value of 0.2 mm a^{-1} was also used to determine the point in time at which the area can be considered stable.

6.4.4. Environmental factors

The cone model algorithms developed in this research are specific to the Boulby research area. The data used to establish the algorithms and angle of draw parameter contain information on the local geology. An important condition for this assumption is that the geology is homogeneous throughout the area. If a variation in geology shows correlation with the deformation rate in the area, this should be included explicitly in the final algorithms.

The geology in the Boulby research area is described in chapter two and consists of a thin layer of Permian evaporites covered by a series of sedimentary layers (Fig. 6.17). The thickness of the different layers is homogeneous but shows a slight tilt in NW-SE direction of approximately 5°(Milne, 1978). With the use of the cone model tool, the levelling dataset was spatially joined to the thickness of three layer combinations. These layer combinations seem to show a correlation with the rate of deformation:

- The Triassic Bunter Sandstone layer, which has a water-bearing capacity and is located immediately above the Permian evaporites (Rayner and Hemingway., 1974).
- The Lower Jurassic Lias, at the top of the geology only covered by boulder clay
- All layers, or the depth of the potash layer from the surface

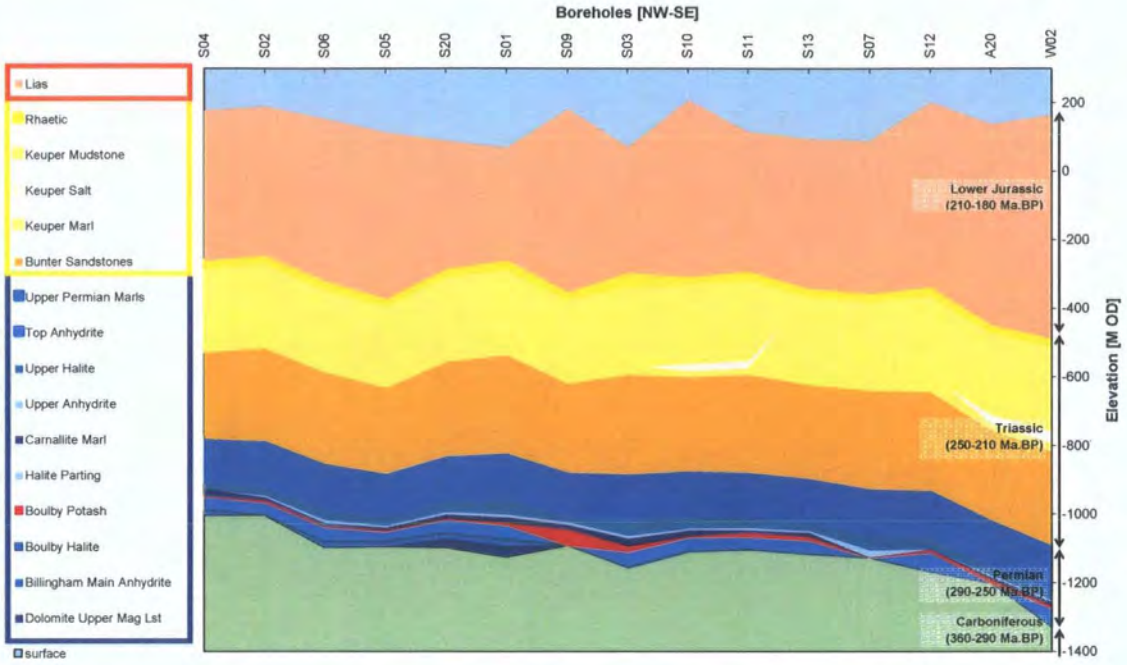

Figure 6.17: Geological layers ordered from NW to SE (chapter three)

To spatially join the geology borehole dataset with the levelling dataset, interpolations of the borehole data were made. The method used for these interpolations was the minimum curvature spline interpolation (Mitas and Mitasova, 1988). The interpolated surface is created with a minimum curvature and crosses the known values at the locations of the boreholes.

The spatial join between the depth of the potash layer and the survey stations is based on the excavation dataset, which includes the depth from the surface of each mine panel (chapter three). The correlation between the estimated thickness of the three layer combinations at the survey stations and the measured deformation rate is demonstrated in Figure 6.18 and spatially in Figures 6.19, 6.20 and 6.21.

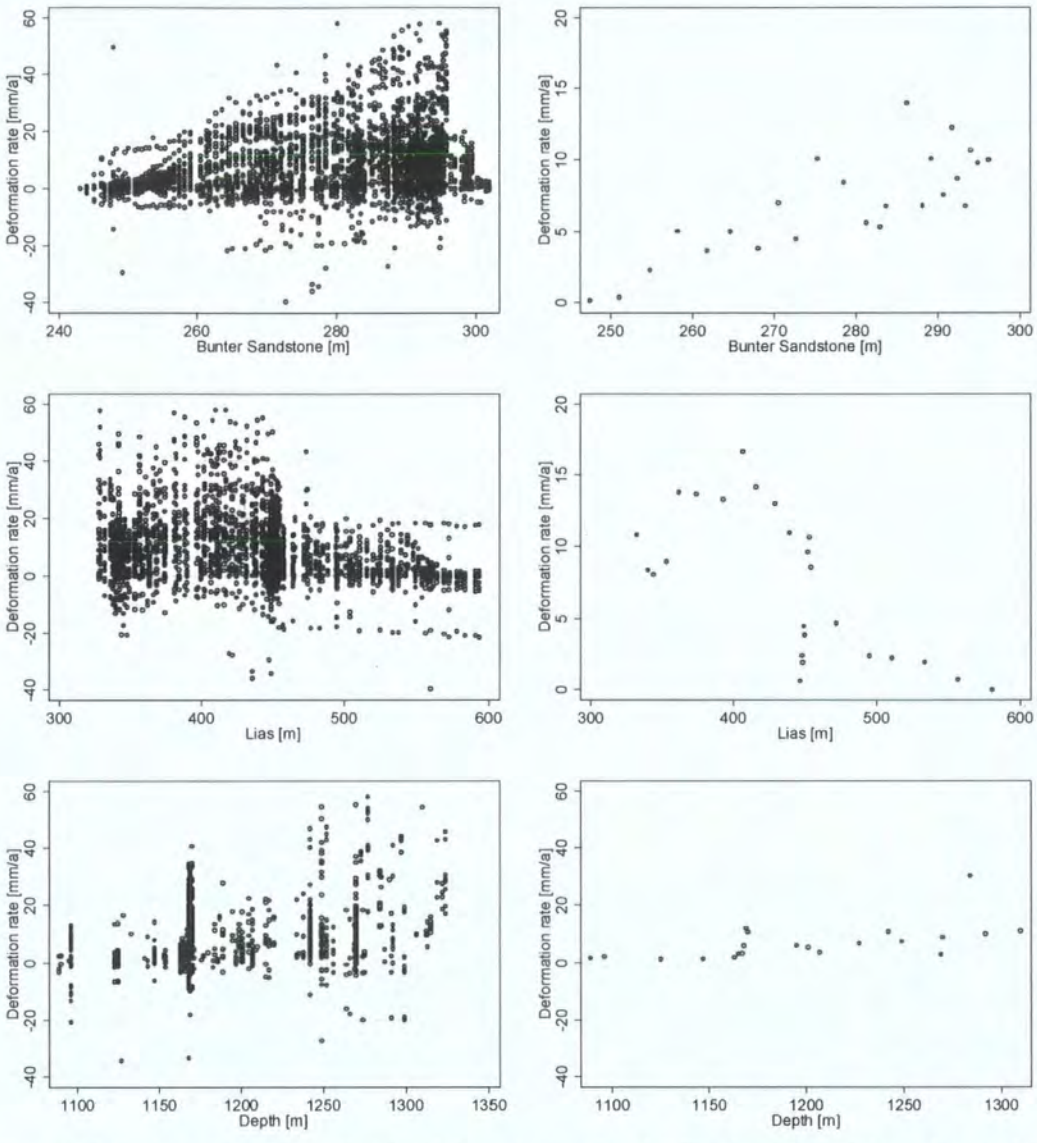

Figure 6.18: Geology variables plotted against deformation rate from levelling data (left) and the medians (right)

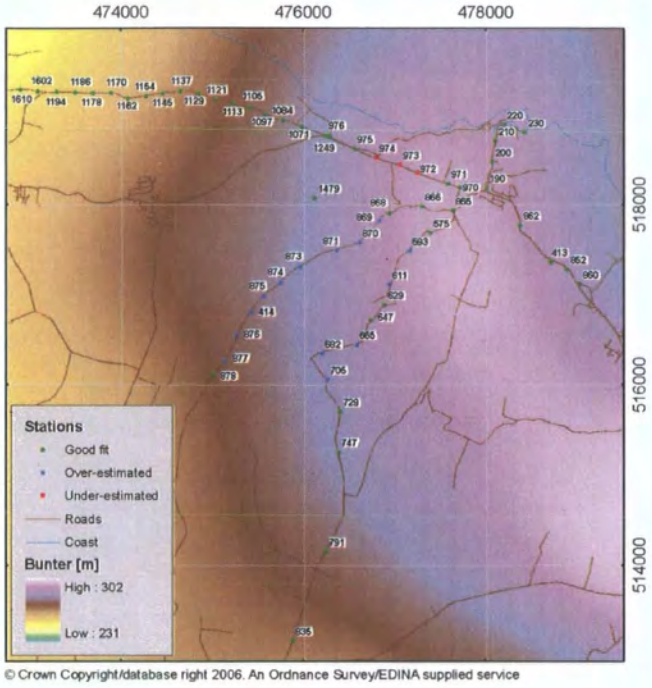

Figure 6.19: Location of classified evaluation stations plotted on the interpolated surface of Bunter Sandstone

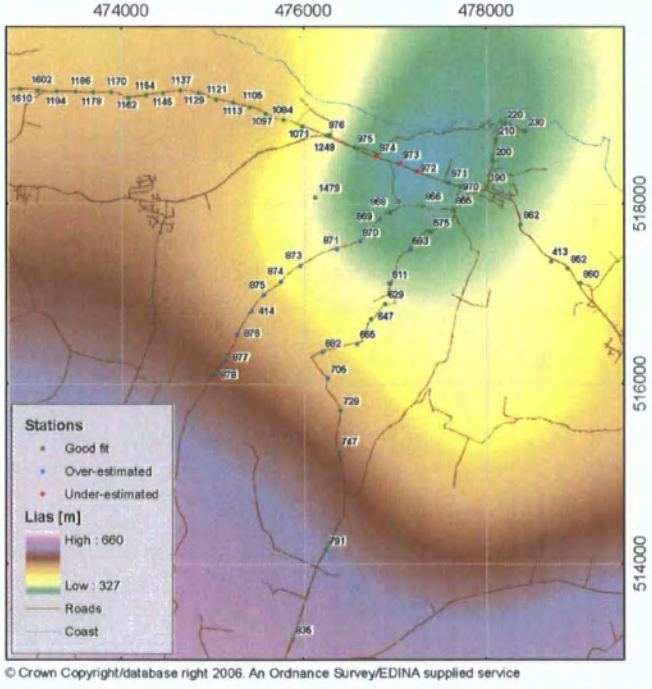

Figure 6.20: Location of classified evaluation stations plotted on the interpolated surface of Lias

Figure 6.21: Location of classified evaluation stations and the depth of the mine panels, in steps of 100 m

The current algorithms used to estimate the deformation rate based on the cone model do not include these variables. The accuracy of the estimation could be improved if these variables were included. The other geology layers such as Keuper marls did not show a consistent correlation with deformation rate (Fig. 6.22).

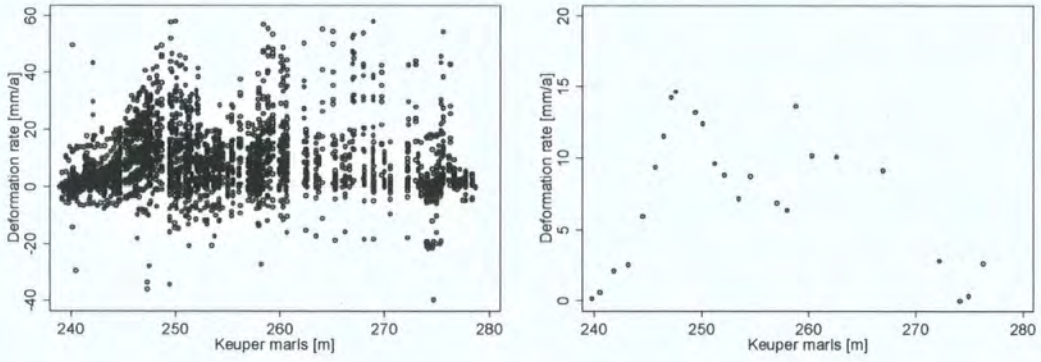

Figure 6.22: Geology variables plotted against deformation rate from levelling data (left) and the medians (right)

An alternative way to include variations in the cone model is by dividing the area up into homogeneous zones and to generate algorithms for each of these zones. This could improve the estimations in areas with distinctly different zones. In the Boulby area a zonal divide could have been made between the sea and the inland parts of the undermined area. However, this would require ground surface deformation data of both zones; only data for the inland part was available. The deformation of the sea floor is assumed to behave in a similar way to the deformation inland.

Another spatial variation in the Boulby area may be related to the presence of old mine workings. Underground mining in the United Kingdom has taken place since pre-historic times and has been an important economic sector since the 17th century. It is likely that a large proportion of the workings is still open at present and may collapse or continue to settle gradually in the future. A problem is that many old workings are not recorded or limited. The production of mine plans only became statutory in 1872 in the United Kingdom (Bell et al., 2000). The use of different algorithms in zones is applied to the influence function model developed for coal mine related ground surface deformation in India. Significantly more subsidence was found in multi-seam workings (Sheorey et al., 2000).

In the Boulby area mine plans of the ironstone mines are available. However, a correlation between the location of the ironstone mines and the location of stations with over- or under-estimation was not found (Fig. 6.23). As a consequence, the same algorithms were used in both single and multi-seam parts of the mine.

The data-driven cone model does not include any environmental variables. However there are two ways in which such variables can be included in situations where these variables have a significant influence on the ground surface deformation. Depending on the amount of spatial variation they can be included in the cone model by including the correlation between this variable and the deformation rate in the algorithms, or by dividing the area into zones.

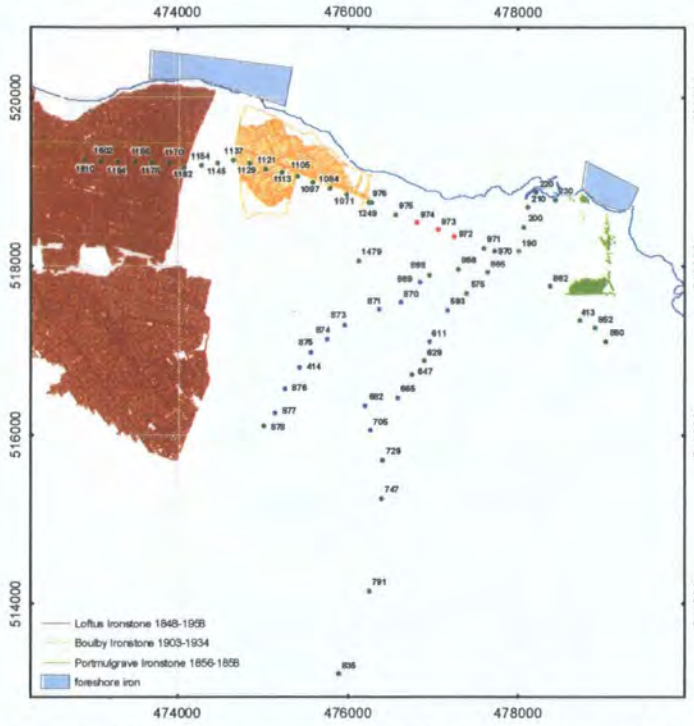

Figure 6.23: Location of classified evaluation stations and the depth of the mine panels, classified steps of 100 m

6.5. Conclusion

The feasibility of conventional InSAR is limited due to its failure to estimate and remove the atmospheric phase on the one hand and its failure to deal with areas of low coherence on the other hand. Atmospheric distortion can lead to considerable errors, such as found in the InSAR DEM of the Boulby area. At short temporal baselines, coherence in a rural area can be acceptable for conventional InSAR, but will decrease rapidly after 35 days where the coherence in an area with rural land-cover approaches the same coherence as that of water bodies.

One of the advantages of the PSI technique is the ability to estimate the atmospheric phase. This is based on the assumption that, in the statistical analysis of a large time series of interferograms, spatial variation in relative deformation within one interferogram is caused by atmospheric distortion. Only the relative deformation that is consistent throughout all interferograms is considered as actual ground surface deformation. The model that is used to validate this rule can be linear or non-linear over time. However, in many actual ground surface deformation processes the deformation is non-linear over both time and space. This makes the separation between atmospheric distortion and ground surface deformation a complex and possibly weak step in the PSI technique.

The PS's found in the research area were clustered around villages and have a low density of 6.4 km^{-2}. The density of potential PS's is much higher, but these were filtered out due to their low ensemble coherence. The use of additional radar datasets may lead to the inclusion of more PS's. In the Groningen gas field example described in chapter two, the density of PS's in a temperate rural area was much higher. A total of 105 radar scenes were used of both descending and ascending orbits (Ketelaar et al., 2005). The large time series of interferograms enabled a more profound statistical analysis of the amplitude dispersion and ensemble coherence of the potential PS's.

The development of geomorphological science and subsidence engineering can benefit from the increased availability of large datasets. The disciplines of geodesy and remote sensing can improve the development of the InSAR technique by incorporating the understanding of Earth surface processes present in geomorphology and subsidence engineering. The data-driven cone model developed in this research has proven that the complex temporally and spatially non-linear ground surface deformation process can be linked to and predicted by the excavation dynamics.

This model is based on the trend found in the median ground surface deformation over four chosen variables. Other variables such as geology or the presence of old mines can be included in the cone model as variables or by stratification of the area into homogeneous zones. To determine boundaries of deformation in space and time, the use of a threshold value at which the ground surface is considered stable is necessary.

CHAPTER 7. CONCLUSIONS

7.1. Summary of results

The relevance of local gradual ground surface deformation is recognised in literature as part of the understanding of our Earth system (Carbognin, 1997; Cloetingh et al., 2005; Goudie and Viles, 1998). In coastal areas the rate of lowering of the ground is similar to the experienced rate of relative sea-level change and will have a similar effect on coastal processes, such as cliff erosion (Humphries, 2001). To accurately estimate the amount of sea-level rise and its total effect on, for example frequency of flooding or salt-water intrusion, the amount of ground surface deformation in the form of either subsidence or uplift, need to be known accurately and at different scales.

In this thesis ground surface dynamics are studied in relation to contemporary underground mining activities by means of a data-driven methodology. Mining-induced deformation has been monitored and modelled extensively to gain an understanding and control over the quantitative impact on the ground surface.

Following the increase in availability of radar scenes suitable for InSAR analysis from 1991, a large number of studies has been carried out on the InSAR technique and its applicability to different geomorphologic and other processes (Bürgmann et al., 2000; Hanssen, 2001; Klees and Massonnet, 1999; Massonnet and Feigl, 1998; Rosen et al., 2000; Wegmuller et al., 2004). Currently the most successful technique is the Persistent Scatterer InSAR (PSI) technique which requires the acquisition of a large number of radar scenes to measure horizontal and vertical ground surface deformation at mm accuracy. The feasibility of this technique to monitor gradual ground surface deformation is theoretically better than conventional InSAR in areas with high decorrelation; however this had not been confirmed with feasibility tests.

The feasibility of conventional InSAR is limited, on the one hand, due to its failure to estimate and remove the atmospheric phase and on the other hand, due to its failure to deal with areas of low coherence. Atmospheric distortion can lead to considerable errors, such as found in the InSAR DEM of the Boulby area. At short temporal baselines coherence in a rural area can be acceptable for conventional InSAR, but will decrease rapidly after 35 days where the coherence in an area with rural land-cover approaches the same coherence as that of water bodies.

In a temperate climate, areas with rural land use have a high temporal decorrelation that result in low coherence and discontinuous fringes in an interferogram. The mean coherence of an interferogram is negatively correlated with the temporal baseline. Scenes taken more than 35 days apart are generally too decorrelated to result in continuous fringes. A perpendicular baseline of more than 200 metres was found to decrease the mean coherence of an interferogram due to the geometric deformation of the individual pixels. Coherence varies in the area and was compared for four land cover types, urban, rural, sea and lake. The coherence was considerably higher for the urban land cover type, which comprises small villages in the research area. To acquire reliable measurements from conventional InSAR, a balance needs to be found between a short enough time interval to conserve coherence and a long enough time interval to allow for a measurable amount of deformation to have taken place. This balance is hard to find in areas with land use of a highly temporally decorrelating nature such as found in the Boulby research area.

In this thesis, the Persistent Scatterer InSAR (PSI) technique is proven to be applicable in situations not suitable for conventional InSAR. It was found that PSI is applicable to a temperate rural area with a low density of artificial or bare structures and high amounts of moisture in the atmosphere. The density of the PS's with an amplitude dispersion of 0.27 and an ensemble coherence higher than 0.8 is 6.4 PS km^{-2}, which is low compared to the density in urban areas of 100-300 PS km^{-2} (Colesanti et al., 2003).

The distribution of the PS's in the research area was found insufficient to replace the levelling survey technique to monitor gradual ground surface deformation. The deformation rates measured with PSI are similar to the rates measured with levelling, but they are more linear. The a-priori model used in the PSI analysis to separate atmospheric distortion from surface deformation was linear and this will have influenced the final outcomes (Kampes, 2006).

Ability to estimate the atmospheric phase is one of the advantages of the PSI technique. This is based on the assumption that in the statistical analysis of a large time series of interferograms, spatial variation in relative deformation within one interferogram is caused by atmospheric distortion. Only the relative deformation that is consistent throughout all interferograms is considered as the actual deformation. The model that is used to validate this rule can be linear or non-linear over time. However in many actual ground surface deformation processes the deformation is non-linear over both time and space. This makes

the separation between atmospheric distortion and ground surface deformation a complex and possibly weak step in the PSI technique.

The density of potential PS's is much higher, but these were filtered out due to their low ensemble coherence. The use of more datasets may lead to the inclusion of more PS's. In the Groningen gas field example described in chapter two, the density of PS's in a temperate rural area was much higher. A total of 105 radar scenes were used of both descending and ascending orbits (Ketelaar et al., 2005). The large time series of interferograms enabled a more profound statistical analysis of the amplitude dispersion and ensemble coherence of the potential PS's.

The main advantages of using a remote sensing technique to monitor ground surface deformation are the independence of this dataset from existing datasets and the ability to choose a reference point far away from the observed process. The reference point can be located anywhere in a radar scene which, in the case of ERS satellite imagery, is 100 km^2. In ground-based monitoring techniques, the reference point has to form part of the levelling sequence and will therefore be placed in close proximity of the observed process. If mine workings progress spatially, the reference point can sometimes be affected by the observed process, which can lead to large errors in the measured relative elevation change at the other monitoring stations (Anderson and Mikhail, 1998).

The development of geomorphological science and subsidence engineering can benefit from the increased availability of large datasets. Simultaneously, the disciplines of geodesy and remote sensing can improve the development of the PSI technique by incorporating the understanding of Earth surface processes present in geomorphology and subsidence engineering. The data-driven cone model developed in this research has proven that the complex temporally and spatially non-linear ground surface deformation process can be linked to and predicted by the excavation dynamics (Fig. 7.1).

The major requirement for this data-driven approach is the availability of monitoring datasets of sufficiently high spatial and temporal resolution to allow meaningful relationships to be established (Kemeling et al., 2004). Recent developments in remote sensing techniques, most notably PSI, are beginning to allow for acquisition of such extensive subsidence datasets, providing greatly enhanced capabilities for the analysis of the behaviour of subsidence processes in space and time (Chilès and Delfiner, 1999).

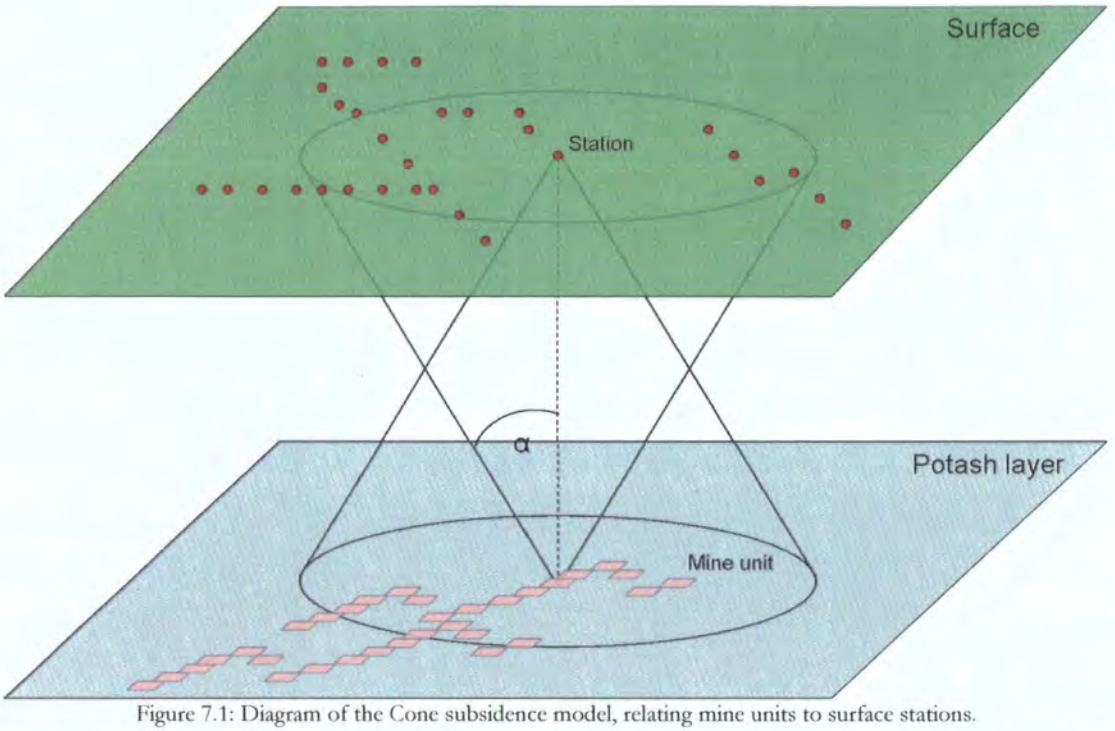

Figure 7.1: Diagram of the Cone subsidence model, relating mine units to surface stations.

The engineering approach to modelling mining deformation is to empirically consider the dynamics of the system in order to calculate the expected strain. Often these predictions are inaccurate when calibrated with real-world data (Ferrari, 1996). This can be due to the fact that the input variables are difficult to measure, or that they are unpredictable or unknown and therefore difficult to model. Many of the engineering laws used in existing functional and empirical models have been developed from coalmines, where excavations are located between 40 to 200 metres below the surface. In cases where mining takes place at more than 1000 metres below the surface, the influence of unknown dynamics is increasingly relevant.

The ability to accurately model the effect of underground mining on ground surface deformation has been limited due to the complexity of the process and the lack of data of sufficient quality and resolution. The two most important limitations of currently existing models are:

- Inability to accurately pre-calculate temporal and spatial variation and extent of ground surface deformation due to limited dimensionality
- Lack of universality in applied method, which translates into the need to establish new variables for each situation

A data-driven approach enables modelling of complex environmental systems such as mining-induced ground surface deformation, when definition of all dynamics affecting the deformation is difficult (Chrzanowski et al., 1997). Instead of using data to calibrate a model, this method applies the statistical knowledge embedded in the datasets. The use of extensive high quality datasets and improved computational capacity enables the inclusion of spatial and temporal dynamics (Whittaker and Reddish, 1989). The raster coverage of the model output gives a representation of the spatial pattern of deformation taking place in the Boulby area (Fig. 7.2).

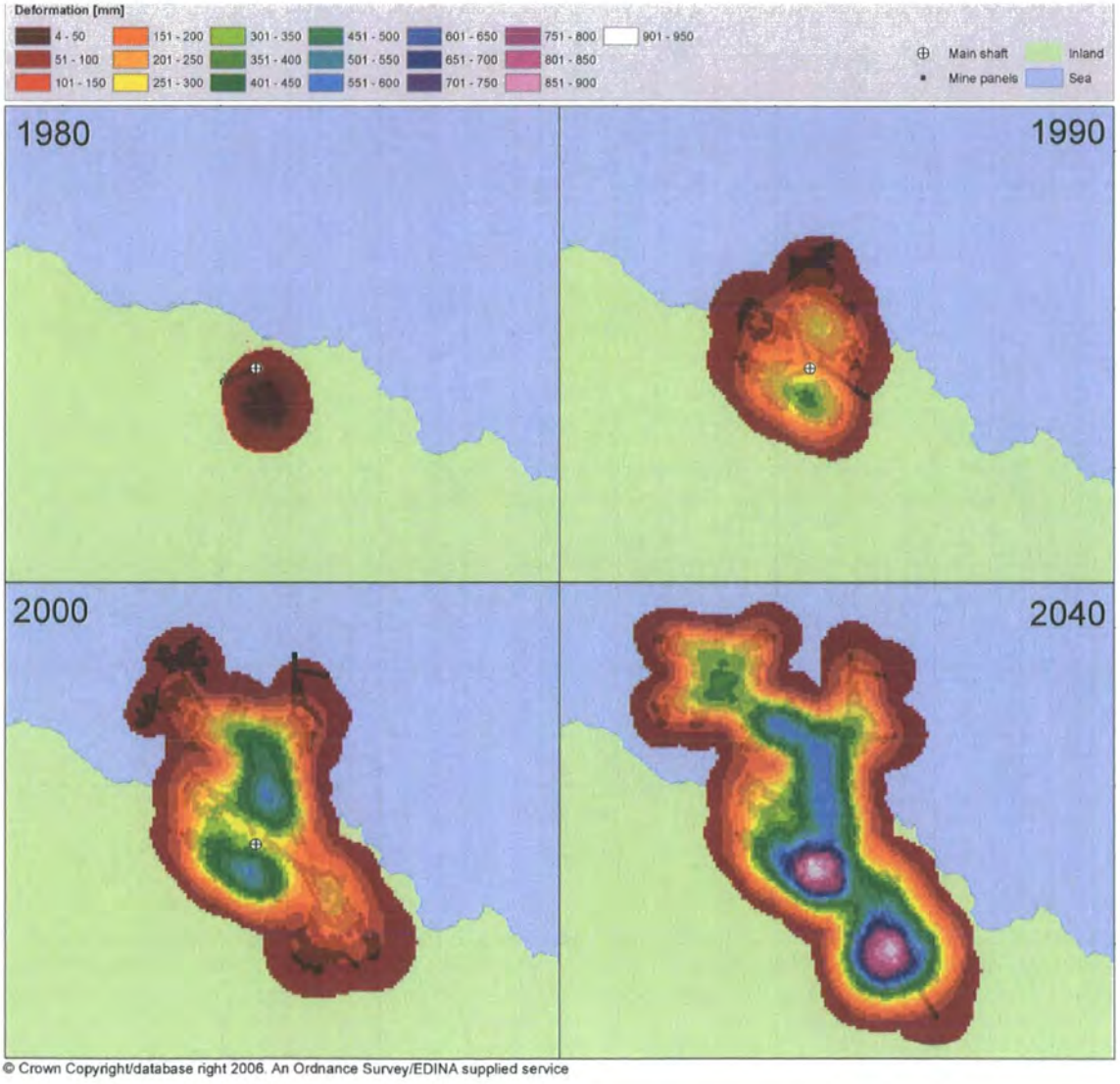

Figure 7.2: Estimated total deformation at four points in time

In this thesis a new data-driven model has been developed based on the spatial and temporal correlation between four variables related to the timing and location of mine panels and annual ground surface deformation rate measured at fixed points at the surface. This was done to analyse the correlation between the variables of a driving process and the variables of a surface deformation process, based on large datasets and ultimately to create and test a tool that enables scenario studies and accurate estimations of future ground surface deformation. This model is based on the trend found in the median ground surface deformation over four chosen variables. Other variables such as geology or the presence of old mines can be included in the cone model as variables or by stratification of the area into homogeneous zones. Because of the gradual decrease in ground surface deformation over space and time, the use of a threshold value at which the ground surface is considered stable, is necessary.

It was found that, based on the angle of draw and four variables, the extent of the disturbed area, the total period of deformation, the peak rate, the moment of the peak rate and the total subsidence can be calculated. These key indicators are relevant to understand the impact of underground excavations on the surface and to place this process in the wider global earth system.

7.2. Recommendations for future research

In the coming years several space borne radar sensors are planned be launched (Kampes, 2006). These new radar sensors, such as the RADARSAT-2, TerraSAR-X and COSMO_SkyMed will have advanced capabilities that differ from the SAR images used in this research. The characteristics include a range of radar wavelengths such as L-band and X-band, shorter revisiting intervals allowing for the acquisition of more images per year and higher spatial resolution of up to one metre. Although technical solutions need to be found to integrate the different sensor characteristics with existing procedures, this suggests both great trust in the potential and a steep increase in the development of InSAR and PSI technology.

An important finding of this thesis is that the PSI technique shows great potential in areas previously considered unsuitable for InSAR to monitor gradual ground surface deformation. The ongoing investigations in the improvement of the statistical analysis of the PSI data will continue to increase this feasibility. It is however essential to understand the spatial and temporal dynamics of the observed process. This is even more important in

areas where atmospheric distortion will lead to spatial variations within the interferogram. More research is needed on the use of improved a-priori models in the PSI technique.

The launch of new satellites specifically designed for InSAR applications will increase the choice in radar imagery in the coming years. The C-band wavelength applied in this thesis is affected by vegetation, which has resulted in high decorrelation (Woodhouse, 2006). The use of L-band radar may improve the feasibility of both conventional InSAR and PSI in rural areas, as the larger wavelength can penetrate dense vegetation and reflect the signal from the ground surface (Chang et al., 2004). The feasibility of L-band InSAR and PSI should be investigated and tested in real situations, such as the Boulby research area.

Horizontal movement caused by underground mining has not been included in this research. According to empirical models, there is a correlation between vertical and horizontal movement caused by underground mining (CPL, 2004; NCB, 1966), more research should be done to confirm or correct this. Due to its side-looking viewing geometry, radar measurements contain horizontal information (Woodhouse, 2006). PSI deformation measurements are initially measured in slant range which is later converted to a vertical and a horizontal component. The horizontal component of a deformation process may contain useful information. The ability to measure horizontal deformation varies and will depend on the aspect of an area in respect to the viewing angle of the used radar. The feasibility of PSI to monitor deformation of steep slopes is a potential area of research.

The coastal cliffs found in the Boulby research area display a high rate of erosion, controlled by climatic and maritime processes. Analysis of the spatial correlation between the cliff erosion and the deformation could lead to a better understanding of the impact of mining on the cliffs. In this thesis the pragmatic cone-model was applied to correlate a deep underground potash mine workings dataset to vertical ground surface deformation rates, the correlation of other datasets of either driving processes or surface deformation processes should be investigated. This type of modelling may be less useful for the understanding of physical mechanics in the ground surface, but because of the spatial and dynamic character of most ground surface deformation processes, the cone model will provide a new and holistic way of integrating cause and effect and may give rise to new ideas about the controls of ground surface deformation.

APPENDIX 1: MATLAB SCRIPT FOR PSI ANALYSIS

```
close all

dbstop if error
 dbstop if warning

% ps_periodogram
%
% This is the main program for PS analysis of real data,
% using the method described in Ferretti et al.,2000,2001
%
% The program consists of a number of modules, which enables
% easy addition of steps and the formulation of alternatives.
%
% The modules are:
% - psc_selection:          reads the data in buffers and
%                     selects the psc, based on amplitude
%                     dispersion.
% - form_network:           forms a network between the psc
%                     by Delauney triangulation.
% - periodogram_psc_est:    estimation of linear deformation
%                     and DEM error of psc by periodogram
%                     technique.
% - periodogram_unwrapping: weighted least-squares unwrapping
%                     of the DEM error, linear velocity
%                     and residual phases
% - periodogram_filtering:  estimation of atmospheric phase
%                     screen (APS) and non-linear defor-
%                     mation by filtering
% - periodogram_APS_kriging: APS interpolation by Kriging.
% - periodogram_ps_est:     estimation of the DEM error
%                     and deformation for ps by periodogram
%                     technique
% - periodogram_viz_ps:     vizualization of the results
%% The program needs an input file 'ps_input_file.txt' (see manual
```

```
% for more information). Besides, you might need to change a few
% parameters at the beginning of this script.
%
% Using 'save [filename]' and 'load [filename]' you can easily save
% and load the workspace after a certain module. This prevents the
% need to re-run the whole program for a certain step.
%
% ------------------------------------------------------------------
% File.............: ps_periodogram.m
% Version & Date..: 1.0, 15-OCT-2004
%                   1.1, 30-DEC-2004
% Author.........: Freek van Leijen
%                   Delft Institute of Earth Observation and Space Systems
%                   Delft University of Technology
% ------------------------------------------------------------------
%

fprintf(1,'\n');
fprintf(1,'PS analysis has started....\n');

% ------------------------------------------------------------------
% Initialize
% ------------------------------------------------------------------

global max_mem_buffer Nlines Npixels az_spacing r_spacing m2ph std_H std_v Fig.
ps_eval_method

max_mem_buffer= 50e7;    % MB, maximal memory size of buffer
input_filename= 'input_file.txt';
Fig.= 0;                          % counter of Figures
lambda= 0.0565646;                % wavelength [m]
m2ph= -4*pi/lambda;               % meters to phase constant
Nlines= 5001;                     % number of lines (azimuth direction)
Npixels= 1428;                    % number of pixels (range direction)
az_spacing= 4/2;             % [m], azimuth spacing, factor 2 for oversampling
r_spacing= 20/2;             % [m], range spacing, factor 2 for oversampling
```

```
psc_selection_method= 3;  % 1 = threshold, 2 = number, 3 = grid
psc_selection_gridsize= 150;        % [m], grid size for psc selection
psc_threshold= 0.27;        % threshold for amplitude dispersion
Npsc_selections= 4;         % number of psc selections, normally 1,
                            % but maybe more for validation
ens_coh_threshold= 0.6;             % ensemble coherence threshold

psp_selection_method= 2;      % 1 = high amplitude in minimal number of images
                            % 2 = amplitude dispersion (higher threshold than
                            % for psc selection)

psp_threshold1= 0.4;        % part of total sic's, recommendation = 0.65 or
                            %amplitude dispersion, recommendation = 0.4
psp_threshold2= -2;         %[dB], for psp_selection_method = 1,
recommendation = -2 dB

ps_eval_method= 1;          % 1 = ps potential, 2 = whole image (overrules
psp_selection_method)
ps_perc= 100;                       % percentage of pixels analyzed for PS

atm_corr_length= 2e3;               % [m]
reference_selection= 'auto';        % choose 'viz' (vizual, using plot), 'input'
                            % or 'auto' (automatic)
ref_cn= [1248 876];         %[azimuth_coordinate range_coordinate] (if 'input'),
                            % overrules reference selection method if not empty

std_H= 100;                 % [m], standard deviation of the DEM used or
                            % measure of expected height differences
std_v= 0.02;                % [m], measure of the expected linear deformation
filter_length= 1.0;         % [year], for low-pass non-linear defo filtering

APS_doplot= 'n';            % APS plots yes ('y') or no ('n')


% ------------------------------------------------------------------------
% step 1
% Read filenames and temporal baselines from input file
% ------------------------------------------------------------------------
```

```
[filenames_slc,filenames_ifgs,filenames_h2ph,filenames_aps,temp_baselines] =
textread(input_filename,'%s %s %s %s %f');
%filenames_slc                  = strvcat(filenames_slc);
%filenames_ifgs          = strvcat(filenames_ifgs(1:end-1,:)); % remove the
dummy values
%filenames_h2ph          = strvcat(filenames_h2ph(1:end-1,:)); % remove the
dummy values
%filenames_aps           = strvcat(filenames_aps(1:end-1,:)); % remove the
dummy values
%temp_baselines(end)     = []; % remove the dummy values
filenames_slc            = strvcat(filenames_slc);
filenames_ifgs                  = strvcat(filenames_ifgs); % remove the
dummy values
filenames_h2ph           = strvcat(filenames_h2ph); % remove the dummy
values
filenames_aps                   = strvcat(filenames_aps); % remove the
dummy values


Nslc = size(filenames_slc,1);
Nifgs = size(filenames_ifgs,1);


save boulby
% ------------------------------------------------------------------
% step 2
% Psc selection, 3 methods available
% ------------------------------------------------------------------
fprintf(1,'\n');
fprintf(1,'psc selection....\n');
[grid_array_az,grid_array_r,Npsc,Npsp] =
psc_selection(filenames_slc,filenames_ifgs,filenames_h2ph,psc_selection_method,
psc_selection_gridsize,psc_threshold,Npsc_selections,psp_selection_method,psp_t
hreshold1,psp_threshold2);


save boulby
% ------------------------------------------------------------------
% step 3
% Form network between psc
% ------------------------------------------------------------------
fprintf(1,'\n');
```

```
fprintf(1,'Forming network between PSC....\n');
Nedges = form_network(Npsc,Npsc_selections,Nifgs,atm_corr_length);

save boulby
% --------------------------------------------------------------------
% step 4
% Psc estimation by periodogram
% --------------------------------------------------------------------
fprintf(1,'\n');
fprintf(1,'Psc estimation by periodogram....\n');
periodogram_psc_est(temp_baselines,Nifgs,Nedges,Npsc_selections);

save boulby
% --------------------------------------------------------------------
% step 5
% Spatial unwrapping
% --------------------------------------------------------------------
fprintf(1,'\n');
fprintf(1,'Spatial unwrapping ....\n');
Nref =
periodogram_unwrapping(ens_coh_threshold,ref_cn,reference_selection,Nifgs,Nps
c,Npsc_selections,Nedges);

save boulby
% --------------------------------------------------------------------
% step 6
% Separation atmosphere and unmodeled deformation
% --------------------------------------------------------------------
fprintf(1,'\n');
fprintf(1,'Separation atmosphere and unmodeled deformation ....\n');
periodogram_filtering(temp_baselines,filter_length,Nifgs,Npsc,Npsc_selections);

save boulby
% --------------------------------------------------------------------
% step 7
% APS interpolation by Kriging
% --------------------------------------------------------------------
ps_eval_method        = 2;
```

```
fprintf(1,'\n');
fprintf(1,'APS estimation by Kriging....\n');
periodogram_APS_kriging(filenames_aps,APS_doplot,Nifgs,Npsc,Npsc_selections,N
psp);
ps_eval_method        = 1;

save boulby
% ------------------------------------------------------------------------
% step 8
% Ps estimation after APS removal
% ------------------------------------------------------------------------
fprintf(1,'\n');
fprintf(1,'Ps estimation after APS removal....\n');
Nps =
periodogram_ps_est(filenames_ifgs,filenames_h2ph,filenames_aps,temp_baselines
,grid_array_az,grid_array_r,ps_perc,ens_coh_threshold,Nifgs,Npsc,Npsc_selections
,Npsp);

save boulby
% ------------------------------------------------------------------------
% step 9
% Vizualize results
% ------------------------------------------------------------------------
fprintf(1,'\n');
fprintf(1,'Vizualize the results....\n');
periodogram_viz_ps(Nifgs,Nps,Npsc,Npsc_selections);

save boulby
% ------------------------------------------------------------------------
% The end
% ------------------------------------------------------------------------
```

APPENDIX 2: MANUAL TO THE CONE MODEL TOOL

This part describes the operation and structure of The Cone Ground surface deformation Model version 2.0. By means of an example the possibilities and limitations of the current version of the model is explained step by step.

The CSM model opens showing the following Index form (Fig. 4.38). This form contains links to all procedures and reports in the model and should be used as the main interface of the CSM.

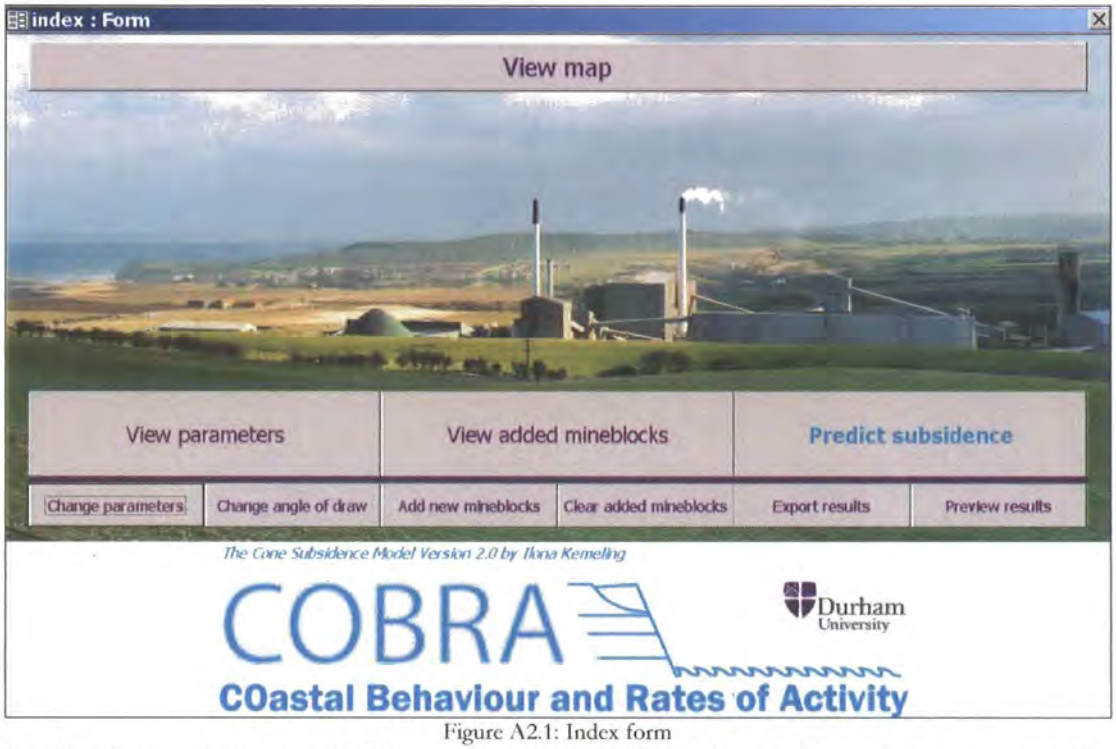

Figure A2.1: Index form

The first large tab is named 'View parameters' and can be used to open a report with a summary of all selected parameters used as input to the model. The two small tabs named 'Change parameters' and 'Change angle of draw' both open a data entry form where changes can be made to the parameters used in the model.

The second large tab is named 'View added mineblocks' and can be used to open a report listing the added mineblocks. These mineblocks are fictional and can be used to predict future deformation under different mining scenarios. The small tab named 'Add new mineblocks' opens a data entry form where an unlimited number of mineblocks can be added to the model. The small tab named 'Clear mineblocks' clears the model of all added mineblocks, without changing the actual non-fictional mineblocks.

The third large tab named 'Predict ground surface deformation' starts the calculation of deformation using inputs determined by the selected parameters and added mineblocks as given in the reports. This process can take some time depending on the inputs of the model. The small tab 'Export results' will save the results as excel files in the output folder. The small tab 'Preview results' will give a preview of the exported tables plus a two-paged report of the estimated deformation. A map can be viewed by clicking on the tap 'View map', at any time. The map shows the area around Boulby, OSGB coordinates and the existing mine layout in 2003.

The Selection Parameters report (Fig. 4.39) is opened by clicking on the 'View parameters' tab in the Main Index. This report gives a list of all parameters to be used as a reference before running the 'Predict Ground surface deformation' procedure.

Selection parameters 07 December 2005

Left easting	476000	**Top northing**	517000
Right easting	480000	**Bottom northing**	513000
Period [y]	100	**Angle of draw [deg]**	45
Length [m]	4000	**Resolution [m]**	500
Width [m]	4000		

Figure A2.2: View Parameters report

The area of interest is determined by the following four parameters:

- Left easting (the minimum x-coordinate);
- Right easting (the maximum x-coordinate);
- Top northing (the maximum y-coordinate).
- Bottom northing (the minimum y-coordinate);

The period of interest starts at the first mining date within the area of interest and end after the selected period has elapsed:

- Period

All mineblocks that were mined or will be mined within the selected period of interest are included in the calculation of the deformation.

From the area of interest two values are calculated:

- Length [m] (measured in East-West direction);
- Width [m] (measured in North-South direction);

Two more parameters that can be changed are given:

- Angle of draw [deg]
- Resolution [m] (distance between prediction points)

NOTE: A large area of interest, a long period of interest and a high resolution will result in a longer processing time.

To change the parameters, click on the 'Change parameters' tab on the Index form. This will open the Change parameters data entry form below (Fig. 4.40). Here you can change the following parameters: the area of interest, the period of interest and the resolution.

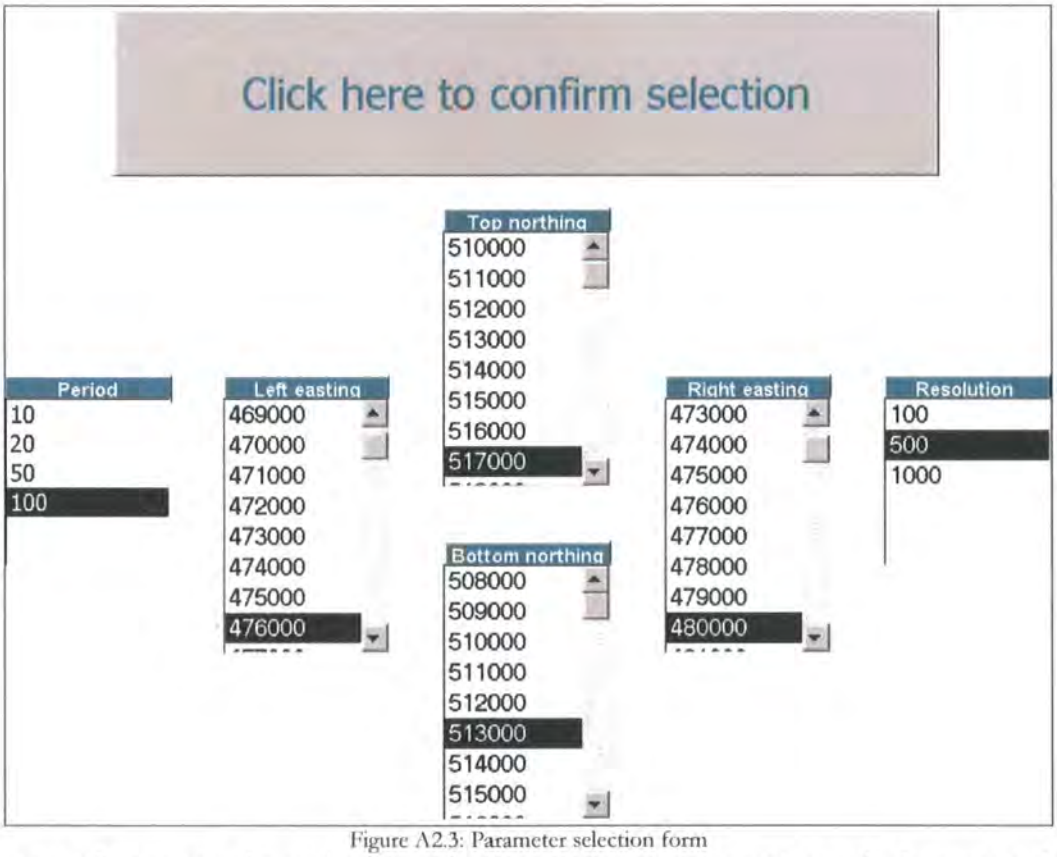

Figure A2.3: Parameter selection form

The area of interest is determined by selecting a left and right easting and a bottom and top northing. Easting and northing values can be selected in multiples of 1000 from a drop down list. Minimum and maximum easting values are 461,000 and 491,000. Minimum and maximum northing values are 508,000 and 538,000.

The period of interest starts at the first mining date within the area of interest and can last for 10, 20, 50 or 100 years from that date. However, the current version of the CSM model is only capable of estimating deformation until the year 2100. The resolution refers to the distance in meters between the prediction points.

NOTE: The highest resolution is 100 meters and the lowest resolution is 1000 meters. A lower resolution should be selected for larger areas.

A crucial parameter in the model is the angle of draw and can be changed in the form shown below (Fig. A2.4), which can be opened by clicking the 'Change angle of draw' tab on the Index form.

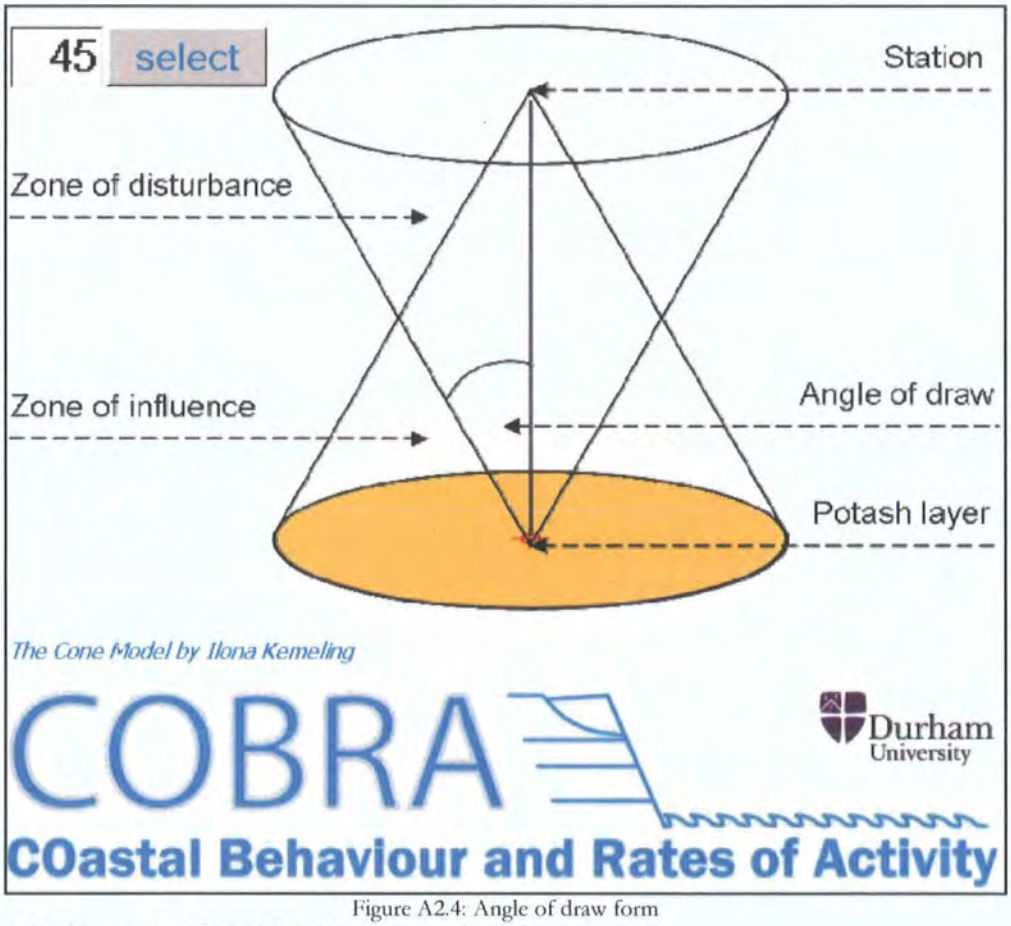

Figure A2.4: Angle of draw form

Any value between 35 and 90 degrees can be entered.

NOTE: A value lower than 45 degrees will reduce the zone of influence and may result in an under-estimation of the deformation.

The Added Mineblocks report (Fig. A2.5) is obtained by clicking the 'View added mineblocks' tab in the Main Index. This report shows all added mineblocks on a list to be

used as a reference before running the 'Predict Ground surface deformation' procedure. The actual (not modelled) mine blocks, are included in the 'Predict Ground surface deformation' procedure, but are not listed in this report.

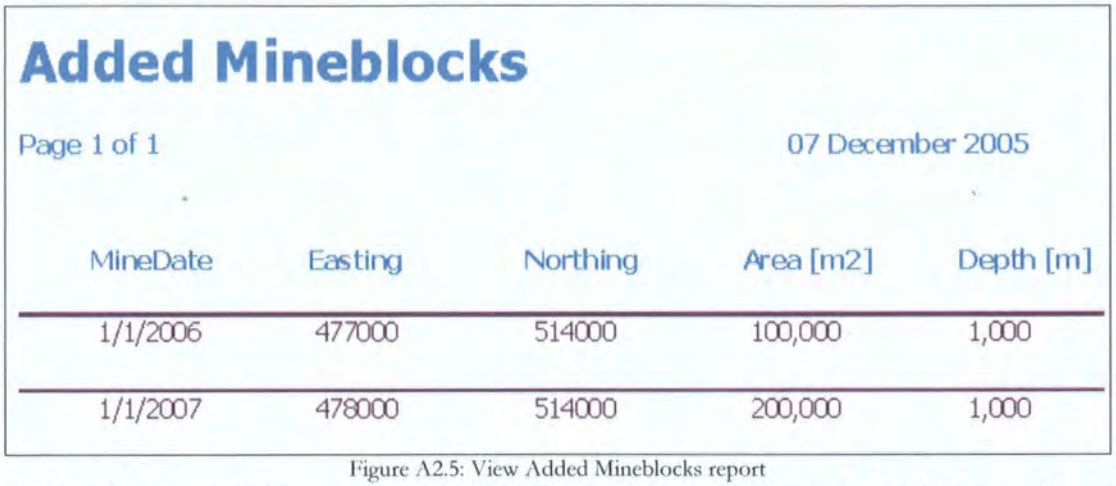

Added Mineblocks

Page 1 of 1 — 07 December 2005

MineDate	Easting	Northing	Area [m2]	Depth [m]
1/1/2006	477000	514000	100,000	1,000
1/1/2007	478000	514000	200,000	1,000

Figure A2.5: View Added Mineblocks report

The listed characteristics of the mine blocks are the values given in the 'add mineblocks' data entry form. Each mine block has a starting mining date, a central easting, a central northing, an undermined squared area and a depth. The area is the two-dimensional size of the mine block, in this example 100,000 m2. The depth is the depth below surface of the centre of the mine block: in this example 1,000 metres.

NOTE: The actual existing mine blocks are not on this list and this list is emptied after the 'Clear mineblocks' procedure is run.

To add new mineblocks click on the 'Add new mineblocks' tab on the Index form. This will open the Add new mineblocks data entry form below (Fig. A2.6). Here you can add an unlimited number of (fictional) mineblocks to the model.

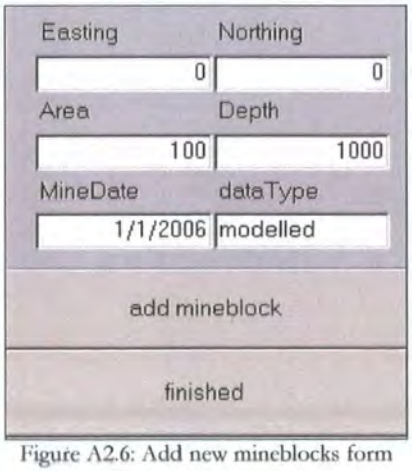

Figure A2.6: Add new mineblocks form

The central coordinates of the mine blocks should be entered in the easting and northing boxes. The following boxes should be used to fill in the area in square meters, the depth in meters below surface and the starting mining date. To enter an additional mine block, click the 'add mine block' tab. After adding all mineblocks, the 'finished' tab should be clicked.

NOTE: To update the existing (non-fictional) mine blocks in the model, the Table named MineBloxs can be replaced or new records can be added. Make sure the design of the Table stays exactly the same (Fig. A2.7).

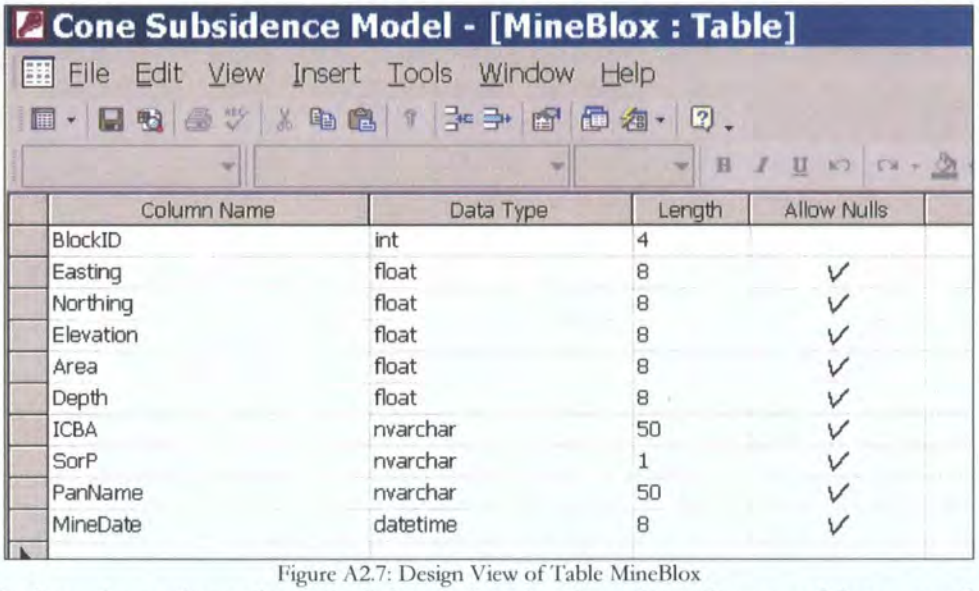

Column Name	Data Type	Length	Allow Nulls
BlockID	int	4	
Easting	float	8	✓
Northing	float	8	✓
Elevation	float	8	✓
Area	float	8	✓
Depth	float	8	✓
ICBA	nvarchar	50	✓
SorP	nvarchar	1	✓
PanName	nvarchar	50	✓
MineDate	datetime	8	✓

Figure A2.7: Design View of Table MineBlox

To calculate the estimated total deformation in the selected area of interest after the selected period of time (View Parameters report) and considering the effects of all mine blocks in the database, fictional (View Added mineblocks) and non-fictional, click the 'Predict ground surface deformation' tab on the Index form.

Depending on the speed of the used computer, the selected period and the size and resolution of the area of interest this will take some time. After successful calculation of the estimated deformation the following box will appear (Fig. A2.8).

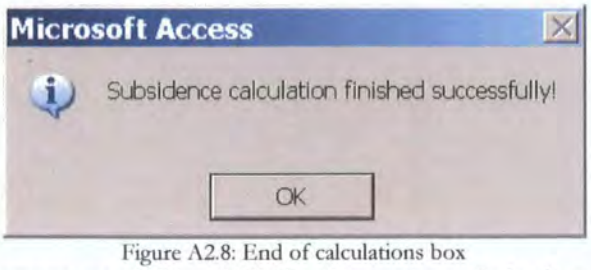

Figure A2.8: End of calculations box

To export the results as two excel files click the 'Export results' tab on the Index form. The results will be saved in the ../CSM_v2/output folder, overwriting previous excel files. To

save previous results, either move or rename the excel files in this folder. The excel files contain the following information:

The regression estimation of the total deformation in millimetres at the prediction points in the area of interest. This estimation is the total deformation from the earliest mining date in the area of interest, till after the selected period (10, 20, 50 or 100 years). The stochastic estimation, subdividing the area of interest into an area with more than 80 %, between 20-80% and less than 20% chance of deformation occurring in the selected period.

To preview the results in two tables and three graphs, click 'Preview results' on the Index form. Following two tables will appear (Fig. A2.9).

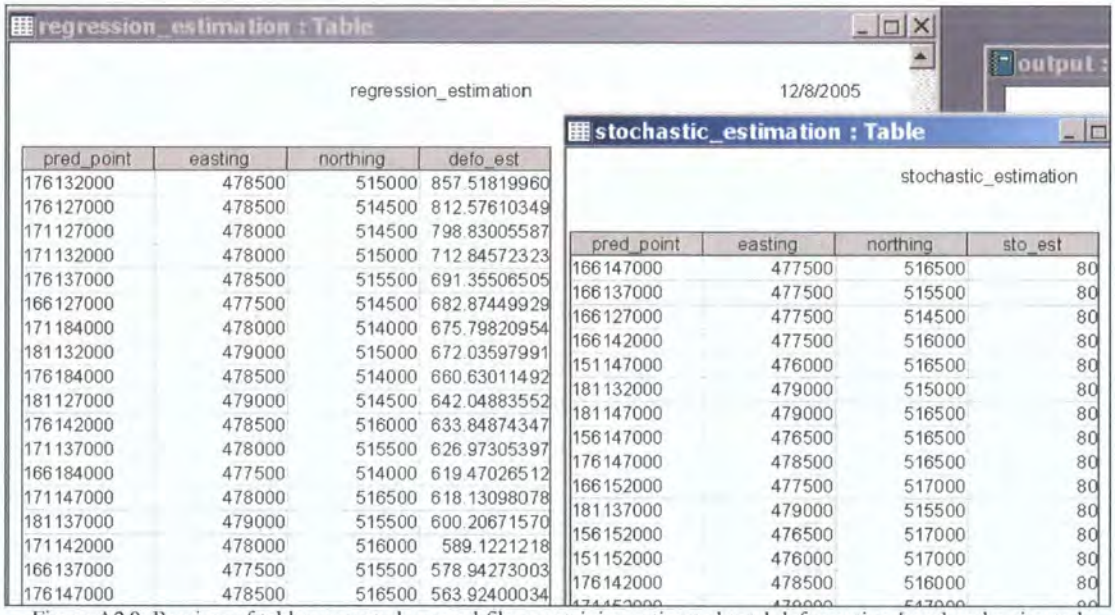

regression_estimation : Table

regression_estimation 12/8/2005

pred_point	easting	northing	defo_est
176132000	478500	515000	857.51819960
176127000	478500	514500	812.57610349
171127000	478000	514500	798.83005587
171132000	478000	515000	712.84572323
176137000	478500	515500	691.35506505
166127000	477500	514500	682.87449929
171184000	478000	514000	675.79820954
181132000	479000	515000	672.03597991
176184000	478500	514000	660.63011492
181127000	479000	514500	642.04883552
176142000	478500	516000	633.84874347
171137000	478000	515500	626.97305397
166184000	477500	514000	619.47026512
171147000	478000	516500	618.13098078
181137000	479000	515500	600.20671570
171142000	478000	516000	589.1221218
166137000	477500	515500	578.94273003
176147000	478500	516500	563.92400034

stochastic_estimation : Table

stochastic_estimation

pred_point	easting	northing	sto_est
166147000	477500	516500	80
166137000	477500	515500	80
166127000	477500	514500	80
166142000	477500	516000	80
151147000	476000	516500	80
181132000	479000	515000	80
181147000	479000	516500	80
156147000	476500	516500	80
176147000	478500	516500	80
166152000	477500	517000	80
181137000	479000	515500	80
156152000	476500	517000	80
151152000	476000	517000	80
176142000	478500	516000	80

Figure A2.9: Preview of tables exported as excel files containing estimated total deformation [mm] and estimated deformation chance [%] at prediction points in selected area.

In addition to the excel tables, a short report will open which shows the point of maximum total deformation in the selected area of interest (Fig. A2.10). For this point, the total deformation in millimetres and the OSBG co-ordinates is given.

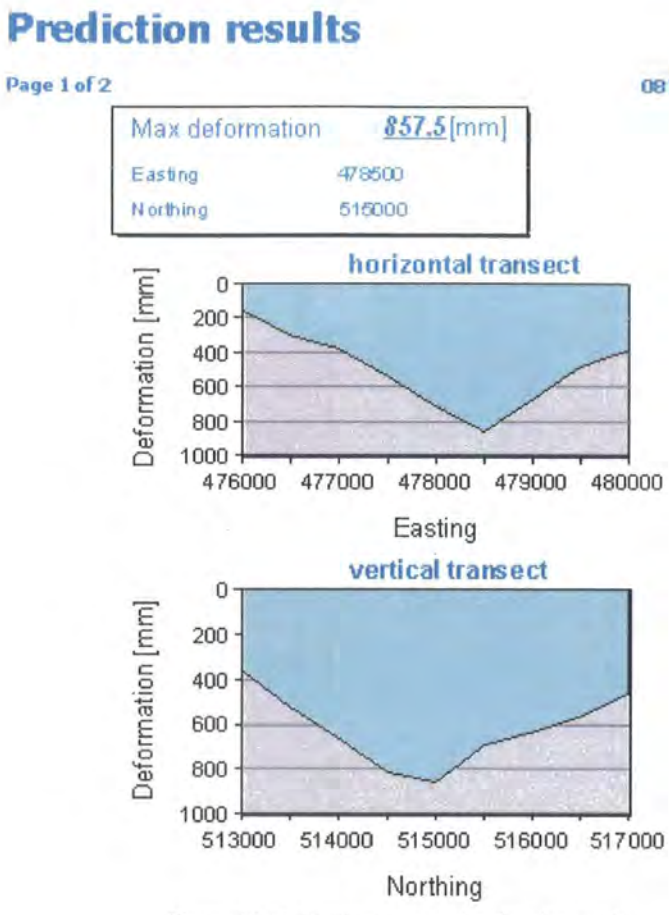

Figure A2.10: Preview report of estimation results

Horizontal transect: Total deformation [mm] along a horizontal line through the point of maximum deformation. Vertical transect: Total deformation [mm] along a vertical line through the point of maximum deformation. Deformation rate over time: Deformation rate [mm a^{-1}] over time [year] at the point of maximum deformation.

APPENDIX 3: THE CONE MODEL SQL SCRIPTS

```
ALTER PROCEDURE     dbo.ma01_get_measurements AS

DROP TABLE          mat01_measurements

SELECT              t004.easting_id + t005.northing_ID + t006.period_id AS pred_id,
                    t004.easting_id+t005.northing_ID AS pred_point,

                    t006.daynumber,
                    t004.Easting,
                    t005.Northing,
                    Mperiod

INTO                mat01_measurements

FROM                t004_easting t004
INNER JOIN          t003_selection t003
ON                  t004.resolution >= t003.resolution
AND                 t004.easting >= t003.min_x
AND                 t004.easting <= t003.max_x
INNER JOIN          t005_northing t005
ON                  t003.resolution <= t005.resolution
AND                 t003.min_y <= t005.Northing
AND                 t003.max_y >= t005.Northing
CROSS JOIN          t006_periods t006


Where               Mperiod>=t003.begin_year
AND                 Mperiod<=t003.end_year
```

STEP1:

In this step a prediction records Table is generated, based on the selection parameters:

Square shape on the surface between minimum X and Y and maximum X and Y OSGB coordinates.

Resolution, in meters between prediction points (e.g. 100, 500 or 1000 m.)

Period of prediction between begin year and end year, including all mine panels mined from January in the begin year until December in the end year.

The output Table consists of a number of unique prediction records, with an X and Y coordinate and a daynumber, which is the 1st January of a year.

```
ALTER PROCEDURE    dbo.ma02_get_mb_radius AS

DROP TABLE         mat02_mb_radius

SELECT             t001.BlockID,
                   t001.depth*TAN(RADIANS(t003.angle_of_draw)) AS radius

INTO               mat02_mb_radius

FROM               t001_excavations t001
CROSS JOIN         t003_selection  t003
```

STEP 2:

In this step the radius of the zone of disturbance at seam level is calculated based on the angle of draw, a given parameter and the Depth variable of the mining panels. A radius for each mine panel is calculated.

```
ALTER PROCEDURE    dbo.ma03_cross_mb AS

DROP TABLE         mat03_cross_mb

SELECT             t001a.BlockID AS BlockID_a,
                   t001b.BlockID AS BlockID_b,
                   cast(SQRT(POWER(t001a.Easting - t001b.Easting, 2) +
                         POWER(t001a.Northing - t001b.Northing, 2)) AS int) AS
distance,
                   t001a.easting as easting_a,
                   t001a.northing as northing_a,
                   t001b.easting as easting_b,
                   t001b.northing as northing_b,
                   t001a.miningday as miningday_a,
                   t001b.miningday as miningday_b


INTO               mat03_cross_mb

FROM               dbo.t001_excavations t001a
INNER JOIN         dbo.t001_excavations t001b
ON                 t001a.BlockID <> t001b.BlockID
INNER JOIN         mat02_mb_radius at02
ON                 at02.BlockID = t001a.BlockID
CROSS JOIN         t003_selection t003

WHERE              SQRT(POWER(t001a.Easting - t001b.Easting, 2) +
                         POWER(t001a.Northing - t001b.Northing, 2)) < at02.radius


AND                t001a.easting< t003.max_x+2000
AND                t001a.easting> t003.min_x-2000
AND                t001b.easting< t003.max_x+2000
AND                t001b.easting> t003.min_x-2000
AND                t001a.northing< t003.max_y+2000
AND                t001a.northing> t003.min_y-2000
AND                t001b.northing< t003.max_y+2000
AND                t001b.northing> t003.min_y-2000
```

```
ORDER BY        t001a.BlockID, SQRT(POWER(t001a.Easting - t001b.Easting, 2) +
                POWER(t001a.Northing - t001b.Northing, 2))
```

STEP3:

In this step the mine panels are linked to each other to generate a 'near mine panels'-Table. This Table gives for each mine panel all mine panels within their zone of disturbance.

The input tables are the excavation dataset and the radius Table generated in STEP2.

```
ALTER PROCEDURE    dbo.ma04_mbday AS

DROP TABLE         mat04_mbday

SELECT DISTINCT    IDENTITY(bigint,1,1) as mb_day,
                   mat03.BlockID_a,
                   t006.daynumber,
                   MIN(mat03.distance) AS min_dist,
                   CAST(SQRT(square(AVG(mat03.easting_a) - AVG(mat03.easting_b))+
                        square(AVG(mat03.northing_a) - AVG(mat03.northing_b))) AS
int) AS                 CG_dist

INTO               mat04_mbday

FROM               mat03_cross_mb mat03
INNER JOIN         t006_periods t006
ON                 mat03.miningday_a < t006.daynumber
AND                mat03.miningday_b < t006.daynumber

GROUP BY           mat03.BlockID_a, t006.Mperiod,t006.daynumber

HAVING             t006.Mperiod>(select begin_year from t003_selection)
AND                t006.Mperiod<(select end_year from t003_selection)



ORDER BY           mat03.BlockID_a, t006.daynumber
```

STEP4:

In this step a summary of the 'near mine panels' Table generated in STEP3 is made, based on the date of mining of each mine panel and the selected prediction period. For each mine panel and at each unique point in time the average distance to all mine panels in the zone of disturbance is calculated.

The input tables are the 'near mine panels'-Table and the periods-Table, which contains periods by year.

```
ALTER PROCEDURE     dbo.ma05_diagonal AS

DROP TABLE          mat05_diagonal

SELECT              at01.pred_id,
                    at04.mb_day

INTO                mat05_diagonal

FROM                mat01_measurements at01
INNER JOIN          mat04_mbday at04
ON                  at01.daynumber = at04.daynumber
INNER JOIN          t001_excavations t001
ON                  at04.BlockID_a =t001.BlockID

WHERE               57.3*ATAN(SQRT(square(at01.easting - t001.easting) +
                          square(at01.northing - t001.northing)) /t001.depth)
                    <(select angle_of_draw from t003_selection)
```

STEP5:

In this step the prediction records generated in STEP1 are joined to the summarized mine panel Table generated in STEP4. This join is controlled by the angle of draw parameter, because only mine panels within the zone of distance of a prediction point are joined to that prediction point.

The new Table consists of unique diagonals, each representing a prediction point at the surface, a mine panel and a point in time.

```
ALTER PROCEDURE   dbo.ma06_by_measurement AS
DROP TABLE        dbo.mat06_by_measurement

SELECT            at01.pred_id,
                  SUM(t001.Area)                                          AS A,
                  CAST(AVG(SQRT(square(at01.easting - t001.Easting) +
                        square(at01.northing - t001.Northing))) AS int)          AS H,
                  CAST(AVG(at01.daynumber - t001.miningday) AS int)       AS T,
                  AVG(at04.CG_dist)                                       AS G,
                  MAX(t001.Depth) AS depth,
                  COUNT(at04.BlockID_a) AS blocks,
                  SUM(1
                  *
                  (1/(4.696-0.2161*Log(t001.Area)) )
                  *
                  (0.6036*EXP(-0.5776E-03*(at04.CG_dist)))
                  *
                  (1/(0.1713E-02*(SQRT(square(at01.easting - t001.Easting) +
                        square(at01.northing - t001.Northing)))+0.6340))
                  *
                  (-0.5857*(EXP(-0.8393E-02*(at01.daynumber - t001.miningday))-EXP(-
                        0.5265E-04*(at01.daynumber - t001.miningday))))
                  ) as est

INTO              dbo.mat06_by_measurement

FROM              dbo.mat01_measurements at01
INNER JOIN        dbo.mat05_diagonal at05
ON                at01.pred_id = at05.pred_id
INNER JOIN        dbo.mat04_mbday at04
ON                at05.mb_day = at04.mb_day
INNER JOIN        dbo.t001_excavations t001
ON                at04.BlockID_a = t001.BlockID

GROUP BY          at01.pred_id
```

STEP6:

In this step the variables are calculated and the deformation rate is calculated for each prediction record. Where, based on inclusion of all those panels that fall in a zone of disturbance of a prediction point at a point in time:

A = the sum of the area of the mine panels

H = the average horizontal distance between all panels and a prediction point

T = the average time difference between the mining dates and the prediction date for

G = the average of the 'near mine panel' distance

```
ALTER PROCEDURE    dbo.ma07_by_station AS

DROP TABLE         mat07_by_station

SELECT             mat01.pred_point,
                   mat01.Easting,
                   mat01.Northing,
                   SUM(ISNULL(mat06.est, 0)) AS defo,
                   max(mperiod) mperiod

INTO               mat07_by_station

FROM               dbo.mat06_by_measurement mat06
RIGHT OUTER JOIN   dbo.mat01_measurements mat01
ON                 mat06.pred_id = mat01.pred_id

GROUP BY           mat01.pred_point, mat01.Easting, mat01.Northing
```

STEP7:

In this step the prediction records are summarized by prediction point, to calculate the total deformation over the selected period.

APPENDIX 4: INTERFEROGRAMS PSI ANALYSIS.

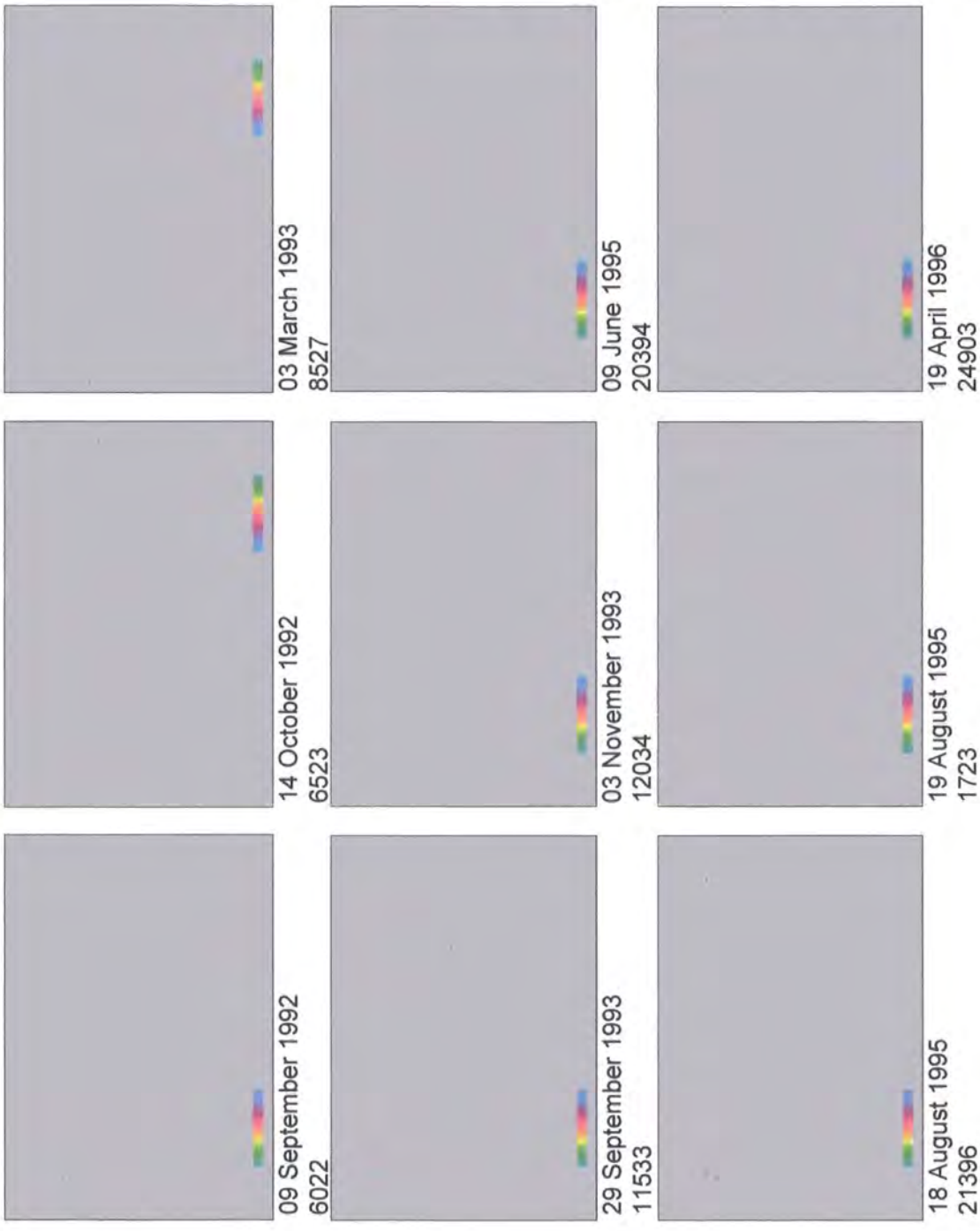

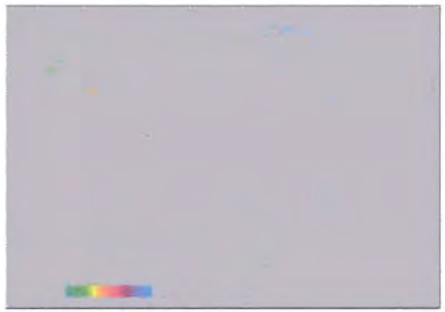

20 April 1996
5230

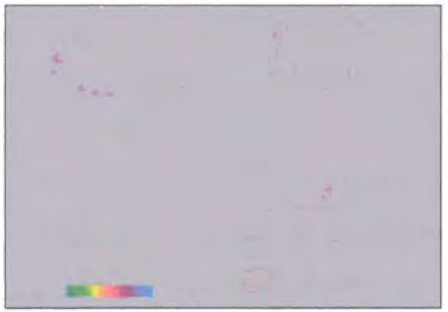

28 June 1996
25905

02 August 1996
26406

03 August 1996
6733

12 October 1996
7735

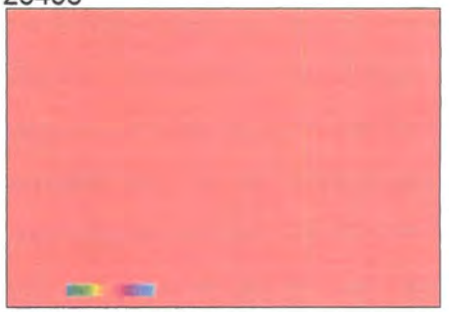

25 January 1997
9238

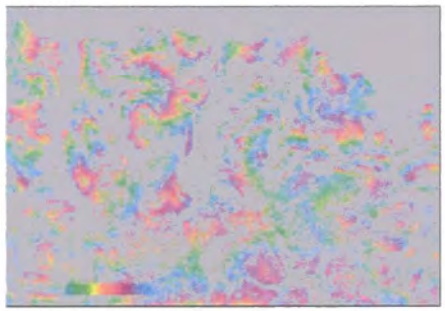

01 March 1997
9739

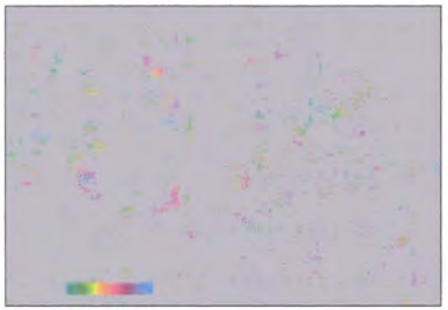

05 April 1997
10240

10 May 1997
10741

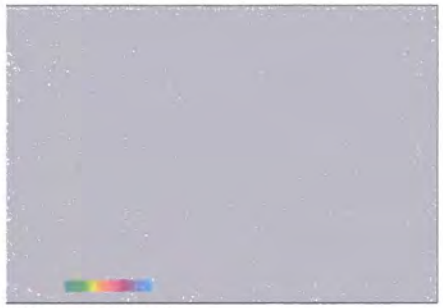

19 July 1997
11743

23 August 1997
12244

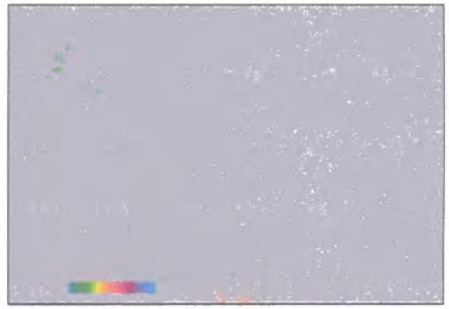

06 December 1997
13747

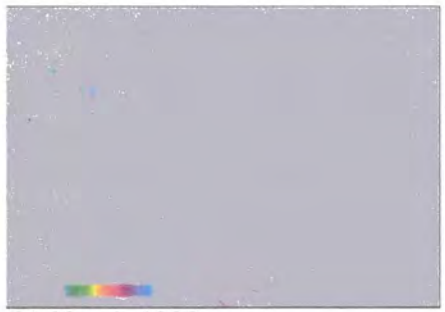

21 March 1998
15250

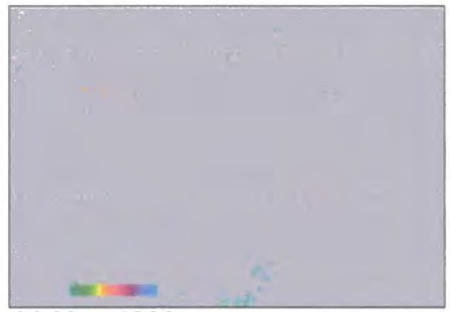

30 May 1998
16252

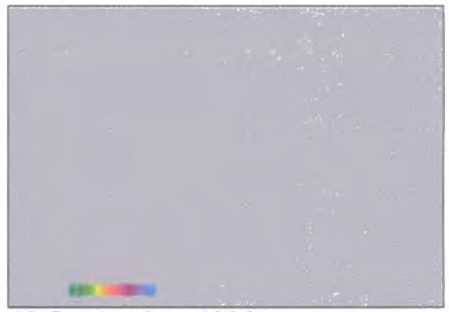

12 September 1998
17755

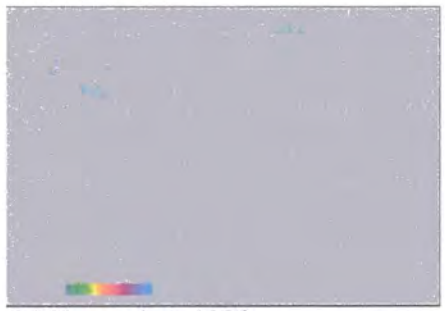

21 November 1998
18757

30 January 1999
19759

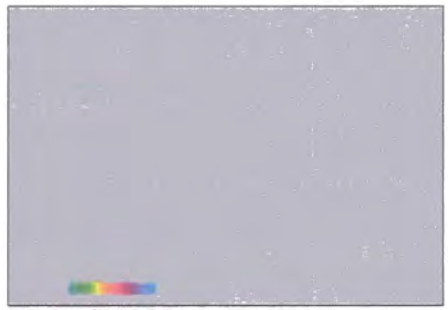

10 April 1999
20761

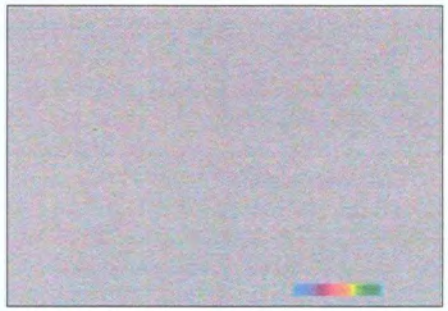

24 July 1999
22264

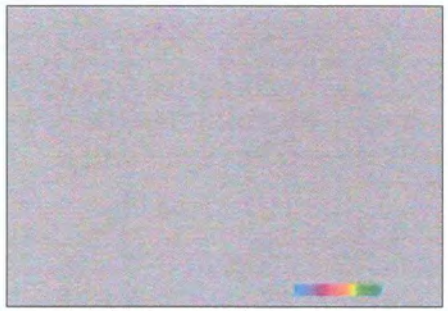

11 December 1999
24268

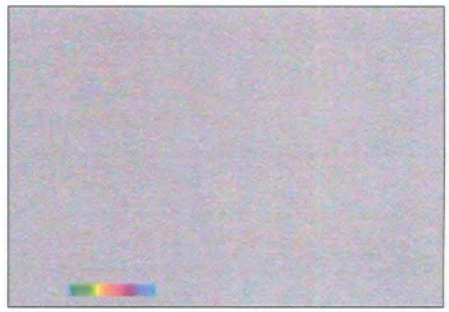

29 April 2000
26272

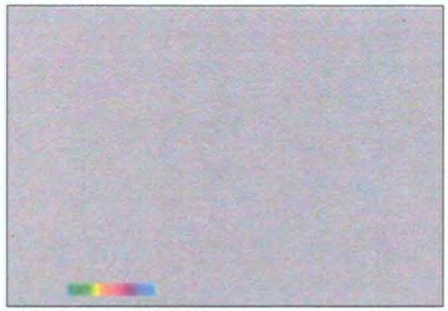

12 August 2000
27775

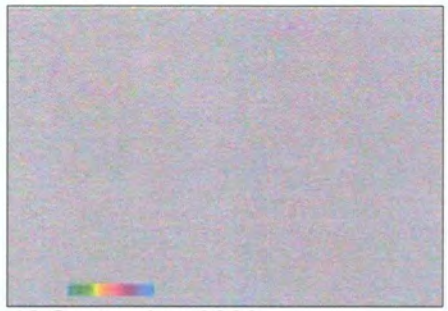

16 September 2000
28276

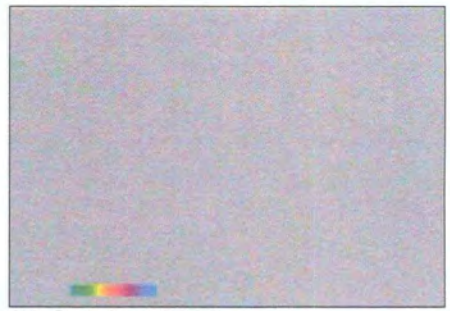

21 October 2000
28777

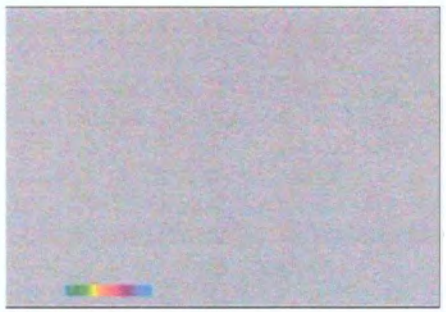

06 October 2001
33787

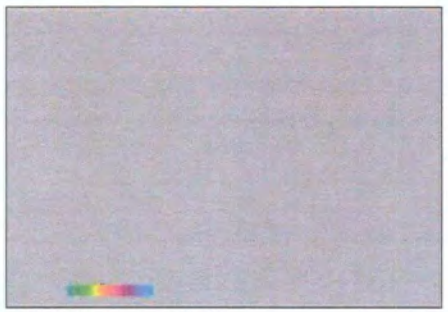

23 February 2002
35791

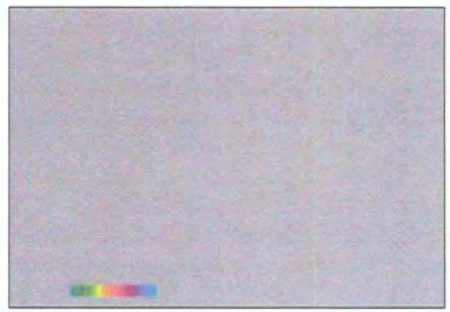

17 August 2002
38296

APPENDIX 5: LONG-TERM DEFORMATION ESTIMATES AT EVALUATION STATIONS

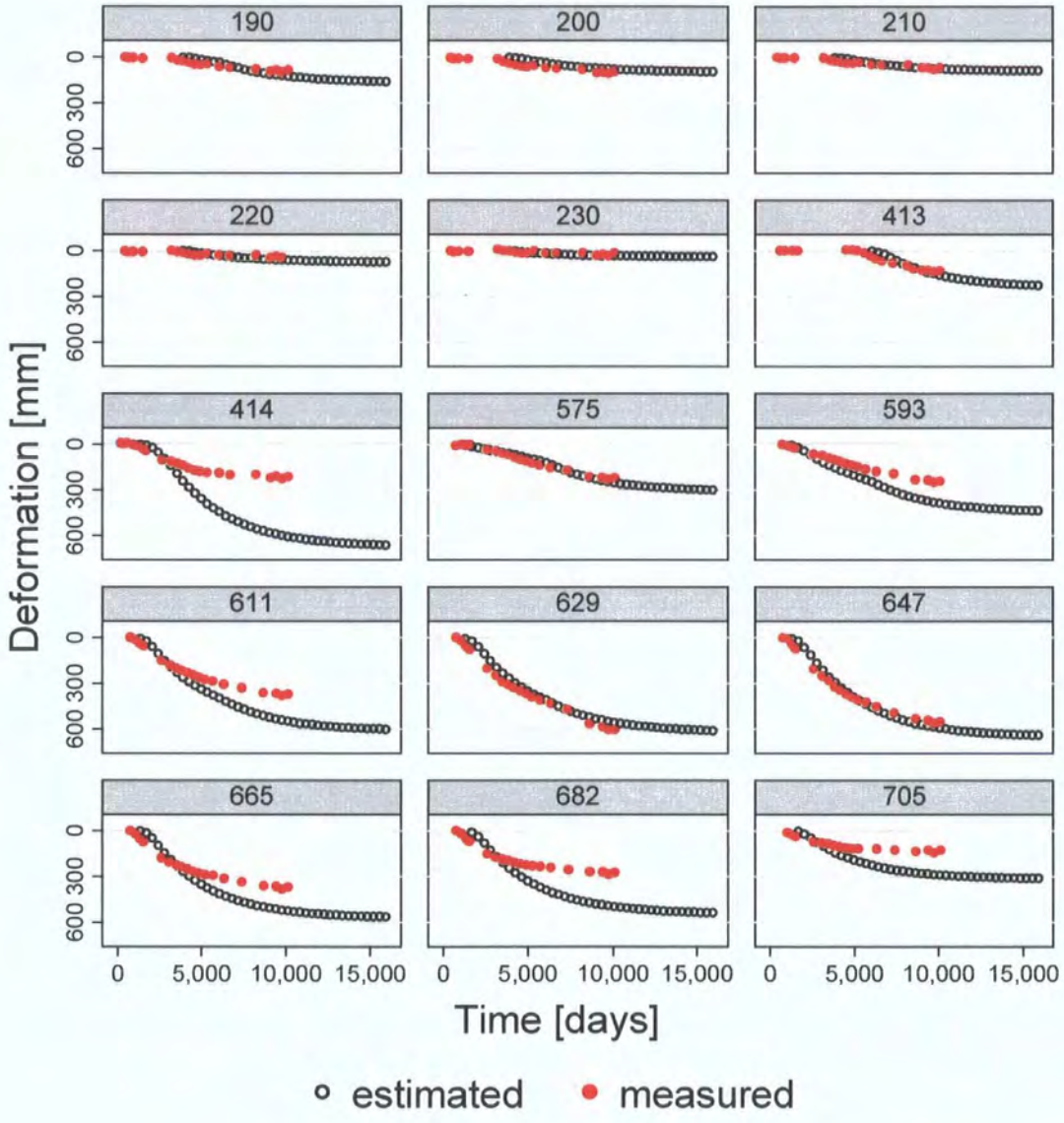

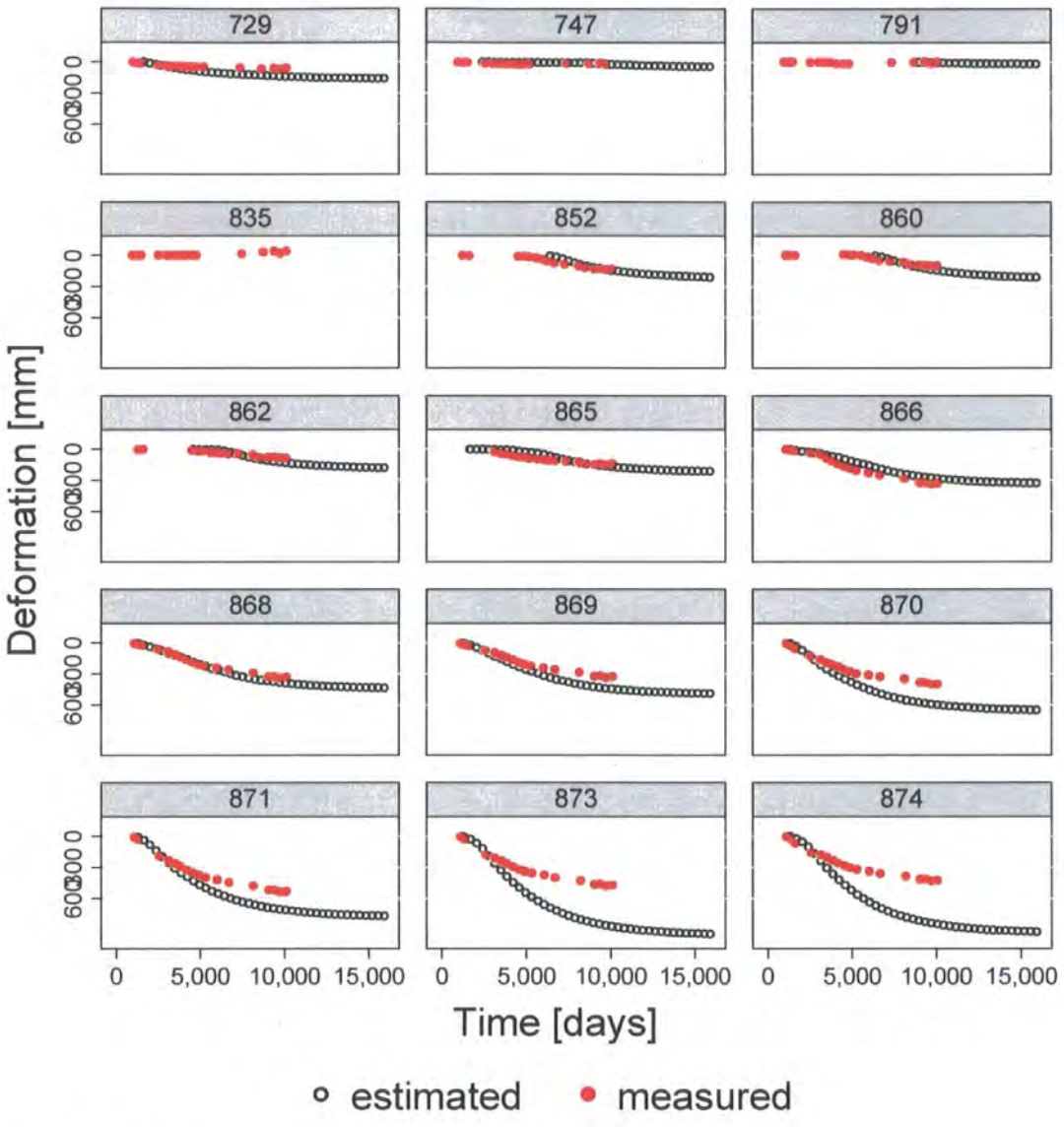
729
747
791
835
852
860
862
865
866
868
869
870
871
873
874
Deformation [mm]
0
5,000
10,000
15,000
Time [days]
estimated
measured
Graphs by station

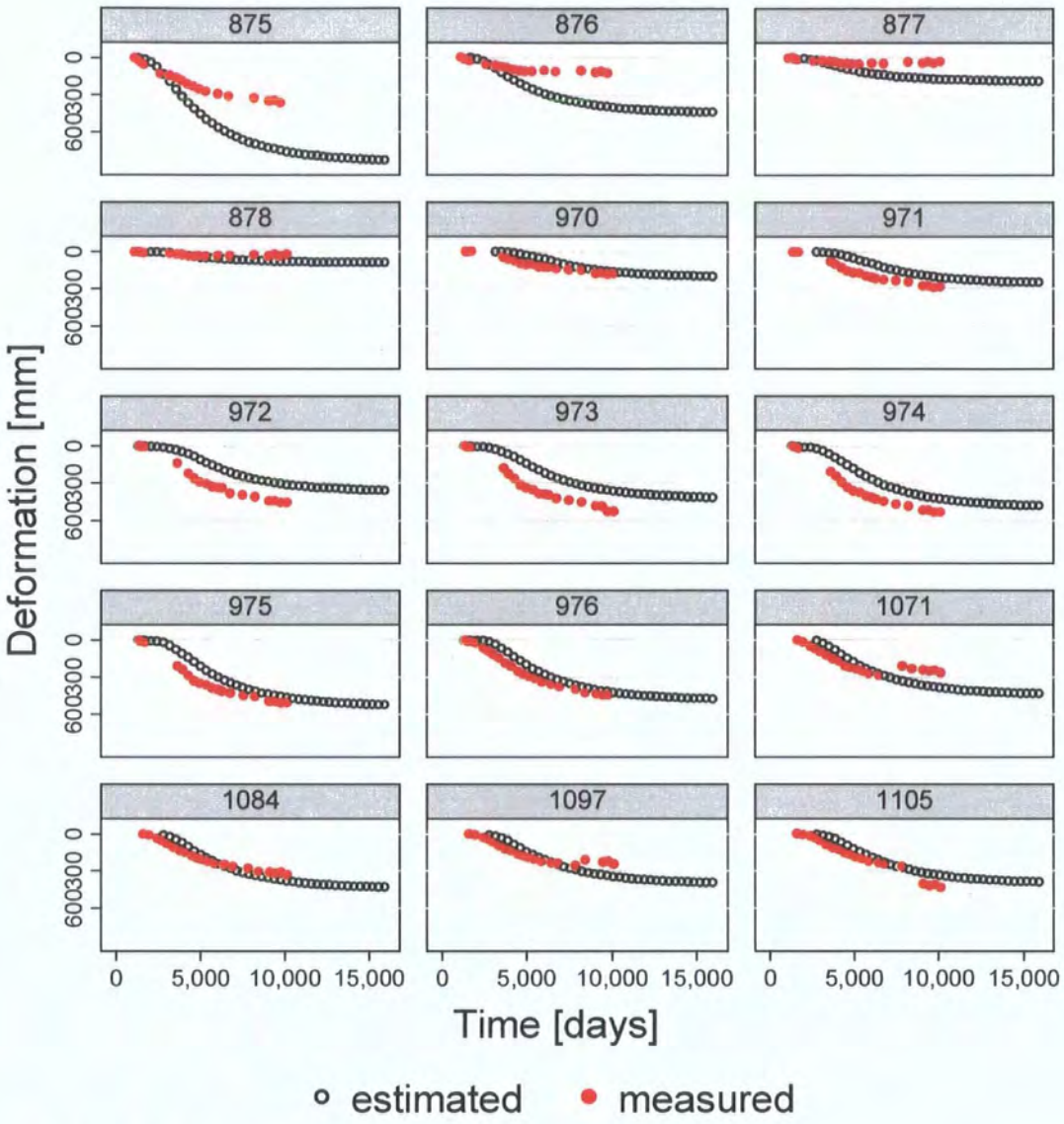
875
876
877
878
970
971
972
973
974
975
976
1071
1084
1097
1105
Deformation [mm]
600300 0
0
5,000
10,000
15,000
Time [days]
estimated
measured
Graphs by station

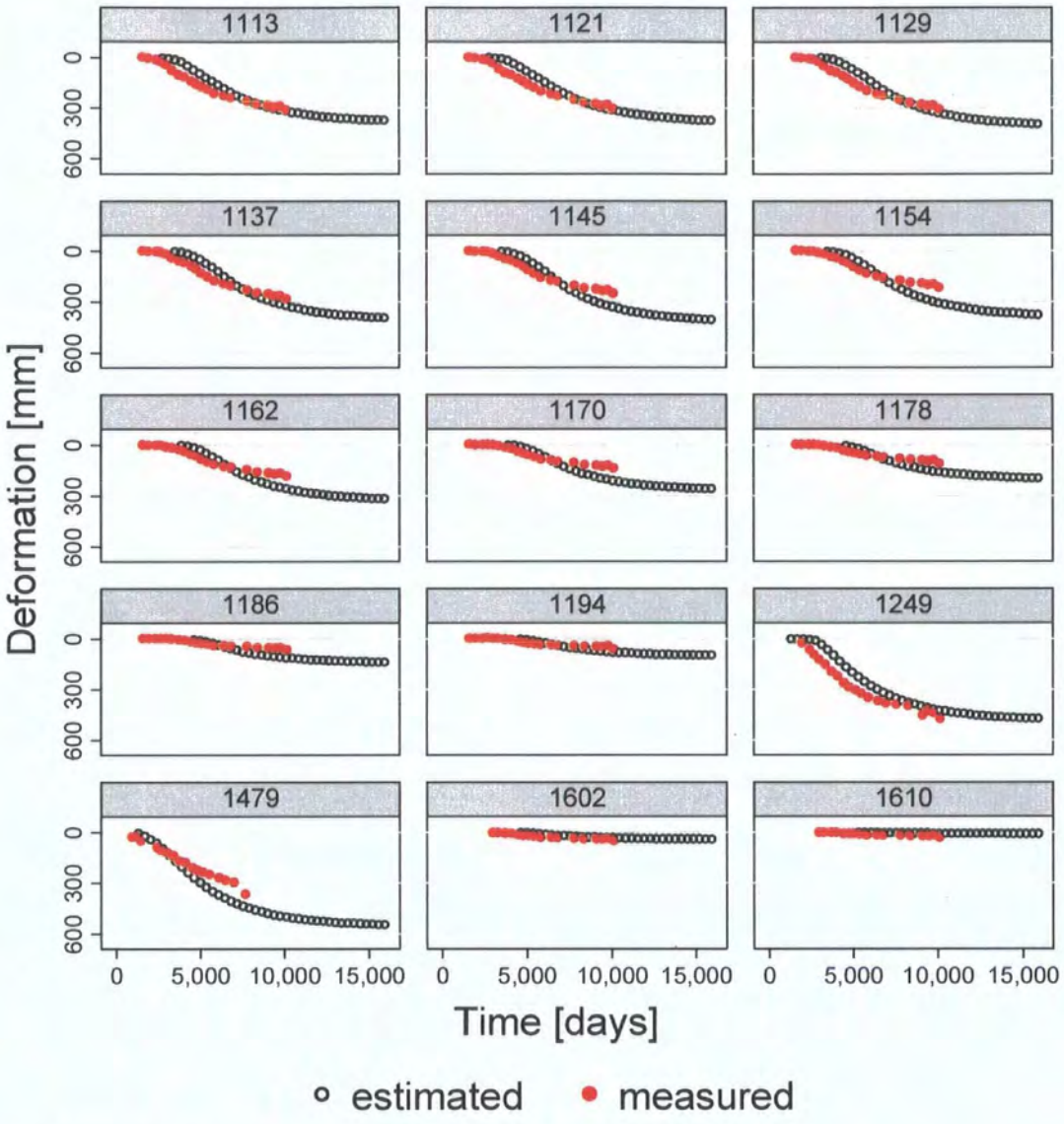
1113
1121
1129
1137
1145
1154
1162
1170
1178
1186
1194
1249
1479
1602
1610
Deformation [mm]
0
300
600
0
5,000
10,000
15,000
Time [days]
estimated
measured
Graphs by station

REFERENCES

Abernethy, R.B., 2000. The New Weibull Handbook, Reliability & Statistical Analysis for Predicting Life, Safety, Survivability, Risk, Cost and Warranty Claims. Abernethy, 308 p.

Aksoy, O., Kose, H., Onargan, T., Koca, Y. and Heasley, H., 2003. Estimation of Limit Angle Using Laminated Displacement Discontinuity Analysis in the Soma Coal Field, Western Turkey. International Journal of Rock Mechanics and Mining Sciences, v.41: pp.547-556.

Al-Rawahy, S.Y.S. and Goulty, N.R., 1995. Effect of Mining Subsidence on Seismic Velocity Monitored by a Repeated Reflection Profile. Geophysical Prospecting, v.43(is.2): pp.191-201.

Allersma, H.B.G., 1995. Simulation of Subsidence in Soil Layers in a Geotechnical Centrifuge. In: F.B.J. Barends, F.J.J. Brouwer and F.H. Schroder (Editors), Fifth International Symposium on Land Subsidence. IAHS Press, The Hague, pp.117-126.

Ambrožic, T. and Turk, G., 2003. Prediction of Subsidence Due to Underground Mining by Artificial Neural Networks. Computers & Geosciences, v.29: pp.627–637.

Anderson, J.G.C. and Owen, T.R., 1980. The Structure of the British Isles. Permagon Press Ltd., Oxford, 251 p.

Anderson, J.M. and Mikhail, E.M., 1998. Surveying, Theory and Practice. McGraw-Hill Companies Inc., Boston, 1167 p.

Bamler, R., 2000. Principles of Synthetic Aperture Radar. Surveys in Geophysics, v.21(is.2): pp.147-157.

Bannister, A., Raymond, S. and Baker, R., 1998. Surveying. Addison Wesley Longman, Harlow, 502 p.

Bell, F.G., Stacey, T.R. and Genske, D.D., 2000. Mining Subsidence and Its Effect on the Environment: Some Differing Examples. Environmental Geology, v.40(is.1-2): pp.135-152.

Bennett, R.A., Wernicke, B.P., Niemi, N.A., Friedrich, A.M. and Davis, J.L., 2003. Contemporary Strain Rates in the Northern Basin and Range Province from Gps Data. Tectonics, v.22(is.2): pp.1-31.

Biasutti, R., D'Elia, V., Genchi, N., Brocco, M., Benagiano, A. and Westbrook, S., 2004. Descw Windows Application. ESA 2001-2004, version 4.46

Boog, H., Krebs, G. and Vogel, D., 2006. The Strategic Air War in Europe and the War in the West and East Asia, 1943-1944/5. Germany and the Second World War, v.VII. Oxford University Press, Oxford, 670 p.

Borgatti, L. and Soldati, M., 2003. Landslide Events as Indicators of Landscape Sensitivity to Climate Change. In: D. Castaldini, B. Gentili, M. Materazzi and G. Pambianchi (Editors), Worksop on "Geomorphological sensitivity and system response", Italy, pp.35-46.

Bree, R.J.P.v., Gens, R., Groot, J.S., Halsema, D.v., Hout, P.v.d., Klees, R., Min, E.J.d., Schrama, E.J.O. and Usai, S., 2000. Deformation Measurements with Sar. USP-2 99-16, Netherlands Remote Sensing Board (BCRS), Delft, The Netherlands.

Brimicombe, A., 2003. Gis, Environmental Modelling and Engineering. Taylor & Francis Inc., London, 312 p.

Burbank, D.W. and Anderson, R.S., 2001. Tectonic Geomorphology. Blackwell Science, Malden, 274 p.

Bürgmann, R., Rosen, P.A. and Fielding, E.J., 2000. Synthetic Aperture Radar Interferometry to Measure Earth's Surface Topography and Its Deformation. Annual Reviews of Earth and Planetary Sciences, v.28: pp.169-209.

Burke, S.P., Potter, H.A.B. and Jarvis, A., 2005. Groundwater Rebound in the South Yorkshire Coalfield: A Review of Initial Modelling. In: J. Loredo and F. Pendás (Editors), 9th International Mine Water Congress. Mine Water 2005 - Mine Closure., Oviedo, pp.223-227.

Capes, R. and Haynes, M., 1996. A Guide to Sar Interferometry, NPA Group, 4 p.

Carbognin, L., 1997. Land Subsidence: A Worldwide Environmental Hazard. In: A. Goudie (Editor), The Human Impact Reader, Readings and Case Studies. Blackwell Publishers Inc., Oxford, pp.20-32.

Carbognin, L., Marabini, F. and Tosi, L., 1995. Land Subsidence and Degradation of the Venice Littoral Zone, Italy. In: F.B.J. Barends, F.J.J. Brouwer and F.H. Schroder (Editors), Fifth International Symposium on Land Subsidence. IAHS Press, The Hague, pp.391-402.

Carnec, C. and Delacourt, C., 2000. Three Years of Mining Subsidence Monitored by Sar Interferometry near Gardanne France. Journal of Applied Geophysics, v.43: pp.43-54.

Cassee, B.N., 2004. Selection of Permanent Scatterer Candidates for Deformation Monitoring [for Msc Degree], Delft University of Technology, Delft, The Netherlands, 77 p.

Chang, Z., Zhang, J., Guo, Q. and Gong, L., 2004. Study on Land Subsidence Evolvement Tendency by Means of "Integrated Dinsar ", Geoscience and Remote Sensing Symposium, IGARSS '04. IEEE International, Anchorage, pp.61-64.

Chilès, J.-P. and Delfiner, P., 1999. Geostatistics, Modelling Spatial Uncertainty. Wiley Series in Probability and Statistics. John Wiley & Sons, Inc, New York, 695 p.

Cho, B.-L., Kong, Y.-K. and Kim, Y.-S., 2005. Interpolation Using Optimum Nyquist Filter for Sar Interferometry. Journal of Electromagnetic Waves and Applications, v.19(is.1): pp.129–135.

Chrzanowski, A., Monahan, C., Roulston, B. and Szostak-chrzanowski, A., 1997. Integrated Monitoring and Modelling of Ground Subsidence in Potash Mines. International Journal of Rock Mechanics and Mining Sciences, v.34(is.3/4): pp.621-637.

Clark, C.D., Evans, D.J.A., Khatwa, A., Bradwell, T. and Jordan, C.J., 2004. Map and Gis Database of Glacial Landforms and Features Related to the Last British Ice Sheet. Boreas, v.33(is.4): pp.359-375.

Cloetingh, S., Ziegler, P.A., Beekman, F., Andriessen, P.A.M., Matenco, L., Bada, G., Garcia-Castellanos, D., Hardebol, N., Dezes, P. and Sokoutis, D., 2005. Lithospheric Memory, State of Stress and Rheology: Neotectonic Controls on Europe's Intraplate Continental Topography. Quaternary Science Reviews, v.24: pp.241-304.

Colesanti, C., Ferretti, A., Prati, C. and Rocca, F., 2003. Monitoring Landslides and Tectonic Motions with the Permanent Scatterers Technique. Engineering Geology, v.68: pp.3-14.

Coulthard, M.A., 1999. Applications of Numerical Modelling in Underground Mining and Construction. Geotechnical and Geological Engineering, v.17: pp.373–385.

CPL, 1999. Coast Erosion Project, Cleveland Potash Limited, Saltburn, pp.1-95.

CPL, 2002a. Personal Correspondence, Production Estimates, Boulby.

CPL, 2002b. Subsidence Contracting. Cleveland Potash Limited, Survey Department, 6 p.

CPL, 2004. Subsidence Reports 2001-2003 to North Yorkshire Moors National Park Planning Committee, Cleveland Potash Limited, Loftus.

Crutzen, P.J., 2002. Geology of Mankind. Nature, 415: pp.23.

ESA, 2002. Ers Sar Calibration: Derivation of Sigma Nill in Esa Ers Sar Pri Products. Issue 2.5d, ESA.

Ferrari, C.R., 1996. Case for Continuing Mining Subsidence Research. Mining Technology, v.78(is.898): pp.171-176.

Ferretti, A., Prati, C. and Rocca, F., 1999. Multibaseline Insar Dem Reconstruction: The Wavelet Approach. IEEE Transactions on geoscience and remote sensing, v.37(is.5): pp.705-715.

Ferretti, A., Prati, C. and Rocca, F., 2000a. Measuring Subsidence with Sar Interferometry: Applications of the Permanent Scatterers Technique. In: G.G. In L Carbognin, and A I Johnson (Editor), Land subsidence; Proceedings of the Sixth International Symposium on Land Subsidence. CNR, pp.67-79.

Ferretti, A., Prati, C. and Rocca, F., 2000b. Nonlinear Subsidence Rate Estimation Using Permanent Scatterers in Differential Sar Interferometry. IEEE Transactions on geoscience and remote sensing, v.38(is.5): pp.2202-2212.

Ferretti, A., Prati, C. and Rocca, F., 2001. Permanent Scatterers in Sar Interferometry. IEEE Transactions on geoscience and remote sensing, v.39(is.1): pp.8-20.

Fialko, Y., Sandwell, D., Simons, M. and Rosen, P., 2005. Three-Dimensional Deformation Caused by the Bam, Iran, Earthquake and the Origin of Shallow Slip Deficit. Nature, v.435: pp.295-299.

Gabriel, A.K., Goldstein, R.M. and Zebker, H.A., 1989. Mapping Small Elevation Changes over Large Areas: Differential Radar Interferometry. Journal of Geophysical Research, v.94(is.B7): pp.9183-9191.

Goldstein, R.M., Caro, E.R. and Wu, C., 1985. Method and Apparatus for Contour Mapping Using Synthetic Aperture Radar. In: U.S. Patent (Editor).

Goudie, A. and Viles, H., 1998. The Earth Transformed, an Introduction to Human Impacts on the Environment. Blackwell Publishers Inc., Oxford, 276 p.

Hanssen, R.F., 2001. Radar Interferometry Data Interpretation and Error Analysis Remote Sensing and Digital Image Processing. Remote Sensing and Digital Image Processing. Kluwer Academic Publishers, Dordrecht, 308 p.

Hanssen, R.F. and Ferretti, A., 2002. Deformation Monitoring by Satellite Interferometry, Design Parameters and Environmental Factors Affecting Feasibility. GIM International, v.16(is.9): pp.52-57.

Hastie, T., Tibshirani, R. and Friedman, J., 2001. The Elements of Statistical Learning. Springer Series in Statistics. Springer, New York, 533 p.

Hemingway, J.E., 1974. Jurassic. In: D.H. Rayner and J.E. Hemmingway (Editors), The Geology and Mineral Resources of Yorkshire. Yorkshire Geological Society, pp.161-223.

Hemingway, J.E. and Wilson, V., 1963. The Jurassic. In: G.T. Raine (Editor), No 34: Geology of the North Yorkshire Coast. Geologists' Association Guides. Benham and Company Limited, Colchester, 34 p.

Hollis, D. and Perry, M., 2004. A New Set of Long-Term Averages for the Uk, Met Office, Exeter, 21 p.

Horton, M.C., 1979. The Story of Cleveland, History, Anecdote and Legend. Cleveland County Library, Hartlepool, 568 p.

Humphries, L., 2001. A Review of Relative Sea Level Rise Caused by Mining-Induced Subsidence in the Coastal Zone: Some Implications for Increased Coastal Recession. Climate research, v.18: pp.147-156.

Kampes, B. and Usai, S., 1999. Doris: The Delft Object-Oriented Radar Interferometric Software, ITC 2nd ORS symposium. ITC, Enschede, 4 p. CD-rom.

Kampes, B.M., 2006. Radar Interferometry, Persistent Scatterer Technique. Remote Sensing and Digital Image Processing. Springer, Dordrecht, 211 p.

Kampes, B.M. and Hanssen, R.F., 2004. Ambiguity Resolution for Permanent Scatterer Interferometry (Pre-Print). Delft technical university, 8 p.

Keller, E.A. and Pinter, N., 1996. Active Tectonics. Prentice-Hall, Inc., Upper Saddle River, 338 p.

Kemeling, I., Scott, I.M., Petley, D.N., Rosser, N.J., Allison, R.J., J.Long, A. and Stein, A., 2004. Data Driven Modelling of a Complex Mining Subsidence Process. In: M. Ehlers, F. Posa, H.J. Kaufmann, U. Michel and G.D. Carolis (Editors), Remote Sensing for Environmental Monitoring, GIS Applications, and Geology IV. The International Society for Optical Engineering, Maspalomas, pp.288-298.

Ketelaar, G., Leijen, F.V., Marinkovic, P. and Hanssen, R., 2005. On the Use of Point Target Characteristics in the Estimation of Low Subsidence Rates Due to Gas Extraction in Groningen, the Netherlands, European Space Agency, Fringe 2005 Workshop. ESA Publications Division, Frascati, Italy, 6 p. in press.

Kinder, J.P.L., 2001. Cleveland Potash Ltd, Boulby Potash Mine, Subsidence Audit, Wardell Armstrong Engineering & Environmental Solutions, Newcastle-under-Lyme, 11 p.

Kircher, M., Hoffmann, J., Roth, A., Kampes, B., Adam, N. and Neugebauer, H.J., 2003. Applications of Permanent Scatterers on Mining-Induced Subsidence, European Space Agency, Fringe 2003 Workshop (ESA SP550). ESA Publications Division, Frascati, Italy, 6 p. CD-rom.

Klees, R. and Massonnet, D., 1999. Deformation Measurements Using Sar Interferometry: Potential and Limitations. Geologie en Mijnbouw, v.77: pp.161-176.

Kooij, M.W.A.v.d., Halsema, D.v., Groenewoud, W., Mets, G.J., Overgaauw, B. and Visser, P.N.A.M., 1995. Sar Land Subsidence Monitoring. NRSP-2 95-13, Netherlands Remote Sensing Board (BCRS), Delft, The Netherlands, 30 p.

Kratzsch, H., 1983. Mining Subsidence Engineering. Springer-Verlag, Berlin Heidelberg New York, 543 p.

Leijen, F.V. and Hanssen, R., 2003. Deformation Monitoring Using Radar Interferometric Time Series: A Review of Methodologies. Delft University of Technology, 1-7.

Lillesand, T.M. and Kiefer, R.W., 2000. Microwave Sensing, Remote Sensing and Image Interpretation. John Wiley & Sons, Inc., Chichester, pp.616-705.

Massonnet, D. and Feigl, K.L., 1998. Radar Interferometry and Its Application to Changes in the Earth's Surface. Reviews of Geophysics, v.36(is.4): pp.441-500.

Milne, J.K., 1978. The Potash Deposits and Their Associates in the Area of the Boulby Mine, Cleveland., University of Edinburgh, Edinburgh, 506 p.

Mitas, L. and Mitasova, H., 1988. General Variational Approach to the Interpolation Problem. Computers and Mathematics with Applications, v.16(is.12): pp.983-992.

Mouchel, L.G. and Partners, 1996. Shoreline Management Plan, Huntcliffe (Saltburn) to Flamborough Head Sub Cell 1d. 48014/3689.0, Scarborough Borough Council, Redcar Borough Council and East Riding of Yorkshire Council.

NAM, 2000. Bodemdaling Door Aardgaswinning Status Rapport 2000 En Prognose Tot Het Jaar 2050. 2000-02-00410, Nederlandse Aardolie Maatschappij B.V., Assen.

NCB, 1966. Subsidence Engineers' Handbook, National Coal Board - Production Department, 130 p.

OS, 2003, Landline, Ordnance Survey, EDINA datacentre, 1:2,500

OS, 2005, Land-Form Profile® - Contours & Digital Terrain Mapping, Ordnance Survey, EDINA datacentre, 1:10,000

OS, 2006, Colour Raster, Ordnance Survey, EDINA datacentre, 1:25,000

Raucoules, D., Maisons, C., Carnec, C., Mouelic, S.L., King, C. and Hosford, S., 2003. Monitoring of Slow Ground Deformation by Ers Radar Interferometry on the Vauvert Salt Mine (France), Comparison with Ground-Based Measurement. Remote Sensing of Environment(is.88): pp.468–478.

Rawson, P.F. and Wright, J.K., 2000. The Yorkshire Coast. Geologists' Association Guide, v.34. Dinkyprint, London, 130 p.

Rayner, D.H. and Hemingway., J.E. (Editors), 1974. The Geology and Mineral Resources of Yorkshire. Maney and son ltd., Leeds, 405 p.

Rees, S., Charles, R. and Wightman, S., 2001. Moorland Research Review 1990-1995. North York Moors National Park Authority, 150 p.

Rocca, F., Prati, C., Guarnieri, A.M. and Ferretti, A., 2000. Sar Interferometry and Its Applications. Surveys in Geophysics, v.21(is.2/3): pp.159-176.

Rosen, P.A., Hensley, S., Joughin, I.R., Li, F.K., Madsen, S.N., Rodriquez, E. and Goldstein, R.M., 2000. Synthetic Aperture Radar Interferomtery. Proceedings of the IEEE, v.88(is.3): pp.333-381.

Rosser, N.J., 2003. Measurement of Cleveland Potash Limited Subsidence Benchmark Positions and Heights Using Differential Gps Method Statement, University of Durham, Durham, 21 p.

Scharroo, R. and Visser, P., 1998. Precise Orbit Determination and Gravity Field Improvement for the Ers Satellites. Journal of Geophysical Research, v.103(is.C4): pp.8113-8127.

Schmidt, D.A. and Bürgmann, R., 2003. Time Dependent Land Uplift and Subsidence in the Santa Clara Valley, California, from a Large Insar Data Set. Journal of Geophysical Research, v.108(is.B9): pp.1-13.

Shennan, I., 1988. Holocene Crustal Movements and Sea-Level Changes in Great Britain. Journal of Quaternary Science, v.4(is.1): pp.77-89.

Shennan, I. and Horton, B., 2002. Holocene Land- and Sea-Level Changes in Great Britain. Journal of Quaternary Science, v.17(is.5/6): pp.511-526.

Sheorey, P.R., Loui, J.P., Singh, K.B. and Singh, S.K., 2000. Ground Subsidence Observations and a Modified Influence Function Method for Complete Subsidence Prediction. International Journal of Rock Mechanics and Mining Sciences, v.37: pp.801-818.

Sigmon, K., 1998. Matlab Primer. CRC Press LLC, London, 130 p.

Simms, M.J., Chidlaw, N., Morton, N. and Page, K.N., 2004. British Lower Jurassic Stratigraphy. Geological Conservation Review Series, v.30. Joint Nature Conservation Committee, Peterborough, 458 p.

Spratt, D.A. and Harrison, B.J.D. (Editors), 1989. The North York Moors Landscape Heritage. The North York Moors National Park, 232 p.

Stephens, J.C., Jr., L.H.A. and Chen, E., 1984. Organic Soil Subsidence. In: T.L. Holzer (Editor), Man-Induced Land Subsidence - Reviews in Engineering Geology Vi. Geological Society of America, Inc., Colorado, pp.107-122.

Stow, R.J. and Wright, P., 1997. Mining Subsidence Land Surveying by Sar Interferometry. In: T.D. Guyenne and D. Danesy (Editors), Third ERS Symposium-Space at the Service of our Environment. ESA Publication Division, Florence, Italy, pp.525-530.

Strozzi, T., Tosi, L., Carbognin, L., Wegmüller, U. and Galgaro, A., 1999. Monitoring Land Subsidence in the Euganean Geothermal Basin with Differential Sar Interferometry, Fringe'99 - Advancing ERS SAR Interferometry from Applications towards Operations (ESA SP-478). ESA Publishing Division, Liège, Belgium, 10 p. CD-rom.

Strozzi, T., Wegmuller, U., Werner, C., Wiesman, A., Tosi, L., Teatini, P. and Carbognin, L., 2003. Venezia Subsidence Monitoring Service in the Lagoon of Venice for Regional Administrative and Water Authorities Data User Programme (Dup), Ii Period, Gamma Remote Sensing and Instituto di Scienze Marine, 25 p.

Teatini, P. and Gambolati, G., 1995. A New Three-Dimensional Nonlineair Model of the Subsidence at Venice. In: F.B.J. Barends, F.J.J. Brouwer and F.H. Schroder (Editors), Fifth International Symposium on Land Subsidence. IAHS Press, The Hague, pp.353-361.

Thomas, D.S.G. and Goudie, A. (Editors), 2000. The Dictionary of Physical Geography. Blackwell Publishers Ltd, 610 p.

Tosi, L., Carbognin, L., Strozzi, T. and Wegmuller, U., 2002. Evidence of the Present Relative Land Stability of Venice, Italy, from Land, Sea, and Space Observations. Geophysical Research Letters, v.29(is.12): pp.1562 3.1-3.4.

Usai, S., 1997. The Use of Man-Made Features for Long Time Scale Insar, Geoscience and Remote Sensing, IGARSS '97. 'Remote Sensing - A Scientific Vision for Sustainable Development'. IEEE International, Singapore, pp.1542-1544.

Usai, S. and Hanssen, R., 1997. Long Time Scale Insar by Means of High Coherence Features. In: T.D. Guyenne and D. Danesy (Editors), Third ERS Symposium-Space at the Service of our Environment. ESA Publication Division, Florence, Italy, pp.225-228.

Walter, D., Hoffmann, J., Kampes, B. and Sroka, A., 2004. Radar Interferometric Analysis of Mining Induced Surface Subsidence Using Permanent Scatterer. In: H. Lacoste and L. Ouwehand (Editors), Proceedings of the 2004 Envisat & ERS Symposium (ESA SP-572). ESA Publications Division, Salzburg, 8 p. CD-rom.

Watts, A.B., 2001. Isostasy and Flexure of the Lithosphere. Cambridge University Press, Cambridge, 458 p.

Waveren, R.H.v., Groot, S., Scholten, H., Geer, F.C.v., Woesten, J.H.M., Koeze, R.D. and Noort, J.J., 1999. Good Modelling Practice Handbook, RIZA The Netherlands, Lelystad, 167 p.

Wegmüller, U., Strozzi, T., Wiesmann, A. and Werner, C., 1999. Land Subsidence Mapping with Ers Interferometry: Evaluation of Maturity and Operational Readiness, Fringe'99 - Advancing ERS SAR Interferometry from Applications towards Operations (ESA SP-478). ESA Publishing Division, Liège, Belgium, 9 p. CD-rom.

Wegmuller, U., Werner, C., Strozzi, T. and Wiesmann, A., 2004. Monitoring Mining Induced Surface Deformation, Geoscience and Remote Sensing Symposium, IGARSS '04. IEEE International, Anchorage, pp.1933-1935.

Whittaker, B.N. and Reddish, D.J., 1989. Subsidence Occurrence, Prediction and Control. Developments in Geotechnical Engineering, 56. Elsevier, Amsterdam, 528 p.

Woodhouse, I.H., 2006. Introduction to Microwave Remote Sensing. Taylor and Francis Group, Edinburgh, 370 p.

Wright, P. and Stow, R., 1999. Detecting Mining Subsidence from Space. International Journal of Remote Sensing, v.20(is.6): pp.1183-1188.

Young, L.E. and Stoek, H.H., 1916. Subsidence Resulting from Mining. Bulletin No.91, University of Illinois Engineering Experiment Station, 204 p.